UNIVERSITY OF LONDON THESIS

Degree PhD Year 2006 Name of Author STONE, Daniel James

Kinetics of Key Peroxy Radical Reactions Involved in Atmospheric Oxidation Processes

Daniel Stone

University College London

A thesis submitted in partial fulfilment for the degree of Doctor of Philosophy

ProQuest LLC
789 East Eisenhower Parkway
P.O. Box 1346
Ann Arbor, MI 48106-1346

Abstract

The aims of this work were to investigate the kinetics of key peroxy radical reactions involved in atmospheric oxidation processes. The principal peroxy radicals in the Earth's atmosphere are the hydroperoxy radical (HO_2) and the methylperoxy radical (CH_3O_2), and both play an important role in determining the oxidising capacity of the atmosphere – the ability of the atmosphere to remove pollutants.

Both HO_2 and CH_3O_2 radicals self-react:

$$HO_2 + HO_2 (+M) \rightarrow H_2O_2 + O_2 (+M)$$
$$CH_3O_2 + CH_3O_2 \rightarrow 2\ CH_3O + O_2$$
$$\rightarrow CH_3OH + HCHO + O_2$$

in addition to reacting with other species in the atmosphere, including each other:

$$HO_2 + CH_3O_2 \rightarrow CH_3OOH + O_2$$

Despite the importance of these reactions in the troposphere, few investigations of their reaction kinetics have been conducted under tropospheric conditions. In addition, comparisons between modelled and observed concentrations of HO_2, H_2O_2 and CH_3OOH have indicated a need for further laboratory studies of the kinetics of HO_2 and CH_3O_2 radicals.

Experiments have been conducted in this work on the HO_2 and CH_3O_2 self-reactions, and on the $HO_2 + CH_3O_2$ cross-reaction, under a wide range of experimental conditions pertinent to the troposphere. This work employed conventional and laser flash photolysis with broadband ultraviolet absorption spectroscopy, incorporating charge coupled device (CCD) detection to facilitate data acquisition over a broad wavelength range, and on rapid timescales. Classical or numerical models were used to simulate and fit to experimental data by optimising the kinetic parameters in the models. Results show the rate coefficient for the HO_2 self-reaction to be more strongly dependent on temperature and water vapour than previously thought, while the rate coefficient for the CH_3O_2 self-reaction was found to be only very weakly dependent on temperature under the conditions employed in this work. Results for the HO_2-CH_3O_2 cross-reaction were found to be in good agreement with previous work. The improvements in both accuracy and precision associated with CCD detection, and the use of experimental conditions directly relevant to the troposphere, have led to a considerable improvement in our understanding of the roles of HO_2 and CH_3O_2 radicals in the Earth's atmosphere, which is also discussed in this thesis.

Acknowledgements

There are a number of people who have been invaluable in getting me to this point, and I would like to say thank you to all those who have provided me with help, support and encouragement along the way.

I would like to thank my supervisor, David Rowley, for providing me with this opportunity, and for never letting me take the easy option. I would also like to thank Kate King, Sarah Dixon and Gavin Boakes, not only for their guidance in the laboratory, but also for their friendship. Thanks must also go to the rest of the Physical Chemistry group at UCL, and to Angela Wolff, Claire Ricketts, Emma Wilson and Susan Creighan in particular.

Technical staff at UCL have been more help than they could possibly imagine, and I would like to extend my gratitude to Dick Waymark and Roy Northeast for greeting every challenge with good humour and endless patience.

Finally, I must thank my parents, sister, family and friends for helping me see this through until the end.

Contents

List of Figures

List of Tables

Chapter 1
Atmospheric Physics and Chemistry

The nature of the Earth's atmosphere has been of interest to man for millennia, and the study of air and the atmosphere is among the oldest branches of science. The Ancient Greeks believed air, and the Earth's atmosphere, to be one of the four elements comprising all matter, and this notion persisted until the seventeenth century and the discovery that air consists of a mixture of gases.

In the last few hundred years, it has been recognised that changes to the Earth's atmosphere resulting from man's actions can have profound effects on the natural environment, and the need to understand the impact of man's actions on the atmosphere has never been greater. Changes to atmospheric composition can occur directly through release of pollutants, but also indirectly through chemical transformation of pollutants, and can potentially result in environmental issues such as ozone depletion, smog formation and global warming. Any approach taken to address such environmental problems arising from changes to chemical composition must be based on a sound understanding of atmospheric chemistry in context of the natural physics and chemistry of the atmosphere. A brief discussion of atmospheric physics and chemistry is given in the following chapter.

1.1 Atmospheric Pressure

The variation in atmospheric pressure with altitude can be calculated from the change in pressure, dp, for an incremental change in altitude, dz:

$$dp = -g\,\rho\,dz \qquad (1.i)$$

since $dp = -dmg/A$ and $dm/A = \rho\,dz$, where g is the acceleration due to gravity (9.81 m s^{-2}), ρ is the density of air (kg m^{-3}) and m is the mass of air above an area A. The density of air, ρ, can be calculated to a good approximation using the ideal gas law:

$$\rho = \frac{m}{V} = \frac{nM}{V} = \frac{p}{RT} \qquad (1.ii)$$

Given that gravitational separation of atmospheric gases is destroyed by mixing at altitudes below 100 km, and that the bulk chemical composition of air is constant (section 1.5), M can be taken as the average molar mass of air (0.0288 kg mol^{-1}).

Combination, and rearrangement, of (1.i) and (1.ii) gives:

$$\frac{dp}{p} = -\frac{dz}{H} \qquad (1.iii)$$

where H is the *scale height*, defined as RT/Mg. Integration of (1.iii) between limits of altitude = 0 and altitude = z gives the hydrostatic equation (1.iv):

$$p_z = p_0 \exp\left(-z/H\right) \qquad (1.iv)$$

where p_0 and p_z are atmospheric pressures at altitude 0 (sea level) and z. Note that the derivation of the hydrostatic equation assumes the temperature to be constant.

As can be seen from the hydrostatic equation, atmospheric pressure decreases exponentially with increasing altitude, with the scale height giving the approximate vertical distance over which atmospheric pressure changes by a factor of $1/e$.

A consequence of the hydrostatic equation is that most of the mass of the atmosphere is found at low altitudes – over 99 % of the mass of the atmosphere resides below 50 km in altitude.

1.2 Atmospheric Temperature

The vertical temperature profile of the atmosphere is more complex than the pressure profile, which essentially decreases exponentially with increasing altitude. A schematic vertical temperature profile of the atmosphere is shown in Figure 1.1.

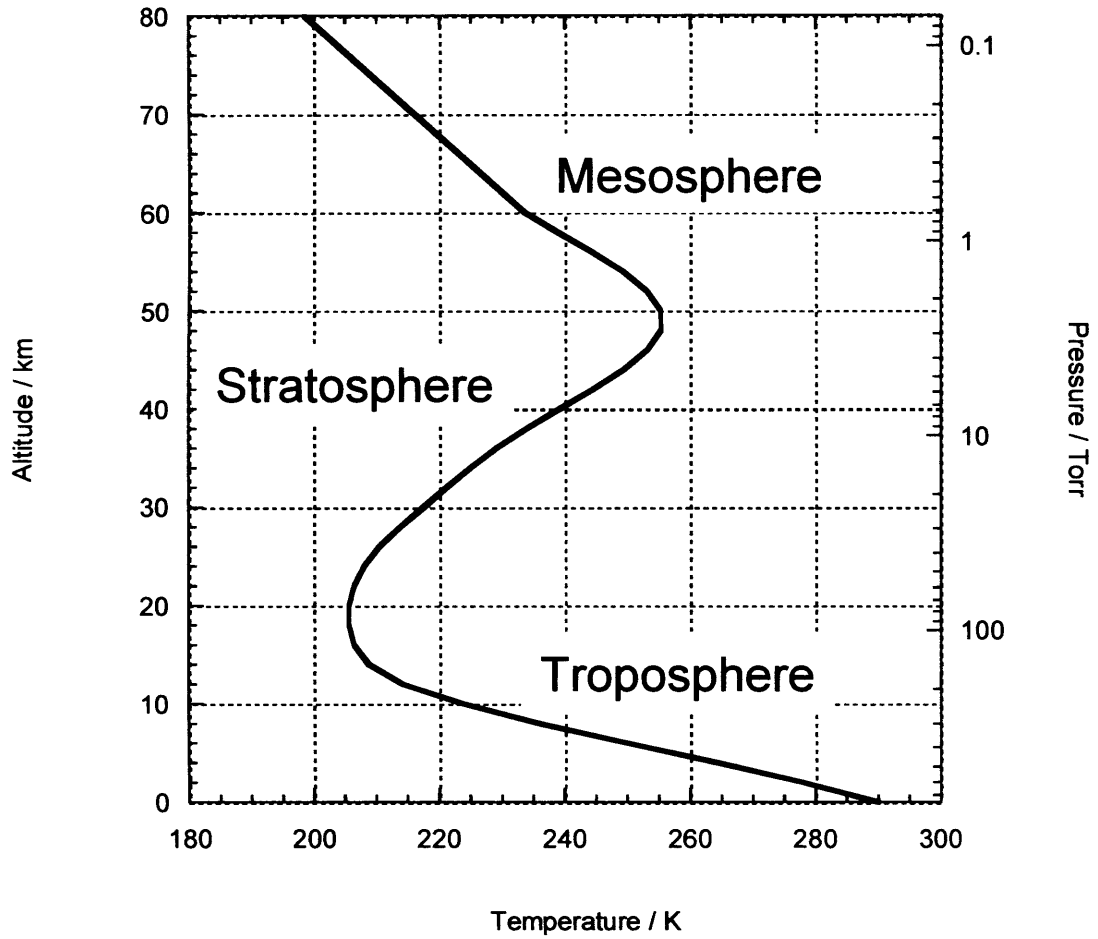

Figure 1.1 : Typical vertical temperature profile of the Earth's atmosphere. Data taken from reference 1.

The rate of change in temperature with increasing altitude, termed the adiabatic lapse rate, is used to define a number of distinct vertical layers in the atmosphere. The lowermost layer of the atmosphere is the troposphere (0 to approximately 15 km in altitude) in which the adiabatic lapse rate is negative, as the temperature falls with increasing altitude. The troposphere is itself often divided into two layers – the boundary layer and the free troposphere. The boundary layer can extend up to 2 km in altitude and is the region of the atmosphere closest to ground level where highly turbulent mixing occurs and interactions between the Earth's surface and its atmosphere are greatest. The free troposphere is the region above the boundary layer where interactions between surface and atmosphere are less significant.

Above the troposphere is the stratosphere, approximately 15 to 50 km in altitude and separated from the troposphere by the tropopause. The adiabatic lapse rate in the stratosphere is positive – the temperature increases with increasing altitude. The

positive lapse rate in the stratosphere results from the interactions between the atmosphere and solar radiation, and absorption of solar UV radiation by ozone in particular.

The region of the atmosphere above the stratosphere is the mesosphere, bounded below by the stratopause and above by the mesopause. The mesosphere extends to approximately 90 km in altitude and has a negative adiabatic lapse rate. Beyond the mesosphere lies the thermosphere, where the adiabatic lapse rate is again positive. The positive lapse rate in the thermosphere is in fact a direct consequence of the low pressure conditions – molecular collisions are so infrequent that any absorption of solar radiation by species in this region leads to high translational velocities, and high apparent temperatures. However, given the low number densities in the thermosphere, thermal equilibration between translational and vibrational and rotational modes does not occur, and the thermosphere does not store much energy.

1.3 Atmospheric Stability

Whilst the lowest 100 km of the atmosphere can be considered to be generally well-mixed, local variations in temperature and pressure can affect the ease of atmospheric mixing, particularly as a function of altitude. Specifically, the adiabatic lapse rate can also be used to determine what is known as the 'stability' of the atmosphere with respect to vertical mixing. For a theoretical atmosphere containing no condensable vapours, the dry adiabatic lapse rate, Γ_d, can be defined from the First Law of Thermodynamics as

$$\Gamma_d = \frac{dT}{dz} = -\frac{g}{c_p} \qquad (1.v)$$

where g is the acceleration due to gravity and c_p is the specific heat capacity of air. For the Earth's atmosphere, the dry adiabatic lapse rate is -9.8 K km^{-1}. In practice, the presence of condensable vapours in the atmosphere, notably water vapour, increases this value to approximately -6.5 K km^{-1} in the troposphere due to condensation and release of latent heat on cooling at higher altitudes. Local variations in Γ_d affect vertical mixing as described below.

Any gas displaced upwards in the atmosphere will expand and cool due to the decrease in pressure. Adiabatic expansion ($dq = 0$), a reasonable approximation in the gas phase due to inefficient thermal transfer, results in a decrease in internal energy and a cooling of the gas. If the adiabatic lapse rate of the vertically displaced gas is greater (less negative) than that of the surrounding atmosphere the gas will be warmer than its surroundings after displacement. The displaced gas will therefore be less dense than the surrounding atmosphere, since they are at the same pressure, and will continue to rise. Similarly, if the gas were displaced downwards it would become cooler and denser than its surroundings and would continue to sink. In this situation, typical of the troposphere, the atmosphere is said to be unstable with respect to vertical mixing, and convection will occur until the displaced gas is sufficiently mixed with the surrounding atmosphere such that the lapse rates of the two are equalised. In contrast, a gas that is displaced upwards with an adiabatic lapse rate less than that of the surrounding atmosphere will become cooler and more dense than its surroundings as it rises. Under these conditions, the atmosphere is said to be stable with respect to vertical mixing. In this case, the displaced gas would experience a restoring force from the surrounding atmosphere, causing it to return to its original altitude. Analogously, any gas displaced downwards would experience a buoyancy force. This situation is the case in the stratosphere, with the result that well-mixed tropospheric air does not readily penetrate the stratosphere.

Although tropospheric and stratospheric air do not readily mix, there is some exchange between the two regions due to an imbalance between the absorbed solar energy and outgoing solar terrestrial radiation with latitude. This imbalance leads to heating of tropospheric air at low latitudes and cooling of tropospheric air at high latitudes. Therefore, at low latitudes tropospheric air rises into the stratosphere, with a reverse flow occurring at higher latitudes. Such meridional circulation is known as Brewer-Dobson circulation, and has important consequences for the water vapour content of the stratosphere. Since air enters the stratosphere only at low latitudes, where the tropopause is particularly cold ($T < 190$ K), very little water vapour enters the stratosphere due to an effective 'freezing out' of water at the tropopause.

1.4 Radiative Balance

Given that the troposphere, comprising most of the mass of the atmosphere, is well-mixed, relatively simple models can give a reasonably good estimate of the Earth's temperature. For example, the temperature of the Earth's surface can be estimated by considering the radiative balance of the troposphere – the difference between the amount of energy supplied by the sun to the Earth and its atmosphere and the amount of energy re-radiated into space by the Earth and its atmosphere. This is described below.

The amount of energy supplied to the Earth by the sun, R_i, is given by the product of the solar irradiance at the top of the atmosphere, S, the cross-sectional area of the irradiance, πr^2, where r is the radius of the Earth, and the fraction of light that is absorbed, $(1 - A)$, where A, the albedo, is the fraction of incoming solar radiation reflected back into space.

$$R_i = S\pi r^2 (1 - A) \qquad \text{(1.vi)}$$

If, for simplicity, the Earth can be considered to act as a black body at temperature T, the amount of energy re-radiated into space, R_o, is related to T by the Stefan-Boltzmann Law:

$$R_o = 4\pi r^2 \sigma T^4 \qquad \text{(1.vii)}$$

where $4\pi r^2$ is the area over which the energy is radiated, the surface area of Earth, and σ is Stefan's constant (5.67×10^{-8} W m^{-2} K^{-4}).

The temperature of the Earth can therefore be estimated by invoking radiative balance and equating the energy supplied to the Earth by the sun to the energy emitted by the Earth:

$$S\pi r^2 (1 - A) = 4\pi r^2 \sigma T^4 \qquad \text{(1.viii)}$$

Substituting typical values[2] of S = 1370 W m^{-2} and A = 0.33 into (1.viii) gives an average surface temperature of 254 K – clearly an underestimation of the true average surface temperature. The main reason for this is that this analysis ignores any absorption of radiation by gases in the atmosphere.

Spectral distributions of emission from black body sources at temperatures of 6000 K (typical of the Sun) and 254 K (typical of the net emission temperature of the Earth) are shown in Figure 1.2. As can be seen, the peak emission of a black body at 6000 K occurs at a wavelength of approximately 0.6 μm in the visible region of the electromagnetic spectrum, while the peak emission for a black body at 254 K occurs at approximately 10 μm, in the infrared region of the electromagnetic spectrum.

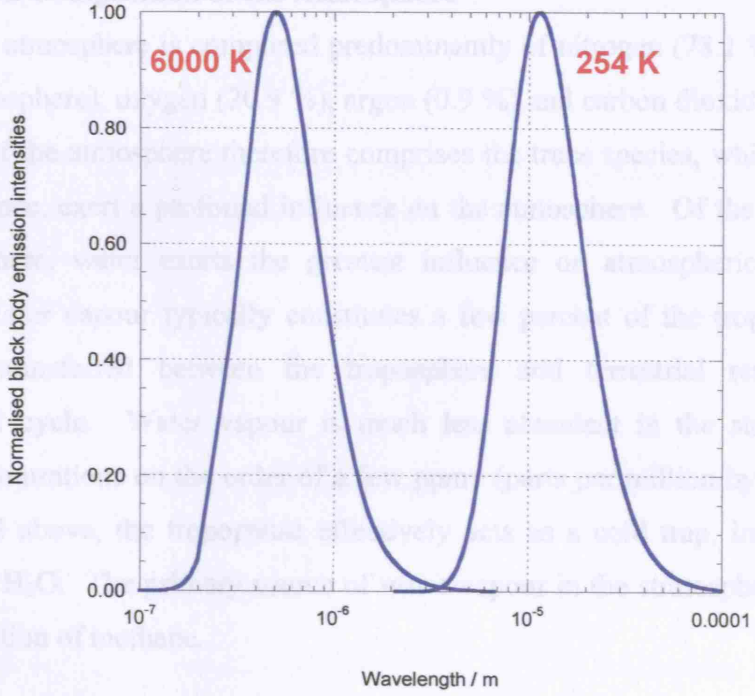

Figure 1.2 : Black body emission curves of the Sun (6000 K) and the Earth (254 K).

While the Earth's atmosphere is largely transparent to visible radiation, resulting in most of the incoming solar radiation reaching the Earth's surface, there is significant absorption of infrared radiation in the atmosphere by trace gases such as CO_2, CH_4, H_2O, O_3, N_2O and chlorofluorocarbons (CFCs). The presence of these gases in the atmosphere results in what is known as the natural greenhouse effect. Infrared radiation

emitted from the Earth's surface is absorbed in the atmosphere by such greenhouse gases (gases with infrared active vibrational modes) before being re-emitted in all directions with a component directed towards the Earth's surface, resulting in elevated surface temperatures. Inclusion of this effect into the above model gives an estimated surface temperature in close agreement with the globally averaged value of *ca.* 288 K. Increases in atmospheric abundances of greenhouse gases as result of human activity has led to concern over the possibility of a consequent increase in global temperature. The Kyoto protocol,[3] which came into force in February 2005, aims to reduce emissions of greenhouse gases, particularly carbon dioxide, by around 5.2 % below their 1990 levels by 2012, but the protocol has not been ratified by a number of nations, and its success remains to be seen.

1.5 Chemical Composition of the Atmosphere

The Earth's atmosphere is composed predominantly of nitrogen (78.1 %, by volume of the dry atmosphere), oxygen (20.9 %), argon (0.9 %) and carbon dioxide (0.04 %). The remainder of the atmosphere therefore comprises the trace species, which, despite their low abundance, exert a profound influence on the atmosphere. Of the trace species in the atmosphere, water exerts the greatest influence on atmospheric chemistry and physics. Water vapour typically constitutes a few percent of the troposphere, and is constantly transferred between the troposphere and terrestrial reservoirs in the hydrological cycle. Water vapour is much less abundant in the stratosphere, with typical concentrations on the order of a few ppmv (parts per million by volume), since, as discussed above, the tropopause effectively acts as a cold trap, inhibiting upward transport of H_2O. The primary source of water vapour in the stratosphere is thought to be the oxidation of methane.

Several other important trace gases are listed in Table 1.1, together with their major natural and anthropogenic sources. Ozone, O_3, is not included in this list, but is an extremely important trace gas and is discussed in detail in section 1.6, below.

Compound	Natural Sources	Anthropogenic Sources
Methane (CH_4)	Emissions from swamps, bogs, wetlands and oceans; enteric fermentation in wild animals.	Natural gas leakage; enteric fermentation in domesticated animals; emissions from paddies; combustion.
Hydrocarbons (HCs) and volatile organic compounds (VOCs)	Vegetation; aerobic biological processes; forest fires.	Natural gas leakage; combustion; vehicle exhausts; paints; solvents.
Carbon monoxide (CO)	Oxidation of natural HCs and VOCs ; oceans; forest fires.	Oxidation of anthropogenic HCs and VOCs; incomplete combustion; blast furnaces.
Nitric oxide (NO)	Anaerobic biological processes in soil; forest fires; electrical storms.	High temperature combustion; aircraft.
Nitrogen dioxide (NO_2)	Forest fires; electrical storms.	High temperature combustion.
Nitrous oxide (N_2O)	Denitrifying bacteria in soil; oceans.	Combustion; industrial processes.
Ammonia (NH_3)	Aerobic biological processes in soil; breakdown of amino acids in organic matter.	Combustion; waste treatment.
Hydrogen sulphide (H_2S)	Anaerobic fermentation; volcanic activity.	Oil refineries; combustion; animal manure.
Sulphur dioxide (SO_2)	Oxidation of H_2S; volcanic activity.	Combustion.
Dimethyl sulphide (CH_3SCH_3)	Aerobic biological processes in oceans.	Animal manure.
Methyl chloride (CH_3Cl)	Biological processes in oceans; algae.	PVC manufacture; tobacco consumption.
Methyl bromide (CH_3Br)	Aerobic biological processes.	Soil fumigation; fire retardants.
Chlorofluorcarbons (CFCs)	None.	Refrigerants; aerosol propellants; solvents.

Table 1.1: Important atmospheric trace gases and their main natural and anthropogenic sources.[2]

The atmosphere also contains a significant amount of matter in condensed phases suspended in air – aerosols. Atmospheric aerosol particles and droplets vary greatly in size and composition, and can be dispersed directly from the Earth's surface or

produced by gas phase chemistry. The Earth's radiation budget is profoundly affected by aerosols due to their interactions with solar radiation and their ability to act as cloud condensation nuclei. Aerosol surfaces also provide sites for adsorption of trace gases, and can result in heterogeneous chemistry and catalysis of trace gas reactions.

Despite large emission rates of many species into the Earth's atmosphere, the bulk composition, while showing diurnal or seasonal cycles, remains largely unaffected. Efficient removal processes must therefore be in operation. Species can be removed from the atmosphere by either physical or chemical means, with the latter often providing a source of other atmospherically important trace species. Physical removal can occur by dry deposition, whereby a species is absorbed at the Earth's surface, or wet deposition, in which a species is either incorporated into cloud particles or droplets as they form (rain out) or dissolved in precipitation as it falls (wash out). Direct solar photolysis is also an important loss process for trace species, and the initiation of a great deal of chemical change in the atmosphere. Chemical removal of trace species following photolysis often occurs by oxidation processes, and necessitates the production of other species such as the OH radical discussed below in section 1.6.2.

1.6 Ozone in the Atmosphere

Ozone, O_3, is a naturally occurring trace gas present throughout the Earth's atmosphere. However, ozone is not uniformly distributed in the atmosphere and its concentration is strongly dependent on altitude, with maximum concentrations found in the stratospheric ozone 'layer',[4,5,6] as shown in Figure 1.3.

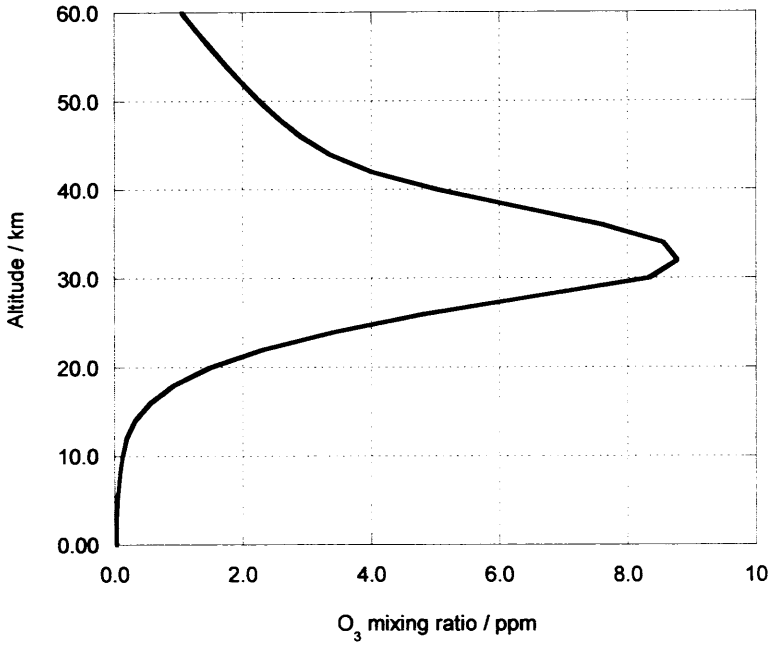

Figure 1.3 : Mixing ratio of ozone as a function of altitude (ppm = parts per million). Data taken from reference 1.

1.6.1 Stratospheric Ozone

Stratospheric ozone is responsible for protecting life on Earth from ultraviolet solar radiation due to its strong absorption of electromagnetic radiation, particularly at wavelengths below 290 nm (the Hartley band). Radiation of wavelengths less than 290 nm is capable of causing severe biological cell damage, and the importance of ozone in the stratosphere cannot therefore be underestimated.[1,2]

The first attempt to rationalise the vertical distribution of ozone in the atmosphere was made by Chapman using an oxygen-only photochemical steady-state model consisting of the following processes:[7]

$$O_2 + h\nu \rightarrow O + O \quad (\lambda < 242 \text{ nm}) \quad (1.1)$$

$$O + O_2 + M \rightarrow O_3 + M \quad (1.2)$$

$$O_3 + h\nu \rightarrow O(^3P) + O_2 \quad (\lambda < 1180 \text{ nm}) \quad (1.3)$$

$$O + O_3 \rightarrow 2\,O_2 \quad (1.4)$$

$$O + O + M \rightarrow O_2 + M \quad (1.5)$$

The balance between the production and loss of ozone sets up a steady state, and while the Chapman model correctly predicts the form of the vertical distribution of atmospheric ozone and the altitude at which the maximum O_3 concentration occurs, the modelled O_3 concentrations are significantly higher than those observed in the atmosphere.[1,2]

Reactions (1.2) and (1.3) have been shown to be rapid processes interconverting O and O_3, making it convenient to consider O and O_3 together as 'odd-oxygen', where the odd-oxygen concentration is given by the sum of [O] and [O_3]. The Chapman model can therefore be simplified by considering only the equilibrium between the reactions resulting in overall production or removal of odd-oxygen, leaving only reactions (1.1), (1.4) and (1.5). Furthermore, given the low pressures in this region, reaction (1.5) has been shown to be too slow to be of importance in the stratosphere, and the principal equilibrium is between reactions (1.1) and (1.4). This balance between processes indicates the reason for the overestimation of odd-oxygen abundances by the Chapman mechanism. Laboratory measurements of $k_{1.4}$ have shown that reaction (1.4) can only account for the removal of about 25 % of the odd-oxygen produced by solar photolysis of O_2.[2,8]

Ozone and oxygen atoms do, in fact, react with many trace species in the atmosphere to produce O_2, often resulting in the generation of catalytic cycles with the same overall effect as (1.4):

$$X + O_3 \rightarrow XO + O_2 \qquad (1.6)$$

$$XO + O \rightarrow X + O_2 \qquad (1.7)$$

$$\text{NET:} \quad O_3 + O \rightarrow 2\,O_2$$

The rates of such cycles often exceed that of the elementary reaction (1.4) either because [X] exceeds [O] or because $k_{1.6}$ is greater than $k_{1.4}$, as is often the case at stratospheric temperatures due to the high activation energy of (1.4) (E_a = 17 kJ mol^{-1}).[8] Several species have been identified as candidates for X and XO in the natural stratosphere, most notably NO/NO_2 (NO_x), OH/HO_2 (HO_x), H/OH, Cl/ClO and Br/BrO.

Although these species are present in the stratosphere at low concentrations (ppbv, parts per billion by volume), they can be responsible for the destruction of relatively large quantities of odd-oxygen (ppmv, parts per million by volume) due to the catalytic nature of the chemistry.

The efficiency of a particular X/XO catalytic cycle in the stratosphere depends on its competition with other processes involving X or XO, such as null cycles and reservoir formation. Null cycles interconvert X and XO without causing loss of odd-oxygen, for example the null cycle:

$$NO + O_3 \rightarrow NO_2 + O_2 \quad (1.8)$$

$$NO_2 + h\nu \rightarrow NO + O \quad (1.9)$$

$$O + O_2 + M \rightarrow O_3 + M \quad (1.2)$$

is of particular importance since the competing NO/NO_2 catalytic cycle is thought to be responsible for up to 50 % of odd-oxygen loss in the unpolluted atmosphere.[2]

Formation of reservoir species for X and XO interrupts the catalytic cycles due to the unreactivity of the reservoirs towards O and O_3, and allows the sequestered X/XO species to be removed from the atmosphere or transported to other regions where photolysis or further chemistry may re-release the catalytically active species. For example, the reservoir species chlorine nitrate, $ClONO_2$, sequesters both chlorine and NO_x (nitrogen oxides, where $[NO_x] = [NO] + [NO_2]$):

$$ClO + NO_2 + M \rightarrow ClONO_2 + M \quad (1.10a)$$

and releases catalytically active species following photolysis:

$$ClONO_2 + h\nu \rightarrow Cl + NO_3 \quad (1.11a)$$

$$\rightarrow ClO + NO_2 \quad (1.11b)$$

The $ClONO_2$ molecule can also produce photolabile products following chemistry on aerosol surfaces:

$$ClONO_2\,(g) + HCl\,(s) \rightarrow \quad Cl_2\,(g) + HNO_3\,(g) \qquad (1.12)$$

$$ClONO_2\,(g) + H_2O\,(s) \rightarrow \quad HOCl\,(g) + HNO_3\,(g) \qquad (1.13)$$

In the 1970s concerns were raised over the impacts of anthropogenic species on catalytic ozone destruction in the stratosphere. Molina and Rowland[9] predicted in 1974 that chlorofluorocarbons (CFCs), used widely for their chemical inertness as refrigerants and aerosol propellants, released into the Earth's atmosphere would be stable enough to undergo transport to the stratosphere since there are no rapid removal mechanisms for CFCs in the lower atmosphere. In the harsh photochemical conditions of the stratosphere, short wavelength solar photolysis could initiate catalytic ozone destruction due to the release of chlorine atoms and participation of chlorine in ozone loss cycles.

In 1985 Farman *et al.*[10] of the British Antarctic Survey reported a decrease in total column ozone over the Antarctic every October since the late 1970s – later termed the 'ozone hole'. The measurements of Farman *et al.* were made using ground based remote sensing techniques, and similar findings have subsequently been observed using other ground based instruments, balloon experiments, and aircraft and satellite measurements. Figure 1.4 shows a comparison between the mean total column ozone abundances over the South Pole in August (Antarctic Winter) and October (Antarctic Spring) 1993, demonstrating the seasonal behaviour of the phenomenon, while Figure 1.5 shows the mean total column ozone abundances for October recorded over the South Pole since 1967, indicating that loss of ozone over the Antarctic has only occurred in recent decades.

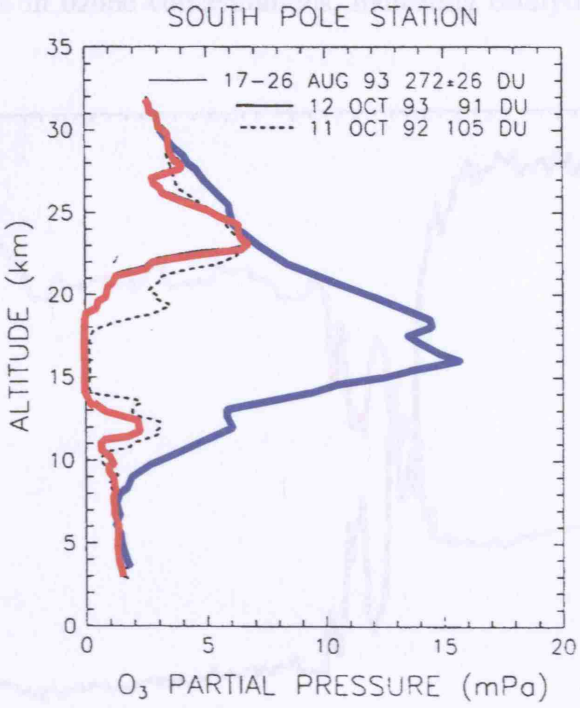

Figure 1.4 : Vertical O_3 abundances measured over the South Pole in August 1993 (blue) and October 1993 (red).[11]

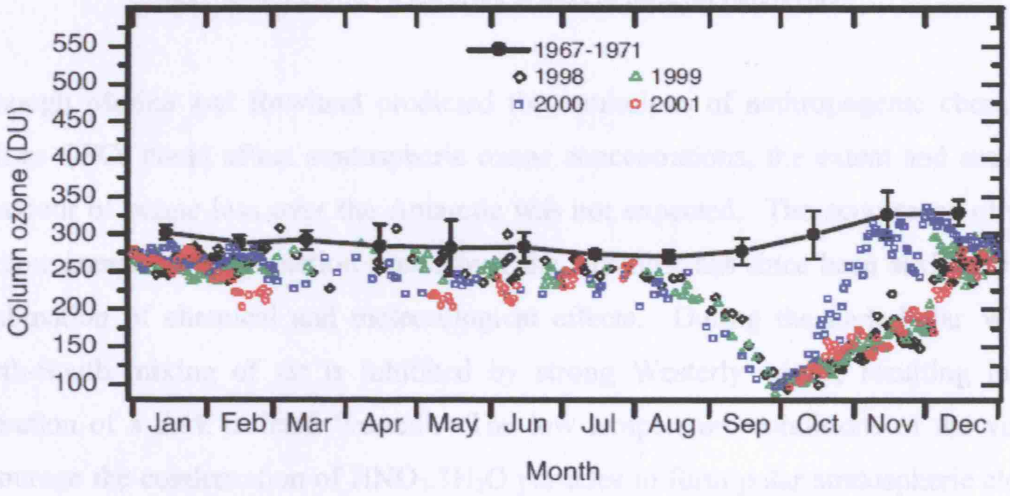

Figure 1.5 : Total ozone abundances measured over the South Pole over several decades.[12] One Dobson unit (DU) is defined as the thickness in hundredths of a mm that the ozone column would occupy, if pure, at standard temperature (273 K) and pressure (760 Torr).

Simultaneous aircraft measurements of O_3 and ClO made over Antarctica in October 1987 revealed a clear anticorrelation between the two species, as shown in Figure 1.6, confirming the role of chlorine species in the destruction of ozone in the Antarctic springtime.[13,14] Furthermore, the concentrations of ClO radicals detected were much

less than the change in ozone concentrations, indicating catalytic nature of the ozone loss.

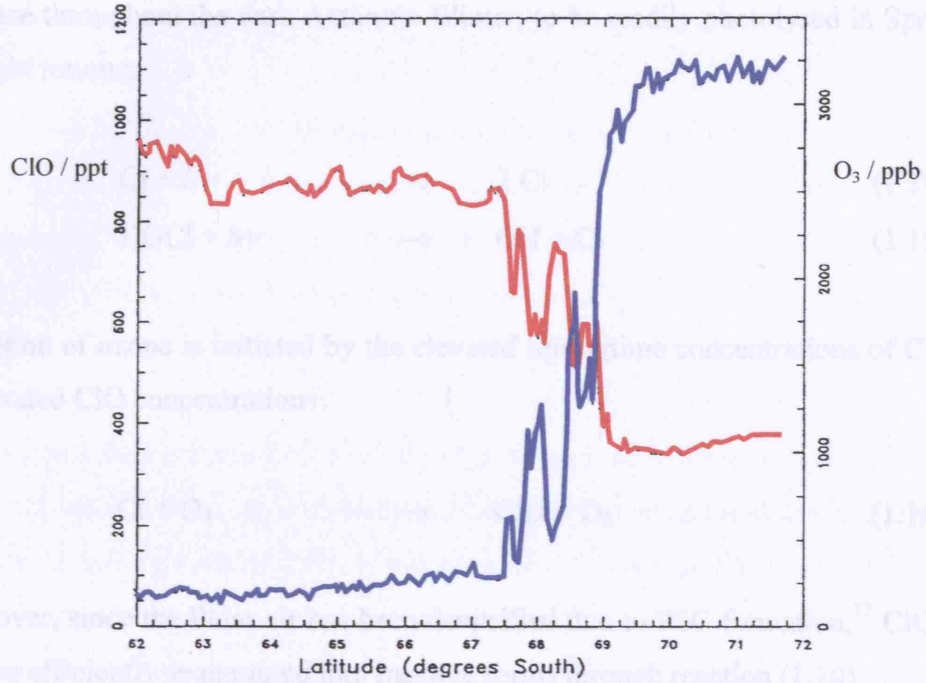

Figure 1.6 : Simultaneous measurements of spatially resolved O_3 (red) and ClO (blue) abundances near the South Pole during October 1987.[14] Note that ClO concentrations are given in units of parts per trillion (ppt), while those of O_3 are given in units of parts per billion (ppb).

Although Molina and Rowland predicted that emissions of anthropogenic chemicals such as CFCs could affect stratospheric ozone concentrations, the extent and seasonal behaviour of ozone loss over the Antarctic was not expected. The occurrence of such extreme annual ozone depletion events over the Antarctic has since been attributed to a combination of chemical and meteorological effects. During the dark Polar Winter North-South mixing of air is inhibited by strong Westerly winds, resulting in the formation of a dark isolated 'vortex'. The low temperature conditions of the vortex encourage the condensation of $HNO_3.3H_2O$ particles to form polar stratospheric clouds (PSCs).[15] Not only do PSCs result in denitrification of the air within the vortex (the sequestration of NO_x), their surfaces also provide a site for heterogeneous reactions such as:[16]

$$ClONO_2\,(g) + HCl\,(s) \rightarrow \quad Cl_2\,(g) + HNO_3\,(g) \qquad (1.12)$$

$$ClONO_2\,(g) + H_2O\,(s) \rightarrow \quad HOCl\,(g) + HNO_3\,(g) \qquad (1.13)$$

The effect of these reactions is to convert relatively stable chlorine reservoir species into more photolabile Cl_2 and HOCl. Concentrations of Cl_2 and HOCl in the polar vortex increase throughout the dark Antarctic Winter, to be readily photolysed in Spring when sunlight returns:

$$Cl + h\nu \rightarrow 2\,Cl \qquad (1.14)$$

$$HOCl + h\nu \rightarrow OH + Cl \qquad (1.15)$$

Depletion of ozone is initiated by the elevated Springtime concentrations of Cl, leading to elevated ClO concentrations:

$$Cl + O_3 \rightarrow ClO + O_2 \qquad (1.16)$$

Moreover, since the Polar air has been denitrified due to PSC formation,[17] ClO radicals are less efficiently sequestered into inactive forms through reaction (1.10).

$$ClO + NO_2 + M \rightarrow ClONO_2 + M \qquad (1.10)$$

Under such conditions, conversion of ClO to Cl through reaction (1.6), completing the catalytic ozone destruction cycle, is reduced due to a combination of low O atom concentrations in the lower stratosphere and the relatively high efficiency of O_3 formation through reaction (1.2).

$$ClO + O \rightarrow Cl + O_2 \qquad (1.6)$$

$$O_2 + O + M \rightarrow O_3 + M \qquad (1.2)$$

Elevated ClO concentrations do, however, lead to the possibility of another catalytic ozone depletion cycle involving the ClO self-reaction and subsequent photolysis of the ClO dimer:[18]

$$2\,(Cl + O_3 \rightarrow ClO + O_2) \qquad (1.16)$$

$$ClO + ClO + M \rightarrow Cl_2O_2 + M \qquad (1.17)$$

$$Cl_2O_2 + h\nu \rightarrow ClOO + Cl \qquad (1.18)$$

$$ClOO + M \rightarrow Cl + O_2 + M \qquad (1.19)$$

NET: $2\,O_3 \rightarrow 3\,O_2$

Throughout Spring, as temperatures rise, PSCs are broken up, re-releasing NO_2. Furthermore, the polar vortex becomes less isolated and polar air mixes with air from mid-latitudes. As a result, chlorine reservoir formation takes place, alleviating the ozone loss and eventually allowing O_3 concentrations to re-equilibrate to 'normal' levels.

Depletion of stratospheric ozone has also been observed more recently over the Arctic,[12] and, to a lesser extent, at mid-latitudes,[12] but neither of these regions experience the severity of the unique conditions of the Antarctic Winter, and the extent of the Antarctic ozone destruction has not been observed elsewhere.[12]

The 1987 Montreal Protocol[12] and its subsequent amendments (London 1990, Copenhagen 1992, Vienna 1995, Montreal 1997 and Beijing 1999) restricted the production of CFCs and other ozone depleting substances. Consequently, the abundance of anthropogenic chlorine compounds in the atmosphere has begun to decrease in the past few years, and the severity of the annual ozone depletion above Antarctica is expected to decrease in the future. This profound environmental change serves to indicate the sensitivity of the atmosphere to chemical processes following anthropogenic activity, and the need to understand, quantify and eventually prevent such changes.

1.6.2 Tropospheric Ozone

Despite being much less abundant in the troposphere than in the stratosphere, ozone is nevertheless an important tropospheric species, and plays a pivotal role in atmospheric oxidation processes responsible for the removal of many anthropogenic chemicals from the atmosphere.[19,20] Ozone is also a greenhouse gas, and at elevated concentrations, ozone is itself a pollutant, linked with increased asthma attacks, eye and lung irritation and crop damage.[12]

Production of O_3 in the troposphere cannot occur following O_2 solar photolysis due to reduced solar intensity at wavelengths below 250 nm in the troposphere – a direct result of UV absorption by oxygen and ozone in the stratosphere. The presence of O_3 in the troposphere is due to downward transport from the stratosphere, with contributions from dissociation of O_2 during electrical storms and a significant fraction formed following solar photolysis of NO_2:[2]

$$NO_2 + h\nu \rightarrow NO + O \quad (1.9)$$

$$O + O_2 + M \rightarrow O_3 + M \quad (1.2)$$

In addition to being an oxidant in its own right, solar photolysis of O_3 at wavelengths below 320 nm is the primary tropospheric source of the hydroxyl radical (OH), the principal oxidising agent of the troposphere in sunlit conditions.

Photolysis of ozone at wavelengths above *ca.* 320 nm produces ground state oxygen atoms, $O(^3P)$, which, in the atmosphere, recombine with O_2 to reform O_3:

$$O_3 + h\nu \rightarrow O_2 + O(^3P) \quad (\lambda>320 \text{ nm}) \quad (1.3)$$

$$O(^3P) + O_2 + M \rightarrow O_3 + M \quad (1.2)$$

At wavelengths below 320 nm, the quantum yield for production of ground state oxygen atoms from ozone photolysis is reduced, as a result of the preferential production of electronically excited oxygen atoms, $O(^1D)$:

$$O_3 + h\nu \rightarrow O_2 + O(^1D) \quad (\lambda<320 \text{ nm}) \quad (1.3)$$

Under the relatively high pressure conditions of the troposphere most $O(^1D)$ atoms produced are rapidly quenched to $O(^3P)$ by collision:

$$O(^1D) + M \rightarrow O(^3P) + M \quad (1.20)$$

However, high tropospheric water vapour concentrations cause reaction of $O(^1D)$ with H_2O to be sufficiently rapid to compete effectively with competition with reaction (1.20), leading to the production of hydroxyl radicals, OH:

$$O(^1D) + H_2O \rightarrow 2\,OH \qquad (1.21)$$

Reaction with OH provides removal mechanisms for many trace gases in the troposphere, and the OH radical is therefore an extremely important species in the lower atmosphere.[2,19,20] Oxidation of carbon monoxide by OH leads to the production of hydrogen atoms and subsequently hydroperoxy radicals (HO_2). In otherwise unpolluted air, HO_2 radicals may then react with ozone to reform OH, resulting in an interconversion between OH and HO_2 and loss of ozone from the troposphere:

$$OH + CO \rightarrow H + CO_2 \qquad (1.22)$$

$$H + O_2 + M \rightarrow HO_2 + M \qquad (1.23)$$

$$HO_2 + O_3 \rightarrow OH + O_2 \qquad (1.24)$$

Since OH and HO_2 rapidly achieve a steady state in this way it is convenient to define OH and HO_2 together as the 'odd hydrogen' family, HO_x, where $[HO_x] = [OH] + [HO_2]$. The amount of atmospheric HO_x is an important factor affecting the oxidising capacity of the atmosphere, and thus the ability of the atmosphere to remove pollutants.

In the absence of NO_x ($NO_x = NO + NO_2$), the major loss process for tropospheric HO_x is the hydroperoxy self-reaction:

$$HO_2 + HO_2\,(+M) \rightarrow H_2O_2 + O_2\,(+M) \qquad (1.25)$$

since the H_2O_2 product is highly soluble in water and consequently readily removed from the troposphere during precipitation.[2,19,20] It should be noted, however, that in some cases, H_2O_2 can facilitate the conversion between OH and HO_2 due to its reaction with OH:[8]

$$H_2O_2 + OH \rightarrow HO_2 + H_2O \qquad (1.26)$$

and, importantly in the upper troposphere, can act as a source of HO_x by solar photolysis:[1,2,8]

$$H_2O_2 + h\nu \rightarrow 2\,OH \qquad (1.27)$$

Despite such competing processes, however, wet deposition remains the dominant fate for H_2O_2 in many regions of the troposphere, particularly the marine boundary layer, due to the presence of high water vapour concentrations.

Another important loss process for HO_x in the unpolluted atmosphere is the cross-reaction (1.28) between HO_2 and methylperoxy radicals (CH_3O_2), since the methyl hydroperoxide product (CH_3OOH) undergoes a similar fate to H_2O_2.

$$HO_2 + CH_3O_2 \rightarrow CH_3OOH + O_2 \qquad (1.28)$$

Methylperoxy radicals are themselves produced in the OH initiated oxidation of methane in a prototypical reaction which mirrors the OH initiated oxidation of other hydrocarbons:

$$CH_4 + OH \rightarrow CH_3 + H_2O \qquad (1.29)$$

$$CH_3 + O_2 + M \rightarrow CH_3O_2 + M \qquad (1.30)$$

The reaction between HO_2 and CH_3O_2 therefore not only represents a loss process for HO_x in the atmosphere, but is also an important step in the atmospheric oxidation of methane. Analogously to HO_2, CH_3O_2 radicals undergo self-reaction in competition with (1.28):

$$CH_3O_2 + CH_3O_2 \rightarrow 2\,CH_3O + O_2 \qquad (1.31a)$$

$$\rightarrow CH_3OH + HCHO + O_2 \qquad (1.31b)$$

This, as can be seen, is a multi-channel reaction, and both channels can result in regeneration of HO_2 through the subsequent chemistry of the products:

$$CH_3O + O_2 \rightarrow HO_2 + HCHO \quad (1.32)$$

$$HCHO + h\nu \rightarrow HO_2 + HCO \quad (1.33)$$

$$H + O_2 + M \rightarrow HO_2 + M \quad (1.23)$$

$$HCO + O_2 \rightarrow HO_2 + CO \quad (1.34)$$

At elevated tropospheric NO_x levels both HO_2 and CH_3O_2 react rapidly with NO:[8]

$$HO_2 + NO \rightarrow OH + NO_2 \quad (1.35)$$

$$CH_3O_2 + NO \rightarrow CH_3O + NO_2 \quad (1.36)$$

The production of the methoxy radical (CH_3O) in (1.36) results in HO_2 formation through the subsequent reactions (1.32), (1.33) and (1.34). The overall result of reactions (1.35) and (1.36) is therefore the conversion of NO to NO_2, without loss of HO_x species. Formation of NO_2 in the troposphere thus results in production of ozone through reactions (1.9) and (1.2):

$$NO_2 + h\nu \rightarrow NO + O \quad (1.9)$$

$$O + O_2 + M \rightarrow O_3 + M \quad (1.2)$$

It can thus be seen that the presence of nitrogen oxides in the troposphere shifts the balance of chemistry from destruction of ozone in the unpolluted troposphere to its production in the polluted atmosphere.

The rate of ozone production in the NO_x polluted troposphere is eventually mitigated by the reaction of O_3 with NO, creating a photostationary state between O_3, NO and NO_2 through reactions (1.9), (1.2) and (1.37).

$$O_3 + NO \rightarrow NO_2 + O_2 \quad (1.37)$$

Numerical modelling has estimated that a ratio of $[NO]/[O_3]$ typically in excess of 2×10^{-4} – a ratio commonly achieved in urban and industrial regions – is sufficient to shift the balance from net destruction to net production of ozone in the troposphere.[21]

Under certain meteorological conditions, elevated NO_x levels coupled with large emissions of HCs and VOCs from vehicle exhausts and industrial processes can lead to the formation of photochemical smog.[2] Photochemical smog, a complex mixture of elevated concentrations of O_3, NO_2, HCs, VOCs and their breakdown products generated by the peroxy radical chemistry described above, has been associated with adverse effects on human health, agriculture and wildlife.[12] Atmospheric measurements of several species, made throughout the course of a day, during a smog event are shown in Figure 1.7. The results of a smog chamber experiment investigating the kinetics of smog formation in the laboratory are shown in Figure 1.8.

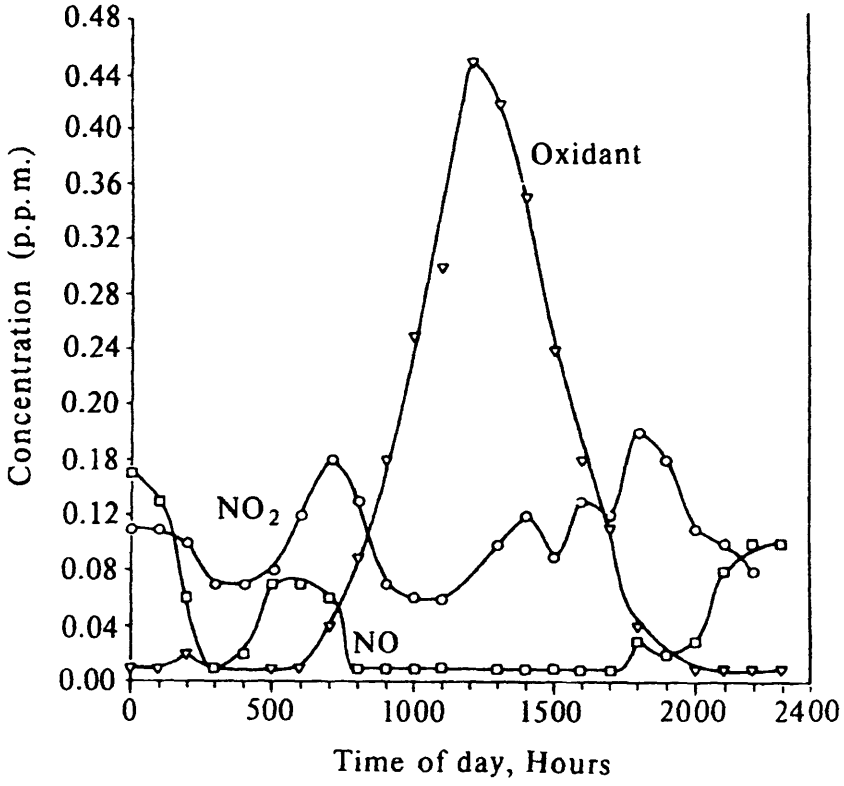

Figure 1.7 : Atmospheric measurements of several species made during a photochemical smog event in Southern California. 'Oxidant' refers mainly to ozone. Taken from reference 2.

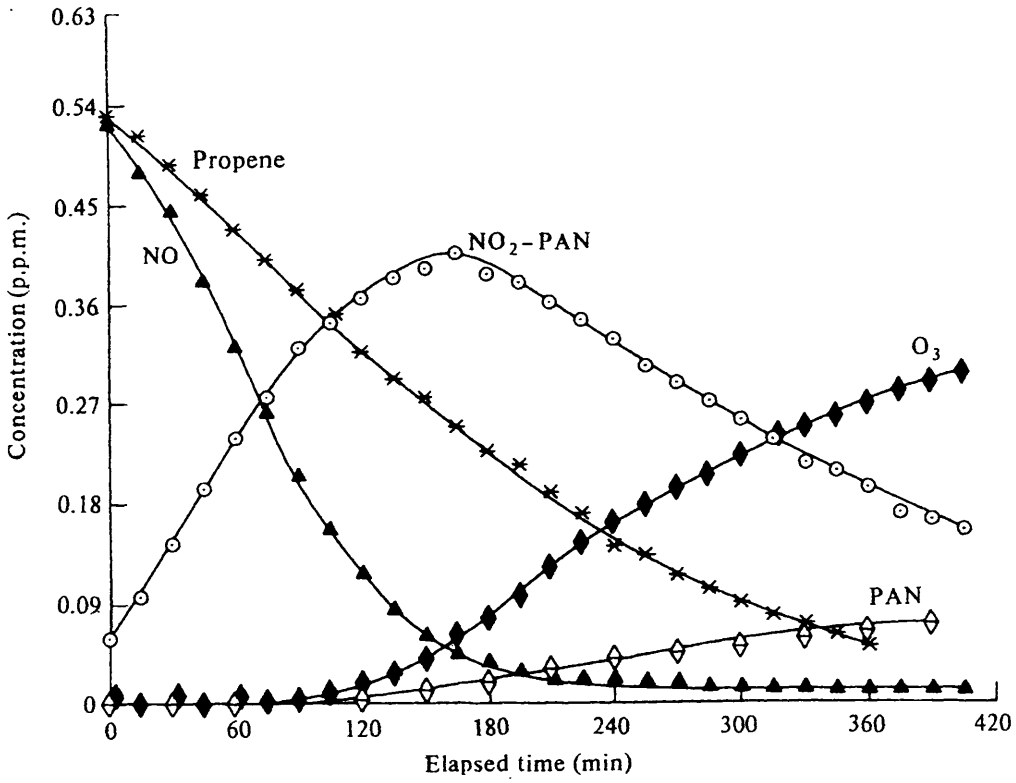

Figure 1.8 : Smog chamber measurements of several species during irradiation of 0.53 ppm propene and 0.59 ppm NO_x in purified air at 760 Torr. PAN = peroxyacetyl nitrate. Taken from reference 2.

At low light intensities – during night-time – when production of OH radicals is limited by reduced solar ozone photolysis, the major oxidising species in the troposphere is the nitrate radical (NO_3). Ozone, however, is still vital to the production of the nitrate radical in its reaction with NO_2:

$$O_3 + NO_2 \rightarrow NO_3 + O_2 \qquad (1.38)$$

Concentrations of NO_3 are typically low under sunlit conditions as a result of its solar photolysis at wavelengths below 630 nm:

$$NO_3 + h\nu \rightarrow NO_2 + O \qquad (1.39a)$$

$$\rightarrow NO + O_2 \qquad (1.39b)$$

and its reaction with NO, produced in NO_2 photolysis, or with NO_2 itself:

$$NO_2 + h\nu \rightarrow NO + O \qquad (1.40)$$

$$NO_3 + NO \rightarrow 2\,NO_2 \quad (1.41)$$

$$NO_3 + NO_2 \rightarrow N_2O_5 \quad (1.42)$$

Oxidation reactions of saturated VOCs by NO_3 generally occur by H atom abstraction, and, analogously to the reactions of OH, reactions of NO_3 with HCs and VOCs result in the generation of peroxy radicals:

$$NO_3 + HCHO \rightarrow CHO + HNO_3 \quad (1.43)$$

$$HCO + O_2 \rightarrow HO_2 + CO \quad (1.34)$$

$$NO_3 + CH_4 \rightarrow CH_3 + HNO_3 \quad (1.44)$$

$$CH_3 + O_2 + M \rightarrow CH_3O_2 + M \quad (1.30)$$

Increased levels of NO_3 at night therefore provides a source of peroxy radicals in the absence of solar O_3 photolysis and the subsequent chemistry of hydroxyl radicals.

1.7 Concluding Remarks

Understanding of the Earth's atmosphere has increased dramatically over the last fifty years. In the 1950s the atmosphere was regarded by many as being chemically inert, and was viewed as simply being a medium for transport of moisture, heat, momentum and pollutants. Trace species in the atmosphere such as CH_4, CO and N_2O were often regarded as curiosities, and their concentrations known only to $\pm$ 50 %.[1]

Progress in atmospheric science since the 1970s has revealed a chemically dynamic atmosphere, and, until the discovery of the Antarctic ozone 'hole' by Farman *et al.*[10] in 1985, atmospheric models were able to replicate observations with an impressive degree of accuracy. Since the discovery of Polar stratospheric ozone depletion, atmospheric science, and atmospheric chemistry in particular, has received greater attention than ever, and our understanding of the atmosphere has continued to increase. There is, however, still work to be done. The atmosphere is an incredibly complex medium, and improvements in detection techniques and measurements of atmospheric species gained by use of aircraft and satellite-based instruments, as well as improvements in models, must be matched by advances in laboratory science.

Detection of highly reactive species in the atmosphere such as the OH radical at concentrations on the order of 10^6 cm^{-3} is now possible. Any attempt to replicate, and indeed validate, such observations with accuracy must require accurate knowledge of the kinetics and photochemistry of the processes affecting chemical change in the atmosphere.

While current understanding of the troposphere enables a remarkable degree of agreement between modelled and observed concentrations of the OH radical, the agreement between models and observations of other important tropospheric species such as HO_2, H_2O_2 and CH_3OOH is still relatively poor.

This work aims to address the need for further laboratory studies of the kinetics of processes affecting atmospheric concentrations of peroxy radicals and peroxides, and some of the fundamental science behind such processes is discussed in the following chapter.

1.8 References

[1] G. P. Brasseur, J. J. Orlando, G. S. Tyndall, *Atmospheric Chemistry and Global Climate Change*, **1999**, Oxford University Press

[2] R.P. Wayne, *Chemistry of Atmospheres*, Third edition, **2000**, Oxford University Press

[3] United Nations Framework Convention on Climate Change http://unfccc.int/2860.php

[4] A. Houzeau, *C. R. Acad. Sci. Paris*, **1858**, 46, 89

[5] W. Hartley, *J. Chem. Soc.*, **1881**, 39, 111

[6] G.M.B. Dobson, *Proc. Roy. Soc. London, Sec. A*, **1930**, 129, 411

[7] S. Chapman, *Phil. Mag.*, **1930**, 10, 369

[8] S. P. Sander, R. R. Friedl, D. M. Golden, M. J. Kurylo, R. E. Huie, V. L. Orkin, G. K. Moortgat, A. R. Ravishankara, C. E. Kolb, M. J. Molina, *Chemical Kinetics and Photochemical Data for Use in Atmospheric Studies*, **2002**, Evaluation Number 14, JPL Publication 02-25, Jet Propulsion Laboratory, Pasadena, CA., USA

[9] M.J. Molina and F.S. Rowland, *Nature*, **1974**, 249, 810

[10] J.C. Farman, B.G. Gardiner, J.D. Shanklin, *Nature*, **1985**, 315, 207

[11] WMO, *Scentific Assessment of Ozone Depletion*, **1994**, World Meteorological Association, Geneva

[12] WMO, *Scientific Assessment of Ozone Depletion*, **2002**, World Meteorological Association, Geneva

[13] J. Anderson, *J. Geophys. Res.*, **1989**, 94, 11465

[14] J.G. Anderson, W.H. Brune, M.H. Proffitt, *J. Geophys. Res.*, **1989**, 95, 15129

[15] P.J. Crutzen and F. Arnold, *Nature*, **1986**, 324, 651

[16] S. Solomon, R. Garcia, F. Rowland, D. Weubbles, *Nature*, **1986**, 321, 755

[17] D.W. Fahey, S. Solomon, S.R. Kawa, M. Loewenstein, J.R. Podolske, S.E. Strahan, K.R. Chan, *Nature*, **1990**, 345, 698

[18] L. Molina and M. Molina, *J. Phys. Chem.*, **1987**, 91, 433

[19] P. Brimblecombe, *Air Composition and Chemistry*, **1995**, Cambridge University Press

[20] B.J. Finlayson-Pitts and J.N. Finlayson, *Chemistry of the Upper and Lower Atmosphere*, **1999**, Academic Press Inc.

[21] P. Crutzen, *Topics in Atmospheric and Interstellar Physics and Chemistry*, **1994**, Les Editions de Physique

Chapter 2
Gas Phase Kinetics and Photochemistry

The ability to understand the chemistry of the atmosphere requires knowledge and understanding of the kinetics and photochemistry of atmospheric species – the rates at which such species interact with each other and with radiation.

2.1 Theory of Gas Phase Kinetics

For the general gas phase reaction

$$aA + bB \rightarrow cC + dD$$

the change in extent of reaction $\delta\xi$ is given by:

$$\delta\xi = \frac{\delta n_Q}{\nu_Q} \qquad (2.i)$$

where δn_Q is the change in amount of species Q in the reaction, and ν_Q the stoichiometric number for species Q (defined as negative for reactants and positive for products). For the general reaction therefore:

$$\delta\xi = \frac{\delta n_A}{-a} = \frac{\delta n_B}{-b} = \frac{\delta n_C}{+c} = \frac{\delta n_D}{+d} \qquad (2.ii)$$

and the rate $\hat{r}$ of reaction is defined as:

$$\hat{r} = \frac{d\xi}{dt} = \frac{1}{\nu_Q}\frac{dn_Q}{dt} \qquad (2.iii)$$

In most situations it is more convenient to consider the intensive rate of change of concentration, r, rather than the extensive rate of change of amount, $\hat{r}$. The rate r of reaction is thus more commonly defined as:

$$r = \frac{1}{\nu_Q}\frac{d\left(n_Q/V\right)}{dt} = \frac{1}{\nu_Q}\frac{d[Q]}{dt} \qquad (2.iv)$$

Experimentally it has been shown that the rate r of reaction is often given by the product of a coefficient k (the rate coefficient or rate constant), and each reactant concentration raised to an experimentally determined exponent in the rate equation:

$$r = k[A]^{\alpha}[B]^{\beta} \qquad (2.v)$$

The exponents α and β are termed the orders of reaction with respect to reactants A and B respectively, and the overall order of the reaction is given by the sum of the exponents in the rate equation ($\alpha + \beta$). For an elementary reaction, one that takes place in a single step, the order of reaction with respect to a particular reactant is equivalent to the stoichiometric number for that reactant. The overall order of an elementary reaction, termed the molecularity of the reaction, therefore corresponds to the total number of reactant molecules participating in the reaction. An elementary reaction involving only one reactant species is therefore termed unimolecular, and is a first order reaction, an elementary reaction of two species is termed a bimolecular reaction and is second order, and an elementary reaction of three species is termed termolecular and is a third order reaction.

For an overall reaction consisting of a number of known elementary reactions it is often possible to derive the overall rate equation from the elementary rate equations using the steady state approximation. The steady state approximation (SSA) assumes that, after an initial induction period, the concentrations of reactive reaction intermediates reach a small and constant level. Thus, for the overall reaction

$$A + B = P$$

consisting of the elementary reactions

$$A + B \rightarrow C \qquad k_1$$

$$C \rightarrow P \qquad k_2$$

the rate equation for formation of product P, which may be written

$$\frac{+d[P]}{dt} = k_2[C] \tag{2.vi}$$

can be simplified by application of the steady state approximation to species C:

$$\frac{+d[C]}{dt} = k_1[A][B] - k_2[C] \approx 0 \qquad \text{(SSA)} \tag{2.vii}$$

giving $k_2[C] = k_1[A][B]$ and hence

$$\frac{+d[P]}{dt} = k_1[A][B] \tag{2.viii}$$

In this case, the steady state approximation has been applied to the intermediate species C. The steady state approximation requires that for species C to have a small and invariant concentration the rate of removal of C far exceeds its rate of production, which is often the case for reactive intermediate species.

2.2 Temperature Dependence of Reaction Rates

An empirical experimental observation is that, for the vast majority of reactions, the rate coefficient k varies with temperature according to the Arrhenius equation:[1]

$$k = A\exp\left(-E_a/RT\right) \tag{2.ix}$$

where A is the pre-exponential factor, E_a the activation energy for reaction, R the gas constant and T the absolute temperature. The pre-exponential factor and the activation energy are described collectively as the Arrhenius parameters, and are used to parameterise the temperature dependence of k. Several theories have been advanced to explain this temperature dependence, and a brief summary of these is given below.

2.3 Bimolecular Gas Phase Reaction Rate Theory

At the most basic level, bimolecular reaction rates in the gas phase can be rationalised in terms of simple collision theory (SCT), in which atoms and molecules are treated as hard, structureless spheres undergoing elastic collisions. It is assumed that elementary bimolecular reactions are collisional processes and that, apart from in collision, no intermolecular forces are in operation. The rate, r, of reaction between two species A and B is thus equated to the collision frequency between the reactants, Z_{AB}, multiplied by the fraction, F, of colliding species with sufficient energy to overcome an energy barrier to rearrangement of electrons occurring during reaction. Thus:

$$r = Z_{AB} F \tag{2.x}$$

The collision frequency, the total number of collisions between A and B in unit time, is obtained from the kinetic theory of gases and is given by:

$$Z_{AB} = V_{col} L^2 [A][B] \tag{2.xi}$$

where V_{col} is the 'collision volume' (the notional volume swept out by a moving molecule in unit time), L is Avogadro's constant and [A] and [B] are the concentrations of A and B in molar units respectively. The collision volume is determined by the product of the collision cross-section for reaction, σ_{AB}, and the mean relative speed of molecules A and B, $\bar{c}_{rel}$. Thus:

$$\begin{aligned} V_{col} &= \sigma_{AB} \bar{c}_{rel} \\ &= \sigma_{AB} \left(\frac{8 k_B T}{\pi \mu} \right)^{1/2} \end{aligned} \tag{2.xii}$$

where k_B is the Boltzmann constant, T the temperature and μ the reduced mass of species A and B. From (2.xi), the collision frequency therefore becomes:

$$Z_{AB} = \sigma_{AB}\left(\frac{8k_B T}{\pi\mu}\right)^{1/2} L^2[A][B] \qquad (2.xiii)$$

The fraction, F, of molecules with sufficient energy to react on collision is given by the fraction of molecules with a kinetic energy above a certain critical value, ε, within a Boltzmann distribution of kinetic energies. The Boltzmann distribution of kinetic energies, $f(E)$, is described by:

$$f(E) = \frac{1}{k_B T}\exp\left(-E/k_B T\right) \qquad (2.xiv)$$

Integration of (2.xiv) between limits of ε, the critical energy for reaction, and infinity gives the fraction, F, of molecules with kinetic energy above the critical value:

$$\begin{aligned} F = f(E \geq \varepsilon) &= \int_{\varepsilon}^{\infty} \frac{1}{k_B T}\exp\left(-E/k_B T\right) dE \\ &= \frac{1}{k_B T}\int_{\varepsilon}^{\infty} \exp\left(-E/k_B T\right) dE \\ &= \exp\left(-\varepsilon/k_B T\right) \end{aligned} \qquad (2.xv)$$

Simple collision theory therefore predicts the rate, r, of a bimolecular reaction between species A and B to be given by:

$$r = \sigma_{AB}\left(\frac{8k_B T}{\pi\mu}\right)^{1/2} L^2[A][B]\exp\left(-\varepsilon/k_B T\right) \qquad (2.xvi)$$

It thus follows that, for an elementary reaction between A and B, collision theory predicts the rate coefficient, k, to be given by:

$$k = \sigma_{AB}\left(\frac{8k_B T}{\pi\mu}\right)^{1/2} L^2 \exp\left(-\varepsilon/k_B T\right) \qquad (2.xvii)$$

which resembles the experimentally determined Arrhenius equation:

$$k = A\exp\left(-E_a/RT\right) \qquad (2.ix)$$

Although simple collision theory qualitatively predicts the broad features of many rate coefficients, notably the exponential dependence of k on temperature, and provides some insight as to the physical significance of the Arrhenius parameters, it cannot make accurate quantitative predictions of rate coefficients.[2] The limitations of the theory arise from the assumptions that molecules act as hard spheres that react instantaneously on collision, if sufficient energy is available, and that intermolecular forces and internal energy distributions are unimportant. Reactions will in fact only occur if molecules collide in such a way that, depending on the species in question, certain steric requirements are met, and reactions will not be instantaneous since a finite time is required for structural and energetic redistributions to occur. Incorporation of these ideas into SCT has proven difficult, and transition state theory, or activated complex theory, has been developed as an alternative. Transition state theory (TST) considers a reaction to take place as a trajectory across a potential energy surface (PES), as shown in Figure 2.1 for the co-linear reaction A + BC $\rightarrow$ AB + C. As A and BC come into proximity they distort and the potential energy rises to a maximum, around which the cluster of atoms is known as the activated complex, $ABC^{\dagger}$. The exact configuration of the cluster at the peak in the potential energy surface is termed the transition state.

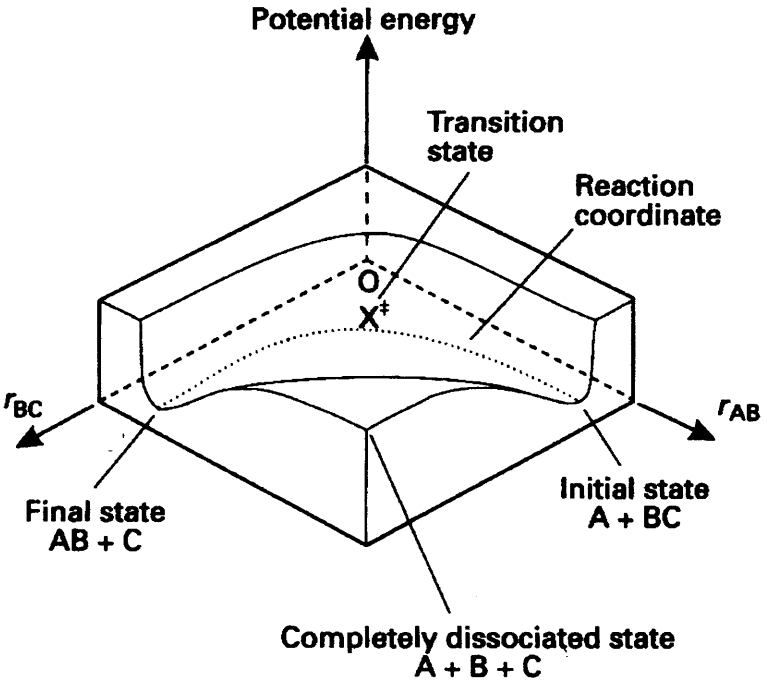

Figure 2.1: Potential energy surface for the reaction A + BC. Reproduced from reference 2.

Transition state theory treats the activated complex as existing in equilibrium with the reactants, and assumes that once the transition state has been reached it is inevitable that reaction products will be formed – the transition state cannot re-form the reactants. It is also assumed that the energy distribution of the reactant molecules is described by a Boltzmann distribution, and that the motion over the energy barrier is a classical process, with a single vibration of the activated complex responsible for the motion over the barrier. The single reactive vibration is considered separable from all the other vibrations and rotations of the complex.

The overall reaction

$$A + BC \rightarrow AB + C \qquad k_{bimol}$$

is therefore treated as

$$A + BC \leftrightarrow ABC^{\dagger} \rightarrow AB + C$$

and the rate of reaction, r, is given by:

$$r = \frac{-d[\mathrm{A}]}{dt} = \frac{-[\mathrm{BC}]}{dt} = k_{\mathrm{bimol}}[\mathrm{A}][\mathrm{BC}] = \frac{+d[\mathrm{AB}]}{dt} = \frac{+d[\mathrm{C}]}{dt} = k^{\dagger}[\mathrm{ABC}^{\dagger}] \qquad \text{(2.xviii)}$$

The concentration $[ABC^{\dagger}]$ can be expressed from equilibrium:

$$[\mathrm{ABC}^{\dagger}] = K_{\mathrm{eq}}[\mathrm{A}][\mathrm{BC}] \qquad \text{(2.xix)}$$

since the equilibrium constant K_{eq} is given by $K_{\mathrm{eq}} = \frac{[\mathrm{ABC}^{\dagger}]}{[\mathrm{A}][\mathrm{BC}]}$.

The rate is therefore described by:

$$r = k^{\dagger} K_{\mathrm{eq}}[\mathrm{A}][\mathrm{BC}] \qquad \text{(2.xx)}$$

Using the general result from statistical mechanics, K_{eq} is given by:

$$K_{\mathrm{eq}} = \frac{Q_{\mathrm{ABC}^{\dagger}}}{Q_{\mathrm{A}} Q_{\mathrm{BC}}} \exp\left(-\varepsilon / k_{\mathrm{B}} T\right) \qquad \text{(2.xxi)}$$

where Q_i is the total partition function for species i, calculated using statistical mechanics and spectroscopic data, and ε the energy difference between the reactants (A + BC) and the products (AB + C) determined by spectroscopy. The rate therefore becomes:

$$r = k^{\dagger} \frac{Q_{\mathrm{ABC}^{\dagger}}}{Q_{\mathrm{A}} Q_{\mathrm{BC}}} \exp\left(-\varepsilon / k_{\mathrm{B}} T\right)[\mathrm{A}][\mathrm{BC}] \qquad \text{(2.xxii)}$$

and the bimolecular rate coefficient, k_{bimol}, for the reaction is thus:

$$k_{\text{bimol}} = k^{\dagger} \frac{Q_{\text{ABC}^{\dagger}}}{Q_{\text{A}} Q_{\text{BC}}} \exp\left(-\varepsilon / k_{\text{B}} T\right) \qquad \text{(2.xxiii)}$$

The total partition function for the activated complex $Q_{\text{ABC}}{}^{\dagger}$ can be separated into two components – the component, q, to the total partition function of $\text{ABC}^{\dagger}$ describing the reactive vibration, and the partition function of $\text{ABC}^{\dagger}$ excluding the reactive vibration, $Q_{\text{ABC}^{\dagger}}{}'$.

$$Q_{\text{ABC}}{}^{\dagger} = q\, Q_{\text{ABC}^{\dagger}}{}' \qquad \text{(2.xxiv)}$$

The partition function q can be approximated to

$$q = \frac{k_{\text{B}} T}{h\nu} \qquad \text{(2.xxv)}$$

where ν is the frequency of the reactive vibration, giving:

$$k_{\text{bimol}} = k^{\dagger} \frac{k_{\text{B}} T}{h\nu} \frac{Q_{\text{ABC}^{\dagger}}{}'}{Q_{\text{A}} Q_{\text{BC}}} \exp\left(-\varepsilon / k_{\text{B}} T\right) \qquad \text{(2.xxvi)}$$

The rate constant $k^{\dagger}$ is determined by the frequency of the reactive vibration, ν, multiplied a transmission coefficient, κ, which accounts for the fraction of reactive vibrations that lead to product formation. The transmission coefficient is often assumed to be unity.

$$k^{\dagger} = \kappa\nu \qquad \text{(2.xxvii)}$$

Combining equations (2.xxvi) and (2.xxvii) therefore gives the result:

$$k_{\text{bimol}} = \kappa \frac{k_{\text{B}} T}{h} \frac{Q_{\text{ABC}^{\dagger}}{}'}{Q_{\text{A}} Q_{\text{BC}}} \exp\left(-\varepsilon / k_{\text{B}} T\right) \qquad \text{(2.xxviii)}$$

which again compares well with the experimental Arrhenius equation.

2.4 Unimolecular Reaction Rate Theory

At high pressures many gas phase dissociation and isomerisation reactions display first order kinetics. The rates of such reactions also usually increase with temperature, showing that the reactant must acquire adequate energy to overcome an energy barrier to reaction. However, the observed first order kinetics apparently preclude collisional activation, which is a bimolecular process. In the 1920s Lindemann[3] proposed a kinetic scheme to explain the overall reaction:

$$A \quad = \quad P$$

consisting of the following elementary reactions:

$$\begin{aligned} A + M &\rightarrow A^* + M & k_1 \\ A^* + M &\rightarrow A + M & k_{-1} \\ A^* &\rightarrow P & k_2 \end{aligned}$$

where M is any other species that can produce or deactivate the energised molecule A*. The rate of formation of product P from this mechanism is given by:

$$\frac{+d[P]}{dt} = k_2[A^*] \qquad \text{(2.xxix)}$$

Application of the steady state approximation to A* gives:

$$\frac{+d[P]}{dt} = \frac{k_2 k_1 [A][M]}{k_{-1}[M] + k_2} \qquad \text{(2.xxx)}$$

Although this is not first order in A, at high pressure $k_{-1}[M] >> k_2$, which allows simplification of (2.xxx) to (2.xxxi):

$$\frac{+d[P]}{dt} = \frac{k_2 k_1}{k_{-1}}[A] \qquad \text{(2.xxxi)}$$

The Lindemann mechanism therefore predicts that the observed rate coefficient ought to decrease as the pressure is reduced, with the reaction eventually becoming second order overall:

$$\frac{+d[P]}{dt} = k_1[A][M] \qquad \text{(2.xxxii)}$$

since at low pressure $k_{-1}[M] << k_2$. The apparent first order rate coefficient as a function of [M] thus takes the form as shown in Figure 2.2.

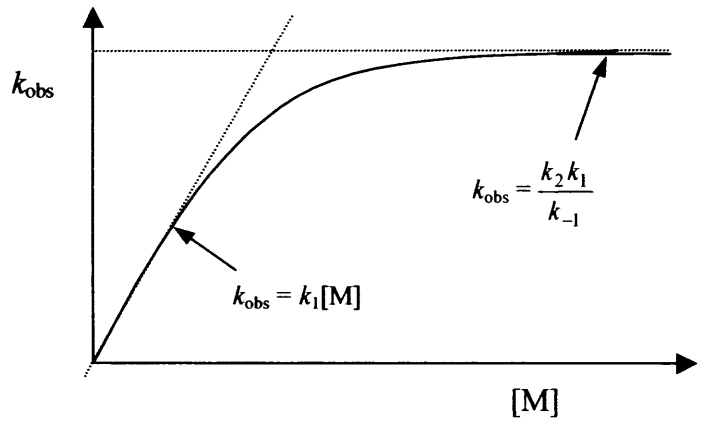

Figure 2.2 : Schematic diagram of the apparent first order rate coefficient, k, as a function of [M]. The observed rate is second order at low pressures and tends to a limiting first order value at high pressures.

2.5 Termolecular Reaction Rate Theory

A similar mechanism to that proposed by Lindemann for unimolecular kinetics can be used to explain the observed pressure dependence of many termolecular association reactions such as:

$$A + B + M = P + M$$

Invoking the elementary reactions:

A + B	→	AB*	k_1
AB*	→	A + B	k_{-1}
AB* + M	→	P + M	k_2

and application of the steady state approximation to the intermediate species AB* yields the expression

$$\frac{+d[\mathrm{P}]}{dt} = \frac{k_2 k_1 [\mathrm{A}][\mathrm{B}][\mathrm{M}]}{k_{-1} + k_2[\mathrm{M}]} \qquad \text{(2.xxxiii)}$$

The observed bimolecular rate coefficient, k_{bimol}, is therefore given by (2.xxxiii):

$$k_{\text{termol}} = \frac{k_2 k_1 [\mathrm{M}]}{k_2[\mathrm{M}] + k_{-1}} \qquad \text{(2.xxxiv)}$$

In a similar fashion to unimolecular reactions, at low pressure, since $k_2[\mathrm{M}] << k_1$, (2.xxxiii) simplifies to

$$\frac{+d[\mathrm{P}]}{dt} = k_0[\mathrm{A}][\mathrm{B}][\mathrm{M}] \qquad \text{(2.xxxv)}$$

resulting in a third order rate equation, where $k_0 = \frac{k_2 k_1}{k_{-1}}$. At high pressure, since $k_2[\mathrm{M}] >> k_1$, (2.xxxiii) simplifies to

$$\frac{+d[\mathrm{P}]}{dt} = k_\infty[\mathrm{A}][\mathrm{B}] \qquad \text{(2.xxxvi)}$$

resulting in a second order rate equation, where $k_\infty = k_1$.

Although such mechanisms describe the qualitative behaviour of unimolecular and termolecular reactions they fail to replicate experimentally determined rate coefficients with any great quantitative accuracy. Several refinements have been made to the Lindemann mechanism, notably those by Rice and Ramsperger,[4] Kassel,[5] and Marcus,[6] leading to the development of RRKM theory. RRKM theory requires accurate thermodynamic data and considers the internal energy distribution of the energised

species A*, and, similarly to transition state theory, separates the formation of A* from that of the activated complex $A^{\dagger}$:

$$\begin{aligned} A + M &\rightarrow A^* + M \\ A^* + M &\rightarrow A + M \\ A^* &\rightarrow A^{\dagger} \\ A^{\dagger} &\rightarrow P \end{aligned}$$

RRKM theory can often accurately reproduce experimental results when reliable thermodynamic data is available. Unfortunately, reliable thermodynamic data is not available for many of the transient species and, as a result, RRKM theory cannot always be used.[2] However, Troe[7] has shown that introduction of a broadening factor, F, itself a function of k_0 and k_∞, applied to (2.xxxiv) can accurately replicate the pressure dependence of many experimentally determined rate coefficients.

$$k_{\text{bimol}} = \frac{k_0[\text{M}]k_\infty}{k_0[\text{M}]+k_\infty} \times F \qquad \text{(2.xxxvii)}$$

where

$$F = F_c^{\left\{1+\left(\log_{10}\left\{k_0[\text{M}]/k_\infty\right\}\right)^2\right\}^{-1}} \qquad \text{(2.xxxviii)}$$

The exact value of F_c depends on the specific reaction in question, but it has been shown that a value of 0.6 provides an adequate description for most termolecular reactions of interest in the atmosphere.[8]

2.6 Photochemistry

Much of the chemistry leading to atmospheric change is initiated by the interaction of molecules with solar radiation. In particular, UV-visible radiation, which provides molecules with energies comparable to bond strengths, can cause significant chemical change. Most fundamentally, absorption of a photon can occur if the energy of levels of the absorbing species permit a transition equivalent in energy to that of the photon.

Photon absorption by a molecule AB results in production of a rotationally, vibrationally or electronically excited molecule AB*, depending on the photon energy.

$$AB + h\nu \rightarrow AB^*$$

The absorbance at a wavelength λ, A_λ, of a species is given by (2.xxxix):

$$A_\lambda = \ln\left(\frac{I_{0,\lambda}}{I_{l,\lambda}}\right) \quad \text{(2.xxxix)}$$

where $I_{0,\lambda}$ is the intensity of the incident light at wavelength λ and $I_{l,\lambda}$ the light intensity at wavelength λ after transmission through the sample of length l. For a species at homogeneous concentration c the absorbance at a given wavelength, λ, is determined by the path length, l, of the light through the sample and the absorption cross-section, σ, of the species at that wavelength and is described in the Beer-Lambert Law:

$$A_\lambda = \sigma_\lambda c l \quad \text{(2.xl)}$$

Knowledge of appropriate cross-sections can therefore allow measurement of species concentration by virtue of absorption spectroscopy. Absorption spectroscopy in the UV/visible region of the electromagnetic spectrum, resulting in electronic excitation of the molecules under consideration, is particularly useful in atmospheric science for determination of species concentration since absorption cross-sections are well known for many atmospherically important species.

Following absorption of a UV-visible photon, a number of possible fates exist for electronically excited molecules, as summarised diagrammatically in Figure 2.3.

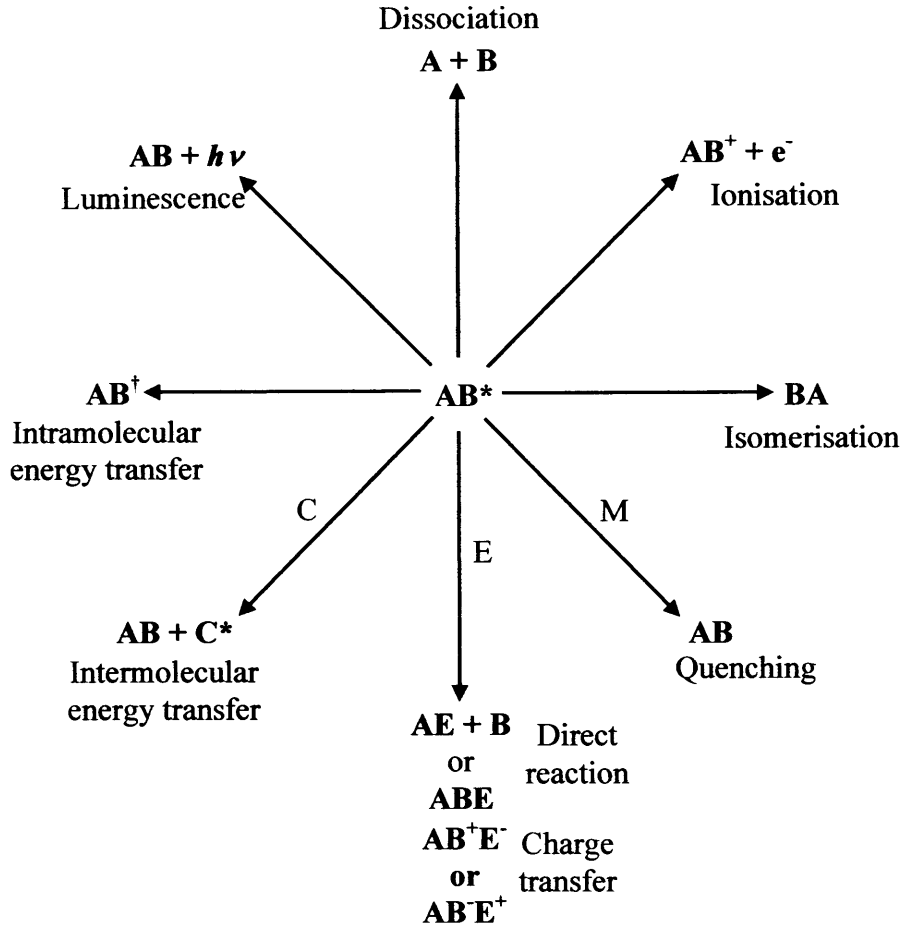

Figure 2.3 : Possible fates of an electronically excited molecule AB*. Adapted from references 2 and 9.

The dissociation pathway

$$AB + h\nu \rightarrow AB^*$$
$$\rightarrow A + B$$

is particularly important in the atmosphere since the photolytically produced fragments A and B are intrinsically reactive and often highly energetic.

The effective rate coefficient at wavelength λ, J_λ, for solar photodissociation of a molecule is given in (2.xli):

$$J_\lambda = \int_{\lambda_1}^{\lambda_2} I_\lambda \sigma_\lambda \phi_\lambda \, d\lambda \qquad \text{(2.xli)}$$

where I_λ is the solar intensity at wavelength λ, σ_λ the absorption cross-section of the molecule at wavelength λ and ϕ_λ the quantum yield for dissociation of the molecule at wavelength λ. Laboratory measurements provide values for σ_λ and ϕ_λ, while radiative transfer models compute I_λ, taking into account the absorption of solar radiation by other species in the atmosphere (principally O_2 and O_3) and factors such as scattering and surface albedo.

2.7 Concluding Remarks

Theoretical descriptions of gas phase kinetics and photochemistry provide valuable insights into the nature of fundamental chemical and physical processes, and developments in such descriptions now enable good approximations to molecular behaviour. However, all theories require experimental verification, and the theory of reaction kinetics is no exception. Experimental principles and techniques used to study gas phase reaction kinetics are discussed in the following chapter.

2.8 References

[1] S. Arrhenius, *Z. Physik. Chem.*, **1889**, 4, 226

[2] M.J. Pilling and P.W. Seakins, *Reaction Kinetics*, **1995**, Oxford University Press

[3] F.A. Lindemann, *Trans. Farad. Soc.*, **1921**, 17, 598

[4] O.K. Rice and H.C. Ramsperger, *J. Am. Chem. Soc.*, **1927**, 49, 1617

[5] L.S. Kassel, *J. Phys. Chem.*, **1928**, 32, 255

[6] R.A. Marcus, *J. Chem. Phys.*, **1952**, 20, 359

[7] J. Troe, *J. Chem. Phys.*, **1977**, 66, 4745

[8] S. P. Sander, R. R. Friedl, D. M. Golden, M. J. Kurylo, R. E. Huie, V. L. Orkin, G. K. Moortgat, A. R. Ravishankara, C. E. Kolb, M. J. Molina, *Chemical Kinetics and Photochemical Data for Use in Atmospheric Studies*, **2002**, Evaluation Number 14, JPL Publication 02-25, Jet Propulsion Laboratory, Pasadena, CA., USA

[9] R.P. Wayne and C.E. Wayne, *Photochemistry*, **1996**, Oxford University Press

Chapter 3
Experimental Investigation of Gas Phase Radical-Radical Kinetics

In order to study gas phase radical-radical reaction kinetics it is necessary that the initiation of reaction be well defined temporally, and that a detection system with suitable time resolution is available to respond to rapidly changing concentrations. Two main methods satisfying the necessary criteria are widely used in experimental studies of gas phase kinetics – known generally as 'flow' methods and 'perturbation' or 'pump-probe' methods. The principles, advantages and disadvantages of these methods are discussed below.

3.1 Flow Methods

In flow methods, the ability of pumping systems to achieve rapid linear gas flow velocities allows the controlled interaction of gases on short timescales. Thus, reactant species are prepared separately and continuously, often by microwave discharge, before being mixed in a flow in the reaction vessel. The common use of microwave discharges with flow methods has given rise to the term *discharge flow* to describe such experiments. Initiation of reaction in discharge flow experiments occurs at the point where mixing of the reactant species occurs. Detection of reactant and/or product species then takes place downstream from the mixing point, with the elapsed time deduced from the flow characterstics. In order to keep the elapsed time comparable to reaction times for radical-radical reactions at typical concentrations, rapid gas velocities are employed. This, along with the need to ensure rapid reactant mixing and a well characterised gas flow, often requires that low pressures are present in the reaction vessel, which limits the conditions under which a reaction can be investigated. Low reaction pressures can also lead to complications due to ready diffusion of reactants and heterogeneous processes, which remove radicals, occurring on the walls of the reaction vessel. Flow tube coatings such as halocarbon wax or Teflon, or passivating agents such as phosphoric acid (H_3PO_4), are often required to reduce heterogeneous chemistry. Other limitations of flow tubes include the need to pre-cool or heat reactant gases, and the requirement to detect species at low pressures, and hence low number densities. In recent years, high pressure flow systems have been developed, which operate in a turbulent flow regime. Such systems require very large pumping capacity, and they are

not yet as widely used as their low pressure counterparts.[1,2,3] A schematic of a typical low pressure discharge flow experiment is shown in Figure 3.1.

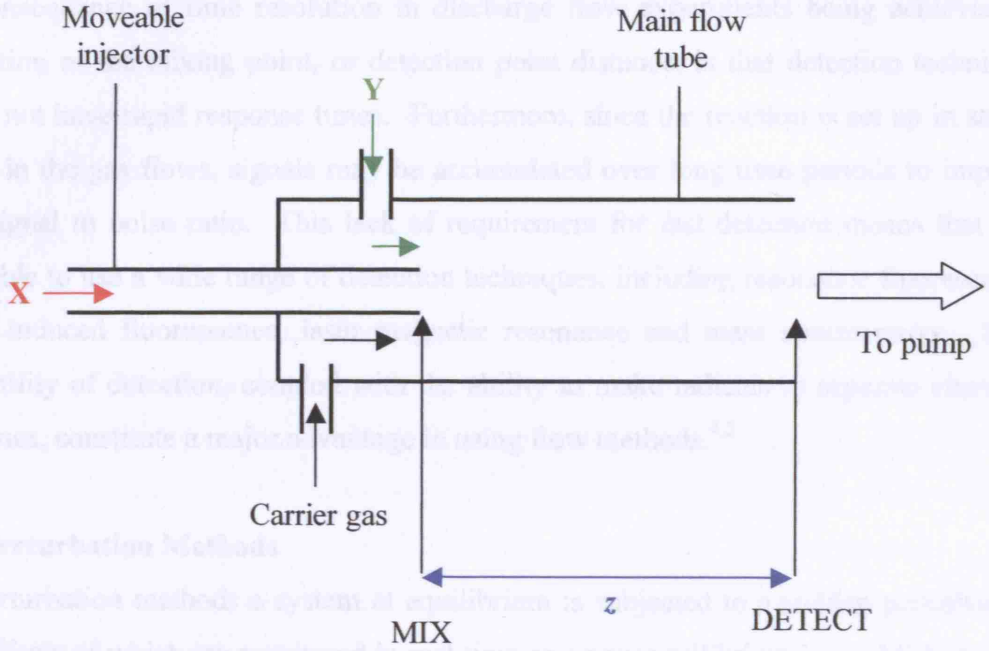

Figure 3.1: Schematic of a typical discharge flow experiment, where X and Y are the reactant species and z the distance between mixing and detection points.

In its simplest form, under which so called 'plug flow' conditions can be assumed, knowledge of the linear flow velocity, v, of the gas in the reaction vessel and the distance, z, between the mixing and detection points allows the reaction time, t, to be calculated from the simple relationship:

$$t = z / v \qquad (3.i)$$

The detection of reactant or product concentration can then be carried out at that time point, and variation of the distance between mixing and detection points provides a series of reactant and/or product concentrations recorded at various times after the initiation of reaction. A concentration-time profile for the reaction can therefore be established, allowing analysis and determination of kinetic parameters. Furthermore, if one of the reacting species is suitably unreactive to be kept present in a constant excess, discharge flow experiments may be conducted under pseudo-first order conditions,

making knowledge of absolute concentrations of the minor reactant species unnecessary.[4]

A consequence of time resolution in discharge flow experiments being achieved by variation of the mixing point, or detection point distance, is that detection techniques need not have rapid response times. Furthermore, since the reaction is set up in steady state in the gas flows, signals may be accumulated over long time periods to improve the signal to noise ratio. This lack of requirement for fast detection means that it is possible to use a wide range of detection techniques, including resonance fluorescence, laser induced fluorescence, laser magnetic resonance and mass spectrometry. Such versatility of detection, coupled with the ability to make radicals in separate chemical schemes, constitute a major advantage in using flow methods.[4,5]

3.2 Perturbation Methods

In perturbation methods a system at equilibrium is subjected to a sudden perturbation, the effects of which are monitored in real time as a new equilibrium is established. The most commonly used perturbation method used to study gas phase radical-radical reaction kinetics is flash photolysis.

In flash photolysis experiments precursor species are mixed in a reaction cell at the required temperature and pressure. A short-lived intense pulse of light from a flashlamp, in conventional flash photolysis, or a laser, in laser flash photolysis, is used to initiate radical production in the reaction cell. The desired radicals may either be generated directly by photolysis, or as a result of further chemistry initiated by photolysis of a precursor species. Radical production must, however, occur on a time scale much shorter than that of the reaction to be investigated, and precursor gas mixtures must be designed carefully to ensure that this is the case.

The pressure range over which flash photolysis can be used is far greater than that for discharge flow, and reactions can be investigated at pressures up to several hundred atmospheres using this technique. The main pressure limitation in flash photolysis is that gases at pressures less than *ca.* 50 Torr undergo adiabatic shock when subjected to the photolysis pulse due to their typically low heat capacity. A result of the pressure ranges used in flash photolysis, combined with the fact that radicals are produced and

monitored in the centre of the reaction cell, is that heterogeneous chemistry occurring on the walls of the reaction cell is usually insignificant.

Kinetic information in flash photolysis is realised by monitoring, and subsequent analysis, of radical concentrations as a function of time. Detection systems must therefore have rapid response times in order to achieve the necessary time resolution. Optical techniques such as absorption or fluorescence are often employed to achieve this.

Absorption spectroscopy provides direct measurement of species concentration – provided that the absorption cross section and path length are known – and allows a complete concentration-time profile to be recorded each time a photolysis event occurs. Absorption techniques do, however, often require relatively high initial radical concentrations (typically 10^{12} to 10^{13} cm^{-3}, depending on the cross-section and optical path length) in order to detect appreciable intensity changes in the analysis light. For many radicals of interest, absorption occurs in the ultraviolet (UV), visible and infrared (IR) regions of the electromagnetic spectrum, and UV absorption cross sections in particular are well known for many species.

Fluorescence techniques can detect much lower radical concentrations (typically 10^{8} cm^{-3}) since the signal is by design specific to the radical of interest and measured relative to a zero background. However, resonance fluorescence is not applicable to all species, since not all excited states fluoresce (as discussed in section 2.6, Chapter 2). Furthermore, as fluorescence typically provides a fixed time point concentration measurement, fluorescence techniques applied to kinetics require a number of experiments to produce a concentration-time profile in which the light source inducing radical fluorescence is operated at a series of known delay times after photolysis.

Whilst flow and perturbation methods constitute the two main categories of kinetic experiment typically conducted, other methods have been developed and used. In all cases, the basic requirements of specificity, sensitivity and ease of radical generation are present, and the technique employed in this work is discussed in the next section.

3.3 Flash Photolysis with Ultraviolet Absorption Spectroscopy

Flash photolysis was developed by Norrish and Porter[6,7] in the late 1940s using flashlamps powered by ex-Royal Navy submarine capacitors charged to high voltage. The pulse of light from the flashlamp was used to initiate chemistry within a reaction cell by the photolysis of gas phase species within the cell. Detection of the flash at a photocell was used to trigger a second, less powerful, flashlamp at a known delay time after the first. Light from the second flashlamp, transmitted through the reaction cell and wavelength resolved by a spectrograph, was detected by a photographic plate. Absorptions by species in the reaction cell were determined manually by comparing the degree of darkening of the photographic plate to that recorded on a plate in the absence of the first flashlamp pulse. The delay time between discharges of the two flashlamps could be varied in successive experiments to generate a series of time resolved plates, an example of which is shown in Figure 3.2, allowing determination of absorption-time profiles.

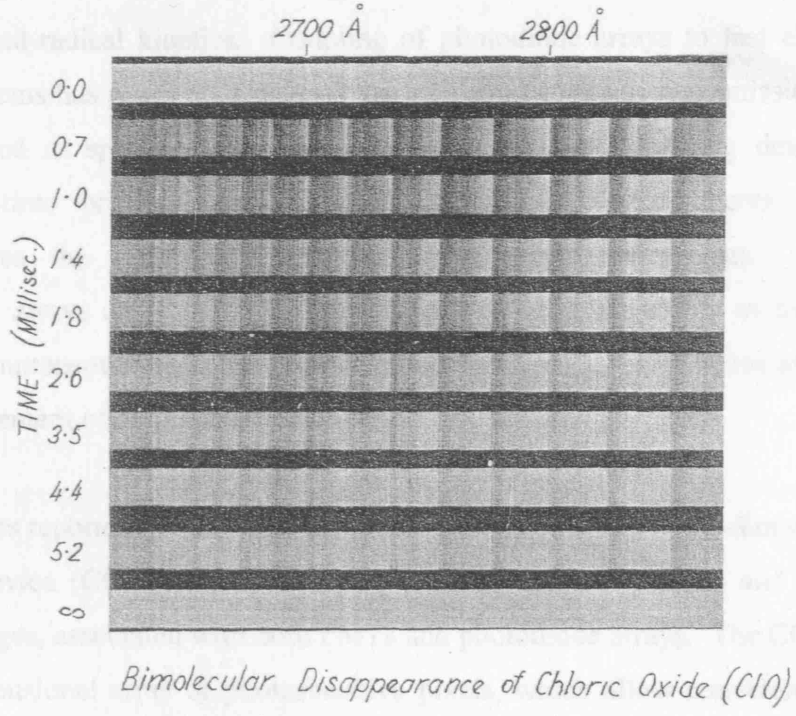

Figure 3.2: Time resolved transmission spectra recorded on photographic plates. Reproduced from reference 8.

The development of photomultiplier tubes (PMTs – electronic photodetectors) in the 1960s allowed continuous electronic time resolved measurement of light intensities

during an experiment.[9] A single experiment employing a PMT and a continuous analysis lamp can therefore provide an entire absorption-time profile, and PMTs are widely used in flash photolysis experiments today thanks to this massive increase in efficiency. PMTs, however, cannot differentiate between photons arriving at different locations on the detector window and, due to their physical size, it is unfeasible to place a row of PMTs in the dispersive plane of a typical spectrograph. Wavelength resolved measurements therefore require repeated experiments at different wavelength settings. Single kinetic experiments employing PMTs are limited to monochromatic light, compromising the ability to identify absorptions unequivocally.

Advances in electronic photodetection led to production of the photodiode array – a series of small, separate, light sensitive elements that can be aligned in the dispersive plane of a spectrograph, enabling simultaneous electronic detection of both time and wavelength resolved light intensities. The time resolution of the experiment is limited, however, by the readout time of the array. Full readout of photodiode arrays is typically on the order of milliseconds, making their use unsuitable for the study of many gas phase radical-radical kinetics. Coupling of photodiode arrays to fast electronic time gating systems has provided a means by which short exposure transmission spectra can be measured at specific time points in an experiment, enabling determination of absorption-time profiles from a series of successive experiments. This again compromises the information gathered in a single experiment. Nevertheless, photodiode arrays do offer several advantages, notably the ability to monitor several species simultaneously and the improvements in signal to noise ratios associated with the measurement of entire absorption bands.

Experiments reported in this work have been conducted using a two-dimensional charge coupled device (CCD) detector array to combine the advantages, and overcome the disadvantages, associated with both PMTs and photodiode arrays. The CCD consists of a two-dimensional array of photosensitive pixels, which allow conversion of incident light to photocharge. Thus, similarly to photodiode arrays, CCDs can be situated in the dispersive plane of a spectrograph, providing the opportunity to record wavelength resolved intensities.[10] Crucially, the CCD also has the facility to transfer photocharge rapidly and efficiently row by row along one axis of the array. Thus, a number of rows of pixels of the CCD are exposed to the incident light exiting the spectrograph,

constituting the illuminated region, while the remainder is shielded from the incident light and constitutes a storage region. Photocharge is then transferred from the illuminated region to the storage region without the need for full readout of the device, allowing continuous acquisition of spectral data throughout the experiment, as shown schematically in Figure 3.3.

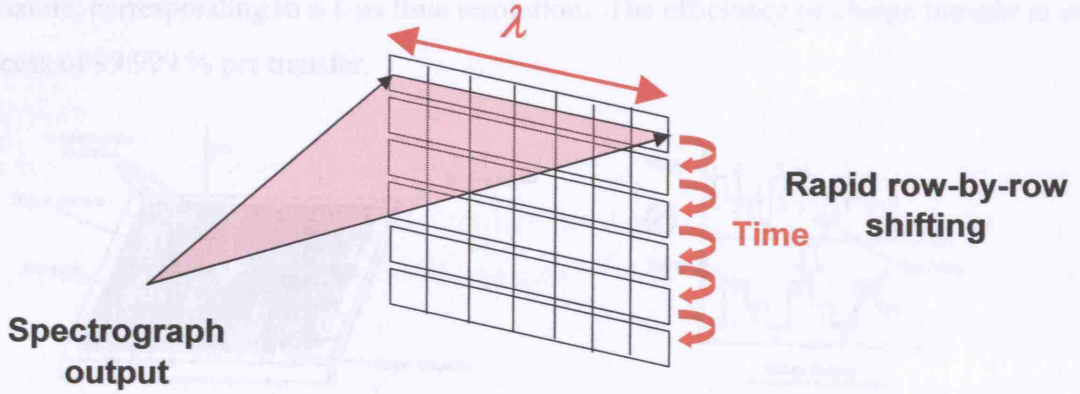

Figure 3.3: Wavelength resolved light is imaged across the top of the CCD, generating photocharge. Photocharge is shifted down the CCD rapidly and efficiently.

Full readout of the device does not take place until the entire storage region has been filled, and the time resolution of the CCD is governed by the rate at which photocharge is transferred from the illuminated region to the storage region of the device. CCD detectors therefore enable the possibility to record rapidly changing transmitted intensities as functions of both time and wavelength.

3.4 Principles of CCD Operation

The CCD employed in this work consists of a grid of metal oxide semiconductor pixels embedded in a silicon substrate. Each pixel converts incident light to photocharge, which is stored in a potential well within the pixel. The quantum efficiency (QE) of light to charge transfer maximises at approximately 60 % at incident wavelengths near 700 nm. To enhance the QE at wavelengths below 400 nm each pixel is coated with a thin layer of phosphor. The phosphor coating emits visible light when UV light is incident upon it, effectively increasing the QE to approximately 20 % at wavelengths between 180 and 400 nm. The emission lifetime of the phosphor coating, on the order of nanoseconds, does not distort the time resolution of the experiment, and the thinness

of the coating (0.3 μm) compared to the pixel size (22.5 μm square) minimises cross talk between adjacent pixels.

Photocharge is transferred from one row to another by the application of suitably phased voltages to a series of parallel electrodes aligned perpendicular to the axis of transfer, as shown schematically in Figure 3.4. Transfer rates (shift times) of up to 1 MHz are possible, corresponding to a 1 μs time resolution. The efficiency of charge transfer is in excess of 99.999 % per transfer.

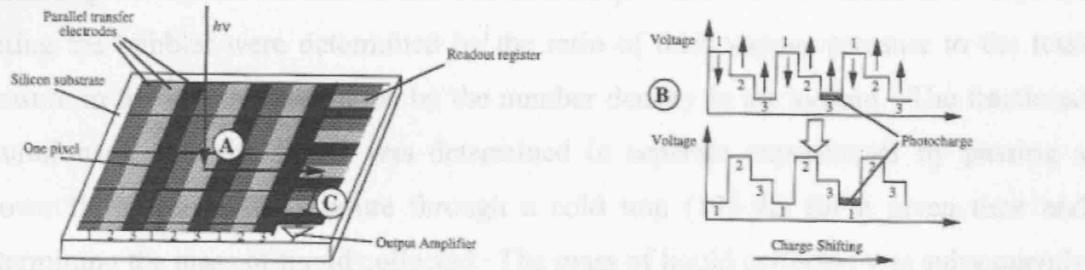

Figure 3.4: Principles of CCD operation and charge transfer. Incident light is converted to photocharge. Three sets of parallel transfer electrodes are charged cyclically to maintain a potential gradient across the device, moving charge. Finally, when the charge has traversed the entire device, the charge is read out *via* the output amplifier. Reproduced from Rowley *et al.*[10]

The major sources of noise associated with the CCD are dark current and photonic noise. Dark current is produced on the device in the absence of incident light, largely as a result of thermal excitation of charge carriers in the device, and is minimised by Peltier cooling of the device to 200 K, combined with enclosure of the device in a vacuum for thermal insulation. In a further attempt to minimise the effects of dark current, the signal on each pixel is measured prior to exposure to the incident light and subtracted from the signal obtained during an experiment. Photonic noise is inherent to the incident light intensity, and, given the Poisson distribution of photon flux, is proportional to the square root of the intensity recorded. A typical full pixel capacity of 2×10^6 photons thus has a corresponding photonic noise level of ± 0.07 %.

3.5 Experimental Details

3.5.1 Gas Handling

Precursor gas mixtures were prepared in a Pyrex mixing line consisting of a carrier gas flow tube into which individual reactive gases were fed *via* gas injectors fitted with greaseless Teflon taps (Young & Co.) and aligned against the carrier flow to ensure efficient mixing. Precursor species in the liquid phase under ambient conditions were introduced into the vapour phase by passing a flow of inert gas through a bubbler containing the liquid at a known and constant temperature. Concentrations of vapours exiting the bubbler were determined by the ratio of their vapour pressure to the total pressure in the system, multiplied by the number density in the system. The fractional saturation of gas with liquid was determined in separate experiments by passing a known flow rate of the mixture through a cold trap (195 K) for a given time and determining the mass of liquid collected. The mass of liquid collected was subsequently compared to the expected value, calculated from the vapour pressure of the liquid at the temperature of the bubbler, the flow rate of the gas, and the time over which the experiment was conducted.

The composition of the gas mixture was determined by controlling the mass flow rates of the individual gases into the mixing line. Flow rates of non-corrosive gases were regulated by use of mass flow controllers (MKS Instruments), while flow rates of corrosive gases were set using stainless steel or teflon needlevalves (Swagelok) and monitored using glass rotameters (Young & Co.). Total flow rates of gas mixtures were typically maintained at 1000 sccm (standard cm^3 per minute) at 760 Torr and adjusted accordingly with pressure to maintain constant number densities for reactive gases and constant residence times within the reaction cell. All flow controllers and rotameters were regularly calibrated, and details of the calibration procedure are described in Appendix 1.

During an experiment gases were passed slowly and continuously from the mixing to the reaction cell *via* Teflon tubing, thus ensuring a fresh mix of gas for each photolysis event, whilst keeping the degree of flowout (the rate of loss of gas from the cell due to its flow rate) minimal during a kinetic experiment. The reaction cell, a spectrosil quartz tube 1 m in length and 1.48 cm in internal diameter, was double jacketed. The inner

jacket was connected to a thermostatting unit (Huber CC180), from which an inert temperature controlled liquid (Galden HT110) was passed continuously to regulate the temperature of the cell in the range 206 to 373 K to an accuracy of ± 0.5 K. The internal temperature of the reaction cell was measured using a ceramic enclosed Pt-100 resistance thermometer (Farnell, PT100) placed in the gas flow. The outer jacket of the reaction cell was connected to a rotary pump and thus could be evacuated to prevent condensation of atmospheric water vapour on the cell walls when working at low cell temperatures. The similarly double windowed endpieces of the reaction cell were also evacuated to prevent condensation on the optical surfaces. Experiments were conducted in order to investigate, and calibrate, the extent of any longitudinal temperature gradients in the reaction cell. Details of these experiments can be found in Appendix 1

The exit to the reaction cell was connected *via* a throttle valve to a rotary pump to allow regulation of the gas pressure within the cell. Cell pressure was continuously monitored at the entrance to the reaction cell using a capacitance manometer (MKS Instruments Baratron).

3.5.2 Radical Generation

Atoms and free radicals were generated within the reaction cell using either flashlamp photolysis (conventional flash photolysis) or laser photolysis (laser flash photolysis), as discussed below.

3.5.2.1 Conventional Flash Photolysis

The flashlamp, a 1 m long xenon arc lamp filled to a pressure of 50 Torr (Perkin Elmer, QDX66), was situated adjacent and parallel to the reaction cell. The lamp was powered by a 25 kV, 2.6 μF rapid discharge capacitor (NWL Ltd.), typically charged to 20 kV using a high voltage power supply (Glassman High Voltage Ltd., EH100). To prevent undesired firing of the flashlamp, activation was controlled by a spark gap (EG&G, GP12B) ionised by a trigger module (EG&G, TM11A). The trigger module, connected to the control computer by an isolated fibre optic cable, was itself activated by a +5 V pulse. The pulse energy of the flashlamp, approximately 520 J over the wavelength range 180 – 700 nm, was completely delivered within 20 μs. The effective photolysis

intensity could be crudely varied by altering the distance between the flashlamp and the reaction cell in the range 3 – 18 cm.

The flashlamp and reaction cell were enclosed in an opaque, baffled, aluminium box to prevent the escape of stray flashlamp light. In order to minimise radiofrequency interference from the flashlamp, the box was earthed to a point remote from the CCD electronics. For the same reason, the flashlamp circuit was housed in a Faraday cage earthed to the same point. All electrical leads into the box connecting the flashlamp to the circuit were screened, and mains power was supplied from a filtered unit.

3.5.2.2 Laser Flash Photolysis

The laser, an excimer laser (Lambda-Physik COMPex 201), was operated at wavelengths of 193 or 351 nm. Firing of the laser was achieved by activation of a trigger module (EG&G, TM11A), controlled in an identical manner to that used to activate the flashlamp. The beam exiting the laser was collimated and expanded horizontally to fill the entire internal diameter of the reaction cell using a pair of fused silica cylindrical lenses (Exitech Ltd.). The expanded beam was directed longitudinally along the length of the reaction cell by a dichroic reflector (Elliot Scientific) mounted on a precision gimbal stage (Melles Griot Ltd.), and directed into a joulemeter (JP25LP-MUV, Photonic Solutions) by an additional dichroic reflector situated at the end of the reaction cell. The pulse energy of the laser, typically 200 to 350 mJ per pulse delivered within 10 ns, was also measured at the laser exit (Lambda-Physik internal powermeter). Precursor gas mixtures were carefully designed in order to prevent the generation of significant longitudinal concentration gradients of photolytically produced species in the reaction cell, which could have distorted observed kinetics.

3.5.3 Species Monitoring

Species within the reaction cell were identified and monitored by time-resolved UV absorption spectroscopy. The UV source, the analysis lamp, was a 30 W high brightness deuterium lamp (Hamamatsu L5499), providing radiation maximising in the wavelength range 200 – 300 nm. Output from the analysis lamp was collimated through the reaction cell and focused onto the entrance slit of a 25 cm focal length astigmatic Czerny-Turner spectrograph (Chromex 250IS) using a pair of 100 mm focal length spectrosil quartz lenses (Comar Ltd.).

The spectrograph contained three interchangeable diffraction gratings. The three gratings, ruled with 150, 300 and 600 grooves per mm, combined with the detector size, gave rise to spectral coverages of approximately 120, 60 and 30 nm respectively, with corresponding limiting resolutions (dispersions) of 0.45, 0.22 and 0.11 nm per pixel. In practice, the entrance slit width determined the spectral resolution used. All experiments reported in this thesis were conducted using the diffraction grating with 300 grooves per mm, and an entrance slit to the spectrograph of width 500 μm. Wavelength, dispersion and instrumental resolution were calibrated relative to the well-defined mercury UV emission spectrum provided by a low pressure Hg Pen-Ray lamp (Oriel) with spectrograph settings identical to those used in kinetic experiments. The calibration procedure is described in Appendix 1.

The CCD detector consisted of a 298 column by 1152 row array of light sensitive pixels (EEV CCD05-10-0-202), mounted in a Peltier cooled camera head (Wright Instruments Ltd.). As discussed above, and shown schematically in Figure 3.3, the CCD was situated in the dispersive plane of the spectrograph with the camera head fitted to the spectrograph by use of an adjustable flange, thus facilitating focusing and translation of the device with respect to the spectrograph light output. The wavelength resolved light exiting the spectrograph was incident across the entire 298 pixel axis of the top 31 rows of the CCD. The 298 pixel axis of columns of the CCD array therefore represented the wavelength resolved axis of the array, while the time resolved axis was represented by the 1152 rows of the array.

Photocharge was shifted row-by-row, as described previously, at a selected rate from the illuminated region of the CCD, the top 31 rows, to the storage region of the CCD. Simultaneous illumination of 31 rows of the CCD gave rise to a distortion of the temporal resolution of the experiment, since each row in the storage region was exposed to the incident light for a time given by the product of the number of rows exposed (31) and the rate at which the signal was shifted from the illuminated region to the storage region. This distortion was accounted for in analysis of data as discussed in Appendix 2. The storage region of the CCD was shielded from the incident radiation with an optical mask and a baffle was situated on the window of the detector to further reduce

the amount of scattered light incident on the device. A rapid mechanical shutter was also placed in the optical line to prevent the accumulation of photocharge between integrations.

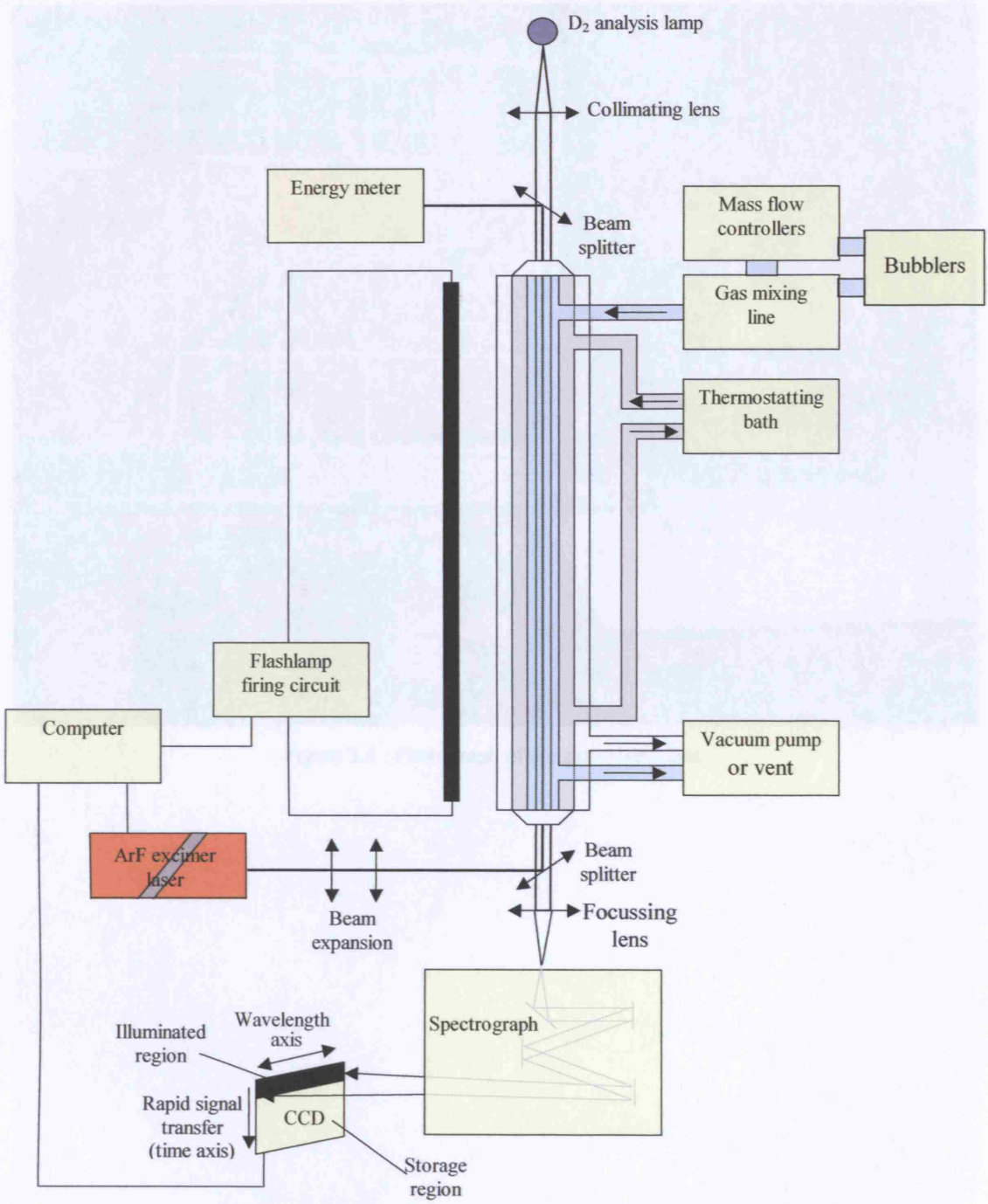

Figure 3.5: Schematic of flash photolysis apparatus employing CCD detection.

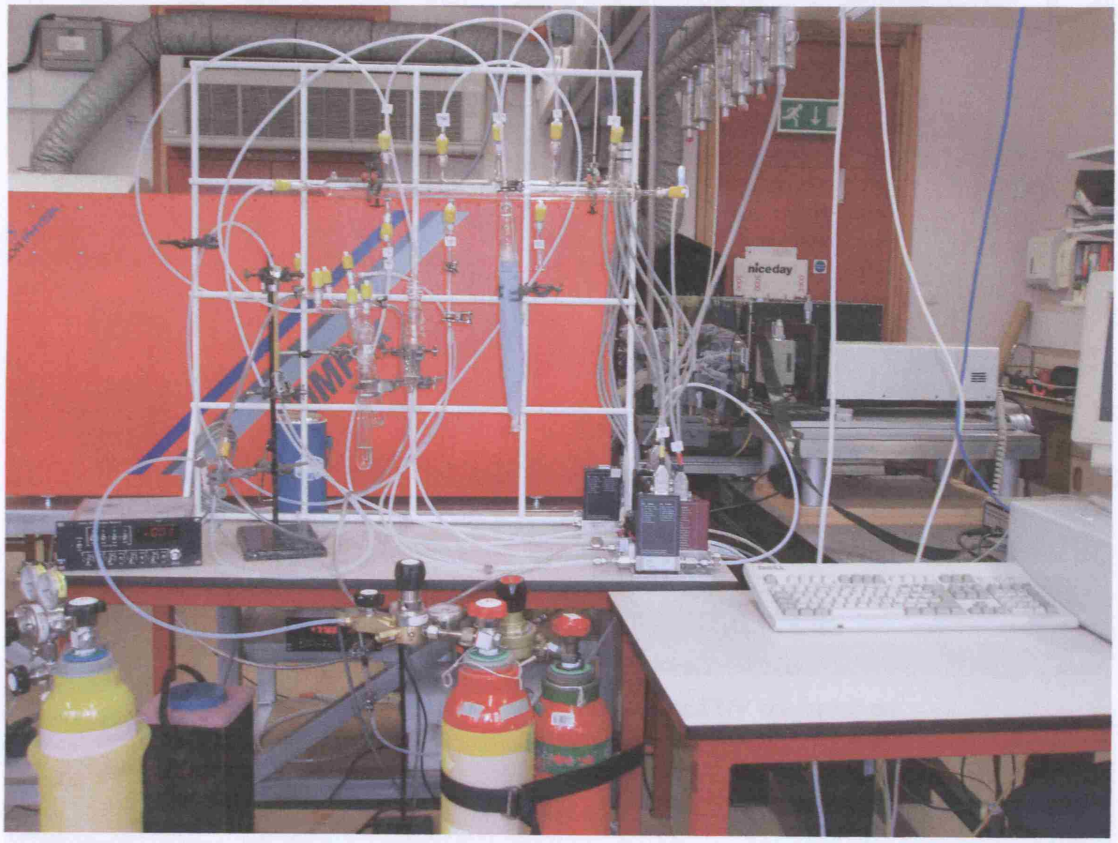

Figure 3.6 : Photograph of the gas mixing line.

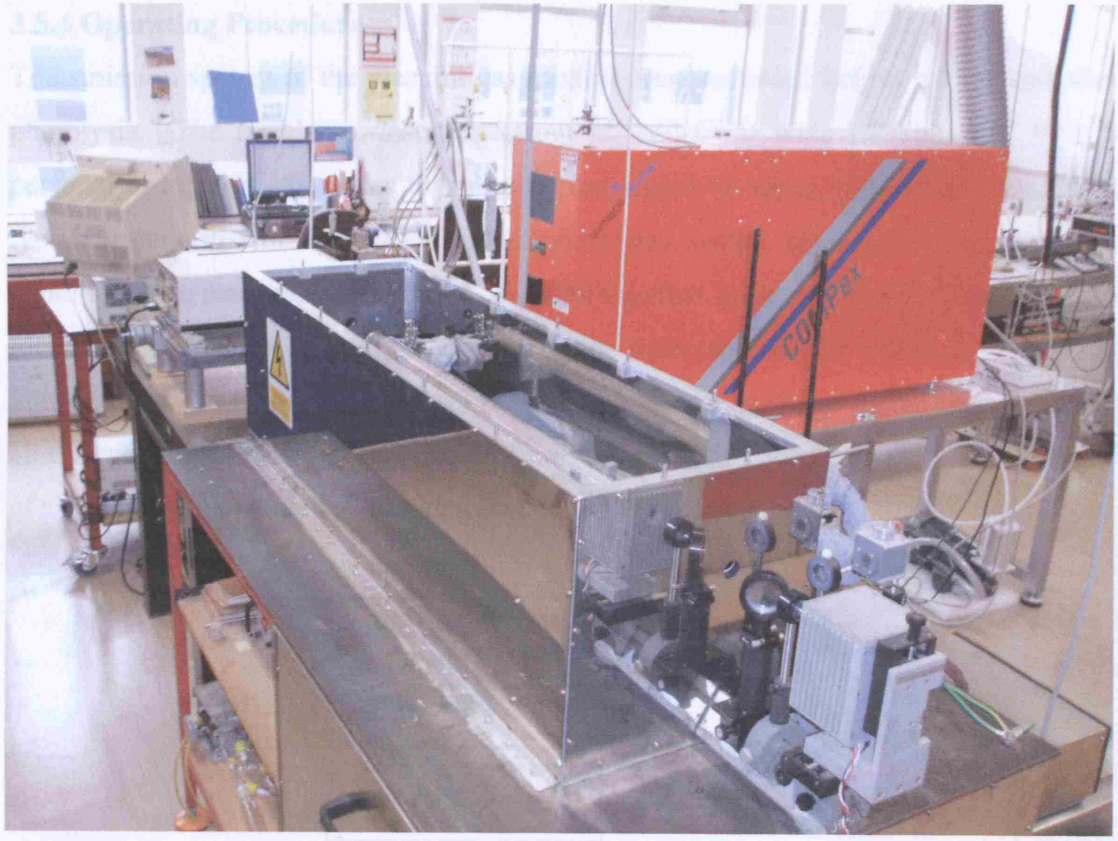

Figure 3.7 : Photograph of the reaction cell and UV source lamps.

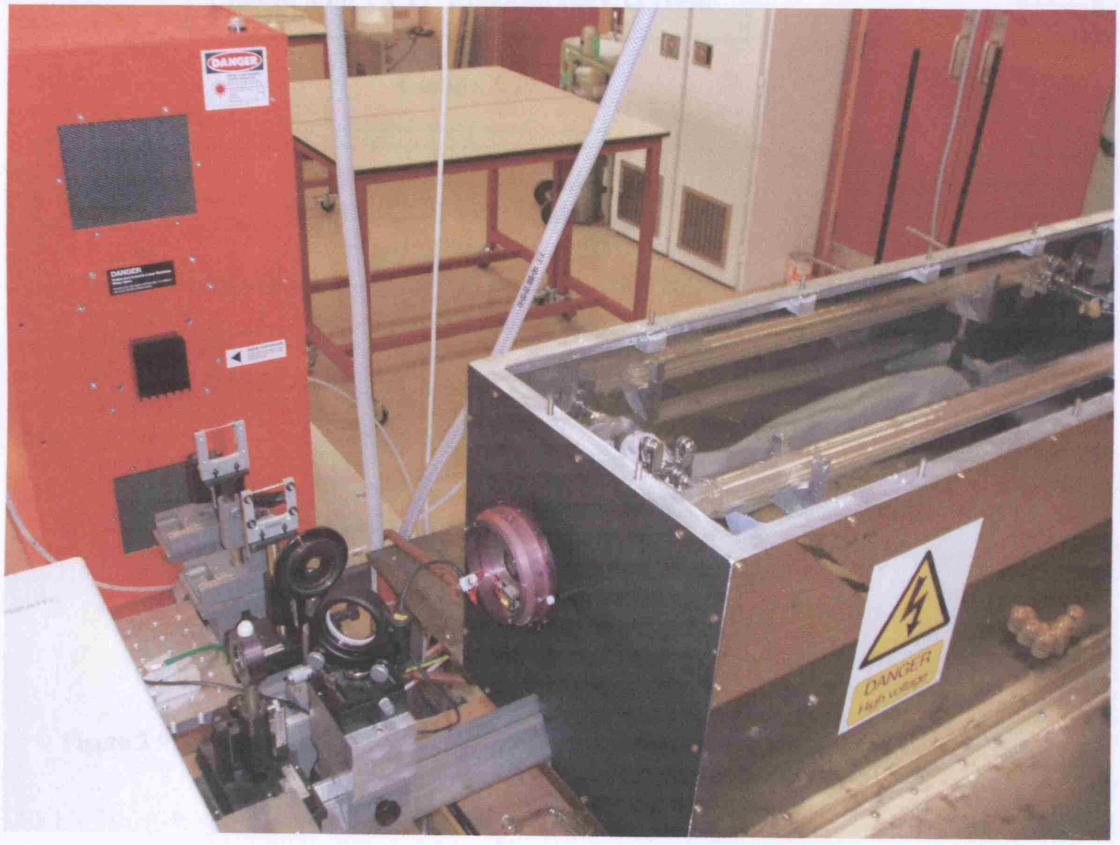

Figure 3.8 : Photograph of the laser optics.

3.5.4 Operating Procedure

Transmission spectra of the reactant gas mixture were recorded before, during and after photolysis. The flashlamp, laser, spectrograph and CCD were all controlled from a personal computer. In order to improve the signal to noise ratio each experiment typically consisted of 20-100 individual photolysis events, conducted under identical conditions, the results of which were co-added together prior to analysis. The repetition rate of the photolysis events was limited by the time required for recharge of the high voltage capacitor (15 s), or, for laser experiments the gas residence time of the cell. In all experiments a fresh gas mixture was present for each photolysis event. The course of a typical experiment is shown schematically in Figure 3.9.

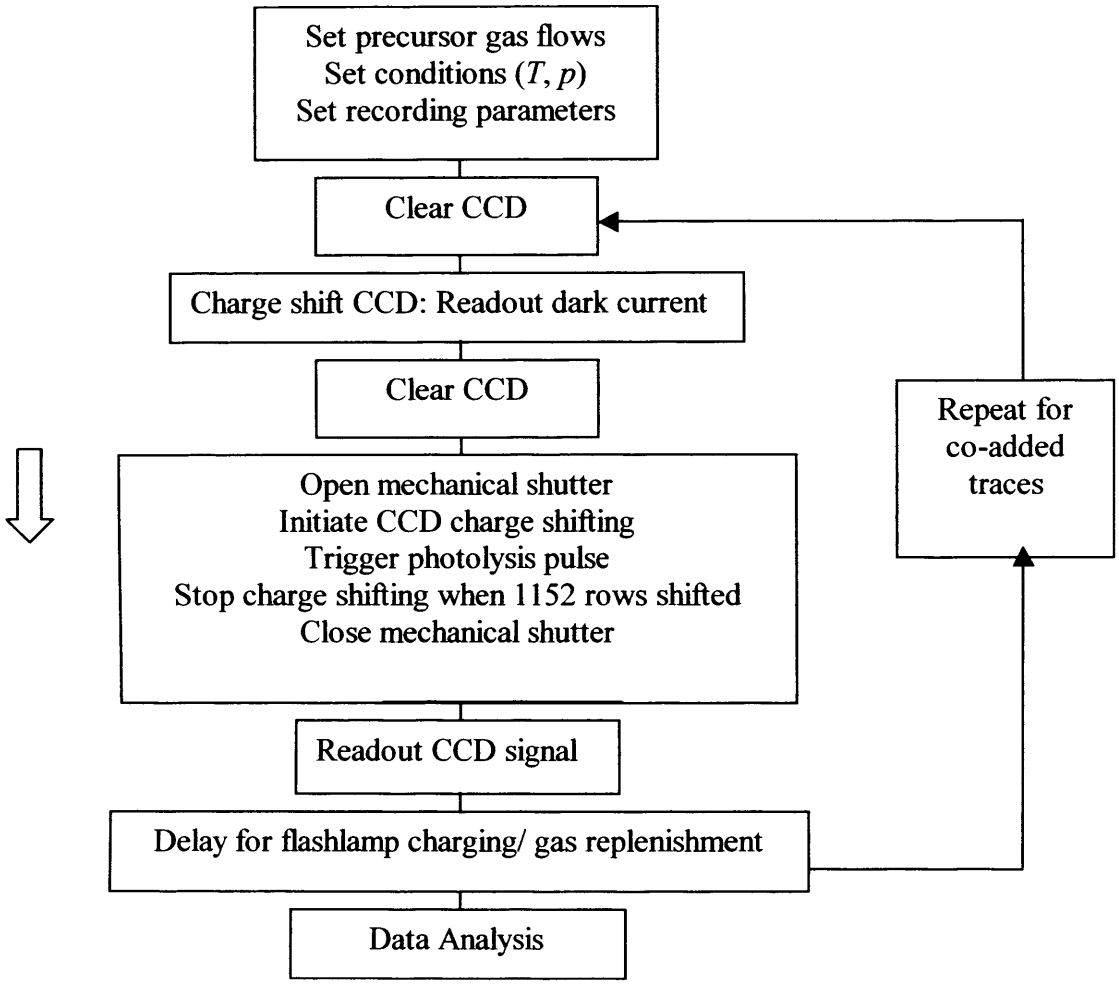

Figure 3.9: Flow chart indicating the operating procedure during a flash photolysis experiment.

3.6 Analytical Procedures

3.6.1 Determination of Absorbance Spectra

Output from the CCD was a matrix consisting of 298 columns by 1152 rows, with each column representative of a time-resolved transmitted intensity at a particular wavelength point and each row representative of a spectrally resolved intensity at a particular time point during the course of the experiment.

In a kinetic experiment, transmission spectra were recorded for the gas mixture in the reaction cell before, during and after photolysis (known as pre- and post-flash). Wavelength and time resolved absorbances, $A_{\lambda,t}$, were calculated relative to those recorded in the pre-flash period using Beer's Law (3.ii):

$$A_{\lambda,t} = \ln\left(\frac{\langle I_{\lambda,0}\rangle}{I_{\lambda,t}}\right) \qquad (3.ii)$$

where $\langle I_{\lambda,t}\rangle$ is the average light intensity recorded at wavelength λ in the pre-flash period, and $I_{\lambda,t}$ is the light intensity recorded at wavelength λ and time t.

Absorption spectra calculated in this way displayed the changes in total gas absorbance occurring as a result of the photolytically initiated chemistry occurring within the reaction cell. It was found, however, that a small complication resulted from the charge shifting process unique to the CCD, leading to an apparent increase in absorbance with time. This complication arose due to the acquisition of spurious additional charge as the photocharge generated from illumination was shifted down the storage region of the CCD throughout the experiment. Acquisition of additional charge was a cumulative effect, depending upon the number of rows of the CCD traversed. Thus, charge from the early stages of an experiment, which was shifted down the entire storage region of the CCD accumulated a greater amount of additional charge than photocharge recorded at later times in the reaction. The consequence of this additional charge was that recorded intensities contained a small component decreasing steadily with experimental time, causing an apparent increase in absorbance, as calculated using equation (3.ii),

with time. In order to correct for the effects of additional charge, experiments were conducted in the absence of a photolytic pulse ('non-flashed' experiments) under otherwise identical conditions, and the absorbances derived from such experiments, $A_{\lambda,t,NF}$, subtracted from those recorded in photolytic ('flashed') experiments, $A_{\lambda,t,F}$, to give the true absorbance, $A_{\lambda,t}$:

$$A_{\lambda,t} = A_{\lambda,t,F} - A_{\lambda,t,NF} \qquad (3.iii)$$

This correction was typically very small, *ca.* 1 % of the intensity, corresponding to a maximum absorbance of *ca.* 10^{-4}.

3.6.2 Determination of Species Concentrations

The total observed absorbance of the reaction mixture at wavelength l and time t, $A_{\lambda,t}$, is related to the concentrations of absorbing species at time t, c_t, by the Beer-Lambert Law (3.iv):

$$A_{\lambda,t} = \sum_i \sigma_{i,\lambda}\, c_{i,t}\, l \qquad (3.iv)$$

where $\sigma_{i,\lambda}$ is the absorption cross-section for species i at wavelength λ, $c_{i,t}$ the concentration of species i at time t, and l the absorption path length. As discussed above for post-photolysis spectra calculated relative to pre-photolysis spectra, the concentrations are the changes in concentration relative to the pre-photolysis values. Thus, species produced by the photolysis and subsequent chemistry contribute positively to the post-photolysis absorbance and those removed by photolysis have a negative contribution to the absorbance calculated in (3.iv).

In all cases, concentrations of absorbing species were determined by least squares fitting of reference absorption cross-sections to the experimental absorbance across the entire wavelength range at each time point. This fitting minimised the sum of squares between parameterised reference cross-sections and experimental absorbances, yielding values of $c_{i,t}\, l$ for each absorbing species. Knowledge of l was then invoked to obtain time resolved species concentrations. The origin of absorption cross-sections for the

absorbing species (peroxy radicals) studied in this work is discussed in detail in the relevant chapters to follow, along with (small) corrections made to the spectral fitting routines to account for product absorbances.

3.6.3 Determination of Kinetic Parameters

Having obtained time-resolved concentrations of photolytically generated species, where possible, classical kinetic solutions were least squares fitted to the experimental concentration-time profiles to determine the rate coefficient and initial species concentration for the reaction of interest. In this case, minimisation of the sum of squares between a simulated and an experimental temporal trace was used. The temporal distortion of the experimental data arising from the simultaneous illumination of several rows of the CCD was accounted for by the application of a sliding averaging function to the classical kinetic solution prior to the fitting procedure. This is discussed in detail in Appendix 2.

Where classical kinetic solutions were not available, the commercially available numerical integration program FACSIMILE[11] was used to simulate concentration-time profiles and to optimise the kinetic parameters in the simulation to best fit the simulation to the experimental data. FACSIMILE models used to simulate experimental data also incorporated subroutines to account for the temporal distortion of experimental data, and contained all known potential gas phase chemistry occurring within the reaction system, as well as flowout of gas from the monitored region. Sensitivity analyses were conducted on each model used in order to investigate possible effects on the kinetic parameters determined from the models due to the occurrence of secondary chemistry. Details of the individual model fits to data and the sensitivity analyses are given in the appropriate chapter below.

3.7 References

[1] J.V. Seeley, J.T. Jayne, M.J. Molina, *Int. J. Chem. Kinet.*, **1993**, 25, 571

[2] J.V. Seeley, J.T. Jayne, M.J. Molina, *J. Phys. Chem.*, **1996**, 100, 4019

[3] C.J. Percival, D.E. Shallcross, C.E. Canosa-Mas, J.M. Dyke, *J. Photochem. Photobiol. A: Chem.*, **2005**, 176, 250

[4] M.J. Pilling and P.W. Seakins, *Reaction Kinetics*, **1995**, Oxford University Press

[5] C.J. Howard, *J. Phys. Chem.*, **1979**, 83, 3

[6] R.G.W. Norrish and G. Porter, *Nature*, **1949**, 164, 658

[7] G. Porter, *Proc. R. Soc.*, **1950**, A200, 284

[8] G. Porter and F.G. Wright, *Disc. Farad. Soc.*, **1953**, 14, 23

[9] G. Porter and P. West, *Proc R. Soc Ser. A.*, **1964**, 279, 302

[10] D.M. Rowley, M. H. Harwood, R.A. Freshwater and R.L. Jones, *J. Phys. Chem.*, **1996**, 100, 3020

[11] A.R. Curtis and W.P. Sweetenham, FACSIMILE, *AERE Harwell Publication R12805*, **1987**, Computer Science and Systems Division, Harwell Laboratory, Oxfordshire

Chapter 4

The Hydroperoxy Self-Reaction

4.1 Introduction

As discussed in Chapter 1, oxidation processes in the lower atmosphere provide efficient removal mechanisms for many gas phase species emitted into the atmosphere, preventing the accumulation of pollutants to dangerous levels.

The major oxidising species in the sunlit troposphere is the hydroxyl radical, OH, produced following the solar photolysis of ozone, O_3. Solar photolysis of ozone at wavelengths above approximately 320 nm results in formation of molecular oxygen and ground state oxygen atoms, $O(^3P)$. In this case, these ground state oxygen atoms subsequently react with O_2 to reform O_3, resulting in no net chemical change.

$$O_3 + h\nu \rightarrow O_2 + O(^3P) \quad (\lambda>320 \text{ nm}) \quad (4.1a)$$

$$O(^3P) + O_2 + M \rightarrow O_3 + M \quad (4.2)$$

Below 320 nm, however, a significant amount of the oxygen atoms generated by ozone photolysis are electronically excited, $O(^1D)$:

$$O_3 + h\nu \rightarrow O_2 + O(^1D) \quad (\lambda<320 \text{ nm}) \quad (4.1b)$$

Most $O(^1D)$ produced in the atmosphere, particularly in the relatively high pressures of the troposphere, are quenched to ground state $O(^3P)$, ultimately resulting in regeneration of O_3:

$$O(^1D) + M \rightarrow O(^3P) + M \quad (4.3)$$

$$O(^3P) + O_2 + M \rightarrow O_3 + M \quad (4.2)$$

However, on account of the relatively high water content of the lower atmosphere, reaction of $O(^1D)$ with water vapour to produce hydroxyl radicals, OH, is often suitably rapid to provide some competition to the quenching of $O(^1D)$ to $O(^3P)$.

$$O(^1D) + H_2O \rightarrow 2\ OH \qquad (4.4)$$

This production of OH represents one of the most important reactions in tropospheric chemistry.[1,2] Hydroxyl radicals produced in the troposphere principally interconvert rapidly with hydroperoxy radicals, HO_2. OH is converted to HO_2 through the reaction of OH with CO, and the subsequent rapid combination of the free H atom with O_2:

$$OH + CO \rightarrow H + CO_2 \qquad (4.5)$$

$$H + O_2 + M \rightarrow HO_2 + M \qquad (4.6)$$

In unpolluted, or 'background', air the HO_2 radical may react with ozone to reform OH:

$$HO_2 + O_3 \rightarrow OH + 2\ O_2 \qquad (4.7)$$

On account of this conversion, OH and HO_2 are often conveniently considered together as the HO_x family, where $[HO_x] = [OH] + [HO_2]$.[1,2] The concentration of HO_x in the troposphere governs the tropospheric oxidising capacity – the ability to remove pollutants through OH initiated oxidation. The steady state HO_x concentration is governed by the relative rates of the HO_x production and loss reactions. Production, as discussed above, depends on ozone photolysis and the presence of water vapour. Loss of HO_x from the atmosphere typically occurs due to recombination of radical species. In the absence of nitrogen oxides, NO_x (where $[NO_x] = [NO] + [NO_2]$), the major loss process for HO_x from the troposphere is the hydroperoxy self-reaction, (4.8), since the H_2O_2 product is highly soluble in water and readily removed from the lower atmosphere in precipitation.[1,2]

$$HO_2 + HO_2\ (+ M) \rightarrow H_2O_2 + O_2\ (+ M) \qquad (4.8)$$

Although solar photolysis of H_2O_2

$$H_2O_2 + h\nu \rightarrow 2\ OH \qquad (4.9)$$

provides a source for HO_x, and can be important in the upper troposphere and lower stratosphere, the hydroperoxy self-reaction remains the dominant removal process for HO_x in the lower troposphere in the absence of NO_x, and the rate of (4.8) can be the most important factor in controlling the removal of HO_x from the troposphere.[1,2]

In the atmosphere polluted by NO_x the reaction of HO_2 with NO:

$$HO_2 + NO \rightarrow OH + NO_2 \qquad (4.10)$$

occurs in competition with (4.8), and the relative rates of (4.8) and (4.10) determine the changes in tropospheric HO_x and NO_x. It should be noted that reaction (4.10) still provides a route back from HO_2 to OH, maintaining the HO_x equilibrium. Importantly, however, production of the pollutant NO_2 in (4.10) may result in O_3 generation, through the ready solar photolysis of NO_2:

$$NO_2 + h\nu \rightarrow NO + O(^3P) \qquad (4.11)$$

$$O(^3P) + O_2 \rightarrow O_3 \qquad (4.2)$$

Enhanced ozone production may lead to an overall increase in HO_x through the HO_x generation chemistry described above. Furthermore, both NO_x and O_3 are pollutants and components of photochemical smog, an environmental problem that can occur under certain meteorological conditions as a result of the above chemistry.[1,2]

In order to achieve accurate and reliable modelling of atmospheric oxidation processes, and prediction of issues such as smog formation, it is essential that the factors affecting the amount of atmospheric HO_x are fully characterised and understood. For example, recent comparisons between tropospheric measurements of HO_x and atmospheric

models have revealed that modelled HO_2 concentrations are typically higher than the measured values.[3] Assuming that the measurements are sound, discrepancies between measurements and models could indicate an incomplete description of tropospheric chemistry used in atmospheric models, or, alternatively, the photochemical and kinetic parameters for the reactions determining the amount of modelled HO_x could be incorrect. The rate coefficient for the HO_2 self-reaction is one such parameter, and, in view of this, the HO_2 self-reaction has been the subject of a number of laboratory based kinetic and mechanistic studies over a range of experimental conditions.

4.2 Previous Work

Previous studies of HO_2 self-reaction kinetics have revealed a number of interesting features. The rate coefficient for reaction (4.8), $k_{4.8}$, defined in (4.i),

$$\frac{-d[HO_2]}{dt} = 2k_{4.8}[HO_2]^2 \qquad (4.i)$$

has been shown to consist of both 'bimolecular' (pressure independent) and 'termolecular' (pressure dependent) components, each exhibiting negative temperature dependence.[4] An enhancement in the rate of the HO_2 self-reaction in the presence of small hydrogen-bonding molecules, such as H_2O, NH_3 and CH_3OH, has also been observed.[5-14]

An early investigation of HO_2 self-reaction kinetics by Cox and Burrows[9] used molecular modulation spectrometry (MMS) over the temperature range 273 – 339 K at pressures from 3 to 760 Torr, using two different reaction schemes for HO_2 radical generation. The first method used chlorine photolysis in the presence of H_2 and O_2:

$$Cl_2 + h\nu \rightarrow 2\,Cl \qquad (4.12)$$

$$Cl + H_2 \rightarrow H + HCl \qquad (4.13)$$

$$H + O_2 + M \rightarrow HO_2 + M \qquad (4.6)$$

This method, however, was found to be unsuitable below 25 Torr due to the dependence of (4.6) on pressure, and a second method was developed in which HCHO replaced H_2:

$$Cl + HCHO \rightarrow HCO + HCl \quad (4.14)$$

$$HCO + O_2 \rightarrow HO_2 + CO \quad (4.15)$$

The MMS technique employed periods of continuous photolysis of the reaction mixture alternated with 'dark' periods, with the mixture probed by UV absorption. Analysis of the UV absorption waveform as a function of time, generally an increase in absorption during photolysis followed by a decrease in the dark period, was used to extract kinetic parameters.

Cox and Burrows reported no significant pressure dependence of $k_{4.8}$ above 25 Torr, although limiting high and low pressure values of $k_{4.8}$ did display a marked difference. A negative dependence of $k_{4.8}$ on temperature was observed, in agreement with an earlier study by Lii *et al.*[15] at a total pressure of 1200 Torr. Further studies by Lii *et al.*[7,8] covered the pressure range 400 – 1500 Torr at temperatures between 276 and 400 K using pulse radiolysis of H_2 and the reaction of H with O_2, reaction (4.6). No dependence of $k_{4.8}$ on pressure was observed by these authors, and a low pressure study by Takacs and Howard[16] in the range 1 – 7 Torr conducted between 253 and 390 K also found $k_{4.8}$ to display a negative temperature dependence and to be independent of pressure.

The combined effects of temperature and pressure on $k_{4.8}$ led Cox and Burrows to propose a reaction mechanism involving the initial formation of a short-lived excited $H_2O_4^*$ complex by combination of two HO_2 radicals. Unless quenched by molecular collision to form the vibrationally relaxed $H_2O_4^\dagger$ species, the $H_2O_4^*$ complex dissociates to reform the reactant HO_2 radicals. Dissociation of the vibrationally relaxed $H_2O_4^\dagger$ either reforms reactants, possibly requiring collisional activation, or leads to product formation. Thus, the reaction sequence can be expressed as:

$$HO_2 + HO_2 \leftrightarrow H_2O_4^* \quad (4.8a)$$

$$H_2O_4^* + M \rightarrow H_2O_4^\dagger + M \quad (4.8b)$$

$$H_2O_4^\dagger (+ M) \rightarrow 2\,HO_2 (+ M) \quad (4.8c)$$

$$H_2O_4^\dagger \rightarrow H_2O_2 + O_2 \quad (4.8d)$$

This mechanism accounts for the effects of pressure on $k_{4.8}$ observed by Cox and Burrows since collisional deactivation of $H_2O_4^*$ to $H_2O_4^\dagger$ at low pressure would be unable to compete with dissociation of $H_2O_4^*$ to reactants, resulting in a decrease in the rate of the HO_2 self-reaction as the pressure is reduced. The negative temperature dependence of $k_{4.8}$ can be rationalised if the initial $H_2O_4^*$ complex formation occurs with a negative or near zero activation energy, and if channel (4.8d), resulting in product formation, has a potential energy barrier below the entrance channel.

Sander *et al.*[10] used flash photolysis with ultraviolet absorption spectroscopy (FP/UVA) to investigate the effects of different bath gases on the rate of the HO_2 and DO_2 self-reactions between 100 and 700 Torr at 298 K. Two methods were used for HO_2 production, one employing photolysis of $Cl_2/H_2/O_2$ mixtures, as used by Cox and Burrows, but it was found that high pressures of O_2 were required to compete with the reaction between H and Cl_2:

$$H + Cl_2 \rightarrow Cl + HCl \quad (4.16)$$

and that high H_2 pressures were necessary to prevent (4.17):

$$Cl + HO_2 \rightarrow HCl + O_2 \quad (4.17)$$

thus limiting the range of experimental conditions that could be used with this radical generation system. The second method used to generate HO_2 was the photolysis of $Cl_2/CH_3OH/O_2$ mixtures:

$$Cl_2 + h\nu \rightarrow 2\,Cl \quad (4.12)$$

$$Cl + CH_3OH \rightarrow CH_2OH + HCl \quad (4.18)$$

$$CH_2OH + O_2 \rightarrow HO_2 + HCHO \qquad (4.19)$$

In contrast to the results of Cox and Burrows and Lii *et al.*, Sander *et al.* found a linear dependence of $k_{4.8}$ on total pressure, with a non-zero value for $k_{4.8}$ on extrapolation to zero pressure. Such behaviour was observed with all collisional partners investigated (SF_6, N_2, O_2, Ar and He), and led to the proposal of a mechanism whereby the $H_2O_4^*$ complex formed by combination of two HO_2 radicals can dissociate back to reactants, or rearrange to form reaction products by either a direct route or by a collisional process. Sander *et al.* noted that more than one H_2O_4 intermediate may be involved, as suggested by Cox and Burrows, and a variation on the mechanism advanced by Sander *et al.* involving more than one H_2O_4 intermediate was proposed by Thrush and Tyndall[17] on the basis of a low pressure study:

$$HO_2 + HO_2 \leftrightarrow H_2O_4^* \qquad (4.8a)$$
$$H_2O_4^* + M \rightarrow H_2O_4^\dagger + M \qquad (4.8b)$$
$$H_2O_4^\dagger \rightarrow H_2O_2 + O_2 \qquad (4.8d)$$
$$H_2O_4^* \rightarrow H_2O_2 + O_2 \qquad (4.8e)$$

The mechanisms advanced by Sander *et al.* and Thrush and Tyndall account for the increase in $k_{4.8}$ with pressure with a non-zero value for $k_{4.8}$ on extrapolation to zero pressure, and can also explain the negative temperature dependence if the barriers for product formation from the $H_2O_4^*$ intermediates lie below the entrance channel.

Generation of H_2O_2 and O_2 as major reaction products of (4.8) was reported by Sander *et al.* on the basis of their UV absorption measurements, providing support for an earlier FTIR product study by Niki *et al.*[18]

Subsequent investigations of the pressure dependence of $k_{4.8}$ have been carried out by Simonaitis and Heicklen,[19] between 5 and 770 Torr at 296 K, Kircher and Sander,[11] in the range 100 – 700 Torr between 240 and 420 K, Kurylo *et al.*,[20] from 25 to 600 Torr at 298 K, and Lightfoot *et al.*,[21] between 100 – 760 Torr at temperatures from 248 to 573 K. Each of these investigations used flash photolysis of $Cl_2/CH_3OH/O_2$ mixtures, and are in agreement with the work of Sander *et al.*,[10] reporting $k_{4.8}$ to have a non-zero value

on extrapolation to zero pressure and to increase linearly with pressure. The studies by Kircher and Sander and by Lightfoot *et al.*, both of which were conducted over a range of temperatures and pressures, allowed determination of the temperature dependences of both the bimolecular and termolecular components to the overall rate coefficient by extrapolation to zero pressure at each temperature.

An enhancement in $k_{4.8}$ in the presence of water vapour was first observed by Hamilton[5] using pulse radiolysis of H_2/O_2 mixtures to produce HO_2 at a total pressure of 1520 Torr at 295 K. The rate coefficient for HO_2 decay was observed to increase linearly as the vapour pressure of water in the system was increased from 0 to 15 Torr. Extrapolation of the rate coefficient measured by Hamilton to higher water vapour concentrations is in good agreement with the results of an earlier study by Hochanadel *et al.*[22] in which photolysis of water vapour itself was used as a source of HO_2, presumably unaware of any rate enhancement effects.

Hamilton also reported a similar enhancement in $k_{4.8}$ when 10 Torr NH_3 was added to the reaction mixture, but the addition of 10 Torr CH_4 had no effect on the HO_2 decay kinetics. Since the enhancement was only observed with polar hydrogen bonding molecules, Hamilton suggested that the enhancement was unlikely to be due to a simple energy transfer mechanism, and that complex formation between HO_2 and H_2O, or NH_3, might be responsible.

No change in the UV absorption spectrum of HO_2 was observed by Hamilton in the presence of water vapour, and the spectrum recorded by Hochanadel *et al.* is in reasonable agreement with those reported in other studies in the absence of water vapour. This led Hamilton to propose that either the concentrations of any HO_2 complexes were significantly less than those of free HO_2, or that the absorption cross-sections of HO_2 remains unchanged on complexation.

The effects of H_2O and NH_3 on $k_{4.8}$ were later studied in further detail by Hamilton and Lii.[6] The results were found to be in agreement with the previous work of Hamilton, and analogous results were reported for a deuterated system, studying DO_2 in the presence of D_2O. On the basis of this study, and an *ab initio* investigation of $HO_2.H_2O$ and $HO_2.NH_3$ complexes by Hamilton and Naleway,[23] Hamilton and Lii postulated a

kinetic scheme for the HO_2 self-reaction in the presence of either H_2O or NH_3, represented as X in the scheme below:

$HO_2 + X$	$\leftrightarrow$	$HO_2.X$	(4.20)
$HO_2 + HO_2$	$\rightarrow$	$H_2O_2 + O_2$	(4.8)
$HO_2 + HO_2.X$	$\rightarrow$	$H_2O_2 + O_2 + X$	(4.21)
$HO_2.X + HO_2.X$	$\rightarrow$	$H_2O_2 + O_2 + 2\,X$	(4.22)

Application of the steady state approximation to $HO_2.X$ gives:

$$k_{obs} = \frac{k_{4.8} + k_{4.21}K_{4.20}[X] + k_{4.22}K_{4.20}^{\ 2}[X]^2}{(1 + K_{4.20}[X])^2} \qquad (4.ii)$$

where $K_{4.20}$ is the equilibrium constant for the association of HO_2 and X.

The *ab initio* study by Hamilton and Naleway predicted the minimum energy configuration of $HO_2.H_2O$ to be a linear hydrogen bonded structure, with HO_2 as the H donor. Hamilton and Naleway did note that the rate of the HO_2 self-reaction might be expected to *decrease* on complexation of HO_2 with H_2O due to steric hindrance, but, equally, that the complexation could allow a chaperone mechanism to operate, whereby the water molecule holds two HO_2 radicals together for sufficient time for reaction to occur.

The $HO_2.H_2O$ complex has in fact subsequently been observed by Nelander[24] using matrix isolation IR spectroscopy. Compared to HO_2 matrix isolated in the absence of water vapour, the wavenumber of the O–H stretch of HO_2 matrix isolated in the presence of water vapour was found to be reduced, while the wavenumbers of the HO_2 O–H bend and O–O stretch were both found to be greater. The wavenumbers of the H_2O symmetric and asymmetric stretches were observed to be reduced in the presence of HO_2. These observations led to the conclusion that the $HO_2.H_2O$ complex is actually cyclic, with the structure as depicted in (S 4.1).

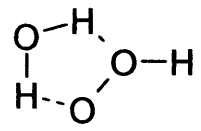

(S 4.1)

The results of the matrix isolation study of Nelander are therefore in conflict with the $HO_2.H_2O$ structure predicted by the *ab initio* investigation by Hamilton and Naleway. More recent *ab initio* investigations of the $HO_2.H_2O$ complex by Aloisio and Francisco[25] and by Belair *et al.*[26] have shown that the structure calculated by Hamilton and Naleway is in fact a saddle point on the $HO_2 + H_2O$ potential energy surface, with the true energy minimum occurring at a structure in agreement with that observed by Nelander. A comparative *ab initio* study of $HO_2.HF$, $HO_2.H_2O$ and $HO_2.NH_3$ complexes also provides support for the structure given in (S 4.1),[27] and suggested the possibility that H_2O acts as an energy sink during reaction, removing the energy released on formation of O_2.

Observation of the $HO_2.H_2O$ in the gas phase was achieved by Aloisio *et al.*[28] using FTIR spectroscopy between 1100 and 1140 cm^{-1}. Experiments were conducted over the temperature range 230 – 298 K to enable experimental determination of the equilibrium constant for association between HO_2 and H_2O, and hence the thermodynamic stability of the complex relative to the free species. Kanno *et al.*[29,30] have also recently measured $K_{4.20}$, and the relative rate enhancement of (4.8) in the presence of water vapour, using IR spectroscopy of HO_2 and H_2O between 250 and 350 K.

The effects of temperature on the water vapour enhancement of $k_{4.8}$ were investigated by Cox and Burrows[9] between 278 and 318 K at 760 Torr, and by Lii *et al.*[8] over the temperature range 298 – 373 K at 1200 Torr. Neither study observed any significant changes in the HO_2 absorption spectrum on addition of H_2O, and both found the rate enhancement to be more pronounced at lower temperatures. Cox and Burrows did, however, report a change in HO_2 decay kinetics from near second-order towards first-order at H_2O vapour pressures above 12 Torr. The change was attributed to the occurrence of surface reactions encouraged by water adsorbed on the walls of the reaction vessel, but has not been reported in any other investigation.

An alternative argument to that given by Hamilton and Lii was given by Cox and Burrows to explain the effects of H_2O on $k_{4.8}$. It was suggested that the reaction of a free HO_2 radical with a complexed $HO_2.H_2O$ species, or of the $HO_2.H_2O$ complex with another $HO_2.H_2O$ complexed species, is capable of producing the vibrationally relaxed $H_2O_4^{\dagger}$ species more efficiently than the reaction of two free HO_2 radicals.

Sander *et al.*[10] and Kircher and Sander[11] investigated the H_2O enhancement of $k_{4.8}$ between 256 and 298 K at 100 Torr and at 270 and 298 K at 700 Torr. The enhancement was observed to increase with decreasing temperature, in good agreement with previous studies. No significant effects of pressure on the enhancement were observed. Kircher and Sander presented a similar explanation to that given by Cox and Burrows for the enhancement in $k_{4.8}$ by H_2O, proposing that a complexed $H_2O_4.H_2O$ intermediate would have a greater stability than a free H_2O_4 intermediate due to its greater number of vibrational degrees of freedom.

Calculations performed by Mozurkewich and Benson,[31] using RRKM theory, lend support to the explanations given by Cox and Burrows and Kircher and Sander, suggesting that the addition of a polar collision partner to the reaction mixture enhances the overall rate of reaction by formation of an adduct that reacts to produce a stabilised H_2O_4 intermediate. It should be noted, however, that the structure for the $HO_2.H_2O$ complex used by Mozurkewich and Benson places a single HO_2–H_2O hydrogen bond between the terminal O atom of HO_2 and one of the H atoms of H_2O, in disagreement with experimental observations and minimum energy calculations of the $HO_2.H_2O$ structure.

Although there have been several investigations of the effects of temperature on the H_2O enhancement of $k_{4.8}$, few have been conducted over temperature ranges relevant to the troposphere, and current recommendations[4] for parameterisation of the enhancement are based solely on the study by Kircher and Sander.[11]

Given the molecular structure of methanol it is perhaps not surprising that an enhancement in $k_{4.8}$ has also been observed in the presence of methanol vapour.[12,13,14] Although the enhancement in $k_{4.8}$ in the presence of methanol vapour does not have the

atmospheric significance of the H_2O enhancement, the use of methanol as a precursor to HO_2 in many laboratory studies of HO_2 kinetics does have important consequences for interpreting such studies.

The dependence of $k_{4.8}$ on methanol vapour was predicted and subsequently observed by Andersson *et al.*[12] using molecular modulation spectrometry. As with water, a linear dependence of $k_{4.8}$ on methanol vapour concentration was reported, and was found to be more significant at 278 K than at 299 K.

The effects of methanol vapour on $k_{4.8}$ have also been investigated using FP/UVA by Bloss *et al.*,[13] at 298 K and 760 Torr, and by Christensen *et al.*,[14] in the range 222 – 295 K at 100 Torr. Bloss *et al.* observed a non-linear dependence of $k_{4.8}$ on methanol, although the maximum methanol concentration used by Bloss *et al.* (5×10^{17} cm^{-3}) was higher than that used by Andersson *et al.* (3×10^{17} cm^{-3}), and the results of the two investigations are in good agreement at the common lower methanol concentrations. Christensen *et al.* observed the effects of methanol on $k_{4.8}$ to increase dramatically with decreasing temperature, particularly below 250 K. For example, on increasing the concentration of methanol from 1×10^{15} cm^{-3} to 5×10^{15} cm^{-3} at 231 K the observed rate of HO_2 decay more than doubled. Extrapolation of the results of Christensen *et al.* to $[CH_3OH] = 0$ cm^{-3} indicates that the true rate of the HO_2 self-reaction may be much slower than expected on the basis of current recommendations, which are potentially influenced by studies employing methanol as a precursor to HO_2. While the rate coefficient for (4.8) determined by Christensen *et al.* is in reasonable agreement with the current recommendation[4] for atmospheric modelling at 295 K, it is only 59 % of the current recommendation at 231 K. Christensen *et al.* also conducted experiments at 231 and 295 K in the absence of methanol, using flash photolysis of $F_2/H_2/O_2/N_2$ mixtures. The results support the conclusion that reaction (4.8) is potentially slower than previously thought.

More recently, Christensen *et al.*[32] have used near-IR spectroscopy on a microsecond timescale to monitor HO_2 in its association reaction with CH_3OH:

$$HO_2 + CH_3OH \quad \leftrightarrow \quad HO_2.CH_3OH \qquad (4.20)$$

Measurement of the equilibrium constant for (4.20) between 231 and 261 K enabled experimental determination of the thermodynamic stability of the $HO_2.CH_3OH$, and an *ab initio* investigation was also conducted in order to determine the thermodynamic stability of the complex by theoretical means. In conjunction with their earlier work,[14] measurement of $K_{4.20}$ allowed estimation of the parameters $k_{4.21}$ and $k_{4.22}$ in (4.ii), and could have important consequences for this work, as discussed below.

In summary, while there have been a number of previous investigations of the HO_2 self-reaction, comparatively few have covered conditions of temperature and pressure relevant to the troposphere. For example, there have been no investigations below 273 K at 760 Torr. Furthermore, few investigations of the water vapour enhancement of $k_{4.8}$ have been conducted over a range of temperatures relevant to the troposphere, and fewer still as a function of pressure. In addition, the effects of methanol vapour on $k_{4.8}$ have received relatively little attention despite the widespread use of CH_3OH as a precursor to HO_2. The majority of previous studies have adopted UV absorption spectroscopy to monitor HO_2 in kinetics experiments. This has the advantage in that the HO_2 absorption spectrum is apparently unperturbed by addition of hydrogen bonding molecules, which is not the case for IR experiments. However, previous studies have typically used single wavelength monitoring of absorbance, in which any absorbing species, transient or otherwise, may contribute to the observed decay.

The aims of this work were to investigate the kinetics of the HO_2 self-reaction under a wide range of conditions of temperature, pressure and water vapour concentration relevant to the troposphere, and to parameterise the effects of methanol vapour on $k_{4.8}$. These experiments also used broadband monitoring, as described in Chapter 3, of a broad section of the HO_2 UV absorption spectrum.

4.3 Radical Generation

Hydroperoxy radicals were generated by conventional flashlamp photolysis of $Cl_2/CH_3OH/O_2/N_2$ gas mixtures:

$$Cl_2 + h\nu \rightarrow 2\,Cl \qquad (4.12)$$

$$Cl + CH_3OH \rightarrow CH_2OH + HCl \quad (4.18)$$

$$CH_2OH + O_2 \rightarrow HO_2 + HCHO \quad (4.19)$$

In order to design experimental conditions, a numerical model of the reaction system, containing all known potential chemistry, was developed in the commercially available numerical integration package FACSIMILE. Preliminary calculations were carried out to find experimental conditions in which the pseudo-first order reactions of Cl with CH_3OH, and CH_2OH with O_2, were rapid compared to the expected rate of the HO_2 self-reaction based on current NASA recommendations.[4] The model was used to simulate HO_2 formation and loss as a function of time to investigate possible effects of secondary chemistry on the rate of HO_2 decay. The reactions included in the model are given in Table 4.1. In turn, simulations were conducted in which the rate coefficients for each individual reaction in the model were sequentially halved and doubled, and a simple classical second order kinetic model was used to obtain a fitted rate coefficient for the HO_2 self-reaction from each simulated HO_2 decay. The sensitivity of HO_2 decay to each reaction in the model was determined by comparison of the fitted rate coefficient for simulated HO_2 decay to the known value entered into the model for the HO_2 self-reaction. Results of the sensitivity analysis are given in Figure 4.1.

Reaction Label	Reaction	$k_{298\ K,\ 760\ Torr}$ / $cm^3\ s^{-1}$	Reference
a	$Cl + CH_3OH \rightarrow CH_2OH + HCl$	5.4×10^{-11}	4
b	$CH_2OH + O_2 \rightarrow HO_2 + HCHO$	9.1×10^{-12}	4
c	$HO_2 + HO_2 \rightarrow H_2O_2 + O_2$	2.9×10^{-12}	4
d	$Cl_2 + CH_2OH \rightarrow Cl + ClCH_2OH$	2.7×10^{-11}	33
e	$Cl_2 + CH_2OH \rightarrow HCl + HCHO$	6.6×10^{-10}	33
f	$Cl + HO_2 \rightarrow HCl + O_2$	3.2×10^{-11}	4
g	$Cl + HO_2 \rightarrow OH + ClO$	9.1×10^{-12}	4
h	$Cl + HCHO \rightarrow HCl + HCO$	7.3×10^{-11}	4
i	$CH_2OH + CH_2OH \rightarrow HOCH_2CH_2OH$	8.6×10^{-11}	34
j	$CH_2OH + CH_2OH \rightarrow CH_3OH + HCHO$	8.0×10^{-12}	35
k	$CH_2OH + HO_2 \rightarrow H_2O_2 + HCHO$	2.0×10^{-11}	35
l	$HO_2 + HCHO \rightarrow ADDUCT$	5.0×10^{-14}	4

Table 4.1 : Reactions included in sensitivity analysis for $k_{4.8}$.

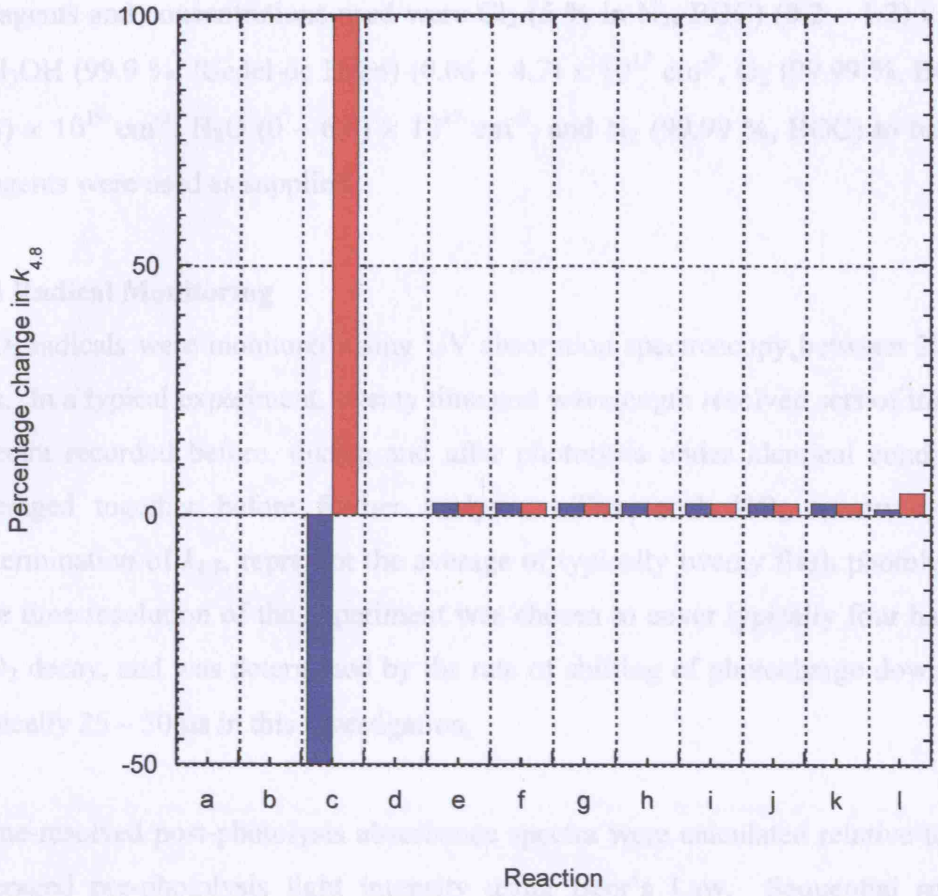

Figure 4.1 : Sensitivity analysis for the HO_2 self-reaction. Effect on $k_{4.8}$ of halving (blue) and doubling (red) the given secondary rate coefficient. Reaction labels refer to those in Table 4.1.

The sensitivity analysis was therefore used to obtain requisite minimum precursor concentrations such that HO_2 radicals would be produced at a much greater rate than that of their subsequent self-reaction, and that their decay as a function of time was solely governed by the rate of the $HO_2 + HO_2$ process. The sensitivity analysis shows that a maximum 5 % deviation in $k_{4.8}$ resulted from variation in secondary chemistry rate coefficients at 298 K. Furthermore, most of the secondary rate coefficients are rather better determined than the 100% potential variation employed here. The *maximum* precursor concentrations that could be used were, in contrast, determined by the ability to admit such concentrations to the reaction cell and, in the case of readily condensable species, to avoid exceeding the saturated vapour pressure of reagents, mixed at 298 K, in the reaction cell, often held at temperatures below 298 K.

Reagents and concentrations used were Cl_2 (5 % in N_2, BOC) (0.2 – 1.2) × 10^{17} cm^{-3}, CH_3OH (99.9 %, Riedel-de Haen) (0.06 – 4.7) × 10^{17} cm^{-3}, O_2 (99.99 %, BOC) (0.1 – 1.3) × 10^{19} cm^{-3}, H_2O (0 – 6.0) × 10^{17} cm^{-3}, and N_2 (99.99 %, BOC) to balance. All reagents were used as supplied.

4.4 Radical Monitoring

HO_2 radicals were monitored using UV absorption spectroscopy between 200 and 250 nm. In a typical experiment, twenty time and wavelength resolved sets of transimission spectra recorded before, during and after photolysis under identical conditions were averaged together before further analysis. Thus each HO_2 spectrum, and each determination of $k_{4.8}$, represent the average of typically twenty flash photolysis events. The time resolution of the experiment was chosen to cover typically four half-lives for HO_2 decay, and was determined by the rate of shifting of photocharge down the CCD, typically 25 – 50 μs in this investigation.

Time-resolved post-photolysis absorbance spectra were calculated relative to the time-averaged pre-photolysis light intensity using Beer's Law. Sequential spectra thus displayed changes in absorbance due to changes in concentrations of gas phase species in the cell resulting from photolysis and subsequent chemistry. A typical representation of the temporal behaviour of the post-photolysis absorbance can be seen in Figure 4.2.

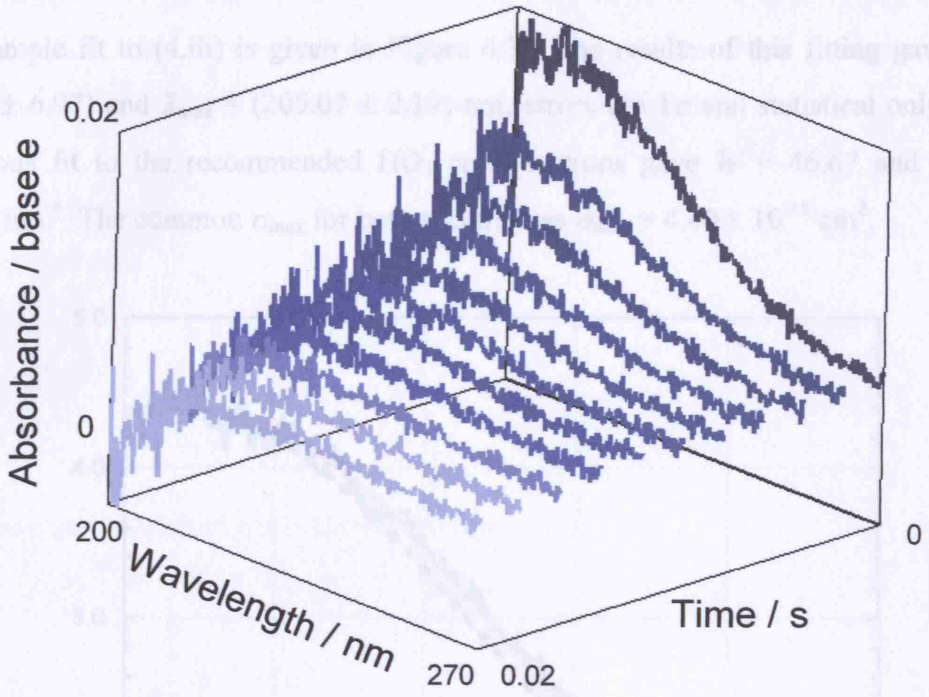

Figure 4.2 : Representation of the temporal evolution of wavelength resolved absorbance. Photolysis is defined as occurring at $t = 0$ s.

In order to obtain HO_2 absorption cross-sections at each wavelength point in an experiment, the experimental absorbance spectra recorded in the first 2.5 ms after photolysis between 205 and 250 nm were parameterised by a semi-logarithmic Gaussian function, (4.iii). The Gaussian function was normalised to the peak of an analogous fit to the recommended and well-established HO_2 absorption cross-sections.[4] Use of such a function has been successfully employed in previous studies of peroxy radical absorption spectra.[36] Over the 2.5 ms time period typically less than 20% of HO_2 had reacted, thus less than 10% of the original HO_2 concentration was present as H_2O_2.

$$\sigma_\lambda = \sigma_{max} \exp\left\{-W\left[\ln\left(\frac{\lambda_{max}}{\lambda}\right)\right]^2\right\} \qquad (4.iii)$$

where σ_λ is the absorption cross-section at wavelength λ, σ_{max} the maximum absorption cross-section, W a width parameter, λ_{max} the wavelength at which maximum absorption occurs and λ the wavelength of interest.

An example fit to (4.iii) is given in Figure 4.3. The results of this fitting gave W = (37.15 ± 6.97) and λ_{max} = (205.07 ± 2.19) nm, errors are 1σ and statistical only. The analogous fit to the recommended HO_2 cross-sections gave W = 46.67 and λ_{max} = 203.59 nm.[4] The common σ_{max} for both spectra was $\sigma_{max} = 4.40 \times 10^{-18}$ cm^2.

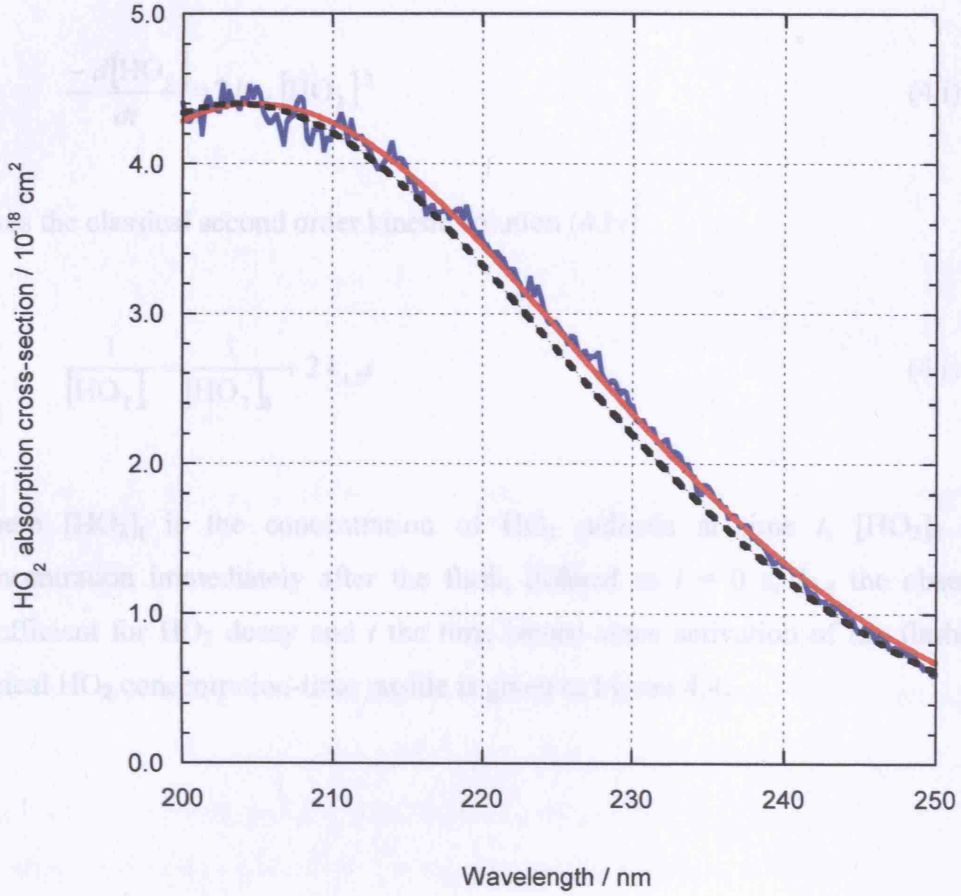

Figure 4.3 : Gaussian fit (red) to experimental HO_2 absorbance recorded in first 2.5 ms after flash (blue). Normalised to maximum recommended absorption cross-sections (broken black line).[4]

The normalised semi-logarithmic Gaussian parameterisation of σ_{HO2} was used to analyse the observed time resolved spectra. Thus, cross-sections for HO_2 were least squares fitted to the experimental absorbance spectra, minimising the difference between σ_{HO2} and absorbance using the Beer-Lambert Law, over the wavelength range 205 to 250 nm, and the known optical path length. HO_2 concentrations were determined at each time point in the experiment. Absorption cross-sections were assumed to be

independent of temperature over the range studied, as recommended by Lightfoot *et al.*[21,37] Parameterisation was necessary in order to provide smoothed absorption cross-sections at each wavelength point recorded on the CCD detector.

4.5 Kinetic Analysis

Integration of (4.i)

$$\frac{-d[HO_2]}{dt} = 2k_{4.8}[HO_2]^2 \qquad (4.i)$$

gives the classical second order kinetic solution (4.iv)

$$\frac{1}{[HO_2]_t} = \frac{1}{[HO_2]_0} + 2k_{4.8}t \qquad (4.iv)$$

where $[HO_2]_t$ is the concentration of HO_2 radicals at time t, $[HO_2]_0$ the HO_2 concentration immediately after the flash, defined as t = 0 s, $k_{4.8}$ the observed rate coefficient for HO_2 decay and t the time lapsed since activation of the flashlamp. A typical HO_2 concentration-time profile is given in Figure 4.4.

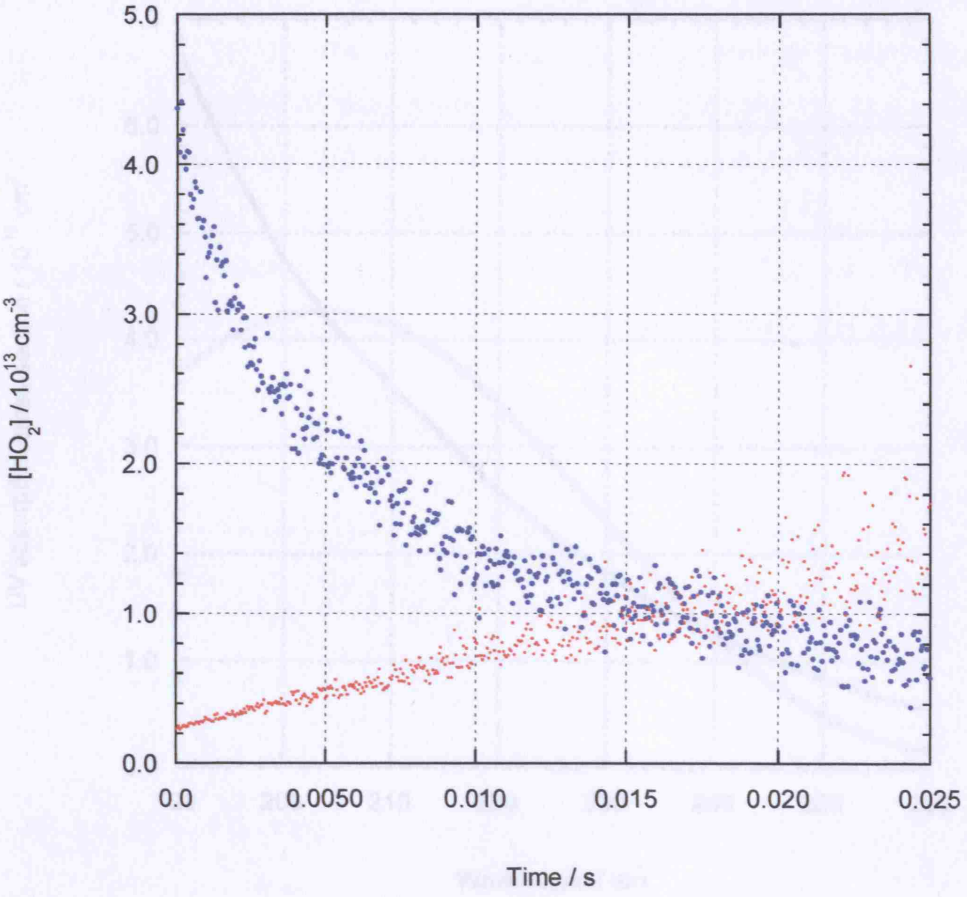

Figure 4.4 : Experimental HO_2 signal as a function of time (blue), with second order reciprocal plot (red).

The classical second order kinetic solution was, however, found to be an inadequate description of the system, as has been observed in previous studies.[9,10,11,13,14,38] This is more apparent in the second order plot for these data, shown in Figure 4.4. Whilst the initial stages of reaction appear to be pure second order, a clear deviation is seen at longer times. The apparent deviation from second order kinetics was attributed to a small contribution of the H_2O_2 reaction product to the fitted HO_2 concentrations, and occurs due to the close similarities in the shapes of the HO_2 and H_2O_2 UV absorption spectra, shown in Figure 4.5.[4]

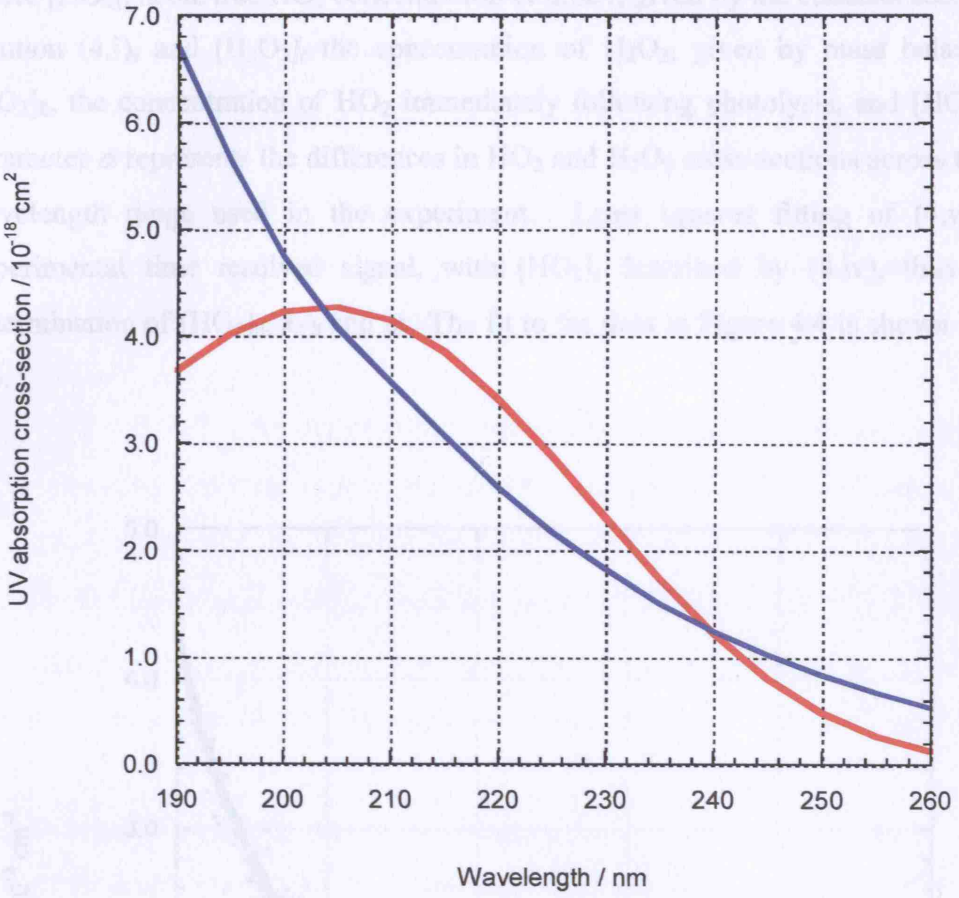

Figure 4.5 : Recommended[4] UV absorption cross-sections for HO_2 (red) and H_2O_2 (blue). H_2O_2 cross-sections have been multiplied by a factor of 10 to emphasise the similarity between the forms of HO_2 and H_2O_2 spectra.

The similarities between the form of σ_{HO_2} and $\sigma_{H_2O_2}$, particularly in the 205 – 250 nm region adopted, coupled with the noise on experimental data probably led to some product H_2O_2 being erroneously fitted as HO_2. Although the two spectra are too similar to deconvolve the HO_2 and H_2O_2 absorptions, it is possible to adapt the classical kinetic solution to account for the absorption by H_2O_2 due to the known stoichiometry of (4.8).[13,38] The apparent HO_2 signal at time t, S_t, determined by spectral fitting is therefore described by (4.v):

$$S_t = [HO_2]_t + \alpha[H_2O_2]_t \qquad (4.v)$$

where $[HO_2]_t$ is the true HO_2 concentration at time t, given by the classical second order solution (4.i), and $[H_2O_2]_t$ the concentration of H_2O_2, given by mass balance from $[HO_2]_0$, the concentration of HO_2 immediately following photolysis, and $[HO_2]_t$. The parameter α represents the differences in HO_2 and H_2O_2 cross-sections across the entire wavelength range used in the experiment. Least squares fitting of (4.v) to the experimental time resolved signal, with $[HO_2]_t$ described by (4.iv), thus allowed determination of $[HO_2]_0$, $k_{4.8}$ and α. The fit to the data in Figure 4.4 is shown in Figure 4.6.

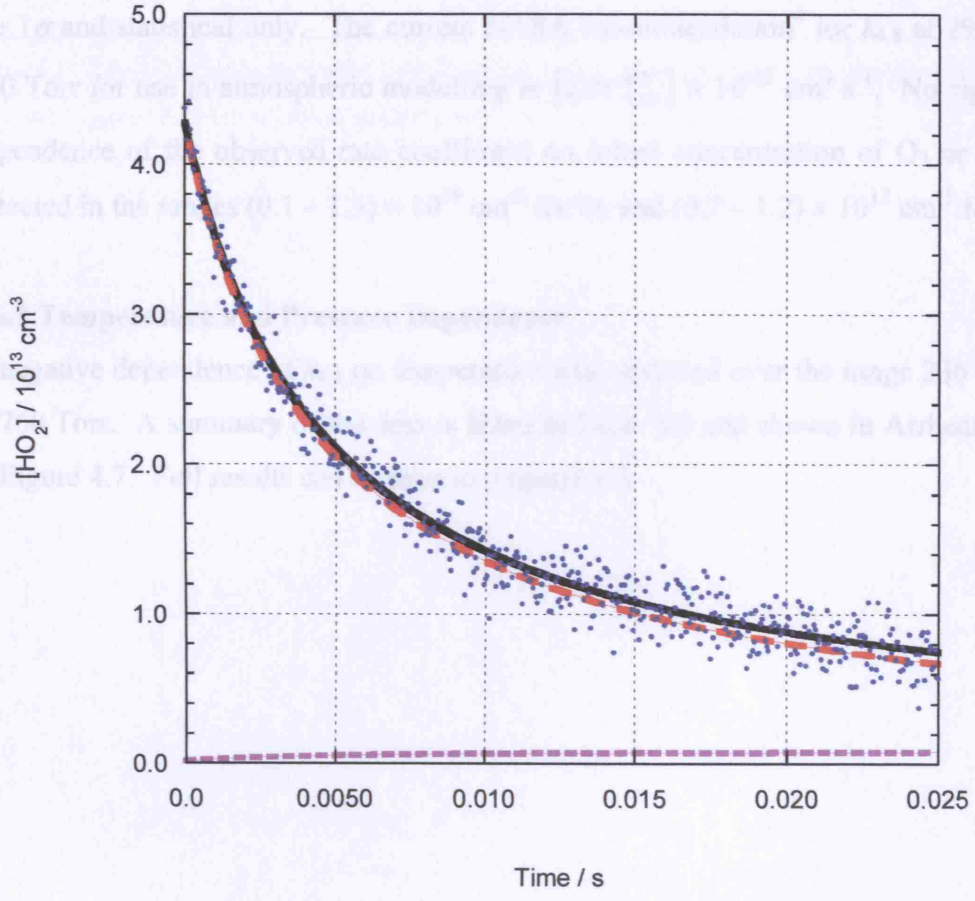

Figure 4.6 : Experimental HO_2 signal as a function of time (blue points) with fit to equation (4.v) (solid black line). Contributions to the signal from HO_2 (broken red line) and H_2O_2 (broken purple line) are also shown.

As can be seen, the deviation from pure second order is small, and the quantity α is typically between 0.10 and 0.20, in keeping with the absolute magnitudes of the HO_2

and H_2O_2 cross-sections. The parameter α did, however, show some variability with signal to noise ratios and wavelength ranges used.

4.6 Results

Kinetics of the HO_2 self-reaction were investigated as a function of temperature, pressure, and water and methanol vapour concentrations. Results presented have been corrected for effects of methanol vapour, described below in section 4.6.3.

At 296 K and 760 Torr the observed rate coefficient for HO_2 decay, corrected for enhancement by methanol vapour, was found to be $(2.86 \pm 0.31) \times 10^{-12}$ cm^3 s^{-1}. Errors are 1σ and statistical only. The current NASA recommendation[4] for $k_{4.8}$ at 298 K and 760 Torr for use in atmospheric modelling is $\left(2.91^{+0.87}_{-0.67}\right) \times 10^{-12}$ cm^3 s^{-1}. No significant dependence of the observed rate coefficient on initial concentration of O_2 or Cl_2 was detected in the ranges $(0.1 - 1.3) \times 10^{19}$ cm^{-3} for O_2 and $(0.2 - 1.2) \times 10^{17}$ cm^{-3} for Cl_2.

4.6.1 Temperature and Pressure Dependence

A negative dependence of $k_{4.8}$ on temperature was observed over the range 236 – 309 K at 760 Torr. A summary of the data is listed in Table 4.2 and shown in Arrhenius form in Figure 4.7. Full results can be seen in Appendix 3.

T / K	$k_{4.8}$ / 10^{-12} cm^3 s^{-1}	Number of experiments
309	2.68 ± 0.27	16
296	2.86 ± 0.31	66
287	3.00 ± 0.29	34
278	3.80 ± 0.19	10
274	3.99 ± 0.29	23
263	6.43 ± 1.30	17
254	7.25 ± 3.03	64
245	7.50 ± 4.28	56
236	11.04 ± 4.52	8

Table 4.2 : Rate coefficients for the HO_2 self-reaction at 760 Torr, corrected for enhancement by methanol vapour. Errors are 1σ and statistical only.

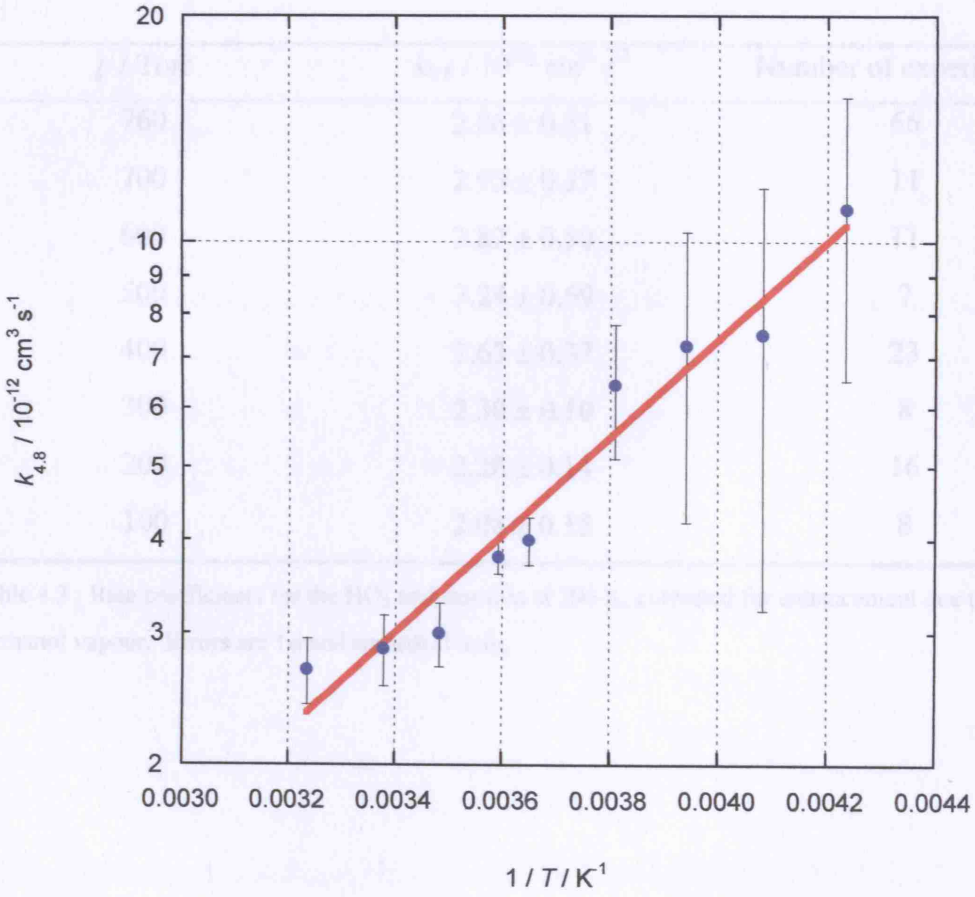

Figure 4.7 : $k_{4.8}$ as a function of temperature at 760 Torr (blue points) with Arrhenius fit (red line). Errors are 1σ and statistical only.

An Arrhenius fit to the data gave (4.vi).

$$k_{4.8} = (1.8 \pm 0.8) \times 10^{-14} \exp\left\{(1500 \pm 120)/T/\mathrm{K}\right\} \quad \mathrm{cm^3\ s^{-1}} \qquad (4.vi)$$

Errors are 1σ, statistical only from the fit.

The dependence of $k_{4.8}$ on pressure was investigated between 100 and 760 Torr at 296 K. A linear increase in $k_{4.8}$ with pressure was observed, with a non-zero value of $k_{4.8}$ on extrapolation to zero pressure, providing further evidence for the existence of both bimolecular and termolecular reaction channels. A summary of the data is listed in Table 4.3 and shown in Figure 4.8.

p / Torr	$k_{4.8}$ / 10^{-12} cm^3 s^{-1}	Number of experiments
760	2.86 ± 0.31	66
700	2.95 ± 0.37	11
600	2.82 ± 0.50	11
500	3.24 ± 0.59	7
400	2.63 ± 0.37	23
300	2.30 ± 0.10	8
200	2.28 ± 0.14	16
100	2.08 ± 0.15	8

Table 4.3 : Rate coefficients for the HO_2 self-reaction at 296 K, corrected for enhancement due to methanol vapour. Errors are 1σ and statistical only.

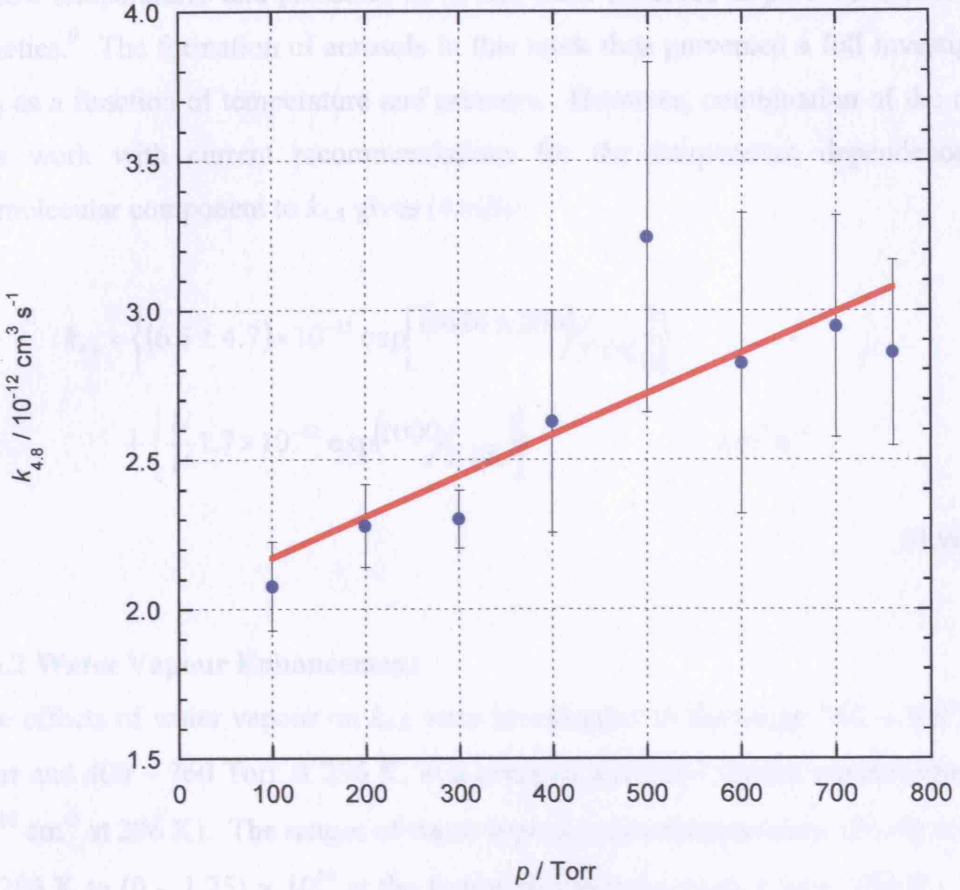

Figure 4.8 : Pressure dependence of $k_{4.8}$ at 296 K (blue points) with linear fit (red line). Errors are 1σ and statistical only.

A linear fit to the data in Table 4.3 gave (4.vii).

$$k_{4.8} = \{(2.0 \pm 0.2) \times 10^{-12}\} + \left\{\frac{N}{V}[(4.2 \pm 1.2) \times 10^{-32}]\right\} \quad \text{cm}^3\ \text{s}^{-1} \qquad (4.\text{vii})$$

where N/V is the total number density in cm^{-3}. Errors are 1σ, statistical only.

Attempts were made to characterise $k_{4.8}$ at temperatures below 230 K at 760 Torr, and as a function of pressure below ambient temperature, but in both cases problems were encountered due to aerosol formation within the reaction cell, precluding UV spectroscopy. Similar problems due to aerosol formation and heterogeneous chemistry

at low temperatures and pressures have also been observed in previous studies of HO_2 kinetics.[9] The formation of aerosols in this work thus prevented a full investigation of $k_{4.8}$ as a function of temperature and pressure. However, combination of the results of this work with current recommendations for the temperature dependence of the termolecular component to $k_{4.8}$ gives (4.viii):

$$k_{4.8} = \left\{(6.5 \pm 4.7) \times 10^{-15} \exp\left[(1640 \pm 200)/T/\mathrm{K}\right]\right\} + \left\{\frac{N}{V} 1.7 \times 10^{-32} \exp\left(1000/T/\mathrm{K}\right)\right\} \quad \mathrm{cm^3\ s^{-1}} \qquad (4.viii)$$

4.6.2 Water Vapour Enhancement

The effects of water vapour on $k_{4.8}$ were investigated in the range 254 – 309 K at 760 Torr and 400 – 760 Torr at 296 K, at a constant methanol vapour concentration (1.3×10^{16} cm^{-3} at 296 K). The ranges of water vapour concentrations were $(0 - 6) \times 10^{17}$ cm^{-3} at 296 K to $(0 - 1.25) \times 10^{16}$ at the lowest temperature studied here, 254 K. This was necessary since the water vapour partial pressure had to be maintained at a value below the saturated vapour pressure at each temperature to avoid condensation of liquid or solid water in the reaction cell. No significant effects of water vapour on the UV absorbance spectrum of HO_2 were observed.

Enhancement in $k_{4.8}$ was observed in the presence of water vapour, and the rate coefficient characterising HO_2 decay was found to increase linearly with increasing water vapour concentration at each temperature and pressure investigated. The degree of rate enhancement was found to increase with decreasing temperature, but no significant effects of pressure were observed on the rate enhancement. Results are given in Appendix 3 and shown in Figures 4.9 to 4.11.

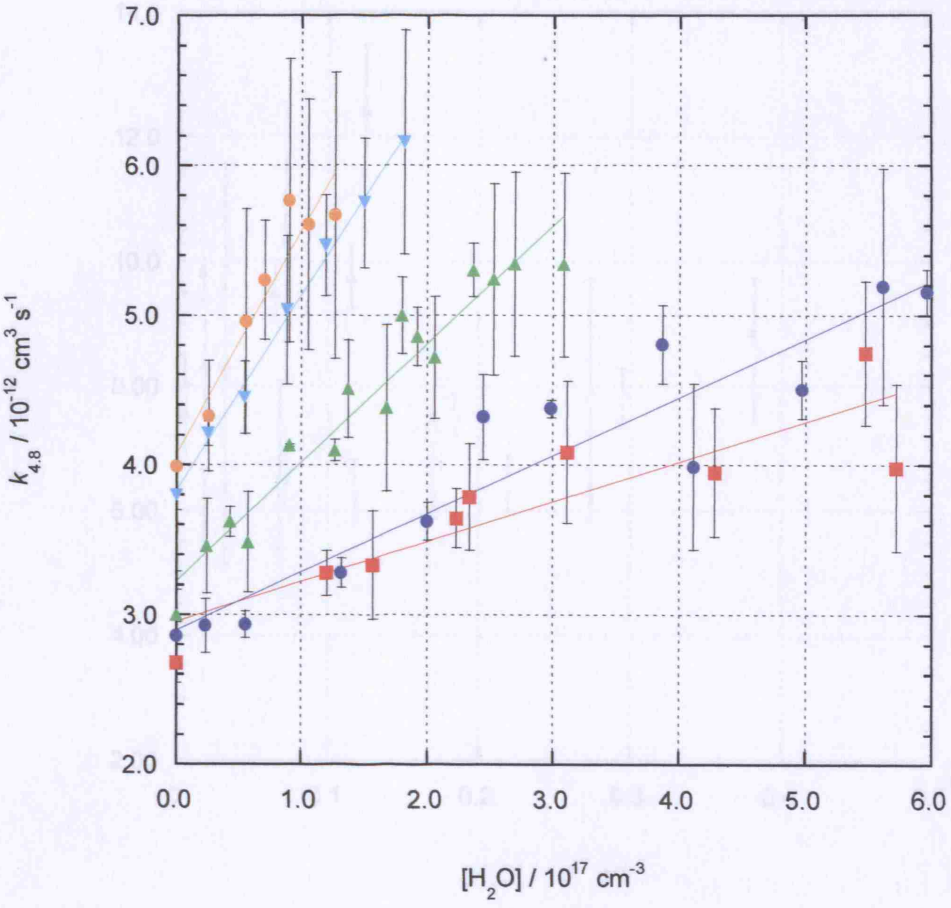

Figure 4.9 : $k_{4.8}$ as a function of water vapour concentration and temperature at 760 Torr, corrected for enhancement due to CH_3OH. Red squares 309 K; blue circles 296 K; green triangles 287 K; light blue inverted triangles 278 K; orange circles 274 K. Linear fits to the data are also shown. Errors are 1σ and statistical only.

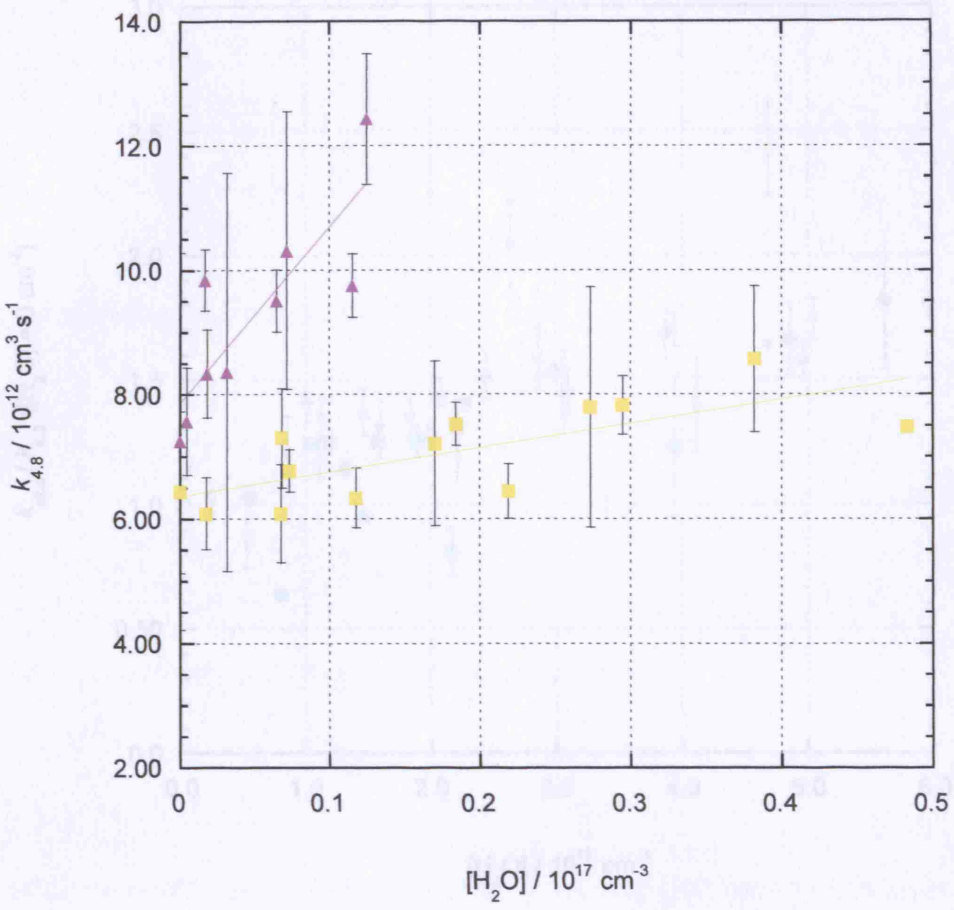

Figure 4.10 : $k_{4.8}$ as a function of water vapour concentration and temperature at 760 Torr at the two lowest temperatures studied here. Results have been corrected for enhancement due to methanol vapour. Yellow squares 263 K; purple triangles 254 K. Linear fits to the data are also shown. Errors are 1σ and statistical only.

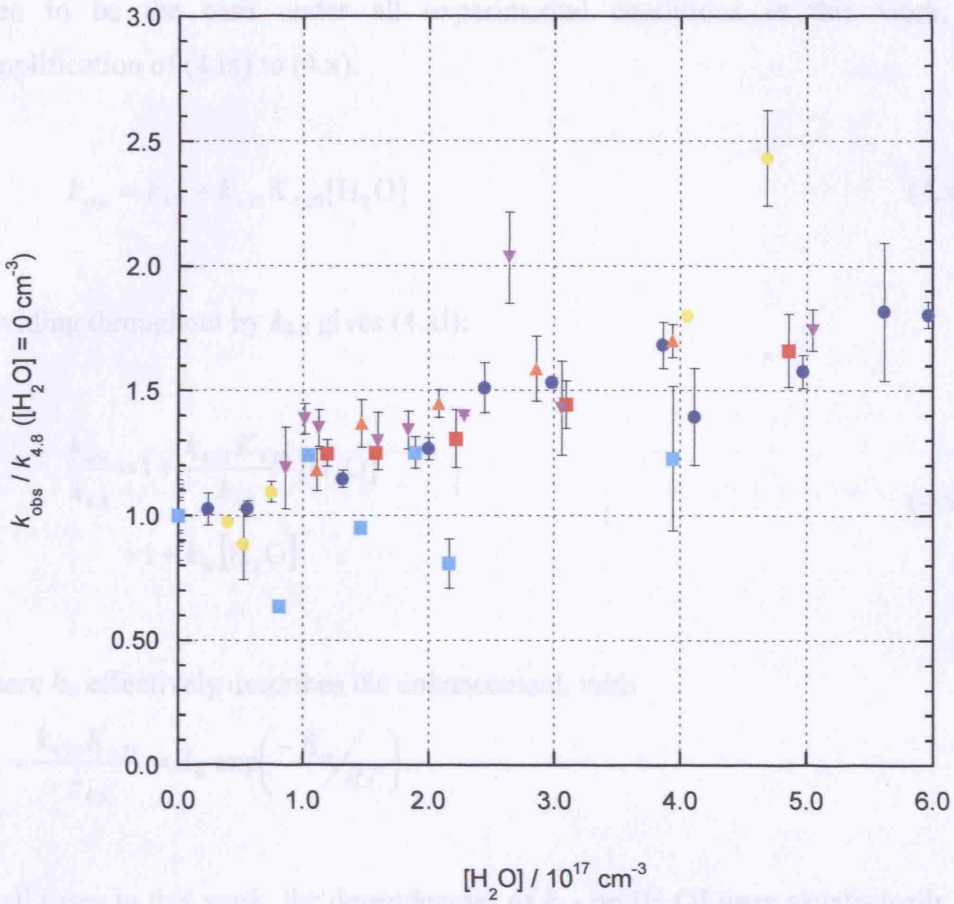

Figure 4.11 : Relative rate enhancement in $k_{4.8}$ as a function of water vapour concentration and pressure at 296 K. Blue circles 760 Torr; red squares 700 Torr; orange triangles 600 Torr; purple inverted triangles 400 Torr; yellow circles 200 Torr; light blue squares 100 Torr. Errors are 1σ and statistical only.

As discussed in section 4.2, Hamilton and Lii[6] postulated a mechanism for the rate enhancement of the HO_2 self-reaction in the presence of water vapour, and showed that the observed rate coefficient for HO_2 decay can be described by (4.ix):

$$k_{obs} = \frac{k_{4.8} + k_{4.21}K_{4.20}[H_2O] + k_{4.22}K_{4.20}{}^2[H_2O]^2}{(1 + K_{4.20}[H_2O])^2} \qquad (4.ix)$$

Kircher and Sander[11] showed that a linear dependence of $k_{4.8}$ on water vapour concentration would be observed if $K_{4.20}[H_2O] << 1$ and $k_{4.22}K_{4.20}[H_2O] << k_{4.21}$, as was

seen to be the case under all experimental conditions in this work, enabling simplification of (4.ix) to (4.x).

$$k_{obs} = k_{4.8} + k_{4.21}K_{4.20}[H_2O] \qquad (4.x)$$

Dividing throughout by $k_{4.8}$ gives (4.xi):

$$\frac{k_{obs}}{k_{4.8}} = 1 + \frac{k_{4.21}K_{4.20}}{k_{4.8}}[H_2O] = 1 + k_w[H_2O] \qquad (4.xi)$$

where k_w effectively describes the enhancement, with $k_w = \frac{k_{4.21}K_{4.20}}{k_{4.8}} = A_w \exp\left(-E_w/RT\right)$.

In all cases in this work, the dependencies of $k_{4.8}$ on $[H_2O]$ were satisfactorily described by linear parameters, thus the results of this study have been analysed in terms of (4.xi), thereby separating the effects of water vapour on $k_{4.8}$ from any additional effects of temperature, pressure, bath gas or methanol vapour concentration. Results for k_w are summarised in Table 4.4 and shown in Figure 4.12 and Figure 4.13. An Arrhenius fit to k_w gave $A_w = (2.0 \pm 4.9) \times 10^{-25}$ cm^3 and $(-E_w/R) = 4760 \pm 690$ K.

T / K	k_w / 10^{-18} cm^3
309	0.90 ± 0.19
296	1.34 ± 0.17
287	2.46 ± 0.19
278	3.40 ± 0.12
274	3.65 ± 0.52
263	6.11 ± 1.72
254	35.97 ± 9.23

Table 4.4 : Summary of results for k_w at 760 Torr as a function of temperature. Errors are 1σ and statistical only.

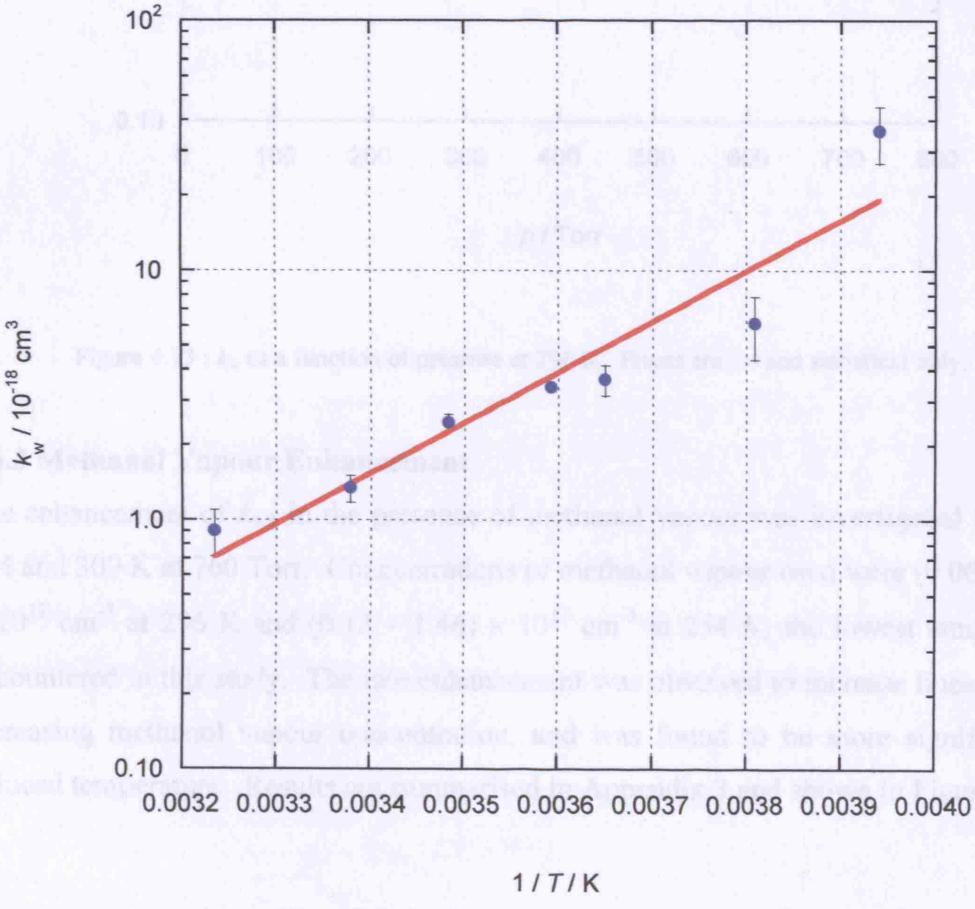

Figure 4.12 : k_w as a function of temperature at 760 Torr. Errors are 1σ and statistical only.

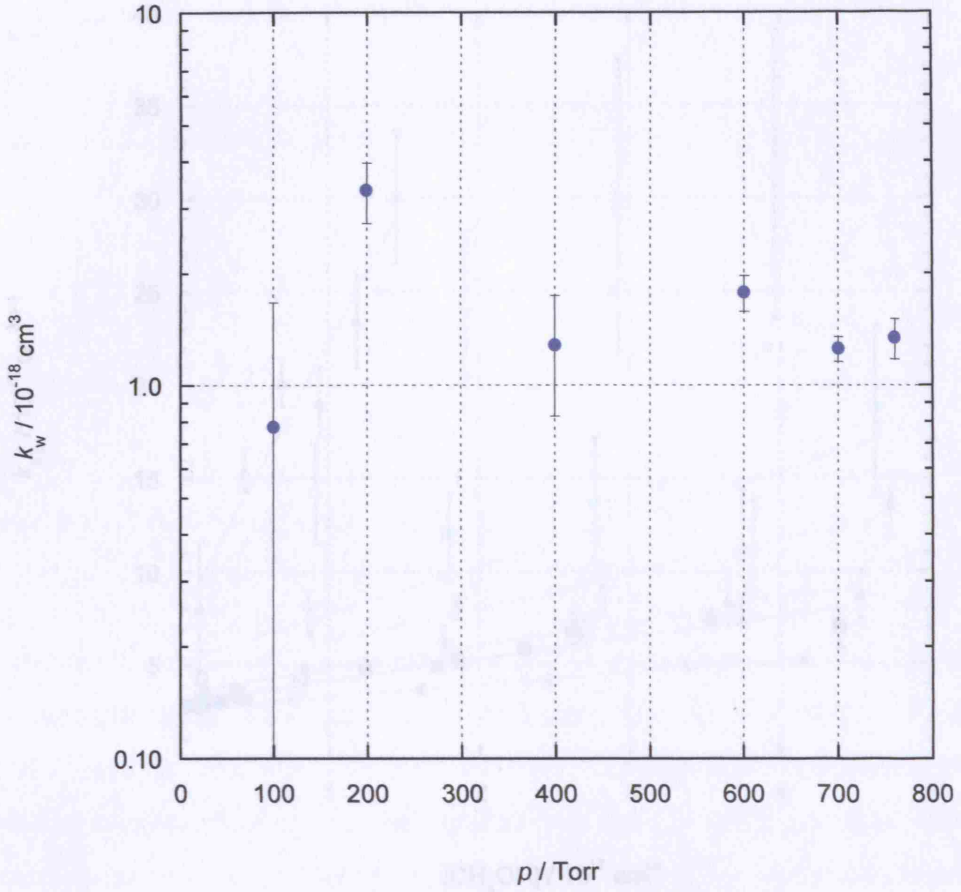

Figure 4.13 : k_w as a function of pressure at 296 K. Errors are 1σ and statistical only.

4.6.3 Methanol Vapour Enhancement

The enhancement of $k_{4.8}$ in the presence of methanol vapour was investigated between 254 and 309 K at 760 Torr. Concentrations of methanol vapour used were (0.06 – 4.40) × 10^{17} cm^{-3} at 296 K and (0.13 – 1.46) × 10^{17} cm^{-3} at 254 K, the lowest temperature encountered in this study. The rate enhancement was observed to increase linearly with increasing methanol vapour concentration, and was found to be more significant at reduced temperature. Results are summarised in Appendix 3 and shown in Figure 4.14.

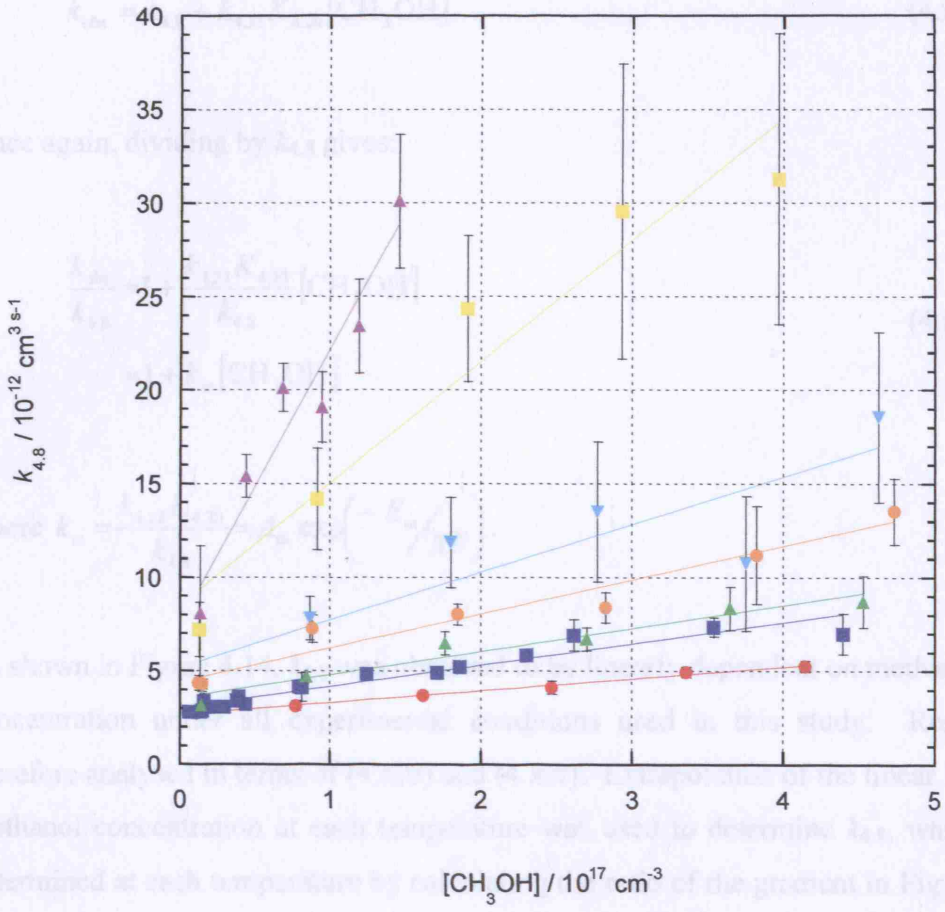

Figure 4.14 : $k_{4.8}$ as a function of methanol vapour concentration and temperature at 760 Torr. Linear fits to the data are shown at each temperature. Red circles 309 K; blue squares 296 K; green triangles 287 K; light blue inverted triangles 278 K; orange circles 274 K; yellow squares 263 K; purple triangles 254 K.

The effects of methanol vapour on $k_{4.8}$ were analysed in an analogous manner to those of water vapour. The dependence of $k_{4.8}$ on methanol vapour is described by (4.xii), as given by Hamilton and Lii[6] for the dependence of $k_{4.8}$ on water vapour.

$$k_{obs} = \frac{k_{4.8} + k_{4.21}K_{4.20}[CH_3OH] + k_{4.22}K_{4.20}{}^2[CH_3OH]^2}{(1 + K_{4.20}[CH_3OH])^2} \qquad (4.xii)$$

Provided that $K_{4.20}[CH_3OH] << 1$ and $k_{4.22}K_{4.20}[CH_3OH] << k_{4.21}$, (4.xii) can be simplified to (4.xiii) and subsequently (4.xiv), resulting in a linear dependence of $k_{4.8}$ on methanol vapour concentration.

$$k_{obs} = k_{4.8} + k_{4.21}K_{4.20}[CH_3OH] \qquad (4.xiii)$$

Once again, dividing by $k_{4.8}$ gives:

$$\frac{k_{obs}}{k_{4.8}} = 1 + \frac{k_{4.21}K_{4.20}}{k_{4.8}}[CH_3OH] = 1 + k_m[CH_3OH] \qquad (4.xiv)$$

where $k_m = \frac{k_{4.21}K_{4.20}}{k_{4.8}} = A_m \exp\left(-E_m/RT\right)$.

As shown in Figure 4.14, $k_{4.8}$ was observed to be linearly dependent on methanol vapour concentration under all experimental conditions used in this study. Results were therefore analysed in terms of (4.xiii) and (4.xiv). Extrapolation of the linear fits to zero methanol concentration at each temperature was used to determine $k_{4.8}$, while k_m was determined at each temperature by calculating the ratio of the gradient in Figure 4.14 to the appropriate intercept. A summary of results for k_m is given in Table 4.5 and shown in Figure 4.15. An Arrhenius fit to k_m gave $A_m = (0.56 \pm 1.00) \times 10^{-21}$ cm^{-3} and $(-E_m/R) = 2550 \pm 500$ K.

T / K	k_m / 10^{-18} cm^3
309	2.42 ± 0.12
296	3.82 ± 0.32
287	3.48 ± 0.57
278	4.94 ± 0.22
274	4.10 ± 0.62
263	7.64 ± 2.51
254	19.30 ± 5.51

Table 4.5 : Summary of results for k_m at 760 Torr as a function of temperature. Errors are 1σ and statistical only.

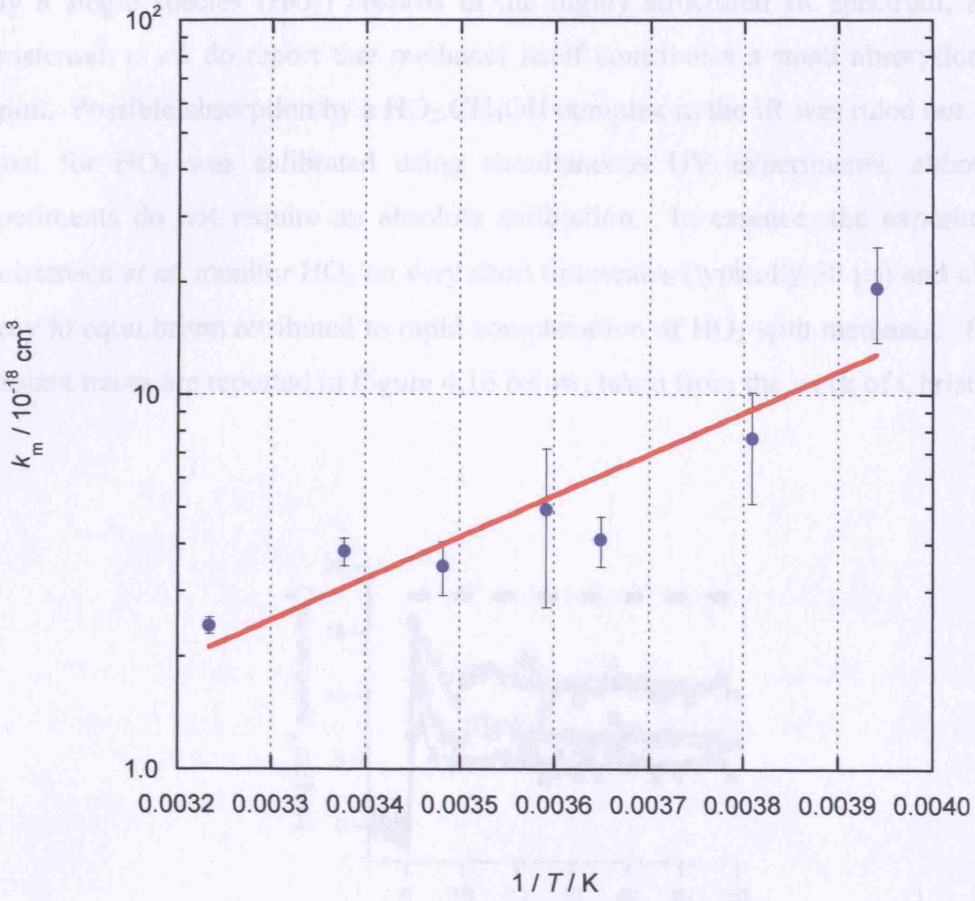

Figure 4.15 : k_m as a function of temperature at 760 Torr. Errors are 1σ and statistical only.

Very recent work of Christensen *et al.*[32] has questioned the validity of this method of analysis. Measurements of $K_{4.20}$, the equilibrium constant for $HO_2.CH_3OH$ complex formation, by Christensen *et al.* indicate that the assumption $K_{4.20}[CH_3OH] << 1$, and hence simplification of (4.xii) to (4.xiii), may not be valid at the maximum methanol vapour concentrations used in this study. By contrast, observation of a linear dependence of $k_{4.8}$ on methanol vapour concentration under all experimental conditions in this work does, however, provide support for such assumptions, and a detailed examination of the Christensen work was therefore carried out.

The experimental work of Christensen *et al.* adopted excimer laser photolysis of $Cl_2/CH_3OH/O_2/N_2$ mixtures in common with the present work. Detection of HO_2 was, however, carried out using near-IR absorption by wavelength modulated diode laser spectroscopy. The diode laser probed a group of blended rovibrational transitions of the OH overtone stretch at 6638.2 cm^{-1}. This technique has the advantage that, in principle,

only a single species (HO_2) absorbs in the highly structured IR spectrum, although Christensen *et al.* do report that methanol itself contributes a small absorption in this region. Possible absorption by a $HO_2.CH_3OH$ complex in the IR was ruled out. The IR signal for HO_2 was calibrated using simultaneous UV experiments, although the experiments do not require an absolute calibration. In essence, the experiments of Christensen *et al.* monitor HO_2 on very short timescales (typically 50 μs) and observe a decay to equilibrium attributed to rapid complexation of HO_2 with methanol. Example transient traces are reported in Figure 4.16 below, taken from the work of Christensen *et al.*

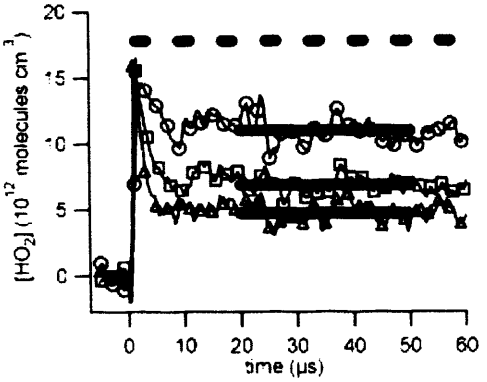

Figure 1. Time dependence of $[HO_2]$ at 240 K and 100 Torr at various methanol concentrations (thin solid lines). Data were acquired at several methanol concentrations (in molecules cm^{-3}): 2.1×10^{16} (○), 5.5×10^{16} (□), 9.1×10^{16} (△). The top dashed line is the sum of $[HO_2]$ + $[HO_2{\cdot}CH_3OH]$, assuming the only loss process for HO_2 was complexation. The thick lines give the final equilibrium concentration of HO_2, $[HO_2]_{eq}$. Note that the symbols labeling the data curves are spaced five data points apart for clarity. The thin solid lines are drawn through every data point.

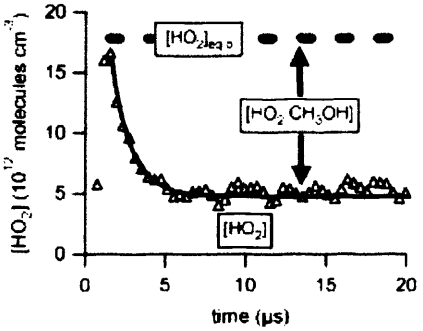

Figure 2. $[HO_2]$ signal vs time at a methanol concentration of 9.1×10^{16} molecules cm^{-3} for 240 K, 100 Torr. The plot is a magnified version of the same run displayed in Figure 1. The solid line is a fit using eq 13. Note that every data point is shown as a symbol.

Figure 4.16 : HO_2 concentration as a function of time, showing the approach and attainment of equilibrium between HO_2 and CH_3OH. Reproduced from the work of Christensen *et al.* (2006).[32]

The recording of multiple transient traces for HO_2, in experiments carried out as a function of methanol concentration under otherwise identical conditions, was used to establish both $K_{4.20}$ (referred to as K_c by Christensen *et al.*) and $k_{4.20}$, the rate coefficient for HO_2 + CH_3OH association (referred to as k_3 by Christensen *et al.*). First, the K_c ($K_{4.20}$) values were obtained from an examination of the equilibrium HO_2 concentrations as a function of methanol concentration. Given the definition of the equilibrium constant for complexation,

$$K_c = \frac{[HO_2.CH_3OH]_{eq}}{[HO_2]_{eq}[CH_3OH]} \qquad (4.xv)$$

and assuming that the complex concentration is the initial HO_2 concentration minus the equilibrium concentration, $[HO_2.CH_3OH] = [HO_2]_0 - [HO_2]_{eq}$, it can readily be shown that

$$\frac{1}{[HO_2]_{eq}} = \frac{1}{[HO_2]_0} + \frac{K_c[CH_3OH]}{[HO_2]_0} \qquad (4.\ xvi)$$

Thus, a plot of the reciprocal $[HO_2]_{eq}$ as a function of $[CH_3OH]$ was used to determine the notional initial HO_2 concentration in the absence of methanol for an entire group of experiments - assuming implicitly that $[HO_2]_0$ was unchanged during the experimental sequence. This common initial HO_2 concentration was then used with the observed $[HO_2]_{eq}$ from each individual temporal trace to obtain the equilibrium $HO_2.CH_3OH$ adduct concentration for that particular experiment, and the ratio of $[HO_2.CH_3OH]_{eq}$ to $[HO_2]_{eq}$ was analysed as a function of $[CH_3OH]$ to obtain the K_c equilibrium constant for association from a simple rearrangement of (4.xv) above:

$$\frac{[HO_2.CH_3OH]_{eq}}{[HO_2]_{eq}} = K_c[CH_3OH] \qquad (4.xvii)$$

It should be noted that the analysis of a group of temporal traces to obtain a common initial radical concentration should yield a value in keeping with that obtained from a fit to the individual traces provided that the HO_2 formation and decay times are decoupled. In the work of Christensen *et al.*, the peak HO_2 concentration observed in the transients was between 65 % and 95 % of $[HO_2]_0$ obtained from the methanol dependence of a group of temporal traces. This was attributed to $HO_2.CH_3OH$ complexation taking place during the formation of HO_2.

The Christensen *et al.* K_c values for HO_2-CH_3OH complexation, recorded at four temperatures between 231 and 261 K, were converted to K_p values in order to carry out thermochemical analysis. Unfortunately, the expression for K_p reported in the manuscript is incorrect, as K_p is the natural thermodynamic variable related to ΔG and the $(RT)^{-1}$ term reported is hence unnnecessary. Nonetheless, the K_p values were calculated correctly, and yield ΔH and ΔS for the complexation (ΔH = -(37.4 ± 4.8) kJ mol^{-1}; ΔS = -(100 ± 19) J mol^{-1}).

The Christensen *et al.* study goes on to determine $k_{4.20}$, the rate coefficient for HO_2 + CH_3OH association, and with a knowledge of K_c, $k_{-4.20}$ (referred to as k_{-3} by Christensen *et al.*), the rate coefficient for the complex decomposition. In this part of the work, a kinetic simulation was directly fitted to the observed HO_2 decay profile in a simple two reaction model. The analytical expression for the HO_2 decay reported in the manuscript of Christensen *et al.* is reproduced in Figure 4.17, below.

$$[HO_2] = [HO_2]_0 \frac{[CH_3OH]}{[CH_3OH] + K_c^{-1}} \{1 - \exp[-k_3 t([CH_3OH] + K_c^{-1})]\}$$

where $[HO_2]_0$ represents $[HO_2]$ at $t = 0$ s.

Figure 4.17 : Analytical expression for HO_2 concentrations as a function of time. Reproduced from Christensen *et al.* The parameters described as K_c and k_3 by Christensen *et al.*[32] are referred to as $K_{4.20}$ and $k_{4.20}$ respectively in this work.

Once again, careful consideration of this expression reveals that it cannot represent HO_2 decay from a peak value, and a detailed derivation of the HO_2 profile is given in Appendix 4. The correct expression for HO_2 decay is:

$$[HO_2]_t = \frac{[HO_2]_0}{K_c^{-1} + [CH_3OH]} \left\{ K_c^{-1} + [CH_3OH] \exp\left(- k_{4.20} t \left\{ [CH_3OH] + K_c^{-1} \right\} \right) \right\} \qquad (4.xviii)$$

and can be visualized as the temporal profile of HO_2 consisting of a baseline $[HO_2]_{eq}$, and an initial amount ($[HO_2]_0$ - $[HO_2]_{eq}$) decaying with the sum of the effective forward and reverse rate coefficients. The expression reported by Christensen *et al.* for this temporal profile actually produces a buildup of HO_2. Moreover, the Christensen *et al.* expression reproduced in Figure 4.17 above predicts $[HO_2] = 0$ at $t = 0$, which evidently cannot model a decay process. If the sign in the bracketed part of the Christensen expression is reversed (*i.e.* 1 + exp...) the expression does give a decay which resembles the experimental profiles reported by Christensen *et al.*, but the expression remains fundamentally incorrect. This evidently opens up the possibility that the values for k_3 ($k_{4.20}$), and consequently k_{-3} ($k_{-4.20}$) reported in the work of Christensen *et al.* are incorrect.

On the basis of their determinations of the equilibrium constant for HO_2 + CH_3OH reversible association, Christensen *et al.* argue for a reinterpretation of the present work at low temperature. Again, however, this argument appears flawed. Figure 4.18, reproduced from the work of Christensen *et al.*, is a re-analysis of data reported in this work at $T = 254$ K. We note that this figure displays, and presumably uses only five data points, whereas six are in fact reported at this temperature - the point at highest methanol concentration was omitted. It is not clear why these authors selectively analyse a subset of data reported here.

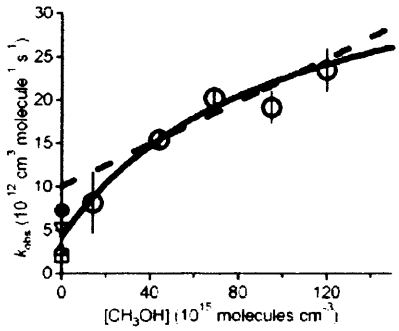

Figure 11. Comparisons of different extrapolations to the Stone and Rowley data at 254 K. 760 Torr. The data reported in their work are depicted by (○). The solid line is a weighted fit using the full equation for k_{obs} (eq 15). The dashed line is a weighted fit assuming a linear dependence. Also shown are the NASA recommended values (at zero methanol) of k_1 760 Torr (▽) and 100 Torr (△) for 254 K and the value of k_1 from the Christensen et al. study at 100 Torr. 254 K. depicted as (□). For reference. the reported value of k_1 from Stone and Rowley (760 Torr) was (7.25 ± 3.03) × 10^{-12} cm^3 molecule^{-1} s^{-1} and is depicted in the figure as (●).

Figure 4.18 : Reproduced from Christensen *et al.* (2006).[32] Note that this work, and that to which Christensen *et al.* refer, reports six data points at 254 K, as shown in Figure 4.14.

Direct fitting of the observed rate constant as a function of methanol concentration to the full expression (4.xii) was therefore carried out to attempt to replicate the Christensen *et al.* results. The fit to the full expression is given in Figure 4.19 below, compared to the linear fit. In contrast to the work of Christensen *et al.*, the full fit to expression (4.xii) yields a functional dependence which lies close to the linear fit, and which therefore gives a zero methanol extrapolation value of $k_{4.8}$ close to that obtained from linear fitting. The linear fit gave $k_{4.8} = (7.50 \pm 1.92) \times 10^{-12}$ cm^3 s^{-1} while the fit to (4.xii) gave $k_{4.8} = (6.41 \pm 31.17) \times 10^{-12}$ cm^3 s^{-1}. Furthermore, the calculated errors on the full fit are very large indeed – unsurprising given fitting four variables to six data points.

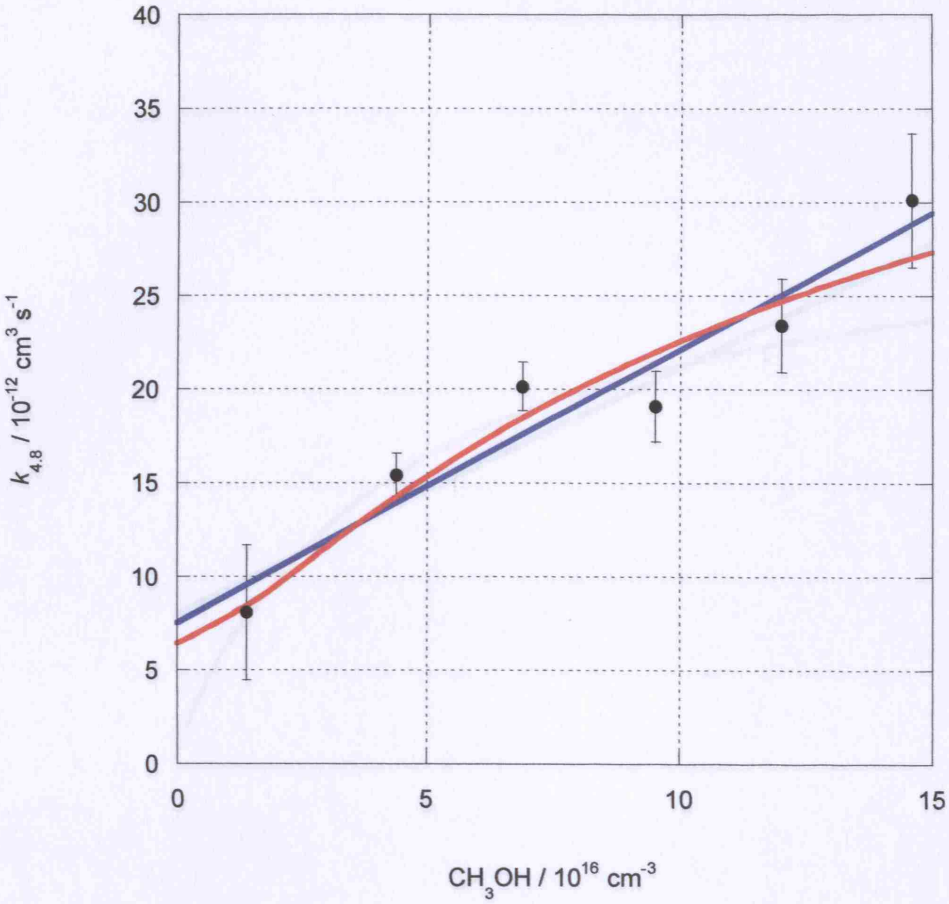

Figure 4.19 : Experimental values of $k_{4.8}$ determined in this work at 254 K as a function of [CH_3OH] (black points), with linear fit (blue) and fit to equation (4.xii) (red).

If the fit is repeated *excluding* the last data point reported in our data, the contrast between the full fit and the linear fit is somewhat more pronounced, as shown in Figure 4.20, below. Here the increased curvature of the dependence is apparent and results in a much lower extrapolation of $k_{4.8}$ to zero methanol.

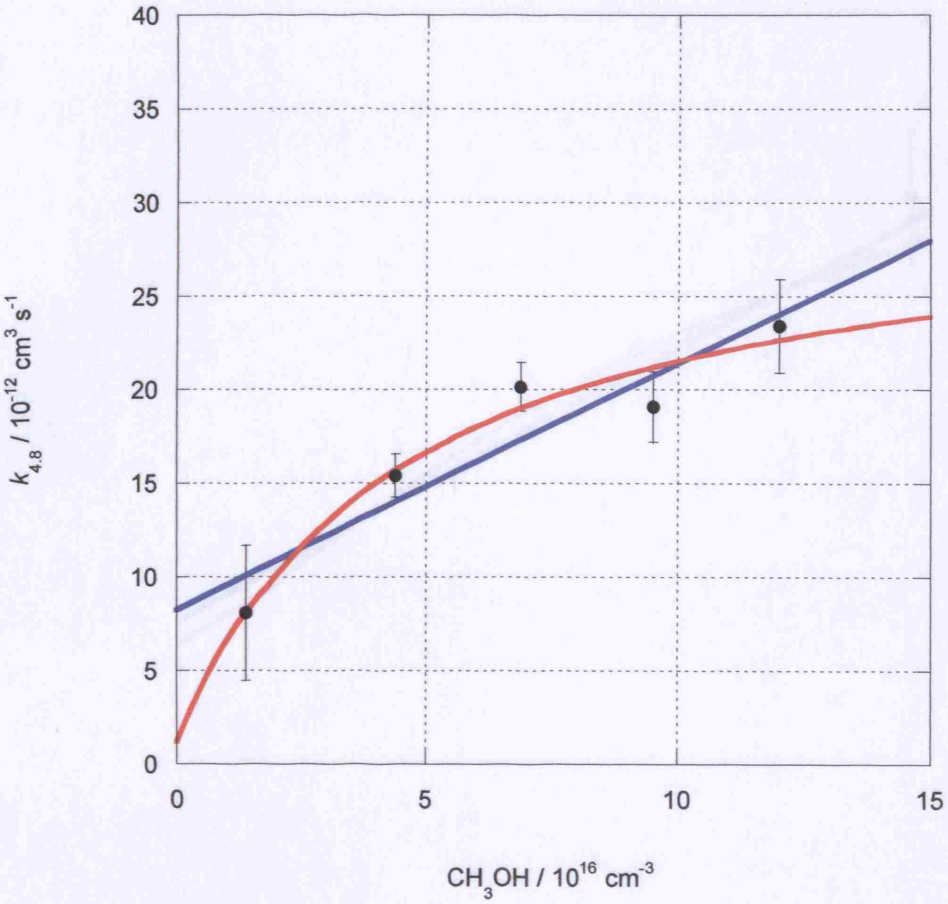

Figure 4.20 : Experimental values of $k_{4.8}$ determined in this work at 254 K as a function of [CH_3OH] (black points), with highest [CH_3OH] point removed. The linear fit to the data is shown in blue, and the full fit to equation (4.xii) in red.

These results are replicated if the parameterisation of the equilibrium constant K_c reported by Christensen *et al.* is used to calculate K_c at 254 K, and this value stipulated in the model. The corresponding analyses are shown in Figure 4.21 (fitting to all data points) and Figure 4.22 (removing the highest methanol point from the fit) respectively.

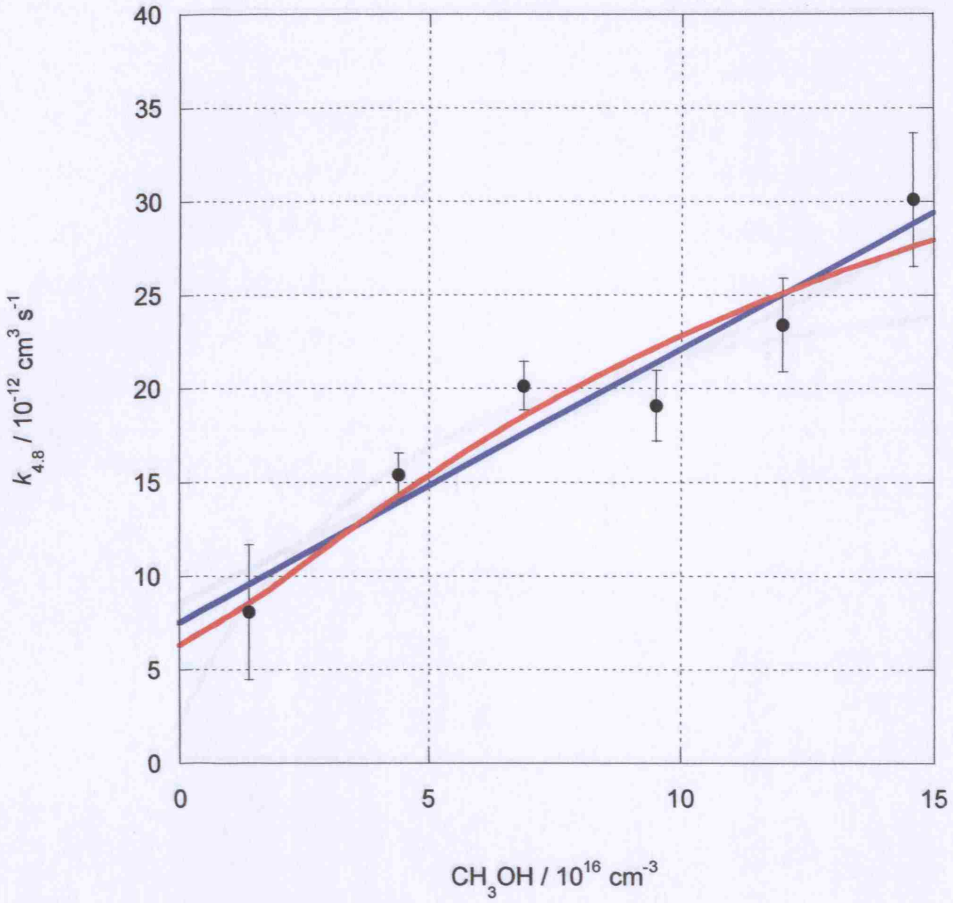

Figure 4.21 : Experimental values of $k_{4.8}$ determined in this work at 254 K as a function of [CH_3OH] (black points), with linear fit (blue) and fit to equation (4.xii) (red). The fit to equation (4.xii) has been constrained to the Christensen *et al*. value of K_c.

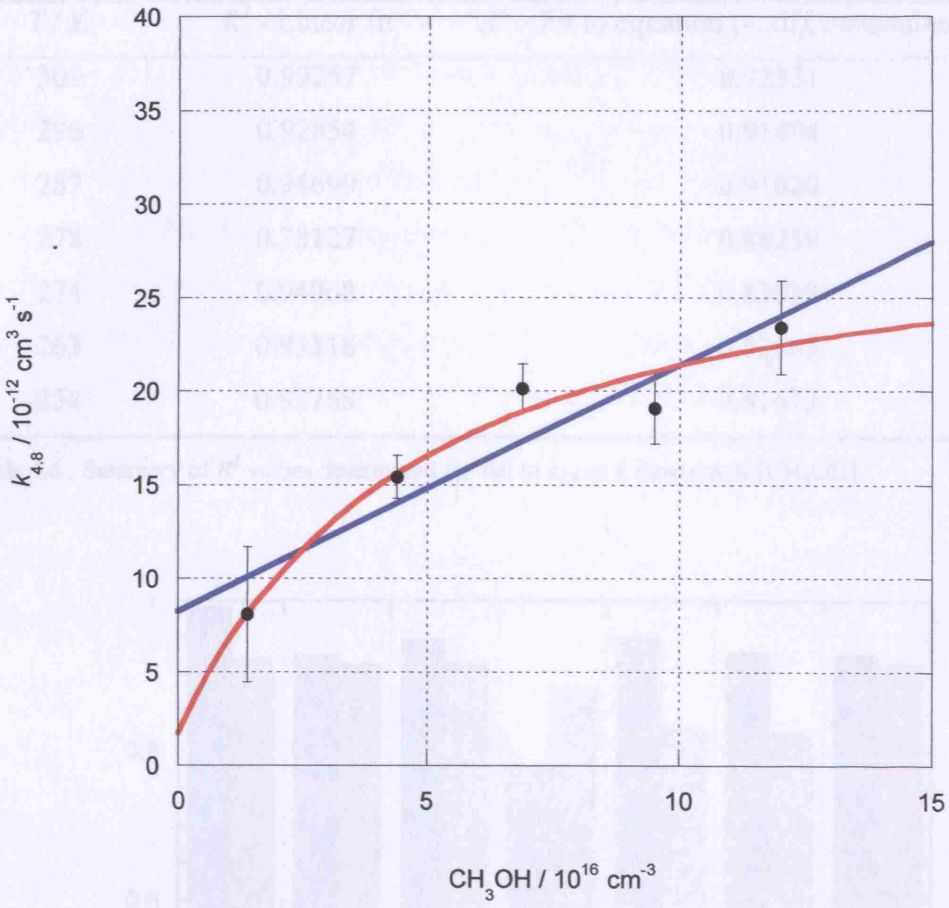

Figure 4.22 : Experimental values of $k_{4.8}$ determined in this work at 254 K as a function of [CH_3OH] (black points), with highest methanol point removed. The linear fit is shown (blue) and the fit to equation (4.xii) (red). The fit to equation (4.xii) has been constrained to the Chrsitensen *et al.* value of K_c.

In none of these fits could the value of $k_{4.8}$ reported by Christensen *et al.* extrapolated to zero methanol be reproduced. This work cannot therefore determine whether the reanalysis of this work presented by Christensen *et al.* used five points as shown in their Figure 11 (Figure 4.18 in this work), or all six. Certainly, the omission of the highest methanol point does increase the differences between a full fit to equation (4.xii) and a linear fit.

In all cases, for the analysis of the $T = 254$ K data reported here, linear fits gave a better description of the data than the curved fits as shown in the comparison of the correlation coefficient, R^2. The R^2 values determined for each type of fit, a statistical measure of the precision of the fit, are given in Table 4.6 and shown in Figure 4.23.

T / K	R^2 - Linear fit	R^2 – Fit to equation (4.xii), constrained to K_c[32]
309	0.99267	0.92331
296	0.92854	0.91494
287	0.94699	0.91620
278	0.78127	0.88239
274	0.94968	0.83039
263	0.93118	0.82563
254	0.92768	0.91673

Table 4.6 : Summary of R^2 values determined for fits to $k_{4.8}$ as a function of [CH_3OH].

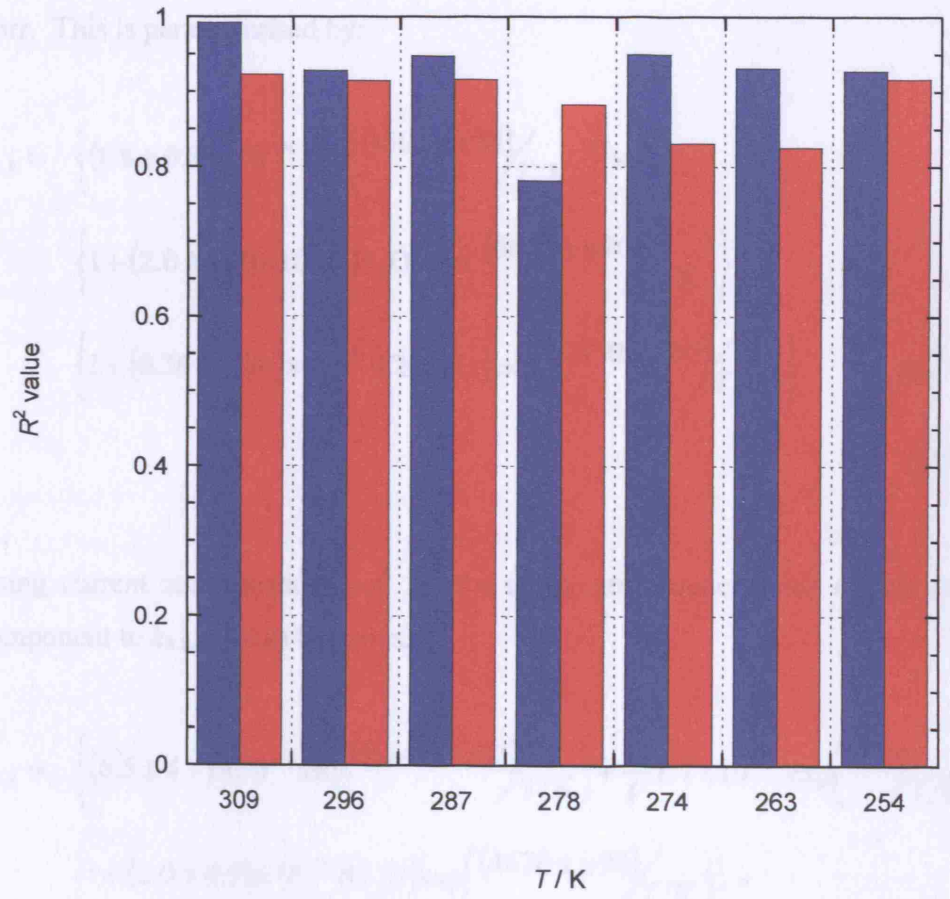

Figure 4.23 : R^2 values for linear fits to $k_{4.8}$ as a function of [CH_3OH] (blue), and R^2 values for the fit to equation (4.xii), constrained to the Christensen *et al.* values for K_c (red).

Given that the results presented here were analysed and published[39] before substantial knowledge of measurements of $K_{4.20}$, and most importantly, in view of the observed

linear dependence of $k_{4.8}$ on methanol concentration, the analysis has been conducted in terms of (4.xiii) and (4.xiv), maintaining the assumption that $K_{4.20}[CH_3OH] << 1$.

To determine the true effects of temperature and pressure on the unenhanced $k_{4.8}$, as reported in section 4.6.1 and described in (4.vi), the parameters A_m and $(-E_m/R)$ were applied to the observed values of $k_{4.8}$ to correct for effects of methanol. Although errors in A_m and $(-E_m/R)$ are rather large, the overall correction to observed rate coefficients was small, and reduced further still by using only data recorded at low methanol vapour concentrations. Data presented in Tables 4.2 and 4.3, and Figures 4.7 and 4.8, therefore represent data recorded with $[CH_3OH] \leq 4.4 \times 10^{16}$ cm^{-3}. Combination of results provides a description of $k_{4.8}$ as a function of temperature, $[H_2O]$ and $[CH_3OH]$ at 760 Torr. This is parameterised by:

$$k_{4.8} = \left\{(1.8 \pm 0.8)\times 10^{-14} \exp\left((1500 \pm 120)/T/\mathrm{K}\right)\right\} \times \left\{1 + (2.0 \pm 4.9)\times 10^{-25}[H_2O]\exp\left((4670 \pm 690)/T/\mathrm{K}\right)\right\} \times \left\{1 + (0.56 \pm 1.00)\times 10^{-21}[CH_3OH]\exp\left((2550 \pm 500)/T/\mathrm{K}\right)\right\} \quad \mathrm{cm^3\ s^{-1}} \qquad (4.xix)$$

Using current recommendations[4] for the temperature dependence of the termolecular component to $k_{4.8}$, (4.xix) becomes:

$$k_{4.8} = \left\{(6.5 \pm 4.7)\times 10^{-15} \exp\left((1640 \pm 200)/T/\mathrm{K}\right) + \frac{N}{V}1.7\times 10^{-33} \exp\left(1000/T/\mathrm{K}\right)\right\} \times \left\{1 + (2.0 \pm 4.9)\times 10^{-25}[H_2O]\exp\left((4670 \pm 690)/T/\mathrm{K}\right)\right\} \times \left\{1 + (0.56 \pm 1.00)\times 10^{-21}[CH_3OH]\exp\left((2550 \pm 500)/T/\mathrm{K}\right)\right\} \quad \mathrm{cm^3\ s^{-1}} \qquad (4.xx)$$

where N/V is the total number density in cm^{-3}.

4.7 Discussion

A comparison between the results of this work with previous measurements at ambient temperature and pressure is given in Table 4.7. Despite the range of techniques and sources of HO_2 used in previous studies of HO_2 self-reaction kinetics, there is good agreement between this and previous work under ambient conditions, and the results of this work at 296 K and 760 Torr compare well to current recommendations.[4]

Reference	Technique	Reaction mixture	T / K	λ / nm	σ / 10^{-18} cm^2	$k_{4.8}$ / 10^{-12} cm^3 s^{-1}
Paukert and Johnston 1972[40]	MMS	H_2O_2	295	210	4.5	3.6 ± 0.5
		O_3/H_2O_2				
		Cl_2/H_2O_2				
Hochanadel *et al.* 1972[22]	FP/UVA	H_2O/O_2	298	205	2.94	9.47 ± 0.83
Hamilton 1975[5]	PR/UVA	H_2/O_2	295	230.5	2.17	3.15
Hamilton and Lii 1977[6]	PR/UVA	H_2/O_2	298	230.5	2.2	2.5
Cox and Burrows 1979[9]	MMS	$Cl_2/H_2/O_2$	298	220	3.45	2.35 ± 0.2
		$Cl_2/HCHO/O_2$				
Hochanadel *et al.* 1980[41]	FP/UVA	H_2O/O_2	296	220	1.48	6.64 ± 1.16
Simonaitis and Heicklen 1982[19]	FP/UVA	$Cl_2/CH_3OH/O_2$	296	220	3.5	2.5 ± 0.1
Sander *et al.* 1982[10 a]	FP/UVA	$Cl_2/CH_3OH/O_2$	298	227.5	3.0	2.97 ± 0.45
Andersson *et al.* 1988[12]	MMS	$Cl_2/CH_3OH/O_2$	299	220	3.5	2.76
Lightfoot *et al.* 1988[42]	FP/UVA	$Cl_2/CH_3OH/O_2$	298	210	4.4	3.34 ± 0.91
Crowley *et al.* 1991[43]	MMS	$Cl_2/H_2/O_2$	298	220	3.4	2.84 ± 0.30
Sehested *et al.* 1997[44]	PR/UVA	$SF_6/H_2/O_2$	295	220	3.47	3.5 ± 1.0
				230	2.30	
				240	1.22	
NASA 2002[4]			298			$2.91^{+0.87}_{-0.67}$
This work	FP/UVA	$Cl_2/CH_3OH/O_2$	296	205	4.4	2.86 ± 0.31

Table 4.7 : $k_{4.8}$ at ambient temperature at 760 Torr. MMS = molecular modulation spectrometry; FP = flash photolysis; PR = pulse radiolysis; UVA = ultraviolet absorption spectroscopy. [a] taken at 700 Torr.

4.7.1 Temperature and Pressure Dependence

The HO_2 self-reaction was found to have a negative apparent activation energy at 760 Torr, resulting from a negative dependence of $k_{4.8}$ on temperature. As shown in Figure

4.24, the present results are in good agreement with previous studies at 760 Torr at the common temperatures. However, this study extends the ambient pressure measurements of $k_{4.8}$ to lower temperatures than previous studies. At such lower temperatures, however, the current work indicates that $k_{4.8}$ is greater than expected on the basis of extrapolation of previous work, despite correction for methanol vapour enhancement in this work. A comparison of Arrhenius parameters for $k_{4.8}$ determined in this and previous work at 760 Torr is given in Table 4.8.

Reference	Technique	T / K	p / Torr	Arrhenius fit
Lii *et al.* 1979,[15] 1980,[7] 1981[8]	PR/UVA	276 – 400	1200	$(1.14 \pm 0.16) \times 10^{-13} \exp(1057 \pm 45/T)$
Cox and Burrows 1979[9]	MMS	273 – 339	3 – 760	$(3.8 \pm 1.4) \times 10^{-14} \exp(1250 \pm 200/T)$
Patrick and Pilling 1982[45]	FP/UVA	298 – 510	700	$(4.14 \pm 1.15) \times 10^{-13} \exp(630 \pm 115/T)$
Thrush and Tyndall 1982[17]	FP/IR	298 – 358	10	$2.4 \times 10^{-13} \exp(560 \pm 200/T)$
Kircher and Sander 1984[11]	FP/UVA	240 – 420	100 – 700	$(2.2 \pm 0.55) \times 10^{-13} \exp(620 \pm 60/T)$ + $(1.9 \pm 0.48) \times 10^{-33}$ [N_2] $\exp(980 \pm 200/T)$
Takacs and Howard 1986[16]	DF/LMR	253 – 390	1 – 7	$(2.0 \pm 0.6) \times 10^{-13} \exp(595 \pm 120/T)$
Lightfoot *et al.* 1990[21]	FP/UVA	248 – 573	100 – 760	$(3.8 \pm 0.4) \times 10^{-13} \exp(580 \pm 32/T)$ + $(1.2 \pm 0.4) \times 10^{-33}$ [M] $\exp(1150 \pm 97/T)$
Dobis and Benson 1993[46]	DF/MS	243 – 368	mTorr	$(4.5 \pm 0.56) \times 10^{-13} \exp(535 \pm 40/T)$
Maricq and Szente 1994[38]	FP/UVA	210 – 363	200	$(2.8 \pm 0.5) \times 10^{-13} \exp(594 \pm 55/T)$
Christensen *et al.* 2002[14]	FP/UVA/IR	222 – 295	100	$(8.8 \pm 0.9) \times 10^{-13} \exp(210 \pm 26/T)$
NASA 2002[4]				$2.3 \times 10^{-13} \exp(600/T)$ + 1.7×10^{-33} [N_2] $\exp(1000/T)$
This work	FP/UVA	236 – 309	760	$(1.8 \pm 0.8) \times 10^{-14} \exp(1500 \pm 120/T)$

Table 4.8 : Summary of previous investigations of $k_{4.8}$ conducted as a function of temperature. PR = pulse radiolysis; UVA = ultraviolet absorption spectroscopy; MMS = molecular modulation spectrometry; FP = flash photolysis; IR = infrared spectroscopy; DF = discharge flow; LMR = laser magnetic resonance.

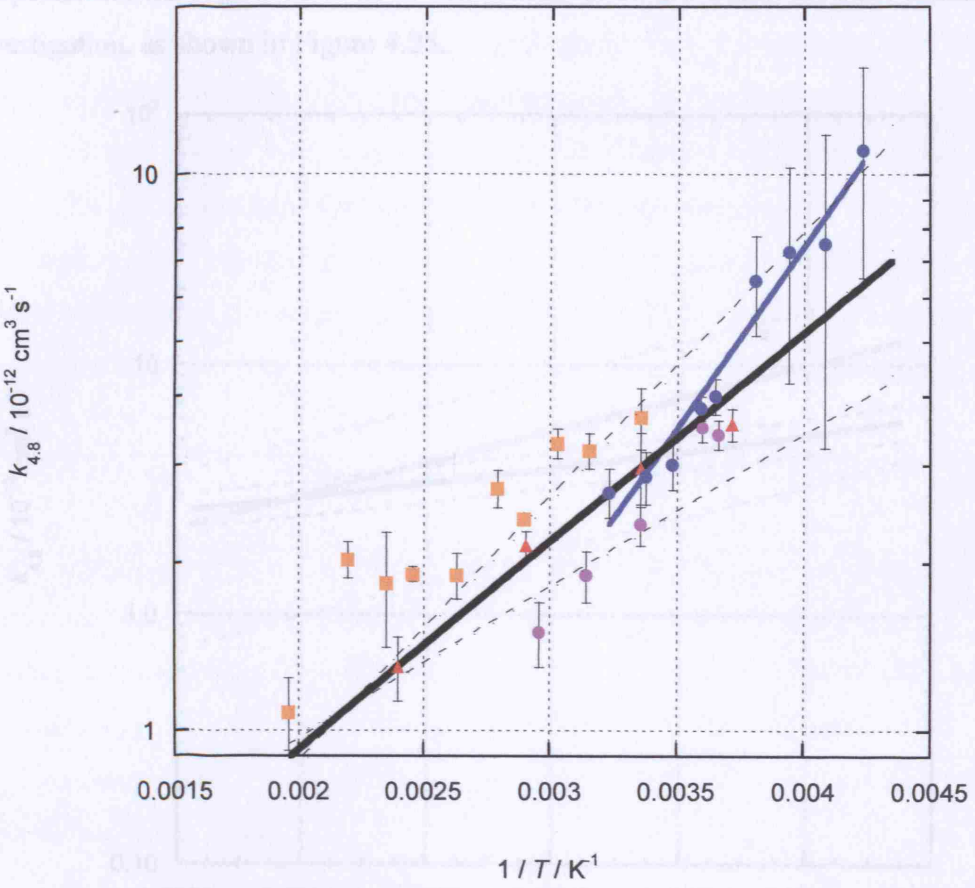

Figure 4.24 : Summary of previous investigations of $k_{4.8}$ as a function of temperature at ambient pressure. Results shown are those of this work 760 Torr (blue circles), Cox and Burrows[9] 760 Torr (purple circles), Patrick and Pilling[45] 700 Torr (orange squares) and Sander *et al.*[10] 700 Torr (red triangles). The fit to this work is given by the solid blue line, and the NASA recommendation[4] by the solid black line. Upper and lower limits to the NASA recommendation are given by the broken black lines. Errors for this work are 1σ and statistical only.

Current recommendations[4] for the temperature dependence of the termolecular component to $k_{4.8}$ can be used to enable comparison between the kinetic parameters reported in the current work and those of Christensen *et al.*,[14] the only other study to correct for effects of methanol vapour. Christensen *et al.* used flash photolysis of $Cl_2/CH_3OH/O_2/N_2$ mixtures between 222 and 295 K at a total pressure of 100 Torr. A limited number of experiments were also carried out by Christensen *et al.* using flash photolysis of $F_2/H_2/O_2/N_2$ mixtures, giving results in good agreement with the $Cl_2/CH_3OH/O_2/N_2$ system when the effects of CH_3OH were removed. The results of this work, however, are in poor agreement with those of Christensen *et al.* at low

temperatures, although the results of Christensen *et al.* are within the error limits for this investigation, as shown in Figure 4.25.

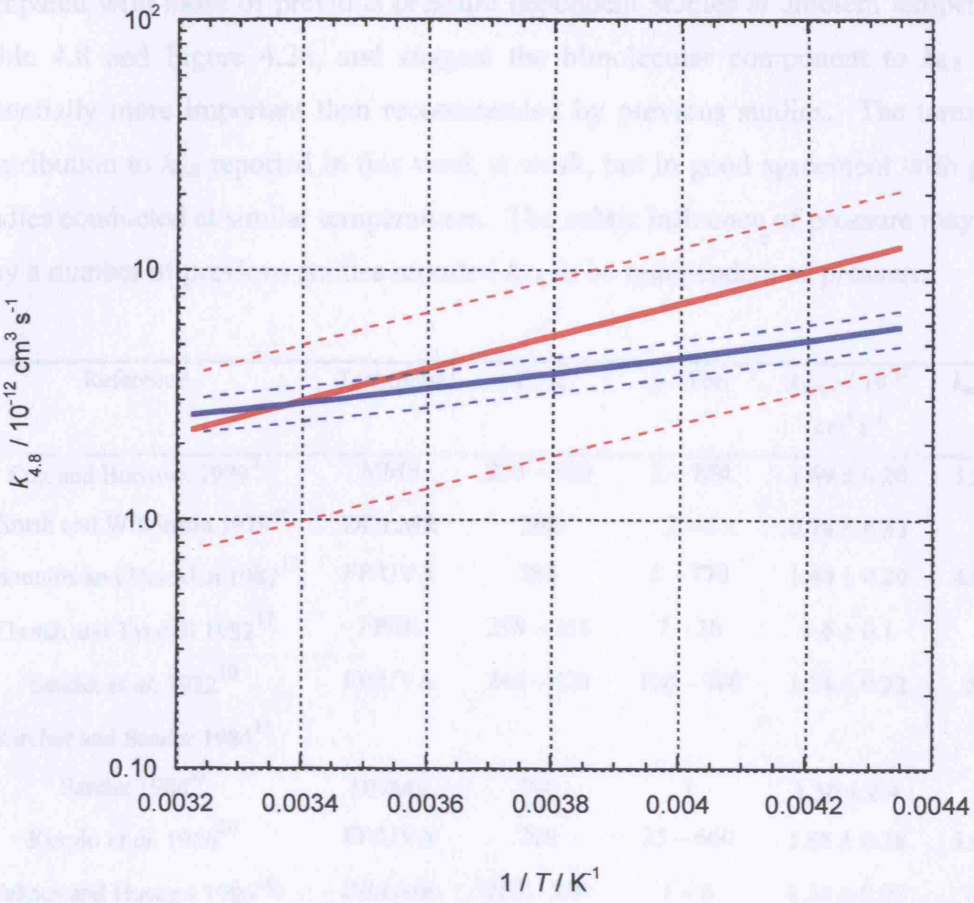

Figure 4.25 : Comparison between Arrhenius fits to this work (solid red line), Christensen *et al.*[14] (solid blue line). Results of Christensen *et al.* have been scaled to 760 Torr using the NASA recommendation for the termolecular component to $k_{4.8}$. Error limits for each investigation are shown by the appropriately coloured broken lines.

The differences between Arrhenius parameters reported in this work and those reported by Christensen *et al.* can be attributed to differences in measurements of the methanol vapour enhancement of $k_{4.8}$, discussed above in section 4.6.3. However, given that the current work extends $k_{4.8}$ to temperatures not previously studied at 760 Torr, the possibility of a curved Arrhenius plot for $k_{4.8}$ cannot be ruled out.

The results of the current work show a weak positive dependence of $k_{4.8}$ on pressure between 100 and 760 Torr, indicating a termolecular component to the overall rate

coefficient, and a non-zero value for $k_{4.8}$ on extrapolation to zero pressure, indicating a bimolecular component to the overall rate coefficient. Results of this work are compared with those of previous pressure dependent studies at ambient temperature in Table 4.8 and Figure 4.26, and suggest the bimolecular component to $k_{4.8}$ may be potentially more important than recommended by previous studies. The termolecular contribution to $k_{4.8}$ reported in this work is weak, but in good agreement with previous studies conducted at similar temperatures. The subtle influence of pressure may explain why a number of previous studies reported $k_{4.8}$ to be independent of pressure.

Reference	Technique	T / K	p / Torr	k_{bimol} / 10^{-12} cm^3 s^{-1}	k_{termol} / 10^{-32} cm^6 s^{-2}
Cox and Burrows 1979[9]	MMS	273 – 339	3 – 760	1.69 ± 0.20	3.52 ± 1.91
Thrush and Wilkinson 1979[47]	DF/LMR	298	2 – 4	0.74 ± 0.33	
Simonaitis and Heicklen 1982[19]	FP/UVA	296	5 – 770	1.40 ± 0.20	4.83 ± 0.30
Thrush and Tyndall 1982[17]	FP/IR	298 – 358	7 – 20	1.6 ± 0.1	
Sander *et al.* 1982[10]	FP/UVA	240 – 420	100 – 700	1.74 ± 0.22	5.4 ± 3.1
Kircher and Sander 1984[11]					
Sander 1984[48]	DF/MS	298	1	1.50 ± 0.4	
Kurylo *et al.* 1986[20]	FP/UVA	298	25 – 600	1.88 ± 0.38	5.95 ± 1.19
Takacs and Howard 1986[16]	DF/LMR	253 – 390	1 – 6	1.54 ± 0.07	
Lightfoot *et al.* 1990[21]	FP/UVA	248 – 573	100 – 760	2.66 ± 0.6	5.69 ± 1.9
Dobis and Benson 1993[46]	DF/MS	243 – 368	mTorr	2.70 ± 0.20	
NASA 2002[4]				1.7	1.2
This work	FP/UVA	296	100 – 760	2.0 ± 0.2	4.2 ± 1.2

Table 4.9 : Summary of previous investigations of $k_{4.8}$ as a function of pressure at ambient temperature. MMS = molecular modulation spectrometry; DF = discharge flow; LMR = laser magnetic resonance; FP = flash photolysis; UVA = ultraviolet absorption spectroscopy; IR = infrared spectroscopy; MS = mass spectrometry.

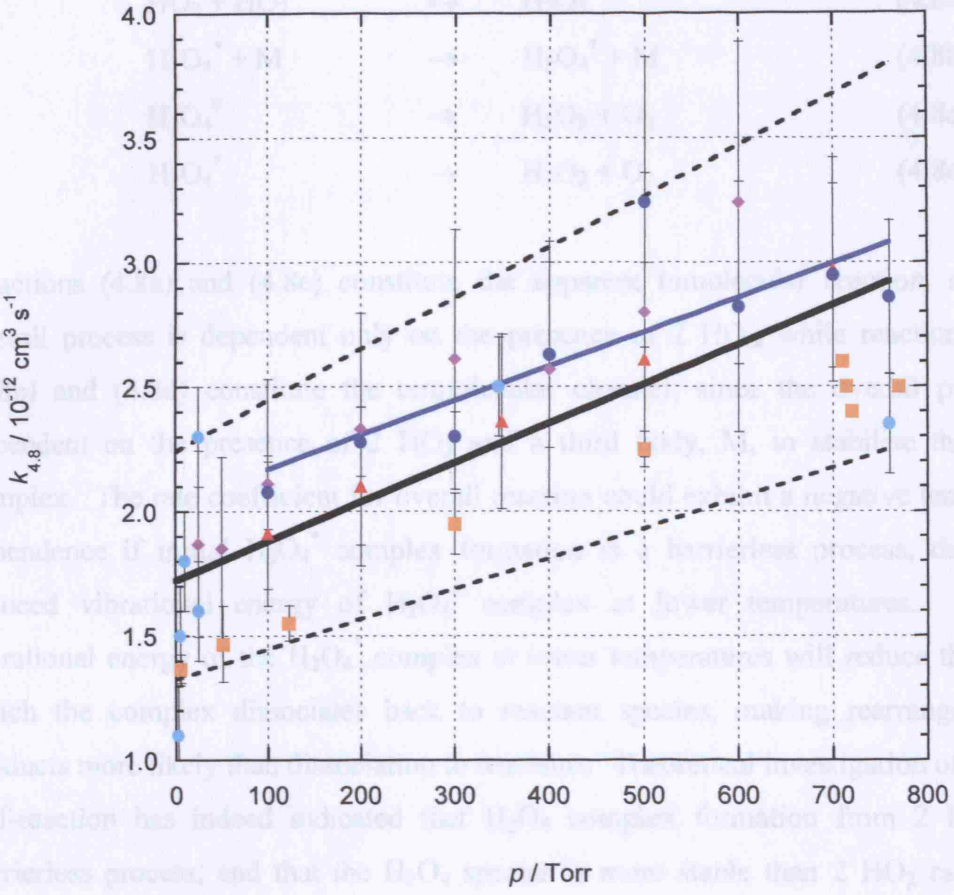

Figure 4.26 : $k_{4.8}$ as a function of pressure at ambient temperature. Results shown are those of this work 296 K (blue circles), Cox and Burrows[9] 298 K (light blue circles), Simonaitis and Heicklen[19] 296 K (orange circles), Sander *et al.*[10] 298 K (red triangles) and Kurylo *et al.*[20] 298 K (purple diamonds). The fit to this work is given by the blue line, and the current NASA recommendation[4] by the black line. Upper and lower limits to the NASA recommendation are given by the broken black lines. Errors for this work are 1σ and statistical only.

The observed dependence of $k_{4.8}$ on temperature and pressure are indicative of a mechanism involving formation of an excited radical complex, and the data are consistent with the mechanisms proposed by Sander *et al.*[10] and Thrush and Tyndall.[17] The excited $H_2O_4^*$ complex, formed by combination of two HO_2 radicals (+ 4.8a), can either dissociate back to reactants (- 4.8a), rearrange directly to generate products (4.8e), or undergo collisional stabilisation to form a stabilised $H_2O_4^\dagger$ complex (4.8b). Formation of the stabilised $H_2O_4^\dagger$ complex potentially also results in product formation by a direct rearrangement (4.8d).

$HO_2 + HO_2$	$\leftrightarrow$	$H_2O_4^*$	(4.8a)
$H_2O_4^* + M$	$\rightarrow$	$H_2O_4^\dagger + M$	(4.8b)
$H_2O_4^\dagger$	$\rightarrow$	$H_2O_2 + O_2$	(4.8d)
$H_2O_4^*$	$\rightarrow$	$H_2O_2 + O_2$	(4.8e)

Reactions (4.8a) and (4.8e) constitute the apparent bimolecular reaction, since the overall process is dependent only on the presence of 2 HO_2, while reactions (4.8a), (4.8b) and (4.8d) constitute the termolecular channel, since the overall process is dependent on the presence of 2 HO_2 and a third body, M, to stabilise the radical complex. The rate coefficient for overall reaction could exhibit a negative temperature dependence if initial $H_2O_4^*$ complex formation is a barrierless process, due to the reduced vibrational energy of $H_2O_4^*$ complex at lower temperatures. Reduced vibrational energy of the $H_2O_4^*$ complex at lower temperatures will reduce the rate at which the complex dissociates back to reactant species, making rearrangement to products more likely than dissociation to reactants. Theoretical investigation of the HO_2 self-reaction has indeed indicated that H_2O_4 complex formation from 2 HO_2 is a barrierless process, and that the H_2O_4 species is more stable than 2 HO_2 radicals by approximately 40 kJ mol^{-1}.[49]

4.7.2 Water Vapour Enhancement

The enhancement in $k_{4.8}$ in the presence of water vapour measured in this work is in good agreement with previous studies at ambient temperature, as shown in Figure 4.27. The agreement between previous studies conducted over a range of pressures indicates that the water vapour enhancement of $k_{4.8}$ is independent of pressure – a conclusion supported by the current work and that of Kircher and Sander.[11]

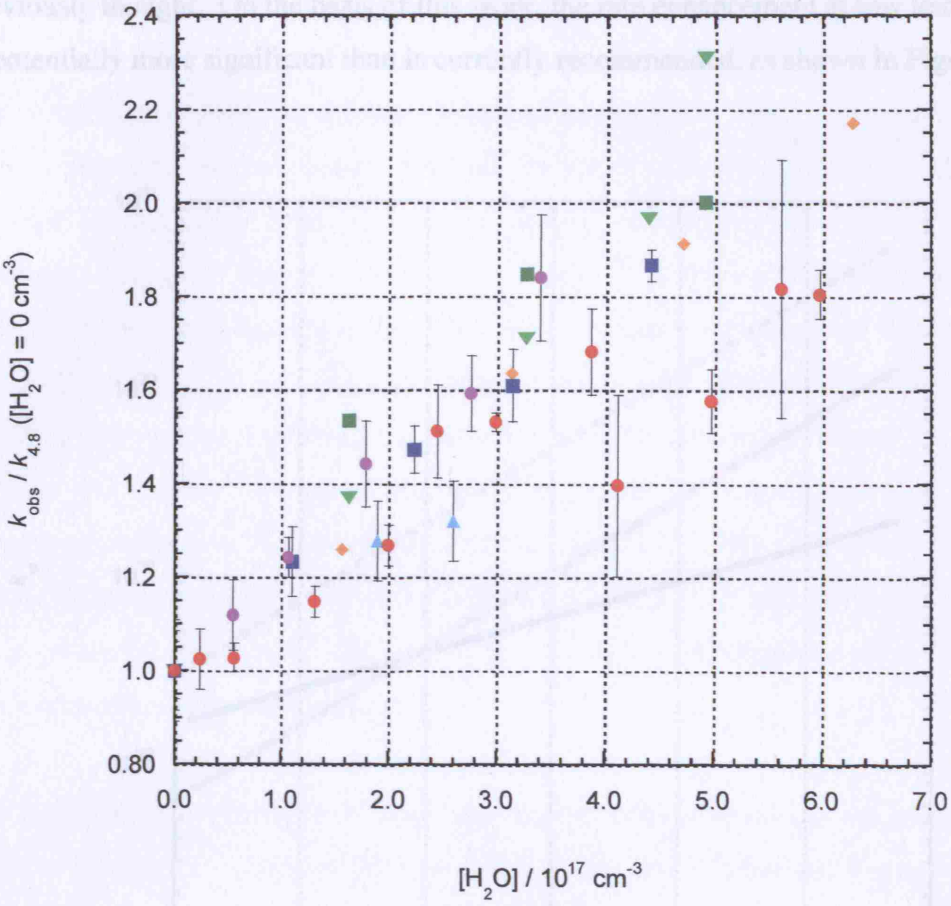

Figure 4.27 : Relative rate enhancement in $k_{4.8}$ in the presence of water vapour at ambient temperature. Results shown are those of this work 296 K, 760 Torr (red circles), Hamilton[5] 295 K, 1520 Torr (dark green squares), Hamilton and Lii[6] 295 K, 1520 Torr (light green inverted triangles), Cox and Burrows[9] 298 K, 760 Torr (light blue triangles), Lii *et al.*[8] 298 K, 1200 Torr (orange diamonds), Sander *et al.*[10] 298 K, 700 Torr (dark blue squares) and Kanno *et al.*[29] (purple diamonds). Errors shown for this work are 1σ and statistical only.

Few studies of HO_2 self-reaction kinetics have investigated the temperature dependence of the water vapour enhancement of $k_{4.8}$, and fewer still at tropospherically relevant temperatures. Current recommendations[4] of the temperature dependence of the water vapour enhancement for use in atmospheric modelling are based solely on the work of Kircher and Sander,[11] and recommend the Arrhenius parameters $A_w = 1.4 \times 10^{-21}$ cm^3 and $(-E_w/R) = 2200$ K. No errors were reported in the work of Kircher and Sander. This work reports $A_w = (2.0 \pm 4.9) \times 10^{-25}$ cm^3 and $(-E_w/R) = (4670 \pm 690)$ K, indicating that the temperature dependence of the water vapour enhancement may be stronger than

previously thought. On the basis of this work, the rate enhancement at low temperatures is potentially more significant than is currently recommended, as shown in Figure 4.28.

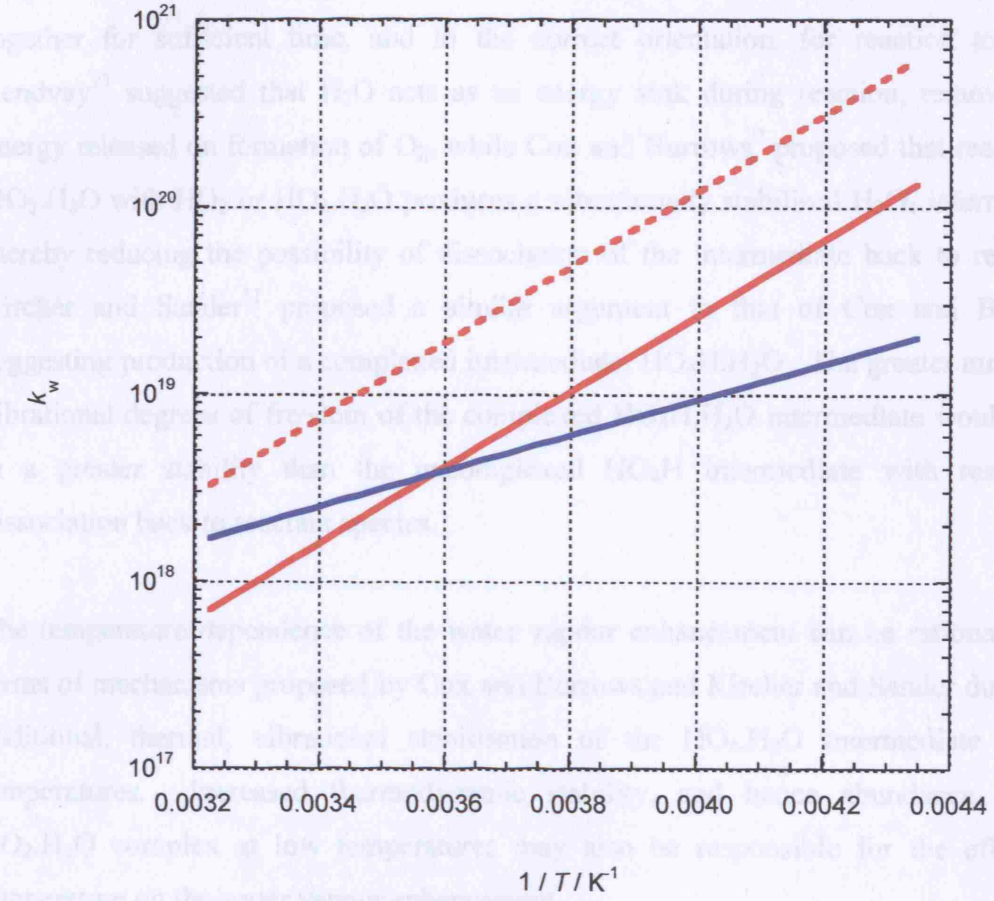

Figure 4.28 : k_w as a function of temperature, as determined in this work (red) and that of Kircher and Sander[11] (blue). The upper limit for this work is given by the broken red line, the lower limit is zero. No errors are available for k_w as reported by Kircher and Sander.

Formation of a gas phase complex between HO_2 and H_2O is generally accepted to be responsible for the effects of water vapour on HO_2 self-reaction kinetics,[5,9,11] and the $HO_2.H_2O$ complex has indeed been observed in the gas phase using IR spectroscopy.[28] Both experimental and theoretical studies report ΔH for $HO_2.H_2O$ formation from HO_2 and H_2O to be approximately –30 kJ mol^{-1}.[25,28,30]

The $HO_2.H_2O$ complex is thought to react more rapidly with HO_2, or other $HO_2.H_2O$ complexes, than uncomplexed HO_2 radicals react with other uncomplexed radicals.[5,9,11]

A number of theories have been proposed to explain the apparent differences in reaction rates between $HO_2.H_2O$ and free HO_2. Hamilton and Naleway[23] proposed that, despite the potential for steric hindrance, complexation of HO_2 with H_2O could enable a chaperone mechanism to operate in which the water molecule holds two HO_2 radicals together for sufficient time, and in the correct orientation, for reaction to occur. Lendvay[27] suggested that H_2O acts as an energy sink during reaction, removing the energy released on formation of O_2, while Cox and Burrows[9] proposed that reaction of $HO_2.H_2O$ with HO_2 or $HO_2.H_2O$ produces a vibrationally stabilised H_2O_4 intermediate, thereby reducing the possibility of dissociation of the intermediate back to reactants. Kircher and Sander[11] proposed a similar argument to that of Cox and Burrows, suggesting production of a complexed intermediate, $HO_4H.H_2O$. The greater number of vibrational degrees of freedom of the complexed $HO_4H.H_2O$ intermediate would result in a greater stability than the uncomplexed HO_4H intermediate with respect to dissociation back to reactant species.

The temperature dependence of the water vapour enhancement can be rationalised in terms of mechanisms proposed by Cox and Burrows and Kircher and Sander due to the additional, thermal, vibrational stabilisation of the $HO_4.H_2O$ intermediate at low temperatures. Increased thermodynamic stability, and hence abundance, of the $HO_2.H_2O$ complex at low temperatures may also be responsible for the effects of temperature on the water vapour enhancement.

4.7.3 Methanol Vapour Enhancement

There have been three previous investigations of the enhancement of $k_{4.8}$ in the presence of methanol vapour. Andersson *et al.*[12] studied the methanol enhancement at 278 and 299 K at 760 Torr, Bloss *et al.*[13] at 298 K, 760 Torr, and Christensen *et al.*[14] between 222 and 295 K at 100 Torr. Andersson *et al.* observed a linear dependence of $k_{4.8}$ on methanol vapour concentration, while the higher maximum methanol vapour concentration used by Bloss *et al.* led to the observation of a curved dependence. The present results are in good agreement with the work of both Andersson *et al.* and Bloss *et al.*, as shown in Figure 4.29.

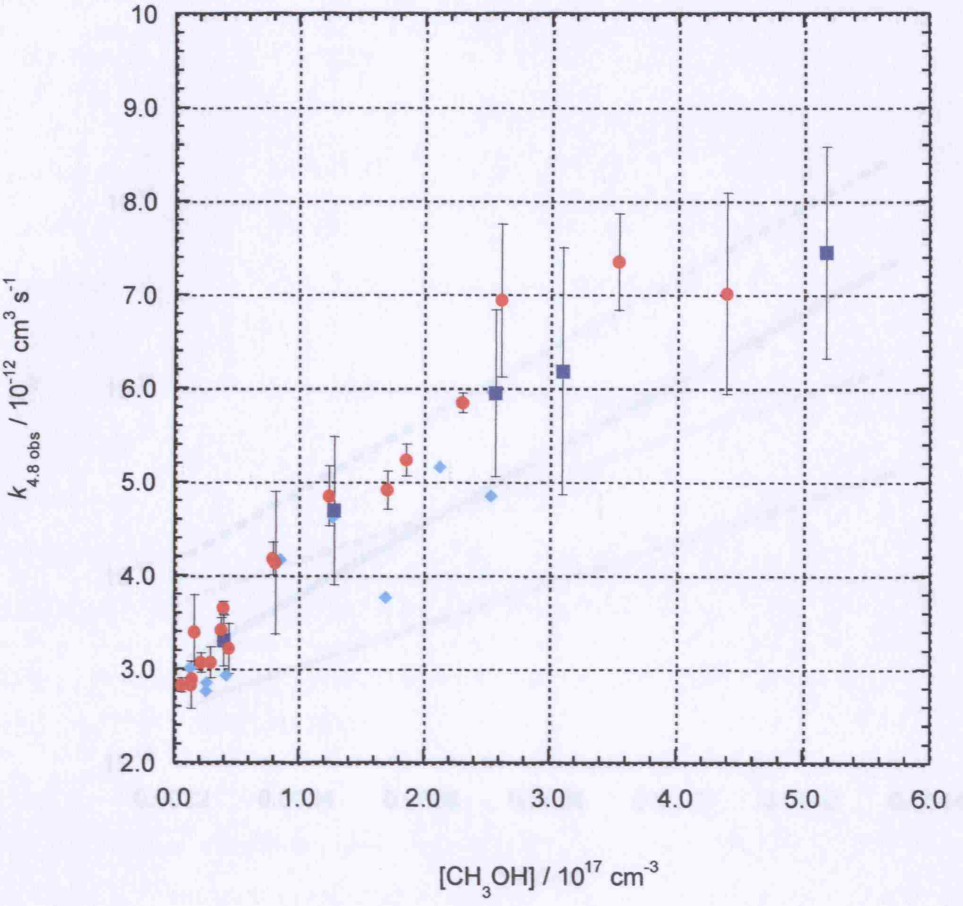

Figure 4.29 : $k_{4.8}$ as a function of methanol vapour concentration at ambient temperature. Results shown are those of this work (red circles), Andersson *et al.*[12] (light blue diamonds) and Bloss *et al.*[13] (dark blue squares). Results of Christensen *et al.*[14] are unavailable at 298 K and have therefore been omitted. Errors for this work are 1σ and statistical only.

The results of Christensen *et al.* are in good agreement with the previous and present work at temperatures near 298 K, but indicate a much stronger dependence of the enhancement on temperature than has been observed in this work, as shown in Figure 4.30. This work reports $A_m = (0.56 \pm 1.00) \times 10^{-21}$ cm^3 and $(-E_m/R) = (2550 \pm 500)$ K, whereas Christensen *et al.* found $A_m = 2.84 \times 10^{-24}$ cm^3 and $(-E_m/R) = 4360$ K. No errors are available for the work of Christensen *et al.*, and it is not clear why such discrepancies exist between the results of Christensen *et al.* and those of this work.

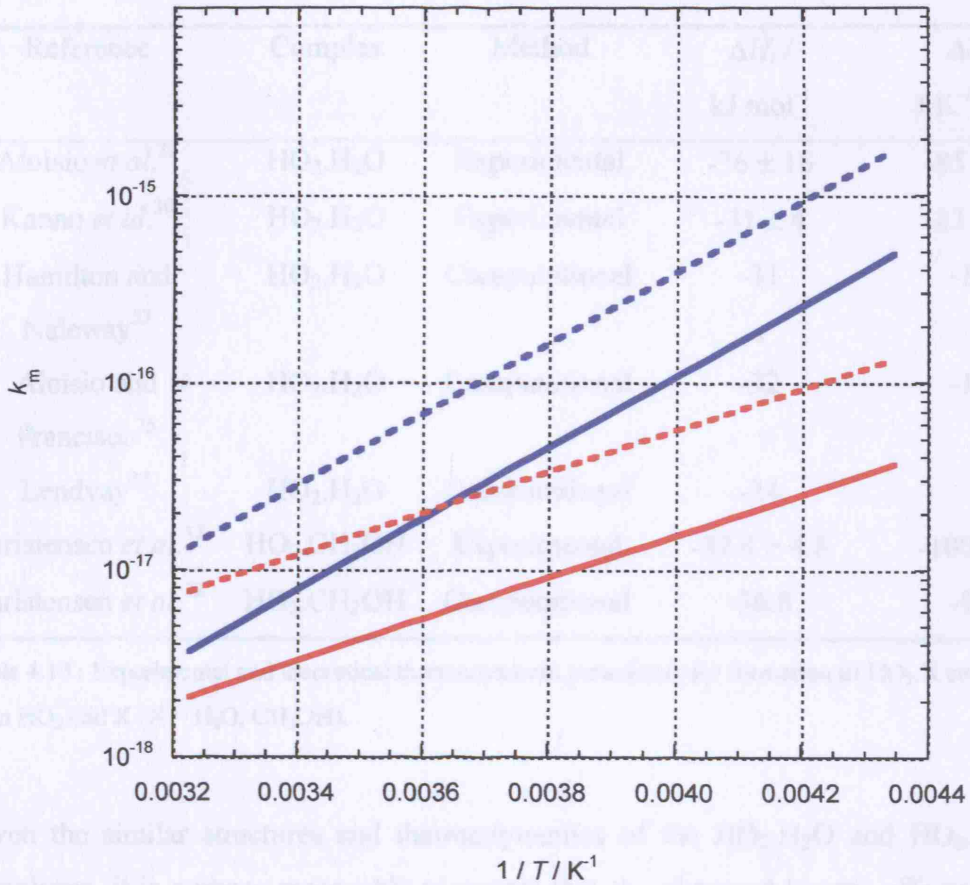

Figure 4.30 : k_m as a function of temperature, as determined in this work (red) and that of Christensen *et al.*[14] (blue). Upper limits to k_m for each investigation are shown by the appropriately coloured broken lines. Lower limits are zero for both investigations.

Theoretical investigation of the $HO_2.CH_3OH$ complex by Christensen *et al.*[32] revealed a minimum energy structure similar to that of the $HO_2.H_2O$ complex, as shown in (S 4.2). The thermodynamic stability of the $HO_2.CH_3OH$ complex, relative to free HO_2 and CH_3OH, were also determined to be similar to that of the $HO_2.H_2O$ complex. Thermodynamic parameters for $HO_2.CH_3OH$ and $HO_2.H_2O$ are given in Table 4.10.

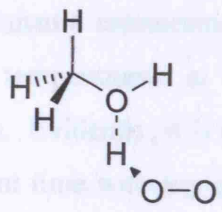

(S 4.2)

Reference	Complex	Method	ΔH_r / kJ mol^{-1}	ΔS_r / J K^{-1} mol^{-1}
Aloisio *et al.*[28]	$HO_2.H_2O$	Experimental	-36 ± 16	-85 ± 40
Kanno *et al.*[30]	$HO_2.H_2O$	Experimental	-31 ± 4	-83 ± 14
Hamilton and Naleway[23]	$HO_2.H_2O$	Computational	-31	-103
Aloisio and Francisco[25]	$HO_2.H_2O$	Computational	-32	-107
Lendvay[27]	$HO_2.H_2O$	Computational	-24	–
Christensen *et al.*[32]	$HO_2.CH_3OH$	Experimental	-37.4 ± 4.8	-100 ± 19
Christensen *et al.*[32]	$HO_2.CH_3OH$	Computational	-36.8	-106

Table 4.10 : Experimental and theoretical thermodynamic parameters for formation of $HO_2.X$ complexes from HO_2 and X (X = H_2O, CH_3OH).

Given the similar structures and thermodynamics of the $HO_2.H_2O$ and $HO_2.CH_3OH$ complexes, it is perhaps reasonable to expect that the observed kinetic effects of H_2O and CH_3OH on $k_{4.8}$ result from the operation of analogous mechanisms. On the basis of the mechanisms proposed by Cox and Burrows and Kircher and Sander for the H_2O enhancement, it might therefore be expected that methanol would have a greater effect on HO_2 self-reaction kinetics. The greater number of vibrational degrees of freedom in $HO_2.CH_3OH$ compared to $HO_2.H_2O$ would lead to a greater vibrational stabilisation of the HO_4H intermediate formed in the presence of methanol compared to that formed in the presence of water. While this work shows that the methanol vapour enhancement is dominant at temperatures above 260 K, below 260 K it appears that water vapour exerts the greater effect on HO_2 self-reaction kinetics, Figure 4.31. It is probable that both vibrational deactivation of the HO_4H intermediate and steric factors contribute to the overall reaction mechanism. It may be that the dominance of the water enhancement over the methanol enhancement at low temperatures is due to the dominance of steric factors at temperatures at which species are less likely to require vibrational deactivation. Evidently, it is not possible to determine which mechanism is in operation at the present time with any certainty. Further theoretical investigation of the potential

energy surfaces for reactions between HO_2 and $HO_2.H_2O$ and $HO_2.CH_3OH$ would provide further insight.

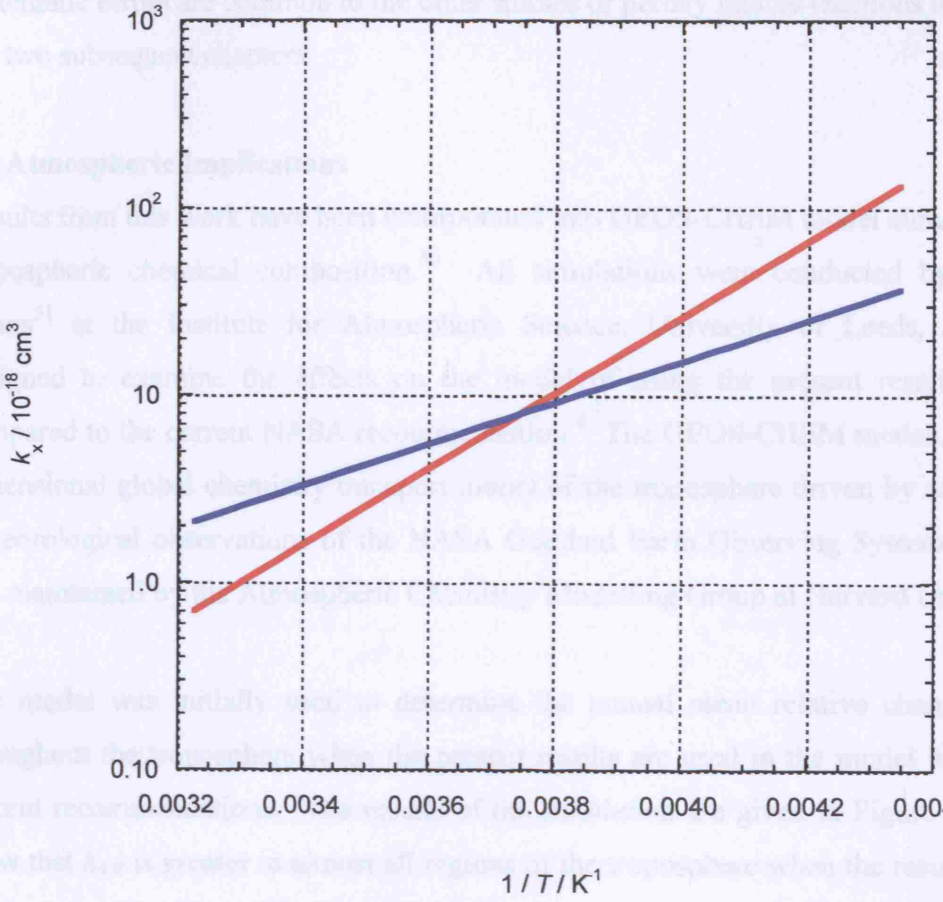

Figure 4.31 : k_w (blue) and k_m (red) as a function of temperature, as determined in this work.

4.8 Potential Sources of Error

The major potential systematic error in this work arises from uncertainty in σ_{HO_2}. Any change in σ_{HO_2} used in spectral fitting would directly influence reported values of $k_{4.8}$, since the parameter actually determined in the experiments is $k_{4.8}/\sigma_{HO_2}$. Parameterisations of the rate enhancements by water and methanol, however, are independent of the adopted value for σ_{HO_2}, since the enhancements have been calculated relative to the unenhanced rate coefficients.

Other possible sources of systematic error are cell temperature and pressure, gas flow rates and saturation of N_2 flow with CH_3OH or H_2O. Instruments used to measure cell temperature and pressure and gas flow rates were calibrated before and after

experiments in order to minimise the possibility for error. Saturation of N_2 with CH_3OH or H_2O was determined as described in section 3.5.1, Chapter 3. Such potential systematic errors are common to the other studies of peroxy radical reactions reported in the two subsequent chapters.

4.9 Atmospheric Implications

Results from this work have been incorporated into GEOS-CHEM model simulations of tropospheric chemical composition.[50] All simulations were conducted by Dr Mat Evans[51] at the Institute for Atmospheric Science, University of Leeds, and were designed to examine the effects on the model of using the present results for $k_{4.8}$ compared to the current NASA recommendation.[4] The GEOS-CHEM model is a three-dimensional global chemistry transport model of the troposphere driven by assimilated meteorological observations of the NASA Goddard Earth Observing System (GEOS), and maintained by the Atmospheric Chemistry Modelling Group at Harvard University.

The model was initially used to determine the annual mean relative change in $k_{4.8}$ throughout the troposphere when the present results are used in the model in place of current recommendations. The results of the simulation are given in Figure 4.32, and show that $k_{4.8}$ is greater in almost all regions of the troposphere when the results of this work are used in the model. The greatest impact of this work on the HO_2 recombination rate is observed in the upper tropical troposphere, where temperatures are at a minimum. The sole exception to the increase in $k_{4.8}$ is observed in the warm conditions of the tropical lower troposphere.

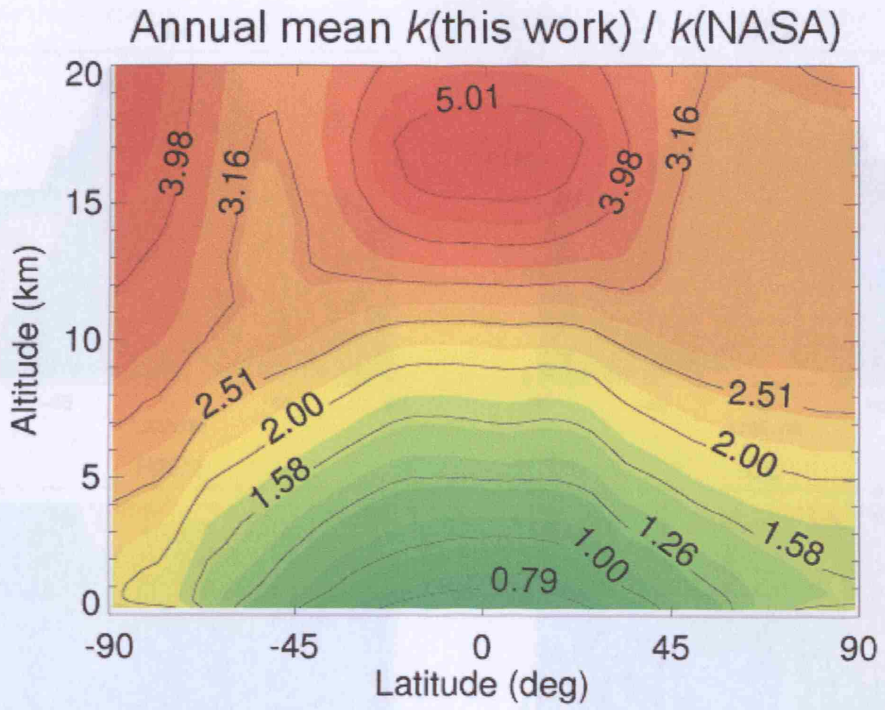

Figure 4.32 : Ratio of $k_{4.8}$ (this work) to $k_{4.8}$ (NASA) as a function of altitude and latitude, as calculated by the GEOS-CHEM model.

Further simulations were subsequently carried out to examine the effects of the present results on modelled concentrations of a number of tropospherically important trace gas species. Results are presented in Figures 4.33 and 4.34 as relative changes in the modelled concentrations occurring as a result of the change in $k_{4.8}$ entered into the model, compared to simulations with $k_{4.8}$ taken from current recommendations.[4]

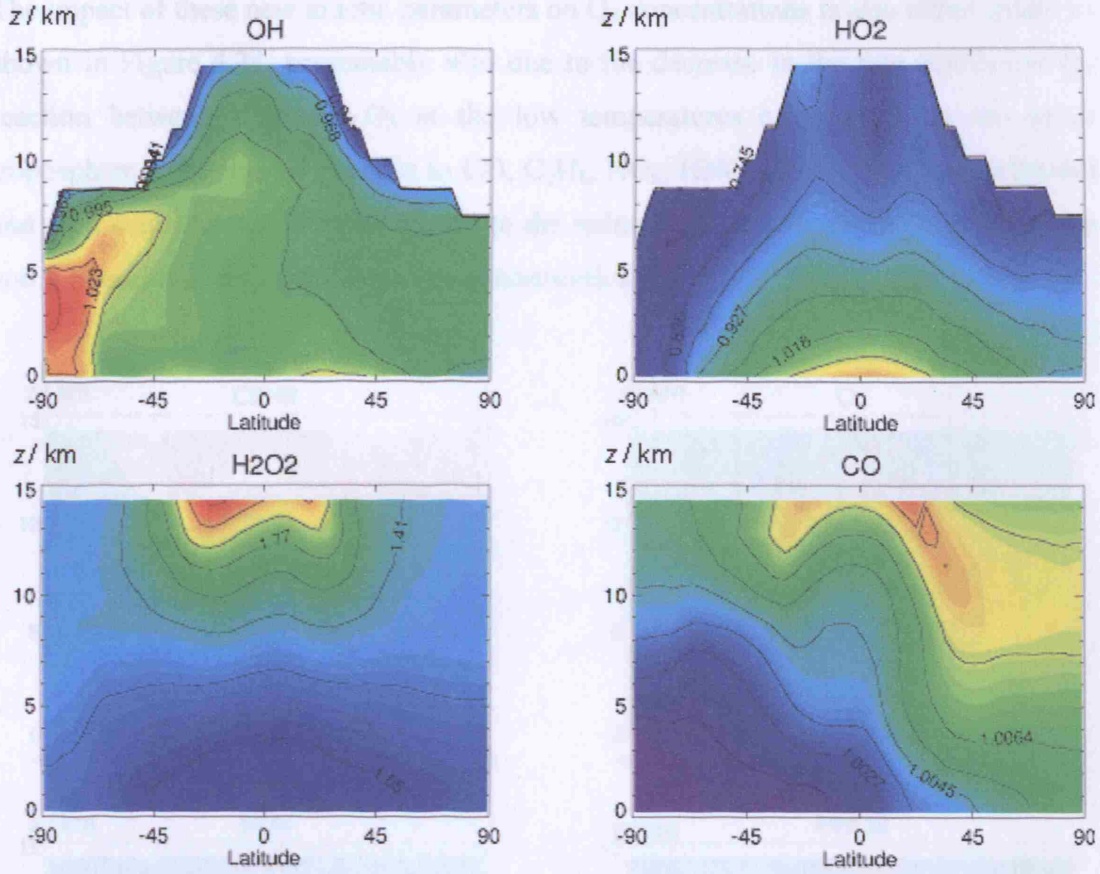

Figure 4.33 : Relative changes in the modelled concentrations of several important atmospheric species on changing the model value of $k_{4.8}$ from that currently recommended[4] to that determined in this work. Results are presented as a function of altitude and latitude.

As would be expected from the change in $k_{4.8}$ in the model, the modelled HO_2 and H_2O_2 concentrations show the most significant changes, with the greatest difference observed in the upper troposphere. The effects on OH concentrations are somewhat limited, even in the upper troposphere. This perhaps surprising result, given that OH and HO_2 are coupled in the troposphere, may reflect a reduction in coupling between OH and HO_2 in this region of the atmosphere. Reduced coupling between OH and HO_2 in the upper troposphere occurs largely due to a decrease in the rate of reaction between HO_2 and O_3 at low temperatures. The decrease in the rate of reaction (4.7) is a direct result of the activation energy for the reaction (E_a = + 490 J mol^{-1}),[4] causing OH production from HO_2 to become less efficient in the upper troposphere.

$$HO_2 + O_3 \rightarrow OH + 2\,O_2 \qquad (4.7)$$

The impact of these new kinetic parameters on O_3 concentrations is also rather small, as shown in Figure 4.34, presumably also due to the decrease in the rate coefficient for reaction between HO_2 and O_3 at the low temperatures experienced in the upper troposphere. The limited changes to CO, C_2H_6, NO_x, HNO_3, DMS (dimethyl sulphide) and total sulphate can all be attributed to the reduction in $k_{4.8}$ in the upper troposphere and the resulting small effects on OH concentrations.

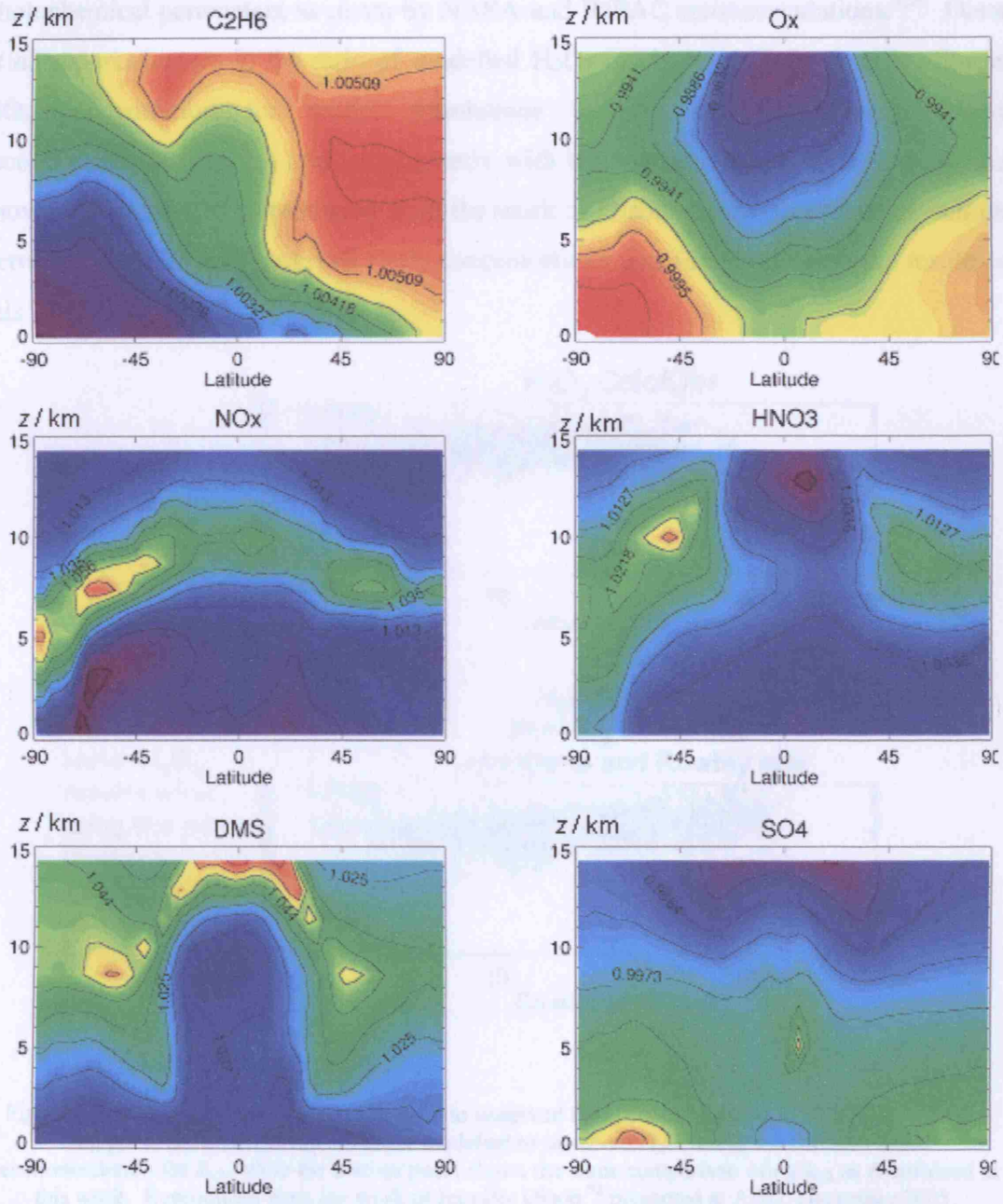

Figure 4.34 : Relative changes in the modelled concentrations of several important atmospheric species on changing the model value of $k_{4.8}$ from that currently recommended[4] to that determined in this work. DMS refers to dimethyl sulphide and SO_4 to total sulphate. Results are presented as a function of altitude and latitude.

In addition to the model simulations described above, the results of this work have been used by Olson *et al.*,[52,53] NASA Langley, to compare atmospheric observations to modelled concentrations of a number of species. Observations were made during the Intercontinental Chemical Transport Experiment (INTEX) campaign in 2004 off the east coast of the North American continent using the NASA DC8 aircraft. The model used in this case was a time dependent photochemical box model, using kinetic and photochemical parameters as given by NASA and IUPAC recommendations.[4,54] Olson *et al.* report changes in the ratio of modelled H_2O_2 to observed H_2O_2 as a function of NO_x concentration for model simulations initially conducted using current recommendations for $k_{4.8}$ and subsequently with the values reported in this work. As shown in Figure 4.35, reproduced from the work of Olson *et al.*,[52] improved agreement between modelled and observed H_2O_2 concentrations was found on using the results of this work.

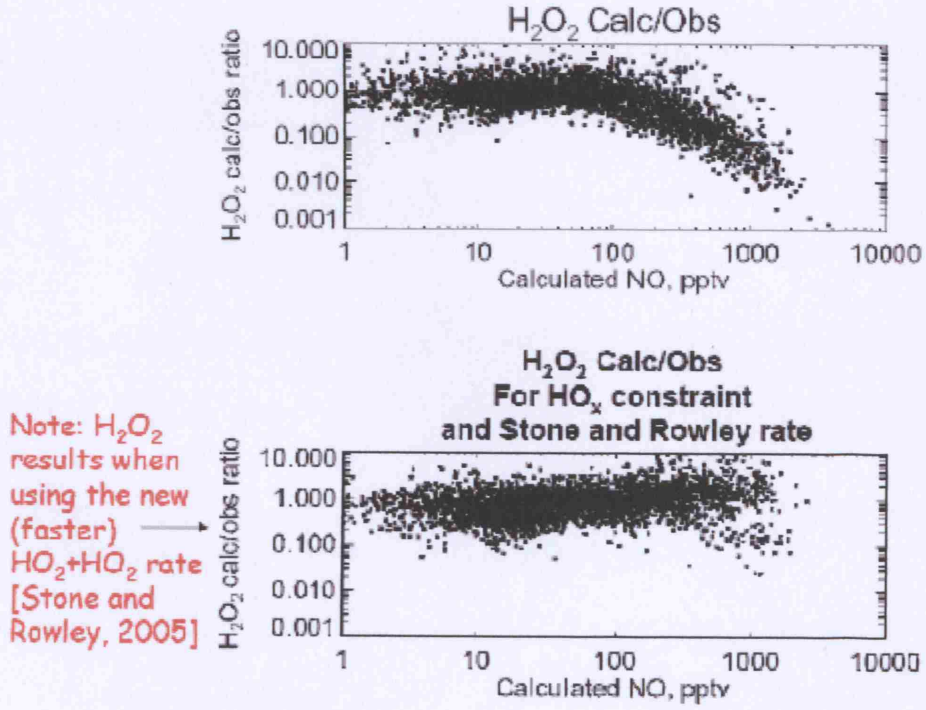

Figure 4.35 : Comaparison of modelled H_2O_2 to observed H_2O_2 concentrations as a function of [NO]. Top panel shows the comparison for modelled to observed H_2O_2 using the current NASA recommendation for $k_{4.8}$, while the bottom panel shows the same comparison using $k_{4.8}$ as determined in this work. Reproduced from the work of Jennifer Olson,[52] presented at AGU, December 2005.

4.10 Conclusions

The rate coefficient for the HO_2 self-reaction, $k_{4.8}$, has been determined over a wide range of conditions of temperature, pressure and water vapour concentration pertinent to the troposphere. Flash photolysis of $Cl_2/CH_3OH/O_2$ mixtures was used to produce HO_2 radicals in the gas phase, necessitating investigation of the effects of methanol vapour concentration on $k_{4.8}$.

This work reports a stronger temperature dependence of $k_{4.8}$ than has been observed in previous studies, and a greater enhancement in $k_{4.8}$ with water vapour at low temperature. The strong temperature dependence of the methanol vapour enhancement of $k_{4.8}$ recently described by Christensen *et al.*[14,32] is not in agreement with this work, although a degree of methanol enhancement has been observed and characterised.

4.11 References

[1] R.P. Wayne, *Chemistry of Atmospheres*, Third edition, **2000**, Oxford University Press

[2] G. P. Brasseur, J. J. Orlando, G. S. Tyndall, *Atmospheric Chemistry and Global Climate Change*, **1999**, Oxford University Press

[3] D. E. Heard and M. J. Pilling, *Chem. Rev.*, **2003**, 103, 5163

[4] S. P. Sander, R. R. Friedl, D. M. Golden, M. J. Kurylo, R. E. Huie, V. L. Orkin, G. K. Moortgat, A. R. Ravishankara, C. E. Kolb and M. J. Molina, *Chemical Kinetics and Photochemical Data for Use in Atmospheric Studies*, **2002**, Evaluation Number 14, JPL Publication 02-25, Jet Propulsion Laboratory, Pasadena, CA., USA

[5] E. J. Hamilton Jr., *J. Phys. Chem.*, **1975**, 63, 3682

[6] E. J. Hamilton Jr. and R. R. Lii, *Int. J. Chem. Kinet.*, **1977**, 9, 875

[7] R. R. Lii, R. A. Gorse Jr., M. C. Sauer Jr., S. Gordon, *J. Phys. Chem.*, **1980**, 84, 813

[8] R. R. Lii, M. C. Sauer Jr., S. Gordon, *J. Phys. Chem.*, **1981**, 85, 2833

[9] R. A. Cox and J. P. Burrows, *J. Phys. Chem.*, **1979**, 83, 2560

[10] S.P. Sander, M. Peterson, R. T. Watson, R. P. Patrick, *J. Phys. Chem.*, **1982**, 86, 1236

[11] C. C. Kircher and S. P. Sander, *J. Phys. Chem.*, **1984**, 88, 2082

[12] B. Y. Andersson, R. A. Cox, M. E. Jenkin, *Int. J. Chem. Kinet.*, **1988**, 20, 283

[13] W. J. Bloss, D. M. Rowley, R. A. Cox, R. L. Jones, *Phys. Chem. Chem. Phys.*, **2002**, 4, 3639

[14] L.E. Christensen, M. Okumura, S. P. Sander, R. J. Salawitch, G. C. Toon, B. Sen, J. F. Blavier and K. W. Jucks, *Geophys. Res. Lett.*, **2002**, 29, 9

[15] R. R. Lii, R. A. Gorse Jr., M. C. Sauer Jr., S. Gordon, *J. Phys. Chem.*, **1979**, 83, 1803

[16] G. A. Takacs and C. J. Howard, *J. Phys. Chem.*, **1986**, 90, 687

[17] B. A. Thrush and G. S. Tyndall, *Chem. Phys. Lett.*, **1982**, 92, 232

[18] H. Niki, P.D.Maker, C.M. Savage, L.P.Brittenbach, *Chem. Phys. Lett.*, **1980**, 73, 43

[19] R. Simonaitis and J. Heicklein, *J. Phys. Chem.*, **1982**, 86, 3416

[20] M. J. Kurylo, P. A. Ouellette, A. H. Laufer, *J. Phys. Chem.*, **1986**, 90, 437

[21] P. D. Lightfoot, B. Veyret, R. Lesclaux, *J. Phys. Chem.*, **1990**, 94, 708

[22] C.J. Hochanadel, J.A. Ghormley, P.J. Ogren, *J. Chem. Phys.*, **1972**, 56, 4429

[23] E. J. Hamilton Jr. and C. A. Naleway, *J. Phys. Chem.*, **1976**, 80, 2037

[24] B. Nelander, *J. Phys. Chem. A*, **1997**, 101, 9092

[25] S. Aloisio and J. S. Francisco, *J. Phys. Chem. A*, **1998**, 102, 1899

[26] S. D. Belair, S. Kais, J. S. Francisco, *Mol. Phys.*, **2002**, 100, 247

[27] G. Lendvay, *Z. Phys. Chem.*, **2001**, 215, 377

[28] S. A. Aloisio, J. S. Francisco, R. R. Friedl, *J. Phys. Chem. A*, **2000**, 104, 6597

[29] N. Kanno, K. Tonokura, A. Tezaki, M. Koshi, *J. Phys. Chem. A*, **2005**, 109, 3153

[30] N. Kanno, K. Tonokura, M. Koshi, in press

[31] M. Mozurkewich and S.W. Benson, *Int. J. Chem. Kinet.*, **1985**, 17, 787

[32] L.E. Christensen, M. Okumura, J.C. Hansen, S.P. Sander, J.S. Francisco, *J. Phys. Chem. A*, **2006**, 110, 6948

[33] G.S. Tyndall, T.J. Wallington, M.D. Hurley, W.F. Schneider, *J. Phys. Chem.*, **1997**, 97, 1576

[34] P. Pagsberg, J. Munk, A. Sillesen, C. Anastasi, *Chem. Phys. Lett.*, **1988**, 146, 375

[35] W. Tsang, *J. Phys. Chem. Ref. Data*, **1987**, 16, 471

[36] D. Maric, J.N. Crowley, J.P. Burrows, *J. Phys. Chem. A*, **1997**, 101, 2561

[37] P.D. Lightfoot and A.A. Jemi-Alade, *J. Photochem. Photobiol. A:Chem.*, **1991**, 59, 1

[38] M. M. Maricq and J. J. Szente, *J. Phys. Chem.*, **1994**, 98, 2078

[39] D. Stone and D.M. Rowley, *Phys. Chem. Chem. Phys.*, **2005**, 7, 2156

[40] T.T. Paukert and H.S. Johnstone, *J. Chem. Phys.*, **1972**, 56, 6, 2824

[41] C.J. Hochanadel, T.J. Sworski, P.J. Ogren, *J. Phys. Chem.*, **1980**, 84, 3274

[42] P.D.Lightfoot, B. Veyret, R. Lesclaux, *Chem. Phys. Lett.*, **1988**, 150, 120

[43] J.N. Crowley, F.G. Simon, J.P. Burrows, G.K. Moortgat, M.E. Jenkin, R.A. Cox, *J. Photochem. Photobiol. A:Chem.*, **1991**, 60, 1

[44] J. Sehested, T. Mogelberg, K. Fagersrtom, G, Mahmoud, T.J. Wallington, *Int. J. Chem. Kinet.*, **1997**, 29, 673

[45] R. Patrick and M. J. Pilling, *Chem. Phys. Lett.*, **1982**, 91, 343

[46] O. Dobis and S. W. Benson, *J. Am. Chem. Soc.*, **1993**, 115, 8798

[47] B.A. Thrush and J.P.T. Wilkinson, *Chem. Phys. Lett.*, **1979**, 66, 441

[48] S. P. Sander, *J. Phys. Chem.*, **1984**, 88, 6018

[49] R. Zhu and M. C. Lin, *Phys. Chem. Comm.*, **2001**, 23, 1

[50] Geos-Chem, Harvard Univerisity, http://www-as.harvard.edu/chemistry/trop/geos/

[51] M. Evans, Institute for Atmospheric Science, School of Earth and the Environment, University of Leeds, personal communication

[52] J.R. Olson, J. Crawford, G. Chen, M. Pippin, AGU December 2005, Poster A43C-0072

[53] J.R. Olson, NASA Langley Research Center, personal communication

[54] R. Atkinson, D. L. Baulch, R. A. Cox, J. N. Crowley, R. F. Hampson, R. G. Hynes, M. E. Jenkin, M. J. Rossi, J. Troe, *Evaluated kinetic and photochemical data for atmospheric chemistry: Volume I - gas phase reactions of O_x, HO_x, NO_x and SO_x species, Atmos. Chem. Phys.*, **2004**, 4, 1461

Chapter 5
The Methylperoxy Self-Reaction

5.1 Introduction

The methylperoxy radical, CH_3O_2, is an important intermediate in combustion chemistry and atmospheric oxidation processes. Production of CH_3O_2 in the troposphere is primarily instigated by the OH initiated oxidation of methane:

$$OH + CH_4 \rightarrow CH_3 + H_2O \quad (5.1)$$

$$CH_3 + O_2 + M \rightarrow CH_3O_2 + M \quad (5.2)$$

While CH_3O_2 radicals do self-react:

$$CH_3O_2 + CH_3O_2 \rightarrow \text{Products} \quad (5.3)$$

the principal atmospheric reaction pathway in the absence of NO_x is reaction with HO_2:[1,2]

$$HO_2 + CH_3O_2 \rightarrow CH_3OOH + O_2 \quad (5.4)$$

The highly soluble methyl hydroperoxide product, CH_3OOH, experiences a similar fate in the atmosphere to hydrogen peroxide, and is readily removed from the lower troposphere during precipitation.

In the presence of NO_x, a major reaction of CH_3O_2, and indeed all organic peroxy radicals, is that with NO:

$$CH_3O_2 + NO \rightarrow CH_3O + NO_2 \quad (5.5)$$

Production of CH_3O leads to generation of HO_2 through the rapid reaction of CH_3O with O_2:[3,4]

$$CH_3O + O_2 \rightarrow HO_2 + HCHO \qquad (5.6)$$

and, as described previously, production and subsequent solar photolysis of NO_2 leads to regeneration of NO and formation of O_3, both of which are components of photochemical smog.[1,2]

$$NO_2 + h\nu \rightarrow NO + O \qquad (5.7)$$
$$O + O_2 + M \rightarrow O_3 + M \qquad (5.8)$$

Although the methylperoxy self-reaction is not generally considered to be of great atmospheric importance,[1,3] it does provide some competition to the reactions of CH_3O_2 with HO_2 and NO, and its inclusion in kinetic and photochemical models of the atmosphere is required if such models are to represent atmospheric composition with any accuracy. Furthermore, laboratory studies of methylperoxy radical chemistry often necessitate higher than typical atmospheric concentrations of CH_3O_2 in order to achieve suitable signal to noise ratios. At such CH_3O_2 concentrations the rate of the self-reaction, proportional to the square of the CH_3O_2 concentration, can become significant, and is therefore an essential factor in analysis of experiments conducted under such conditions.

5.2 Previous Work

Several methods have been developed for production of CH_3O_2 in the laboratory. Early studies of the methylperoxy self-reaction used photodissociation of azomethane, $CH_3N_2CH_3$, to produce methyl radicals, CH_3, which react rapidly with an excess of O_2 to produce CH_3O_2:[5,6,7,8,9]

$$CH_3N_2CH_3 + h\nu \rightarrow 2\,CH_3 + N_2 \qquad (5.9)$$
$$CH_3 + O_2 + M \rightarrow CH_3O_2 + M \qquad (5.2)$$

Subsequent studies, however, have generally favoured the photolysis of Cl_2 in the presence of methane and oxygen:[10-19]

$$Cl_2 + h\nu \rightarrow 2\,Cl \qquad (5.10)$$

$$Cl + CH_4 \rightarrow CH_3 + HCl \quad (5.11)$$

$$CH_3 + O_2 + M \rightarrow CH_3O_2 + M \quad (5.2)$$

Other methods for CH_3O_2 generation have also been investigated, involving O_2 photolysis at high temperatures ($T > 600$ K), and the subsequent reactions of O atoms with CH_4 to produce CH_3 radicals and reaction of the CH_3 radicals with O_2 to produce CH_3O_2.[20] Methyl iodide (CH_3I) photolysis[21] and methyl chloride (CH_3Cl) photolysis[22] have also been used to generate the CH_3 fragment, which is then reacted with excess O_2 to produce CH_3O_2. Photolysis of methyl iodide was used in a molecular modulation experiment,[21] and the presence of transient iodine containing species resulted in complications to the UV spectrum in the region of interest. Although methyl chloride was used primarily in a laser flash photolysis investigation of the kinetics of CH_3O_2 with other peroxy radicals, it was claimed that the kinetics of the methylperoxy self-reaction were also studied and compared favourably with previous studies. However, no kinetic data were reported for this reaction.[22]

Investigation of the methylperoxy self-reaction, using both molecular modulation techniques and flash photolysis with UV absorption spectroscopy, has shown the rate coefficient $k_{5.3}$ to exhibit a weak negative temperature dependence over the range 228 – 650 K.[13,16,19,20,21] The rate of reaction (5.3) therefore increases as the temperature decreases, in common with many radical-radical reactions. Ultraviolet absorption cross-sections for CH_3O_2 have been shown to be independent of temperature over the range 248 – 419 K investigated, and therefore do not contribute to the apparent temperature dependence of $k_{5.3}$.[3,19,23] In contrast to the rate coefficient for the hydroperoxy self-reaction, which has both pressure dependent and independent components,[4] the rate coefficient $k_{5.3}$ has been shown to be independent of pressure between 10 and 800 Torr at 298 K.[8,11-14,16,19,21]

Possible effects of water vapour on $k_{5.3}$ were first investigated by Sanhueza *et al.*[11] using flash photolysis of $Cl_2/CH_4/O_2$ mixtures with UV absorption spectroscopy, employing CH_3O_2 absorption cross-sections as determined by Hochanadel *et al.*[6] Sanhueza *et al.* did not observe any significant effects of H_2O on $k_{5.3}$. Subsequent studies by Kan and Calvert,[24] Kurylo *et al.*[15] and Lightfoot *et al.*[19] have also reported CH_3O_2 self-reaction

kinetics to be independent of water vapour concentration at 298 K, although Kan and Calvert did report a shift in the methylperoxy UV absorption spectrum towards higher wavelengths as the humidity was increased. The shift in CH_3O_2 absorption was attributed to complex formation between CH_3O_2 and H_2O, but such findings have not been replicated elsewhere.

The products of the CH_3O_2 self-reaction have been studied by several groups using FTIR spectroscopy, and all generally imply the presence of two main reaction channels:[25,26,27,28]

$$CH_3O_2 + CH_3O_2 \rightarrow 2\,CH_3O + O_2 \qquad (5.3a)$$

$$\rightarrow CH_3OH + HCHO + O_2 \qquad (5.3b)$$

A third, minor, reaction channel producing CH_3OOCH_3 has also been proposed by Weaver *et al.*[29] on the basis of an investigation of $CD_3N_2CD_3$ photooxidation, but its existence has been disputed by a number of others in direct product studies of reaction (5.3).[25-28]

$$CH_3O_2 + CH_3O_2 \rightarrow CH_3OOCH_3 + O_2 \qquad (5.3c)$$

Niki *et al.*[27] investigated the products of reaction (5.3) using FTIR spectroscopy at 297 K and noted that CH_3OOCH_3 is difficult to identify uniquely due to a lack of sharp, distinctive features in its IR absorption spectrum. Niki *et al.* did, however, place an upper limit of 0.08 on the branching ratio for channel (5.3c), with branching ratios of 0.32 for channel (5.3a) and 0.60 for channel (5.3b). Similarly, neither Kan *et al.*,[25] using gas phase FTIR spectroscopy, Tyndall *et al.*,[28] also employing gas phase FTIR, nor Horie *et al.*,[26] using matrix isolation techniques, found any evidence for production of CH_3OOCH_3 within their detection limits. Kan *et al.* and Tyndall *et al.* did, however, place upper limits of 0.08 and 0.06 respectively to the branching ratio for channel (5.3c) at ambient temperature.

Introduction of the non-terminating channel (5.3a) to the reaction mechanism results in complication of the kinetics for the CH_3O_2 self-reaction as observed in the laboratory.[19]

The methoxy radical, CH_3O, produced in the non-terminating channel (5.3a) reacts rapidly with excess oxygen usually present in the system to produce HO_2 radicals in reaction (5.6), each of which can subsequently consume a further CH_3O_2 radical in reaction (5.4):

$$CH_3O + O_2 \rightarrow HO_2 + HCHO \qquad (5.6)$$

$$CH_3O_2 + HO_2 \rightarrow CH_3OOH + O_2 \qquad (5.4)$$

Given that O_2 is usually present in excess in laboratory studies of CH_3O_2, and that the cross-reaction (5.4) between CH_3O_2 and HO_2 is rapid, application of the steady state approximation to CH_3O and HO_2 reveals that the observed rate coefficient for CH_3O_2 decay, k_{obs}, is enhanced relative to the true rate coefficient, $k_{5.3}$. The enhancement, which does not result in deviation from second order kinetics, is by a factor of $(1+\beta)$, where β is the branching ratio for the non-terminating channel (5.3a):

$$k_{obs} = (1 + \beta)\, k_{5.3}$$

This can be shown as follows, by considering reactions (5.3a), (5.3b), (5.6) and (5.4):

$$CH_3O_2 + CH_3O_2 \rightarrow 2\,CH_3O + O_2 \qquad (5.3a)$$

$$\rightarrow CH_3OH + HCHO + O_2 \qquad (5.3b)$$

$$CH_3O + O_2 \rightarrow HO_2 + HCHO \qquad (5.6)$$

$$CH_3O_2 + HO_2 \rightarrow CH_3OOH + O_2 \qquad (5.4)$$

$$\frac{-d[CH_3O_2]}{dt} = 2(k_{5.3a} + k_{5.3b})[CH_3O_2]^2 + k_{5.4}[CH_3O_2][HO_2] \qquad (5.i)$$

$$\frac{+d[HO_2]}{dt} = k_{5.6}[CH_3O][O_2] - k_{5.4}[CH_3O_2][HO_2] = 0 \quad (SSA) \qquad (5.ii)$$

$$\frac{+d[CH_3O]}{dt} = 2k_{5.3a}[CH_3O_2]^2 - k_{5.6}[CH_3O][O_2] = 0 \quad (SSA) \qquad (5.\ iii)$$

From (5.ii)

$$k_{5.4}[CH_3O_2][HO_2]=k_{5.6}[CH_3O][O_2] \qquad (5.iv)$$

From (5.iii)

$$2k_{5.3a}[CH_3O_2]^2=k_{5.6}[CH_3O][O_2] \qquad (5.v)$$

Combining (5.iv) and (5.v) gives

$$2k_{5.3a}[CH_3O_2]^2=k_{5.4}[CH_3O_2][HO_2] \qquad (5.vi)$$

and substituting (5.vi) into (5.i) gives an overall expression for the rate of CH_3O_2 loss:

$$\begin{aligned}\frac{-d[CH_3O_2]}{dt} &= 2(k_{5.3a}+k_{5.3b})[CH_3O_2]^2+2k_{5.3a}[CH_3O_2]^2 \\ &= 2(2k_{5.3a}+k_{5.3b})[CH_3O_2]^2\end{aligned} \qquad (5.\ vii)$$

Therefore

$$\begin{aligned}k_{obs} &= k_{5.3a}+2k_{5.3b} \\ &= k_{5.3}+k_{5.3b} \\ &= k_{5.3}(1+\beta)\end{aligned} \qquad (5.\ viii)$$

since, by definition, $k_{5.3} = k_{5.3a} + k_{5.3b}$ and $k_{5.3a} = \beta k_{5.3}$.

The effect of the non-terminating reaction channel (5.3a) on the observed kinetics of CH_3O_2 must therefore be accounted for in the analysis of any investigation of methylperoxy radical self-reaction kinetics in systems where O_2 is in excess.

The aims of this work are to characterise the kinetics of the methylperoxy self-reaction under experimental conditions pertinent to both atmospheric chemistry and laboratory

studies of other methylperoxy radical chemistry, in particular the hydroperoxy-methylperoxy cross-reaction discussed in Chapter 6.

5.3 Radical Generation

Methylperoxy radicals were generated by laser flash photolysis of gas mixtures of $CH_3Cl/CH_4/O_2/N_2$, referred to below as the 'methyl chloride' system, or $Cl_2/CH_4/O_2/N_2$, referred to as the 'chlorine' system.

5.3.1 Methyl Chloride System

Laser flash photolysis of methyl chloride at 193 nm in the presence of methane and oxygen resulted in production of methylperoxy radicals through reactions (5.12), (5.11) and (5.2):

$$CH_3Cl + h\nu \rightarrow CH_3 + Cl \quad (\lambda = 193 \text{ nm}) \quad (5.12)$$

$$Cl + CH_4 \rightarrow CH_3 + HCl \quad (5.11)$$

$$CH_3 + O_2 + M \rightarrow CH_3O_2 + M \quad (5.2)$$

Although precursor gas concentrations were maintained sufficiently high to ensure rapid radical production with respect to radical decay, in practice it was necessary to limit CH_3Cl and O_2 concentrations. High methyl chloride concentrations ($[CH_3Cl] > 4.0 \times 10^{17}$ cm^{-3}) would have resulted in the generation of significant radical concentration gradients along the length of the reaction cell due to gradients in the amount of laser radiation absorbed by CH_3Cl. At lower CH_3Cl concentrations the amount of laser radiation absorbed is more uniform along the length of the cell and CH_3O_2 concentration gradients are minimised. Oxygen concentrations were constrained in order to minimise ozone production resulting from O_2 photolysis at 193 nm, and subsequent combination of O atoms with O_2:

$$O_2 + h\nu \rightarrow 2\,O \quad (\lambda = 193 \text{ nm}) \quad (5.13)$$

$$O_2 + O + M \rightarrow O_3 + M \quad (5.14)$$

To determine optimum experimental conditions, a simple photolysis model, employing absorption cross-sections for CH_3Cl and O_2 at 193 nm ($\sigma_{CH_3Cl} = 7.08\times10^{-20}$ cm^2; $\sigma_{O_2} = 1.07\times10^{-23}$ cm^2)[4,30] was constructed to determine optimum concentrations of CH_3Cl and O_2 in the reaction mixture. Absorption of laser radiation along the reaction cell was calculated along the length of the cell and initial concentrations of CH_3O_2 and O_3 calculated, assuming all CH_3 radicals and O atoms reacted exclusively with excess O_2. Current recommendations[4] for $k_{5.3}$ were used to simulate the CH_3O_2 decay in different sections along the cell, and the average 'line of sight' CH_3O_2 decay along the length of the entire cell was analysed in a classical second order kinetic model. The rate coefficient determined from the model for the average CH_3O_2 decay along the cell was compared to the current recommendation in order to ensure small concentration gradients in CH_3O_2 would not significantly affect the observed kinetics, as shown in Figure 5.1.

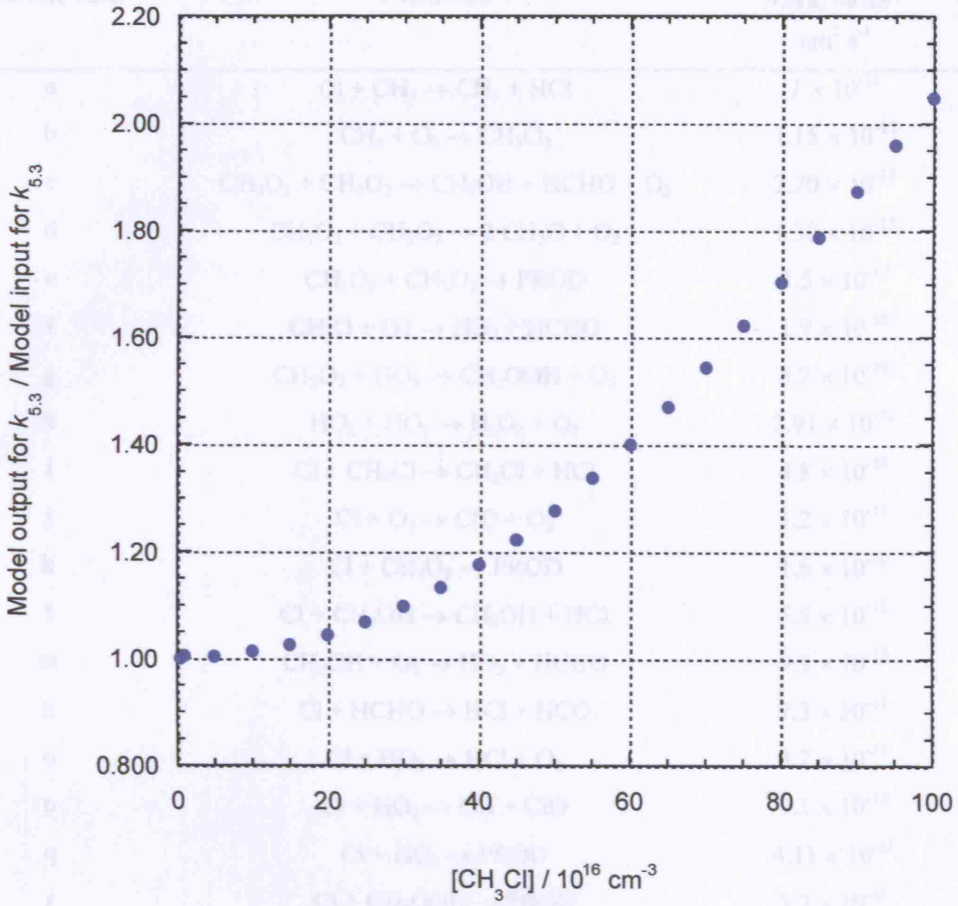

Figure 5.1 : Ratio of modelled output for $k_{5.3}$ to the model input for $k_{5.3}$ as a function of CH_3Cl concentration. The model was used to determine the effects of changing the $[CH_3Cl]$ on the optical depth of the reaction cell, and the subsequent effects on modelled $[CH_3O_2]_0$ and $k_{5.3}$.

Whilst the initial analysis designed conditions to preclude concentration gradients of CH_3O_2 radicals, the numerical integration package FACSIMILE was subsequently used to develop a complete chemical model of the reaction system containing all the known potential chemistry in the system. Details of the reactions and rate coefficients entered into the model are given in Table 5.1.

Reaction label	Reaction	$k_{298\ K,\ 760\ Torr}$ / $cm^3\ s^{-1}$	Reference
a	$Cl + CH_4 \rightarrow CH_3 + HCl$	1×10^{-13}	4
b	$CH_3 + O_2 \rightarrow CH_3O_2$	1.15×10^{-12}	4
c	$CH_3O_2 + CH_3O_2 \rightarrow CH_3OH + HCHO + O_2$	2.20×10^{-13}	4
d	$CH_3O_2 + CH_3O_2 \rightarrow 2\ CH_3O + O_2$	1.30×10^{-13}	4
e	$CH_3O_2 + CH_3O_2 \rightarrow PROD$	3.5×10^{-13}	4
f	$CH_3O + O2 \rightarrow HO_2 + HCHO$	1.9×10^{-15}	4
g	$CH_3O_2 + HO_2 \rightarrow CH_3OOH + O_2$	5.2×10^{-12}	4
h	$HO_2 + HO_2 \rightarrow H_2O_2 + O_2$	2.91×10^{-12}	4
i	$Cl + CH_3Cl \rightarrow CH_2Cl + HCl$	4.8×10^{-13}	4
j	$Cl + O_3 \rightarrow ClO + O_2$	1.2×10^{-11}	4
k	$Cl + CH_3O_2 \rightarrow PROD$	1.6×10^{-10}	4
l	$Cl + CH_3OH \rightarrow CH_2OH + HCl$	5.5×10^{-11}	4
m	$CH_2OH + O_2 \rightarrow HO_2 + HCHO$	9.1×10^{-12}	4
n	$Cl + HCHO \rightarrow HCl + HCO$	7.3×10^{-11}	4
o	$Cl + HO_2 \rightarrow HCl + O_2$	3.2×10^{-11}	4
p	$Cl + HO_2 \rightarrow OH + ClO$	9.1×10^{-12}	4
q	$Cl + HO_2 \rightarrow PROD$	4.11×10^{-11}	4
r	$Cl + CH_3OOH \rightarrow PROD$	5.7×10^{-11}	4
s	$Cl + H_2O_2 \rightarrow HCl + HO_2$	4.1×10^{-13}	4
t	$O_3 + CH_3 \rightarrow PROD$	2.6×10^{-12}	4
u	$O_3 + CH_3O_2 \rightarrow PROD$	1×10^{-17}	4
v	$O_3 + HO_2 \rightarrow OH + 2\ O_2$	1.9×10^{-15}	4
w	$HO_2 + HCHO \rightarrow ADDUCT$	5×10^{-14}	4
x	$CH_2Cl + CH_2Cl \rightarrow CH_2ClCH_2Cl$	2.8×10^{-11}	31
y	$CH_2Cl + O_2 \rightarrow ClCH_2O_2$	2.25×10^{-12}	4
z	$ClCH_2O_2 + CH_3O_2 \rightarrow PROD$	2.5×10^{-12}	22
a'	$ClCH_2O_2 + HO_2 \rightarrow PROD$	5.2×10^{-12}	4
b'	$ClCH_2O_2 + ClCH_2O_2 \rightarrow PROD$	3.3×10^{-12}	32

Table 5.1 : Reactions included in the sensitivity analysis for $k_{5,3}$ using the methyl chloride system. Where reactions are shown as having more than possible reaction channel, reactions c and d for example, the sensitivity analysis has been conducted on each individual channel separately, and then on the total rate coefficient for the reaction, with products not identified in the model. The model did not simultaneously include the total rate coefficient and each individual reaction channel, for example, the model either included reactions c and d, but not e, or e, but not c and d.

The model was used to determine the optimum initial reagent concentrations for CH_3O_2 production, and a sensitivity analysis was performed on each reaction in the model to

explore possible effects of secondary chemistry on the observed kinetics. The sensitivity analysis was conducted using the method as described for the HO_2 self-reaction in section 4.3, Chapter 4. Briefly, each rate coefficient in the model was sequentially halved and doubled, and a second order kinetic model fitted to the model output to determine the rate coefficient for CH_3O_2 decay. The rate coefficient for CH_3O_2 decay was subsequently compared to the rate coefficient for the reaction (5.3) entered into the model. Results from the sensitivity analysis are displayed in Figure 5.2.

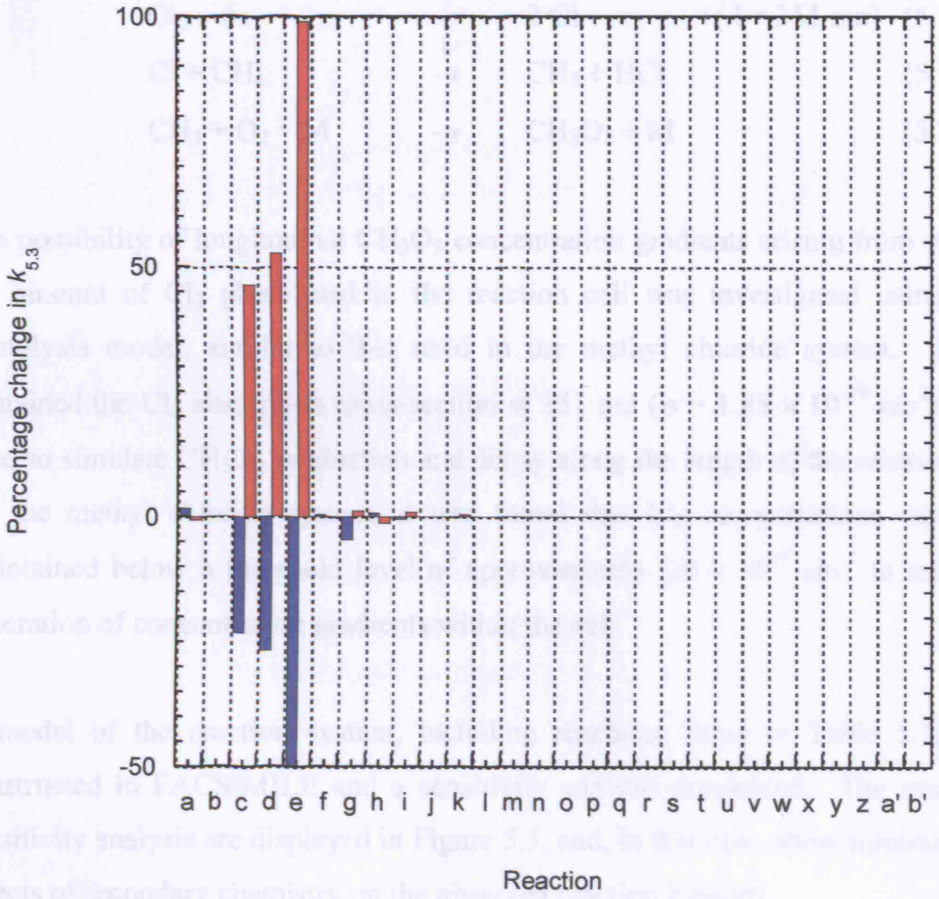

Figure 5.2 : Sensitivity analysis for the CH_3O_2 self-reaction using the methyl chloride system. Effect on $k_{5.3}$ of halving (blue) and doubling (red) the given secondary rate coefficient. Reaction labels refer to those displayed in Table 5.1.

The sensitivity analysis was used to determine optimum reagent concentrations for investigation of the CH_3O_2 self-reaction, placing an upper limit of 5 % on the deviation between the rate coefficient for reaction (5.3) entered into the model and that fitted to the model output. Reagents and concentrations used were CH_3Cl (10 % in N_2, BOC)

$(2.36 - 36.3) \times 10^{16}$ cm^{-3}, CH_4 (99.99 %, BOC) $(2.29 - 11.0) \times 10^{18}$ cm^{-3}, O_2 (99.99 %, BOC) $(1.12 - 2.27) \times 10^{18}$ cm^{-3} and N_2 (99.99 %, BOC) to balance. All reagents were used as supplied.

5.3.2 Chlorine System

Methylperoxy radicals were generated in the chlorine system by the 351 nm laser flash photolysis of molecular chlorine in the presence of excess methane and oxygen:

$Cl_2 + h\nu$	$\rightarrow$	2 Cl	($\lambda = 351$ nm)	(5.10)
$Cl + CH_4$	$\rightarrow$	$CH_3 + HCl$		(5.11)
$CH_3 + O_2 + M$	$\rightarrow$	$CH_3O_2 + M$		(5.2)

The possibility of longitudinal CH_3O_2 concentration gradients arising from gradients in the amount of Cl_2 photolysed in the reaction cell was investigated using a simple photolysis model, similar to that used in the methyl chloride system. The model contained the Cl_2 absorption cross-section at 351 nm ($\sigma = 1.85 \times 10^{-19}$ cm^2)[33] and was used to simulate CH_3O_2 production and decay along the length of the reaction cell. As for the methyl chloride system, it was found that Cl_2 concentrations needed to be maintained below a threshold level of approximately 1.0×10^{17} cm^{-3} to minimise the generation of concentration gradients within the cell.

A model of the reaction system, including reactions listed in Table 5.2, was also constructed in FACSIMILE and a sensitivity analysis conducted. The results of the sensitivity analysis are displayed in Figure 5.3, and, in this case, show minimal expected effects of secondary chemistry on the observed reaction kinetics.

Reaction label	Reaction	$k_{298\ K,\ 760\ Torr}$ / $cm^3\ s^{-1}$	Reference
a	$Cl + CH_4 \rightarrow CH_3 + HCl$	1×10^{-13}	4
b	$CH_3 + O_2 \rightarrow CH_3O_2$	1.15×10^{-12}	4
c	$CH_3O_2 + CH_3O_2 \rightarrow CH_3OH + HCHO + O_2$	2.20×10^{-13}	4
d	$CH_3O_2 + CH_3O_2 \rightarrow 2\ CH_3O + O_2$	1.30×10^{-13}	4
e	$CH_3O + O_2 \rightarrow HO_2 + HCHO$	1.9×10^{-15}	4
f	$HO_2 + CH_3O_2 \rightarrow CH_3OOH + O_2$	5.2×10^{-12}	4
g	$HO_2 + HO_2 \rightarrow H_2O_2 + O_2$	2.91×10^{-12}	4
h	$Cl_2 + CH_3 \rightarrow CH_3Cl + Cl$	2.14×10^{-12}	34
i	$Cl + Cl \rightarrow Cl_2$	5.5×10^{-33}	35
j	$Cl + O_2 \rightarrow ClOO$	2.7×10^{-33}	4
k	$Cl + CH_3O_2 \rightarrow PROD$	1.6×10^{-10}	4
l	$Cl + CH_3OH \rightarrow CH_2OH + HCl$	5.5×10^{-11}	4
m	$Cl + HCHO \rightarrow HCl + HCO$	7.3×10^{-11}	4
n	$Cl + HO_2 \rightarrow HCl + O_2$	3.2×10^{-11}	4
o	$Cl + HO_2 \rightarrow OH + ClO$	9.1×10^{-12}	4
p	$Cl + CH_3OOH \rightarrow PROD$	5.7×10^{-11}	4
q	$Cl + H_2O_2 \rightarrow HCl + HO_2$	4.1×10^{-13}	4
r	$CH_3 + CH_3O_2 \rightarrow CH_3O + CH_3O$	4×10^{-11}	36
s	$CH_3 + HCl \rightarrow CH_4 + Cl$	3×10^{-14}	37
t	$CH_3 + H_2O_2 \rightarrow CH_4 + HO_2$	5.5×10^{-14}	36
u	$CH_3 + CH_3O \rightarrow HCHO + CH_4$	2×10^{-11}	36
v	$CH_3 + CH_3O \rightarrow CH_3OCH_3$	4×10^{-11}	36
w	$CH_3 + HO_2 \rightarrow CH_4 + O_2$	6×10^{-12}	36
x	$CH_3 + HO_2 \rightarrow OH + CH_3O$	3×10^{-11}	36
y	$CH_3O_2 + CH_3O \rightarrow PROD$	2.6×10^{-12}	38
z	$CH_2OH + O_2 \rightarrow HO_2 + HCHO$	9.1×10^{-12}	4
a'	$HO_2 + HCHO \rightarrow ADDUCT$	5×10^{-14}	4

Table 5.2 : Reactions included in the sensitivity analysis for $k_{5,3}$ using the chlorine system.

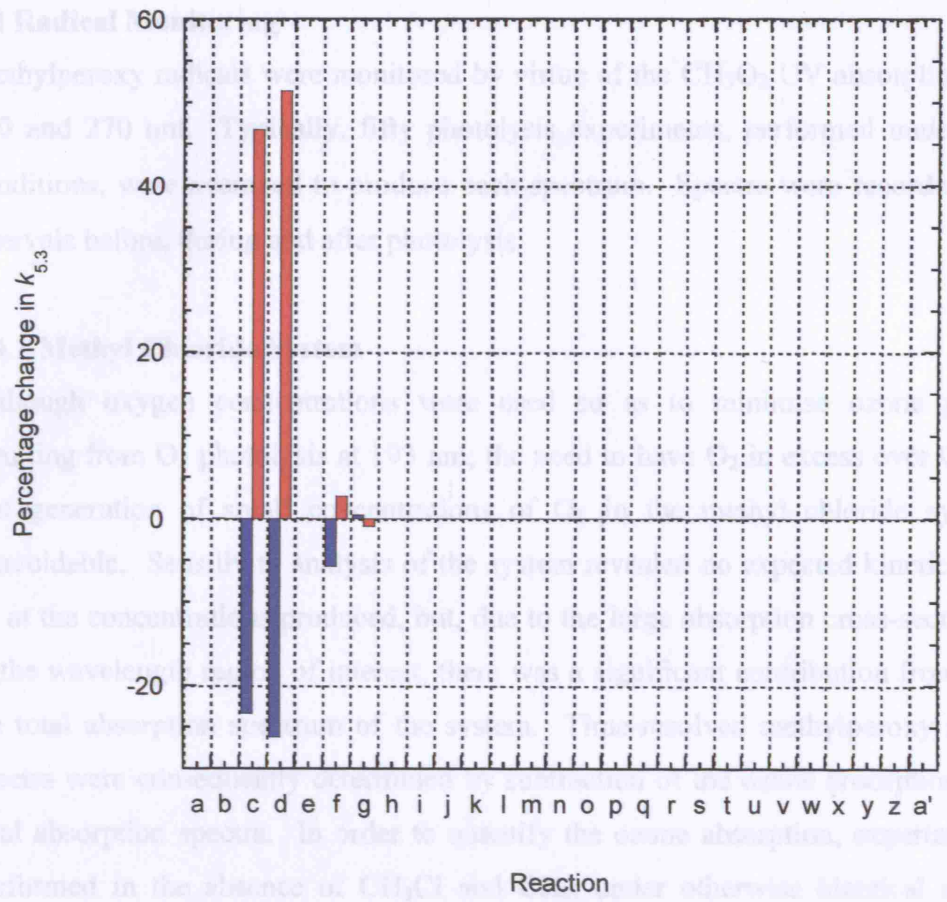

Figure 5.3 : Sensitivity analysis for the CH_3O_2 self-reaction using the chlorine system. Effect on $k_{5.3}$ of halving (blue) and doubling (red) the given secondary rate coefficient. Reaction labels refer to those displayed in Table 5.2.

Analogously to the conditions selected for use with the methyl chloride system, an upper limit of 5 % was placed on the deviation between the rate coefficient for reaction (5.3) entered into the model and that fitted to the model output after variation of a given secondary rate coefficient. Reagents and concentrations used were Cl_2 (5 % in N_2, BOC) (0.90 – 4.46) × 10^{16} cm^{-3}, CH_4 (99.99 %, BOC) (3.53 – 8.52) × 10^{18} cm^{-3}, O_2 (99.99 %, BOC) (1.12 – 2.27) × 10^{18} cm^{-3} and N_2 (99.99 %, BOC) to balance. All reagents were used as supplied.

In both the methyl chloride and the chlorine systems reagent concentrations were designed such that CH_3O_2 radicals were produced at a much greater rate than that of their decay.

5.4 Radical Monitoring

Methylperoxy radicals were monitored by virtue of the CH_3O_2 UV absorption between 210 and 270 nm. Typically, fifty photolysis experiments, performed under identical conditions, were averaged to produce each spectrum. Spectra were recorded at 50 μs intervals before, during and after photolysis.

5.4.1 Methyl Chloride System

Although oxygen concentrations were used so as to minimise ozone production resulting from O_2 photolysis at 193 nm, the need to have O_2 in excess over CH_3 meant that generation of small concentrations of O_3 in the methyl chloride system was unavoidable. Sensitivity analysis of the system revealed no expected kinetic effects of O_3 at the concentrations produced, but, due to the large absorption cross-sections of O_3 in the wavelength region of interest, there was a significant contribution from ozone to the total absorption spectrum of the system. Time-resolved methylperoxy absorption spectra were consequently determined by subtraction of the ozone absorption from the total absorption spectra. In order to quantify the ozone absorption, experiments were performed in the absence of CH_3Cl and CH_4, under otherwise identical conditions, immediately prior to the experiments in the presence of CH_3Cl and CH_4. Absorbances were calculated from experimental intensities using Beer's Law. A typical ozone spectrum, normalised to the recommended maximum absorption cross-section ($\sigma = 1.17 \times 10^{-18}$ cm^2) at 253.6 nm,[4] is shown in Figure 5.4. Variation of the maximum O_3 absorbance, recorded in the first 2.5 ms after the laser pulse, with O_2 concentration in the reaction cell was also investigated, and is shown in Figure 5.5.

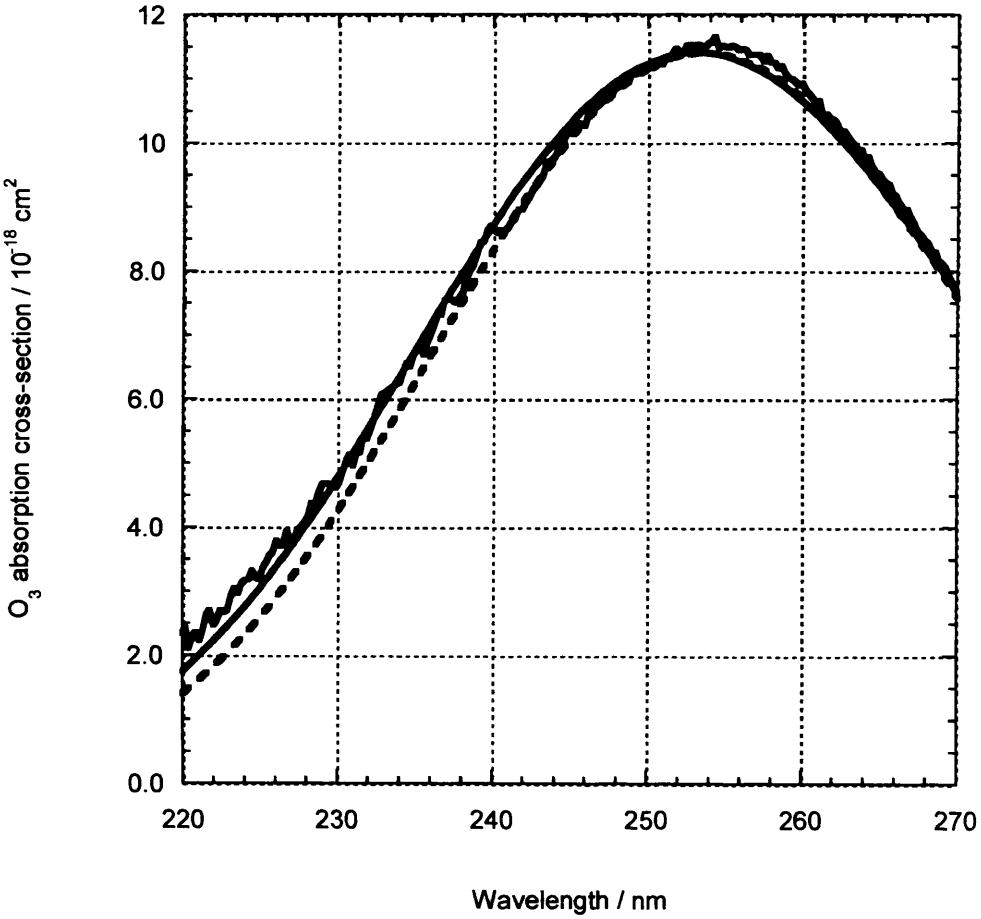

Figure 5.4 : Gaussian fit (red) to experimental O_3 absorbance recorded in first 2.5 ms following photolysis (blue). Normalised to maximum recommended[4] absorption cross-section (broken black line).

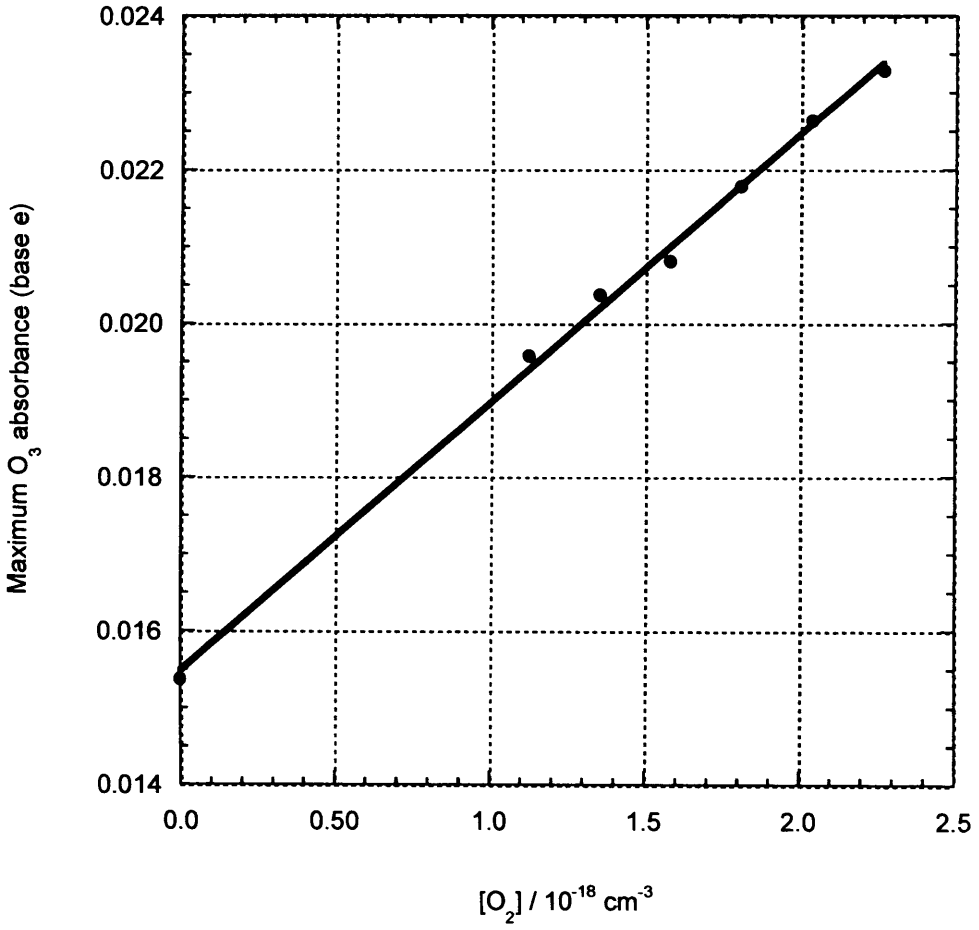

Figure 5.5 : Maximum O_3 absorbance (base e) as a function of initial O_2 concentration in the reaction cell (blue) with fit to data (red).

Taking into account the contribution of ozone to the observed absorption spectra required consideration of several factors. First, some ozone was produced even with $[O_2] = 0$ cm^{-3} within the cell. This was attributed to extracellular ozone formed in the laboratory, from photolysis of atmospheric O_2, along the path of the laser beam within the optical path of the analysing UV beam. Second, the slight change in optical depth of the reaction system on addition of CH_3Cl, CH_4, and, where applicable, H_2O, was calculated using absorption cross-sections of O_2, CH_3Cl and H_2O at 193 nm.[4,30,39] The ozone absorption over and above the intercept, $[O_2]_{cell} = 0$ cm^{-3}, absorption recorded in the absence of CH_3Cl and CH_4 in the first 2.5 ms after the laser pulse was then scaled appropriately to account for the change in optical depth. The O_3 absorbance was then subtracted from the total absorption recorded in the presence of CH_3Cl and CH_4 in the first 2.5 ms after the laser pulse to yield the CH_3O_2 absorption spectrum. A typical

CH_3O_2 spectrum, normalised to the recommended maximum absorption cross-section $(4.26 \times 10^{-18}\ cm^2)^4$ is displayed in Figure 5.6.

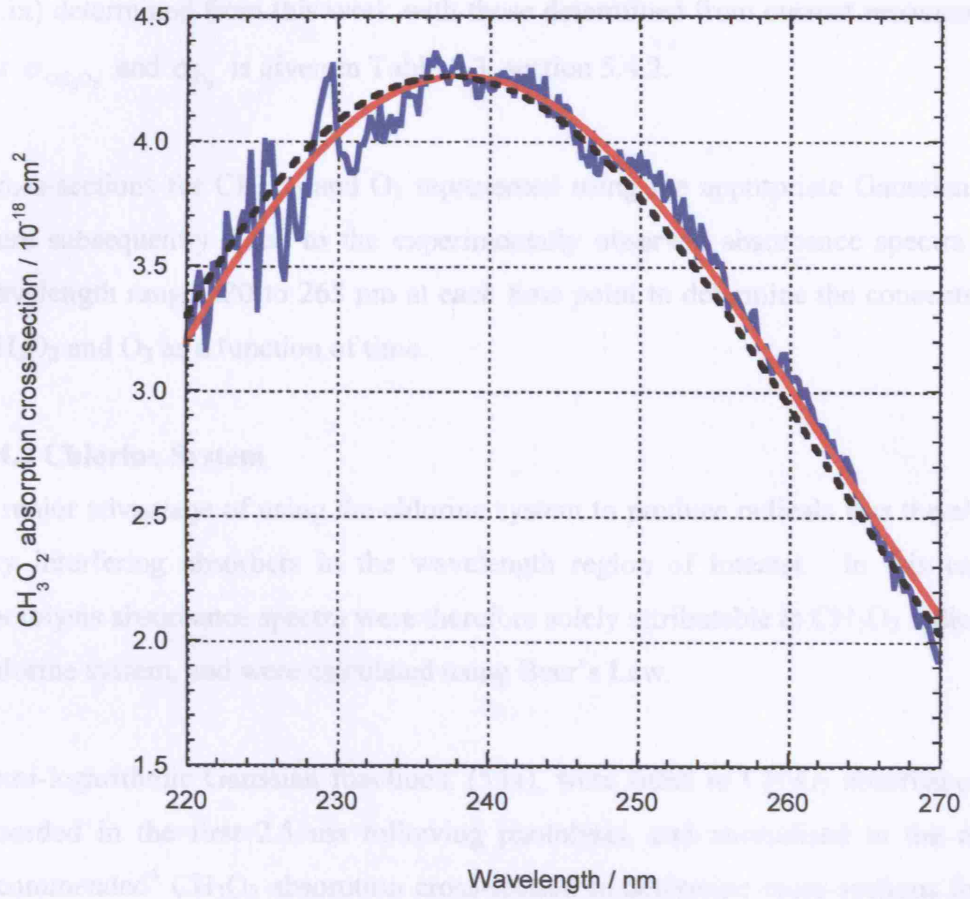

Figure 5.6 : Gaussian fit (red) to experimental CH_3O_2 absorbance recorded in first 2.5 ms following photolysis (blue). Normalised to maximum recommended[4] absorption cross-section (broken black line).

In order to generate absorption cross-sections at each wavelength point in the experiment, semi-logarithmic Gaussian functions were least squares fitted to the normalised CH_3O_2 and O_3 experimental spectra. As discussed for HO_2 (Chapter 4), this function has been shown to be a good representation of alkylperoxy UV absorption spectra.[40]

$$\sigma_\lambda = \sigma_{max} \exp\left\{-W\left[\ln\left(\frac{\lambda_{max}}{\lambda}\right)\right]^2\right\} \qquad (5.ix)$$

Here, σ_λ is the absorption cross-section at wavelength λ, σ_{max} the maximum absorption cross-section, W the width parameter, λ_{max} the wavelength at which maximum absorption occurs and λ the wavelength of interest. A comparison of the parameters in (5.ix) determined from this work with those determined from current recommendations for $\sigma_{CH_3O_2}$ and σ_{O_3} is given in Table 5.3, section 5.4.2.

Cross-sections for CH_3O_2 and O_3 represented using the appropriate Gaussian function were subsequently fitted to the experimentally observed absorbance spectra over the wavelength range 220 to 265 nm at each time point to determine the concentrations of CH_3O_2 and O_3 as a function of time.

5.4.2 Chlorine System

A major advantage of using the chlorine system to produce radicals was the absence of any interfering absorbers in the wavelength region of interest. In this case, post-photolysis absorbance spectra were therefore solely attributable to CH_3O_2 radicals in the chlorine system, and were calculated using Beer's Law.

Semi-logarithmic Gaussian functions, (5.ix), were fitted to CH_3O_2 absorbance spectra recorded in the first 2.5 ms following photolysis, and normalised to the maximum recommended[4] CH_3O_2 absorption cross-section to determine cross-sections for CH_3O_2 on the relevant experimental wavelength grid. A typical fit is given in Figure 5.7. A comparison between recommended parameters for (5.ix) and those determined in this work is made in Table 5.3. The normalised CH_3O_2 spectrum from the CH_3Cl system is also shown in Figure 5.7 for comparison.

Parameterised absorption cross-sections were least squares fitted to the experimental absorbance spectra over the wavelength range 220 to 265 nm to determine the CH_3O_2 concentration at each time point in the experiment.

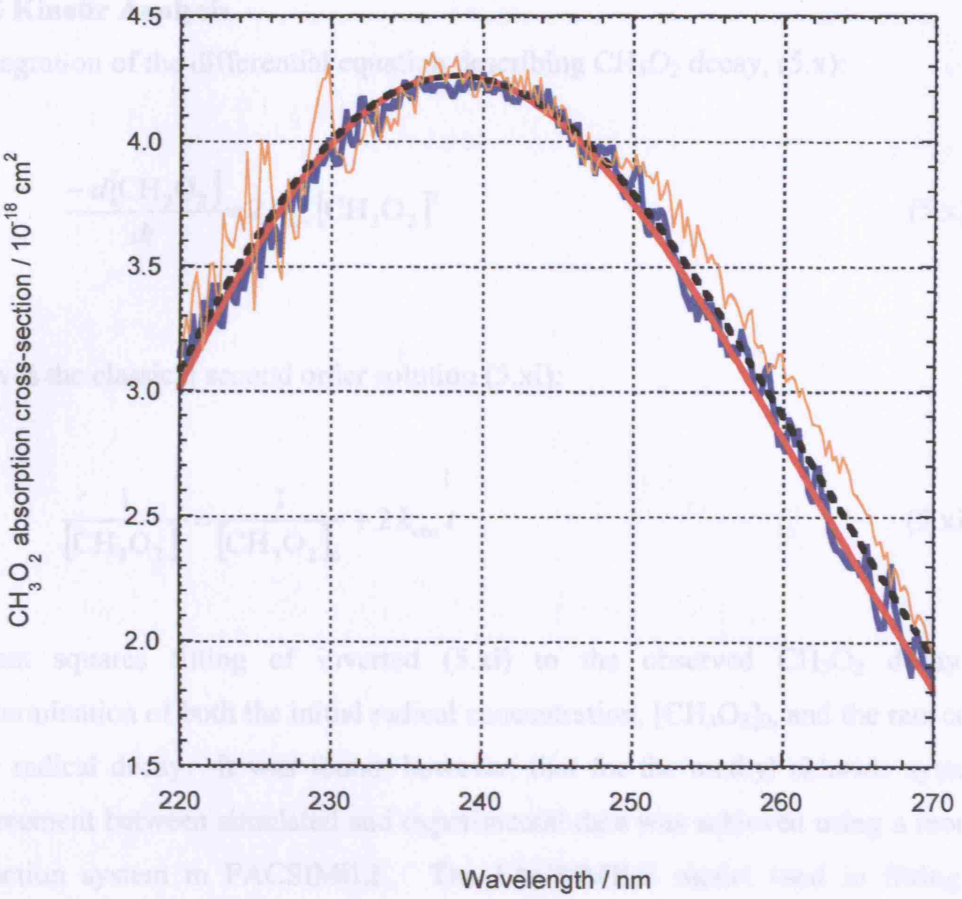

Figure 5.7 : Gaussian fit (red) to experimental CH_3O_2 absorbance recorded in first 2.5 ms following photolysis obtained using the chlorine system (blue). Results obtained from the methyl chloride system are shown in orange. All spectra have been normalised to the maximum recommended[4] absorption cross-section (broken black line).

Species (System)	σ / 10^{-18} cm^2	W	λ_{max} / nm
CH_3O_2 (CH_3Cl)	-	45.75 ± 6.30	238.90 ± 2.11
CH_3O_2 (Cl_2)	-	50.41 ± 5.16	237.36 ± 0.99
CH_3O_2 (NASA)[4]	4.26	44.46	237.31
O_3 (CH_3Cl)	-	96.36 ± 2.71	253.08 ± 0.44
O_3 (NASA)[4]	1.17	103.53	253.60

Table 5.3 : Summary of Gaussian parameters from both systems fitted to CH_3O_2 and O_3 absorption spectra. Errors are 1σ and statistical only.

5.5 Kinetic Analysis

Integration of the differential equation describing CH_3O_2 decay, (5.x):

$$\frac{-d[CH_3O_2]}{dt} = 2k_{obs}[CH_3O_2]^2 \qquad (5.x)$$

Gives the classical second order solution (5.xi):

$$\frac{1}{[CH_3O_2]_t} = \frac{1}{[CH_3O_2]_0} + 2k_{obs}t \qquad (5.xi)$$

Least squares fitting of inverted (5.xi) to the observed CH_3O_2 decay enables determination of both the initial radical concentration, $[CH_3O_2]_0$, and the rate coefficient for radical decay. It was found, however, that for the methyl chloride system better agreement between simulated and experimental data was achieved using a model of the reaction system in FACSIMILE. The FACSIMILE model used in fitting $k_{5.3}$ and $[CH_3O_2]_0$ to the experimental data is as described in section 5.3.1, with the rate coefficient for the HO_2 self-reaction as determined in Chapter 4 of this work. For the chlorine system no significant difference between fitting the classical second order solution (5.xi) and fitting in FACSIMILE was observed. Furthermore, the signal to noise ratio for the Cl_2 system was typically better than that in the CH_3Cl system. Example fits for each reaction system are shown in Figures 5.8 and 5.9.

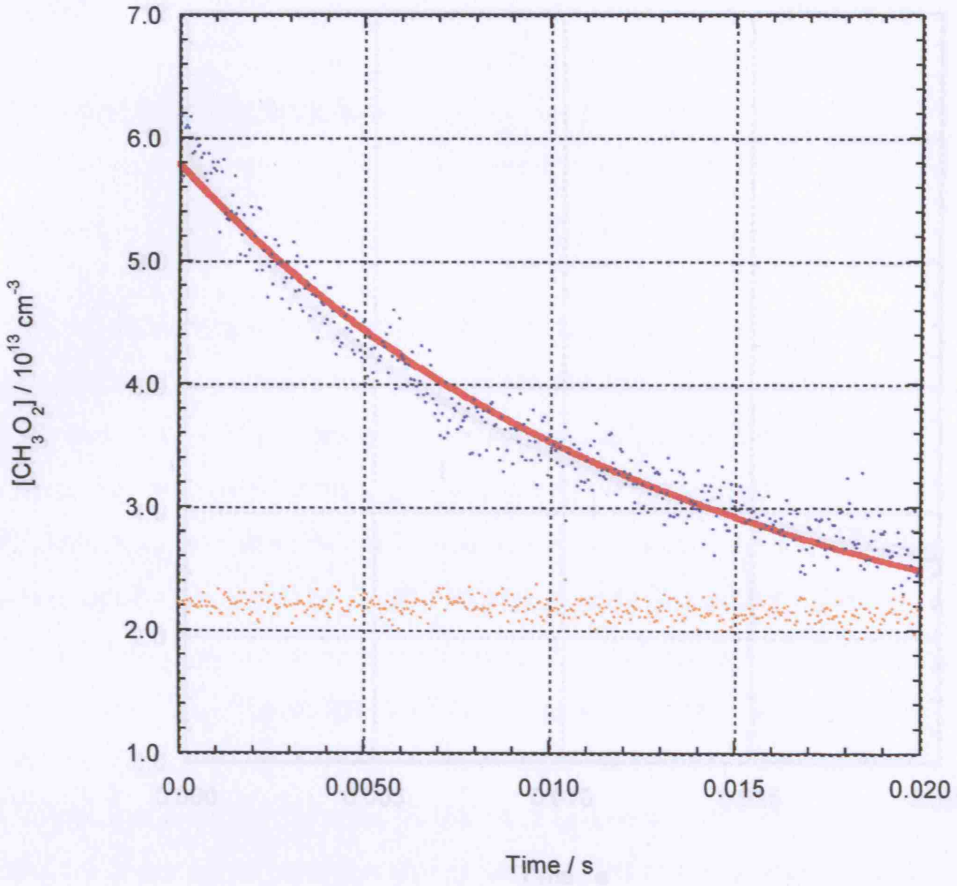

Figure 5.8 : Experimental CH_3O_2 (blue) and O_3 (orange) concentrations as a function of time using the methyl chloride system. The fit to the CH_3O_2 signal as determined by FACSIMILE is also shown (red).

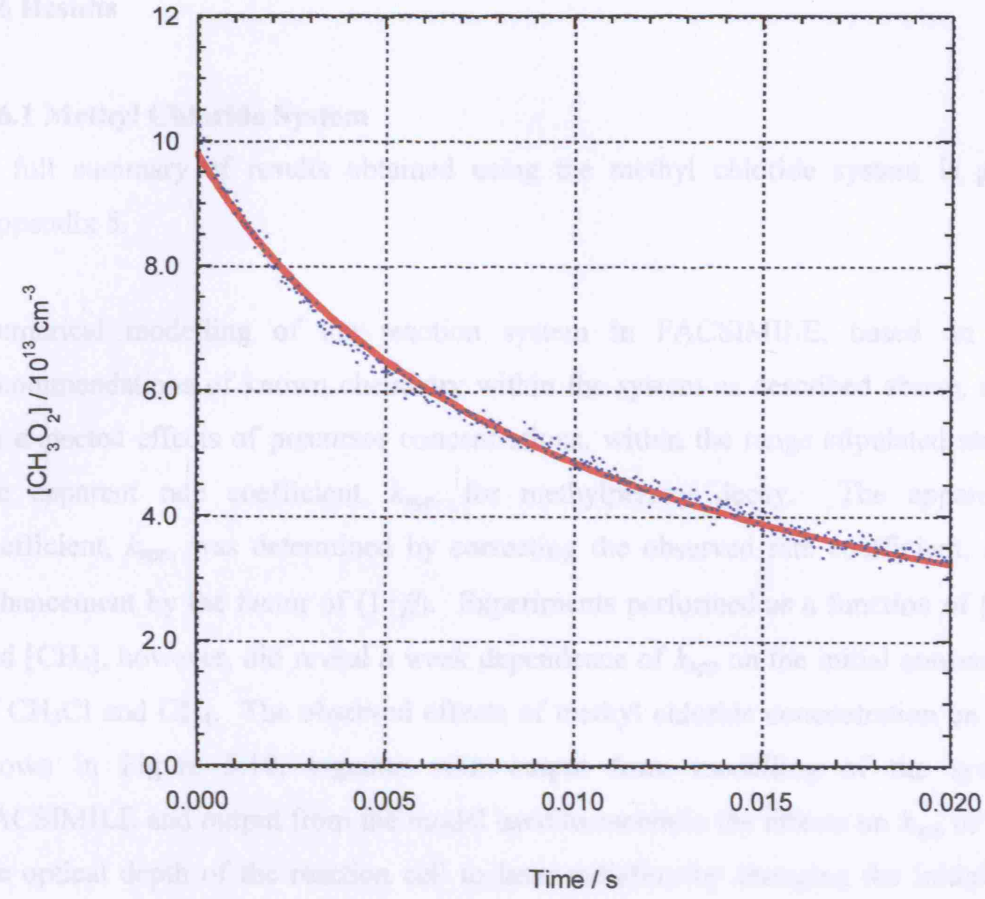

Figure 5.9 : Experimental CH_3O_2 concentrations as a function of time using the chlorine system (blue), with classical second order fit to the data (red).

As described in section 5.2, the observed rate coefficient for CH_3O_2 decay, in the presence of excess O_2, is enhanced by a factor $(1+\beta)$, where β is the branching ratio for CH_3O production in the CH_3O_2 self-reaction. This is due to the unavoidable production and subsequent reaction of HO_2 radicals in the reaction system:

$CH_3O_2 + CH_3O_2$	$\rightarrow$	$2\ CH_3O + O_2$	(5.3a)
	$\rightarrow$	$CH_3OH + HCHO + O_2$	(5.3b)
$CH_3O + O_2$	$\rightarrow$	$HO_2 + HCHO$	(5.2)
$CH_3O_2 + HO_2$	$\rightarrow$	$CH_3OOH + O_2$	(5.4)

Recommended values of β were applied to observed rate coefficients for CH_3O_2 decay to determine the true value for $k_{5.3}$.

5.6 Results

5.6.1 Methyl Chloride System

A full summary of results obtained using the methyl chloride system is given in Appendix 5.

Numerical modelling of the reaction system in FACSIMILE, based on current recommendations of known chemistry within the system as described above, revealed no expected effects of precursor concentrations, within the range stipulated above, on the apparent rate coefficient, k_{app}, for methylperoxy decay. The apparent rate coefficient, k_{app}, was determined by correcting the observed rate coefficient, k_{obs}, for enhancement by the factor of $(1+\beta)$. Experiments performed as a function of $[CH_3Cl]$ and $[CH_4]$, however, did reveal a weak dependence of k_{app} on the initial concentrations of CH_3Cl and CH_4. The observed effects of methyl chloride concentration on k_{app} are shown in Figure 5.10, together with output from modelling of the system in FACSIMILE and output from the model used to ascertain the effects on k_{app} of varying the optical depth of the reaction cell to laser radiation by changing the initial CH_3Cl concentration, as described above in section 5.3.1.

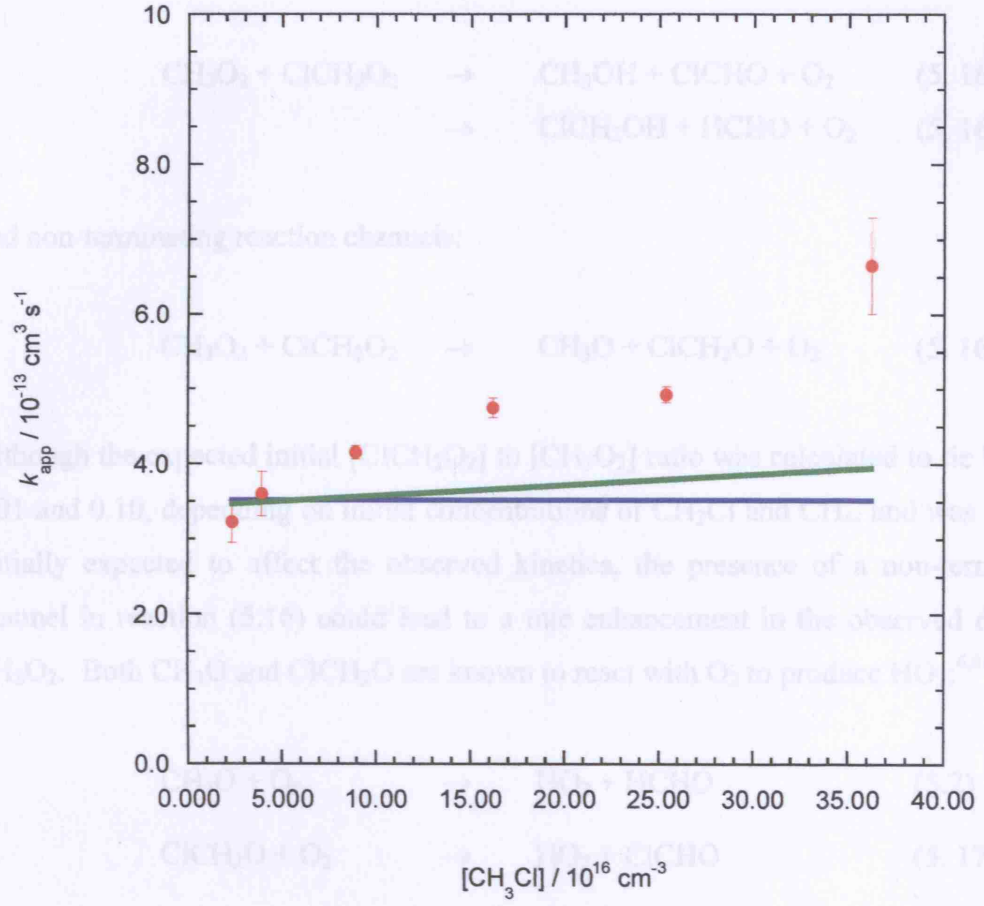

Figure 5.10 : Experimental (red) and modelled values of k_{app} as a function of initial CH_3Cl concentration. Results from the FACSIMILE model are given in blue, while those from the optical depth model are given in green. The rate coefficient k_{app} has been corrected for $(1+\beta)$ enhancement. Errors are 1σ and statistical only.

As can be seen in Figure 5.10, the effects of CH_3Cl on k_{app} cannot be explained by known chemistry occurring in the system, or by the effects of $[CH_3Cl]$ on the longitudinal concentration gradient of initially formed radicals in the reaction cell. On further inspection of the chemistry included in the FACSIMILE model, given in Table 5.1, it was proposed that the small fraction of Cl reacting with the parent molecule CH_3Cl, forming $ClCH_2$ and subsequently $ClCH_2O_2$ on reaction with excess O_2, would be followed by the reaction

$$CH_3O_2 + ClCH_2O_2 \rightarrow \text{Products} \qquad (5.15)$$

Reaction (5.15) may, analogously to $CH_3O_2 + CH_3O_2$, have both terminating:

$$CH_3O_2 + ClCH_2O_2 \rightarrow CH_3OH + ClCHO + O_2 \quad (5.16a)$$

$$\rightarrow ClCH_2OH + HCHO + O_2 \quad (5.16b)$$

and non-terminating reaction channels:

$$CH_3O_2 + ClCH_2O_2 \rightarrow CH_3O + ClCH_2O + O_2 \quad (5.16c)$$

Although the expected initial $[ClCH_2O_2]$ to $[CH_3O_2]$ ratio was calculated to lie between 0.01 and 0.10, depending on initial concentrations of CH_3Cl and CH_4, and was thus not initially expected to affect the observed kinetics, the presence of a non-terminating channel in reaction (5.16) could lead to a rate enhancement in the observed decay of CH_3O_2. Both CH_3O and $ClCH_2O$ are known to react with O_2 to produce HO_2:[4,41]

$$CH_3O + O_2 \rightarrow HO_2 + HCHO \quad (5.2)$$

$$ClCH_2O + O_2 \rightarrow HO_2 + ClCHO \quad (5.17)$$

The presence of HO_2 in the reaction system does indeed lead to an increase in the observed rate for CH_3O_2 decay, as discussed in section 5.2. The reaction system was subsequently modelled in FACSIMILE with the branching ratio for the non-terminating reaction channel set to its maximum possible value of 1.0. As shown in Figure 5.11, while the model does exhibit the same general trend as the observed results, it does not replicate them with any accuracy.

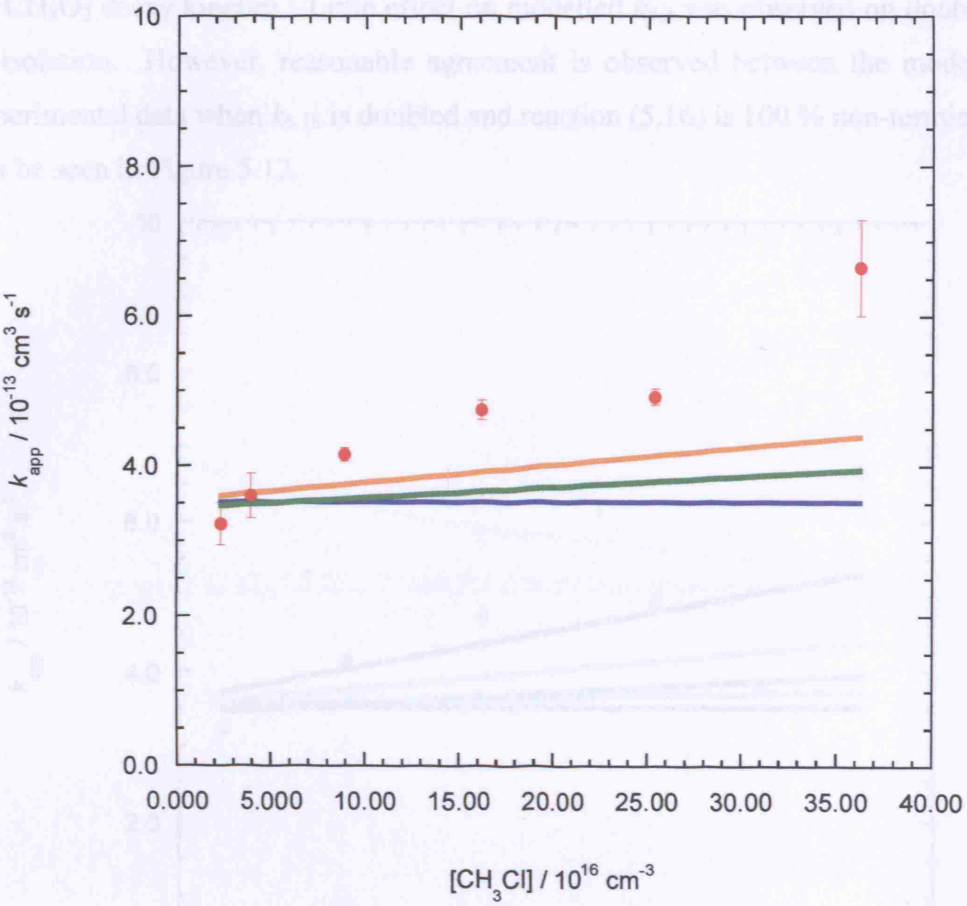

Figure 5.11 : Experimental (red) and modelled values of k_{app} as a function of initial CH_3Cl concentration. Modelled results are shown for FACSIMILE, with reaction (5.16) set to 0% non-terminating (blue) and 100% non-terminating (orange). Results from the optical depth model are given in green. The rate coefficient k_{app} has been corrected for $(1+\beta)$ enhancement. Errors are 1σ and statistical only.

There have been few studies of the kinetics of reaction (5.16),[4,22,33] and it is conceivable that $k_{5.16}$ is in fact greater than the value adopted in the model. In addition, the rate coefficient for reaction (5.18)

$$Cl + CH_3Cl \rightarrow CH_2Cl + HCl \qquad (5.18)$$

is relatively ill-defined in the literature – current recommendations,[4] as used in this work, are based on few previous investigations.[42,43,44] The current NASA recommendation[4] for $k_{5.18}$ is $\left(3.5^{+1.00}_{-0.58}\right) \times 10^{-11}$ cm^3 s^{-1}. An underestimation of $k_{5.18}$ in the model would lead to an underestimation of the amount of $ClCH_2O_2$ produced following photolysis of CH_3Cl, and hence an underestimation of the potential effects of $ClCH_2O_2$

on CH_3O_2 decay kinetics. Little effect on modelled $k_{5.3}$ was observed on doubling $k_{5.18}$ in isolation. However, reasonable agreement is observed between the modelled and experimental data when $k_{5.18}$ is doubled and reaction (5.16) is 100 % non-terminating, as can be seen in Figure 5.12.

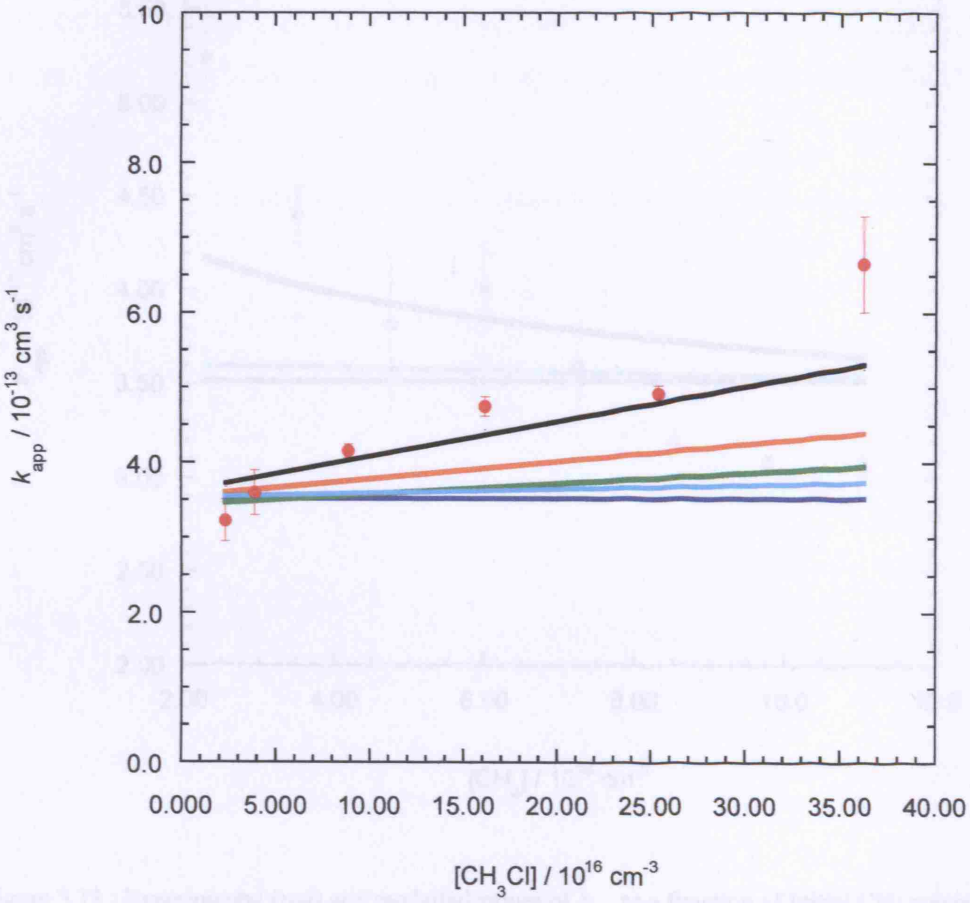

Figure 5.12 : Experimental (red) and modelled values of k_{app} as a function of initial CH_3Cl concentration. Modelled results are shown for FACSIMILE, with a literature value for $k_{5.18}$ and reaction (5.16) set to 0% non-terminating (blue) and 100% non-terminating (orange), and for FACSIMILE with $k_{5.18}$ set to double the literature value and reaction (5.16) set to 0% non-terminating (light blue) and 100% terminating (black). Results from the optical depth model are given in green. The rate coefficient k_{app} has been corrected for $(1+\beta)$ enhancement. Errors are 1σ and statistical only.

The relative amounts of $ClCH_2O_2$ and CH_3O_2 produced on photolysis is evidently dependent on the competition between CH_3Cl and CH_4 for available Cl atoms, and thus on the relative amounts of CH_3Cl and CH_4 in the system. If the effects of CH_3Cl concentration on k_{app} do result from uncertainty in $k_{5.18}$, or the branching ratio for reaction (5.16), or indeed both, then it might therefore be expected that k_{app} would also be affected by CH_4 concentration in an analogous fashion. Initial methane concentration was indeed observed to affect k_{app}, as shown in Figure 5.13, and the

general trend of k_{app} with [CH_4] is consistent with the arguments proposed to explain the effects of [CH_3Cl].

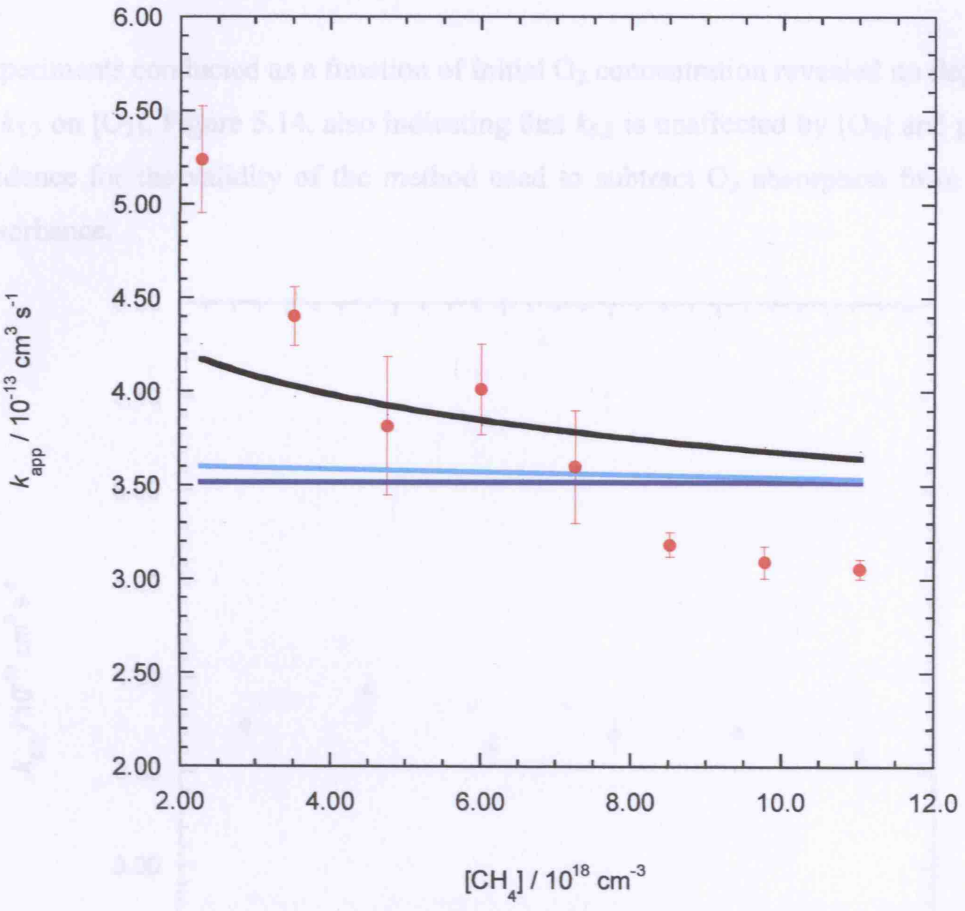

Figure 5.13 : Experimental (red) and modelled values of k_{app} as a function of initial CH_4 concentration. Modelled results are shown for FACSIMILE, with a literature value for $k_{5.18}$ and reaction (5.16) set to 0% non-terminating (blue) and with $k_{5.18}$ set to double the literature value and reaction (5.16) set to 0% non-terminating (light blue) and 100% terminating (black). The rate coefficient k_{app} has been corrected for $(1+\beta)$ enhancement. Errors are 1σ and statistical only.

Agreement between modelled and observed results, however, could not be achieved by variation of $k_{5.18}$, or the branching ratio for reaction (5.16), to the same extent as for the experiments as a function of CH_3Cl concentration, as shown in Figure 5.13. The production and fate of $ClCH_2O_2$ in this system clearly require further investigation to permit a full analysis of the effects of CH_3Cl and CH_4. It should be noted that the limiting value of $k_{5.3}$ at low CH_3Cl concentrations ($< 5 \times 10^{16}$ cm^{-3}) and at high CH_4 concentrations ($> 9 \times 10^{18}$ cm^{-3}) were comparable, *ca.* 3×10^{-13} cm^3 s^{-1}. In order to minimise secondary chemistry subsequent experiments with the CH_3Cl system were

conducted at low CH_3Cl concentration ($< 5 \times 10^{16}$ cm^{-3}) and high CH_4 concentration ($> 9 \times 10^{18}$ cm^{-3}).

Experiments conducted as a function of initial O_2 concentration revealed no dependence of $k_{5.3}$ on $[O_2]$, Figure 5.14, also indicating that $k_{5.3}$ is unaffected by $[O_3]$ and providing evidence for the validity of the method used to subtract O_3 absorption from the total absorbance.

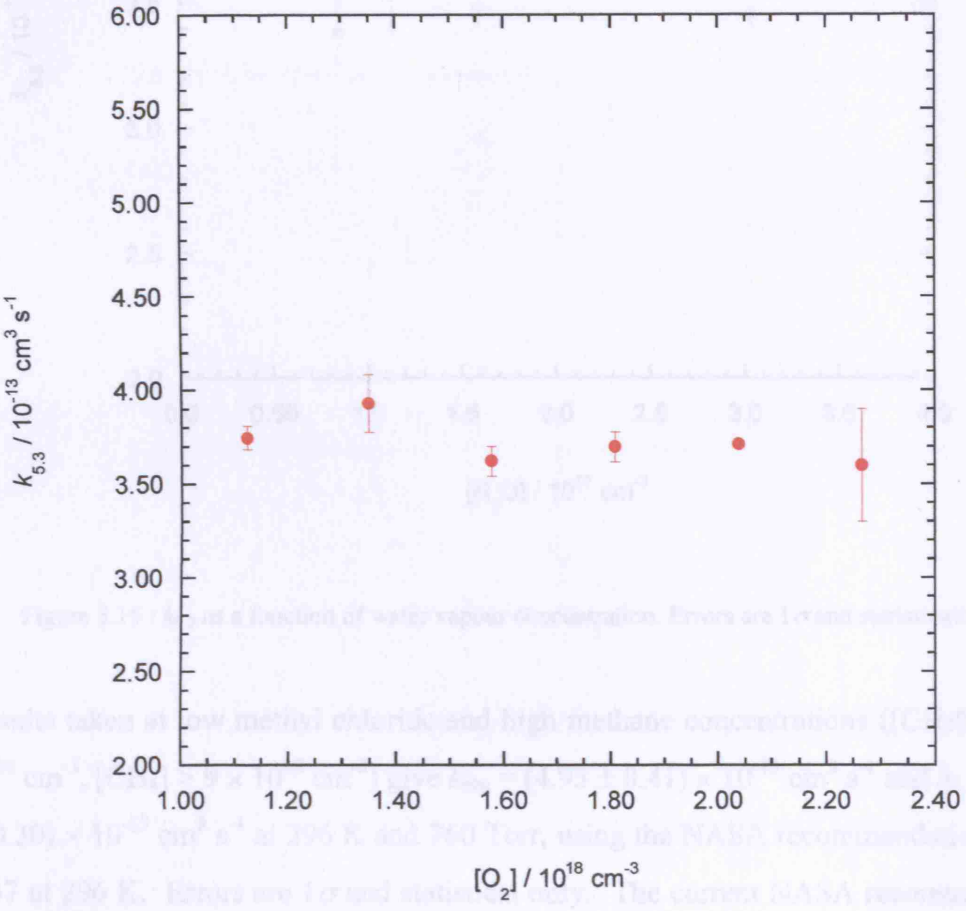

Figure 5.14 : $k_{5.3}$ as a function of initial O_2 concentration. Errors are 1σ and statistical only.

Addition of water vapour to the reaction mixture was also investigated in the range ($0 - 3.90$) $\times 10^{17}$ cm^{-3} at 296 K. No evidence was observed for effects of water vapour on methylperoxy self-reaction kinetics at 296 K, as shown in Figure 5.15, in contrast to the hydroperoxy self-reaction but in agreement with previous studies.[11,15,19,24] Furthermore, the shape and position of the methylperoxy UV absorbance spectrum were also unaffected by the presence of water vapour.

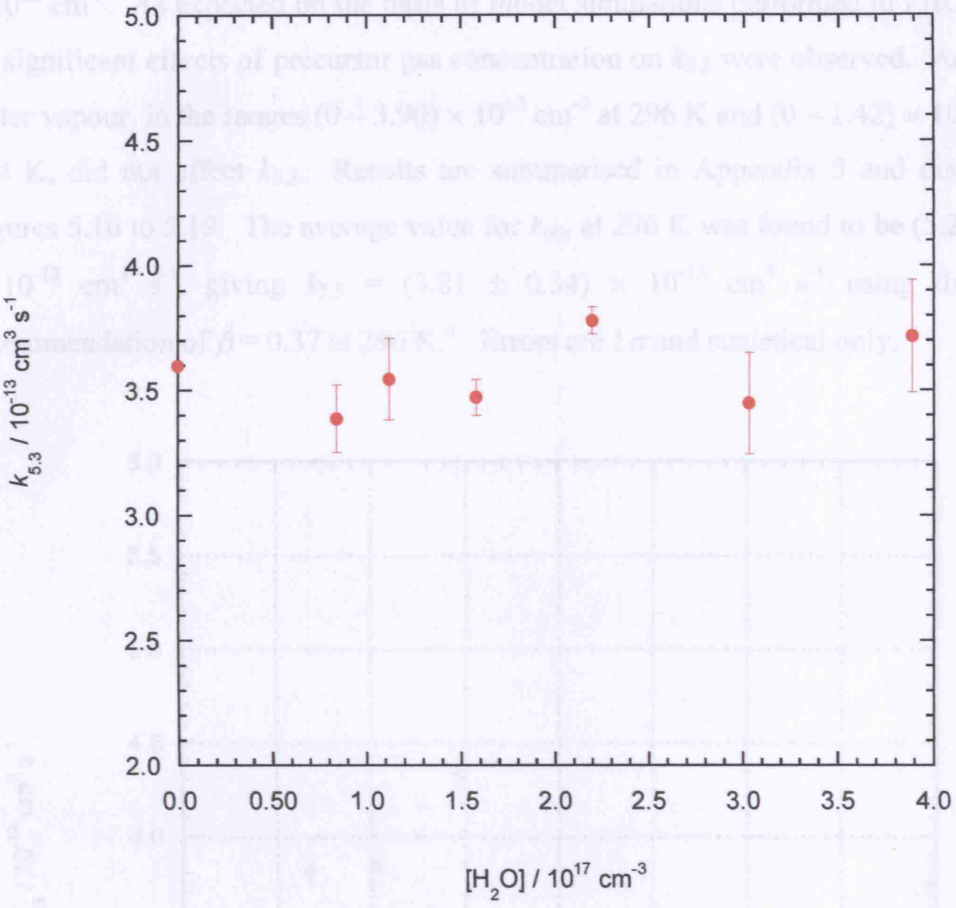

Figure 5.15 : $k_{5.3}$ as a function of water vapour concentration. Errors are 1σ and statistical only.

Results taken at low methyl chloride and high methane concentrations ([CH_3Cl] < 5 × 10^{16} cm^{-3}, [CH_4] > 9 × 10^{18} cm^{-3}) give k_{obs} = (4.93 ± 0.41) × 10^{-13} cm^3 s^{-1} and $k_{5.3}$ = (3.60 ± 0.30) × 10^{-13} cm^3 s^{-1} at 296 K and 760 Torr, using the NASA recommendation of β = 0.37 at 296 K. Errors are 1σ and statistical only. The current NASA recommendation for $k_{5.3}$ at 298 K is $\left(3.5^{+1.00}_{-0.58}\right)$ × 10^{-13} cm^3 s^{-1}.[4] Given the unavoidable secondary chemistry in this chemical system, further experiments to cover a range of temperatures were carried out using the alternative source of CH_3O_2.

5.6.2 Chlorine System

Using photolysis of $Cl_2/CH_4/O_2/N_2$ gas mixtures at 351 nm, experiments were conducted at 296 K, 760 Torr, as a function of precursor gas concentrations in the ranges Cl_2 (0.90 – 4.46) × 10^{16} cm^{-3}, CH_4 (3.53 – 8.52) × 10^{18} cm^{-3} and O_2 (1.12 – 2.27)

$\times 10^{18}$ cm^{-3}. As expected on the basis of model simulations performed in FACSIMILE, no significant effects of precursor gas concentration on $k_{5.3}$ were observed. Addition of water vapour, in the ranges $(0 - 3.90) \times 10^{17}$ cm^{-3} at 296 K and $(0 - 1.42) \times 10^{17}$ cm^{-3} at 274 K, did not affect $k_{5.3}$. Results are summarised in Appendix 5 and displayed in Figures 5.16 to 5.19. The average value for k_{obs} at 296 K was found to be $(5.20 \pm 0.46) \times 10^{-13}$ cm^3 s^{-1}, giving $k_{5.3} = (3.81 \pm 0.34) \times 10^{-13}$ cm^3 s^{-1} using the NASA recommendation of $\beta = 0.37$ at 296 K.[4] Errors are 1σ and statistical only.

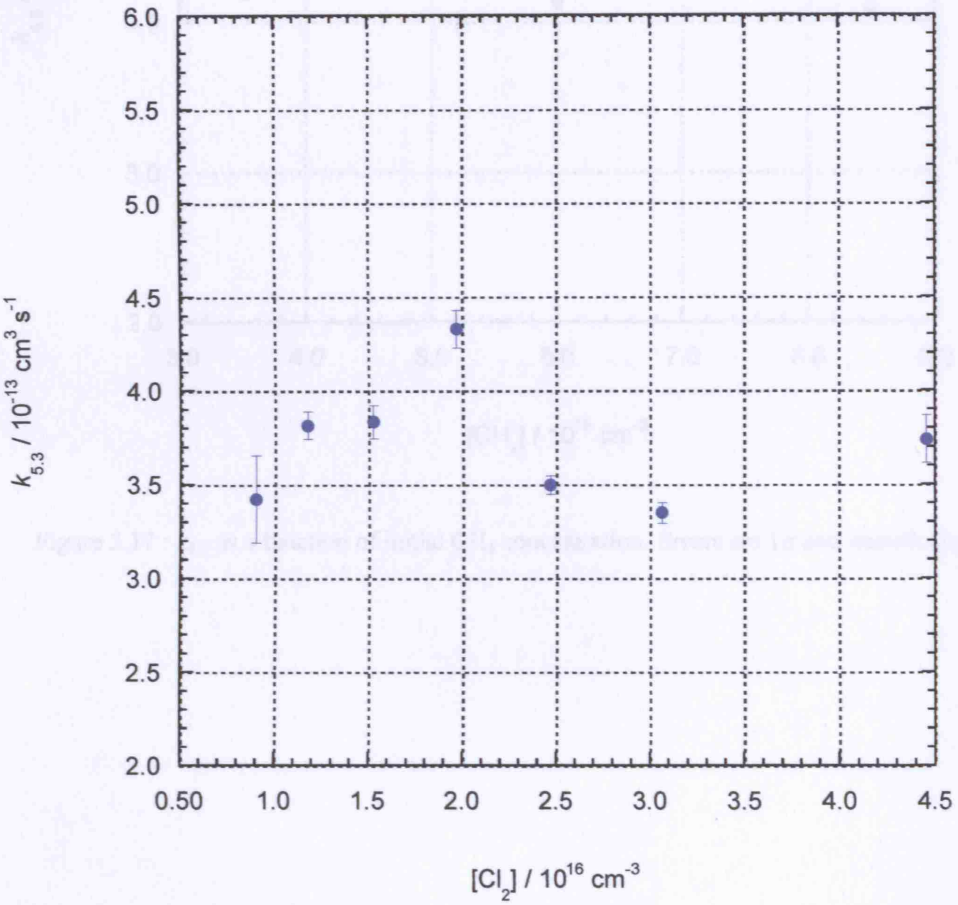

Figure 5.16 : $k_{5.3}$ as a function of initial Cl_2 concentration. Errors are 1σ and statistical only.

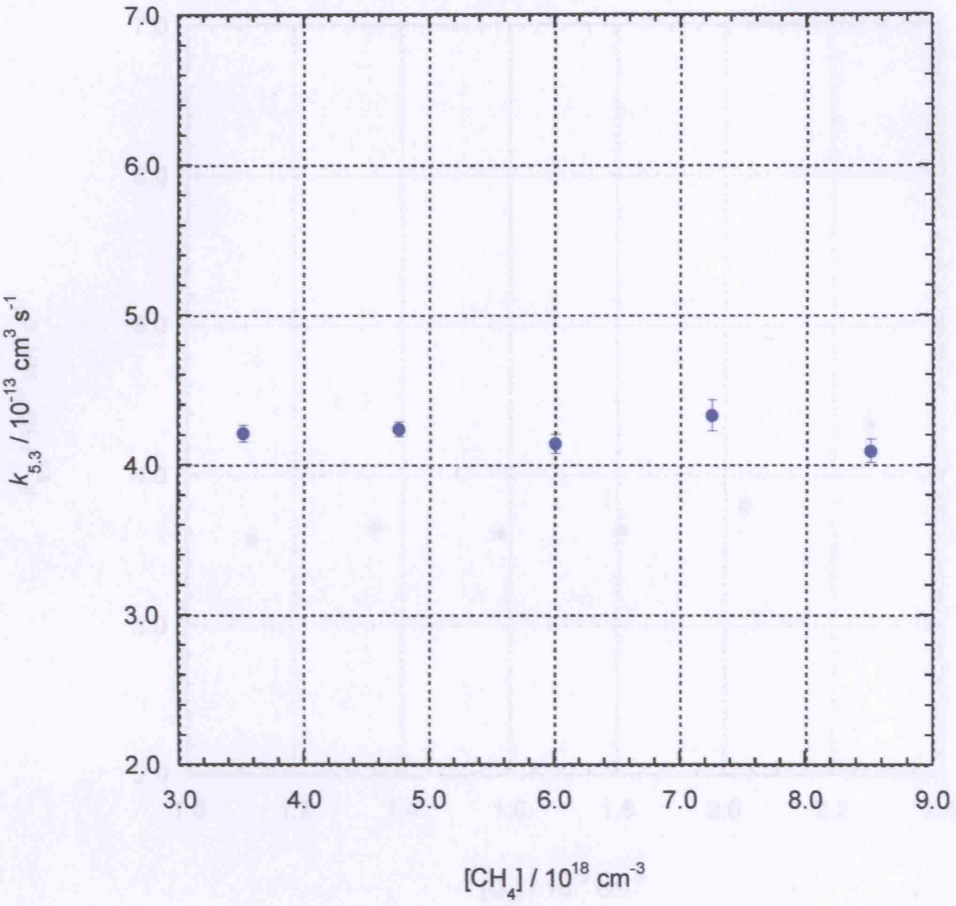

Figure 5.17 : $k_{5.3}$ as a function of initial CH_4 concentration. Errors are 1σ and statistical only.

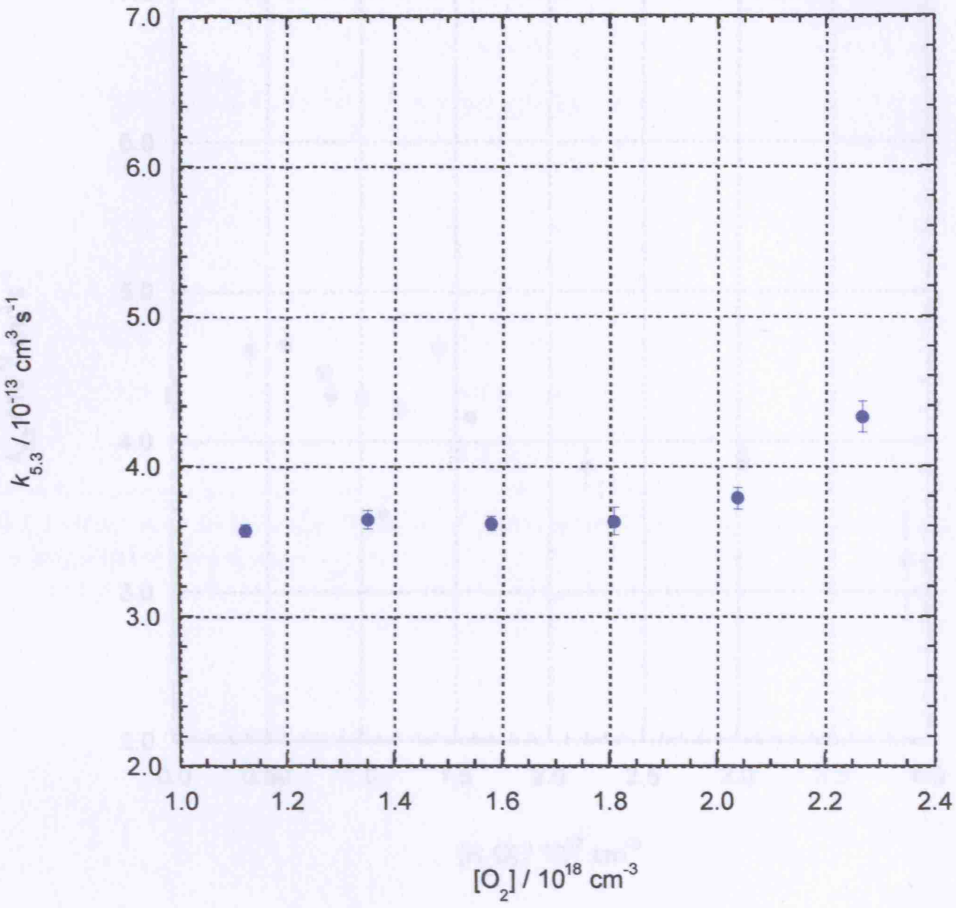

Figure 5.18 : $k_{5.3}$ as a function of initial O_2 concentration. Errors are 1 σ and statistical only.

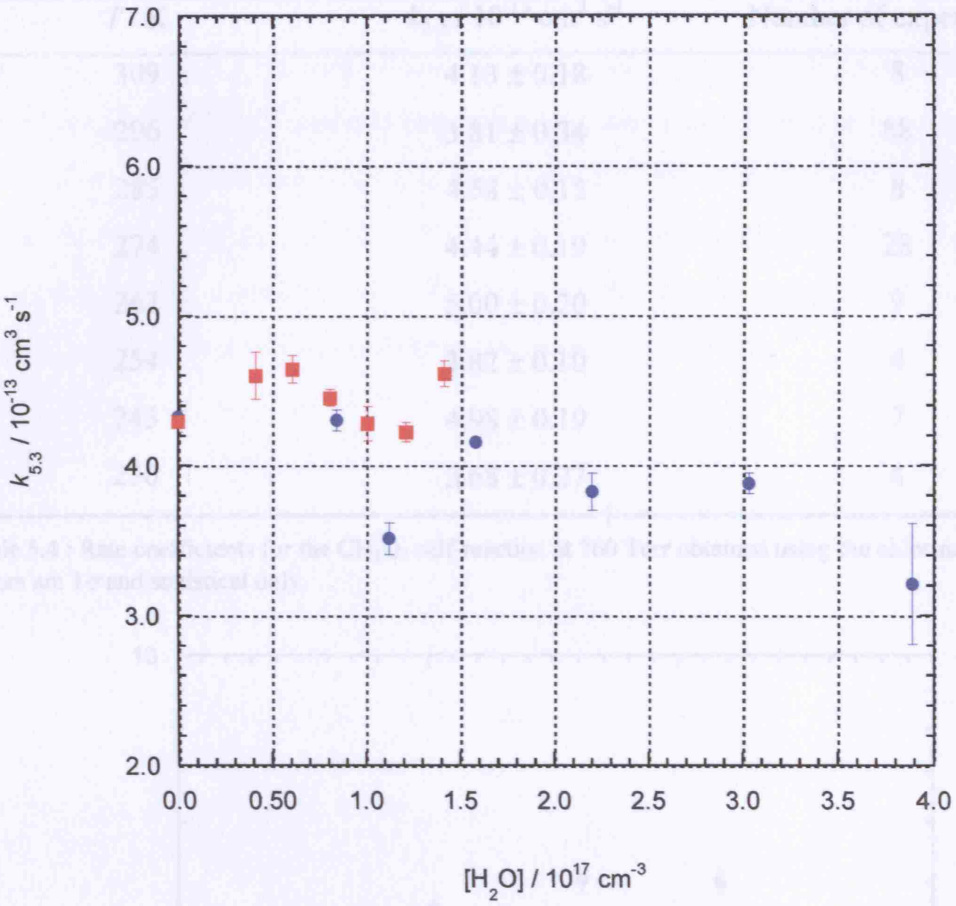

Figure 5.19 : $k_{5.3}$ as a function of water vapour concentration at 296 K (blue) and 274 K (red). Errors are 1σ and statistical only.

The temperature dependence of $k_{5.3}$ was investigated at 760 Torr between 236 and 309 K, revealing $k_{5.3}$ to be only weakly dependent on temperature. An Arrhenius fit to the data, summarised in Table 5.4 and shown in Figure 5.20, gave $A = (4.14 \pm 2.21) \times 10^{-13}$ cm^3 s^{-1} and $-E/R = (8 \pm 140)$ K. Errors are 1σ and statistical only.

T / K	$k_{5.3}$ / 10^{-13} cm^3 s^{-1}	Number of experiments
309	4.13 ± 0.18	8
296	3.81 ± 0.34	88
285	4.58 ± 0.15	8
274	4.44 ± 0.19	28
263	5.00 ± 0.20	9
254	3.82 ± 0.10	4
245	4.98 ± 0.19	7
236	3.68 ± 0.27	4

Table 5.4 : Rate coefficients for the CH_3O_2 self-reaction at 760 Torr obtained using the chlorine system. Errors are 1σ and statistical only.

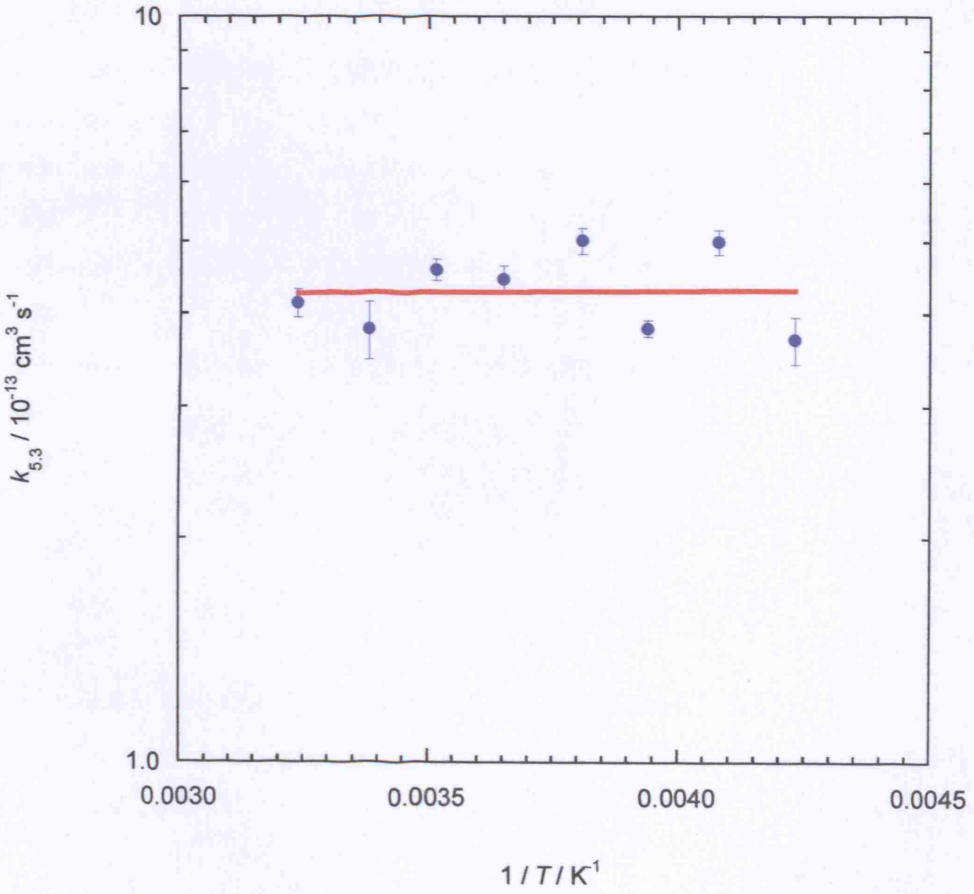

Figure 5.20 : Arrhenius fit (red) to experimental values of $k_{5.3}$ (blue). Errors are 1σ and statistical only.

5.7 Discussion

Results obtained using the methyl chloride system as a source of CH_3O_2 radicals, at low methyl chloride and high methane concentrations, are in excellent agreement with those obtained using the chlorine system, giving average values of $k_{5.3} = (3.60 \pm 0.30) \times 10^{-13}$ cm^3 s^{-1} and $k_{5.3} = (3.81 \pm 0.34) \times 10^{-13}$ cm^3 s^{-1} at 296 K and 760 Torr respectively. Errors are 1σ and statistical only. Furthermore, the results compare well to previous studies, and to current recommendations, as shown in Table 5.5.

Reference	Technique	Reaction mixture	T / K	λ / nm	σ / 10^{-18} cm^2	k_{obs} / 10^{-13} cm^3 s^{-1}	$k_{5,3}$ / 10^{-13} cm^3 s^{-1}
Hochanandel *et al.* 1977[6]	FP/UVA	$CH_3N_2CH_3/O_2$	295	248	1.24	3.82 ± 0.50	2.79 ± 0.36
Cox and Tyndall 1979[10]	MMS	$Cl_2/CH_4/O_2$	298	250	3.9	5.2 ± 0.9	3.88 ± 0.66
Sanhueza *et al.* 1979[11]	FP/UVA	$Cl_2/CH_4/O_2$	298	254	1.30	3.7 ± 0.3	3.70 ± 0.22
Kan *et al.* 1979[8]	FP/UVA	$CH_3N_2CH_2/O_2$	296	265	0.88	4.15 ± 0.50	3.03 ± 0.36
Adachi *et al.* 1980[9]	FP/UVA	$CH_3N_2CH_3/O_2$		240	0.26	5.81 ± 0.50	4.24 ± 0.36
Sander and Watson 1980[12]	FP/UVA	$Cl_2/CH_4/O_2$	298	245	1.5	3.6 ± 0.7	2.63 ± 0.51
Sander and Watson 1981[13]	FP/UVA	$Cl_2/CH_4/O_2$	248 – 417	250	2.45	2.98 ± 0.52	2.18 ± 0.38
McAdam *et al.* 1987[14]	FP/UVA	$Cl_2/CH_4/O_2$	298	250	4.4	5.9 ± 1.0	4.31 ± 0.73
Kurylo *et al.* 1987[15]	FP/UVA	$Cl_2/CH_4/O_2$	298	250	3.3	3.7 ± 0.3	2.70 ± 0.22
Kurylo and Wallington 1987[16]	FP/UVA	$Cl_2/CH_4/O_2$	228 – 380	250	3.3	3.64 + 0.45	2.66 ± 0.33
Jenkin *et al.* 1988[17]	MMS	$Cl_2/CH_4/O_2$	298	250	4.25	4.7 ± 0.5	3.43 ± 0.36
Simon *et al.* 1990[18]	MMS	$Cl_2/CH_4/O_2$	300	250	4.14	4.8 ± 0.5	3.50 ± 0.36
Lightfoot *et al.* 1990[19]	FP/UVA	$Cl_2/CH_4/O_2$	248 – 573	210 240 260	2.5 4.8 3.6	5.6 ± 0.9	4.09 ± 0.66
Jenkin and Cox 1991[21]	MMS	CH_3I/O_2	268 – 350	230	4.92	4.97 ± 0.44	3.63 ± 0.32
NASA 2002[4]							$\left(3.5^{+1.00}_{-0.58}\right)$
This work	FP/UVA	$CH_3Cl/CH_4/O_2$	296			4.93 ± 0.41	3.60 ± 0.30
This work	FP/UVA	$Cl_2/CH_4/O_2$	236 – 309			5.20 ± 0.46	3.81 ± 0.34

Table 5.5 : Summary of previous investigations of $k_{5,3}$ at ambient temperature. FP/UVA = flash photolysis with UV absorption spectrospcopy; MMS = molecular modulation spectrometry.

Previous investigations of the temperature dependence of the methylperoxy self-reaction have reported a weak negative dependence of $k_{5.3}$ on temperature. Sander and Watson[13] reported a value of $-E/R$ of (223 ± 41) K, Kurylo and Wallington[16] reported a value of (220 ± 70) K, and Jenkin and Cox,[21] at 760 Torr, a value of (220 ± 72) K. Lightfoot *et al.*[19] reported a value of (365 ± 41) K. Results of Sander and Watson, Kurylo and Wallington and Jenkin and Cox, however, are presented for the *observed* rate coefficient for CH_3O_2 decay, while only those of Lightfoot *et al.* correct for the enhancement in observed CH_3O_2 decay due to the production of HO_2 radicals through reactions (5.3a) and (5.2) and the subsequent reaction of HO_2 with CH_3O_2:

$CH_3O_2 + CH_3O_2$	→	$2\ CH_3O + O_2$	(5.3a)
	→	$CH_3OH + HCHO + O_2$	(5.3b)
$CH_3O + O_2$	→	$HO_2 + HCHO$	(5.2)
$CH_3O_2 + HO_2$	→	$CH_3OOH + O_2$	(5.4)

The temperature dependence of the branching ratio β, where $\beta = k_{5.3a}/(k_{5.3a}+k_{5.3b})$, has been measured by both Horie *et al.*,[26] between 223 and 333 K using matrix isolation FTIR spectroscopy, and by Lightfoot *et al.*[19] using flash photolysis with UV spectroscopy. Lightfoot *et al.* measured the temperature dependence of β by monitoring absorption signals from both CH_3O_2 and HO_2 at high temperatures ($T > 373$ K). At such conditions the rate of reaction between CH_3O_2 and HO_2 is sufficiently slow, relative to the CH_3O_2 self-reaction, to allow direct observation of HO_2 and hence measurement of the branching ratio for channel (5.3a). The true rate coefficient for the CH_3O_2 self-reaction is given by $k_{obs}/(1+\beta)$, as described in section 5.2. Application of the temperature dependent parameter β, as currently recommended by NASA,[4] to the results of Sander and Watson, of Kurylo and Wallington, and those of Jenkin and Cox at 760 Torr, gives $-E/R$ values of (401 ± 74) K, (398 ± 127) K and (398 ± 130) K respectively.

The observation of a negative temperature dependence of $k_{5.3}$ in previous studies has been attributed to an initial barrierless formation of a $CH_3O_4CH_3$ tetroxide intermediate on combination of two CH_3O_2 radicals,[3,16,19] and the $CH_3O_4CH_3$ species has been

observed in a matrix isolation study of CH_3O_2.[45] The proposed mechanism for the CH_3O_2 self-reaction is analogous to that proposed for the HO_2 self-reaction (Chapter 4), in which the tetroxide complex can dissociate back to reactants or rearrange to form products. Possible structures and rearrangement pathways for the tetroxide intermediate have been discussed by Lightfoot *et al.*,[19] and are shown in Figure 5.21.

$$CH_3O_2 + CH_3O_2 \leftrightarrow CH_3O_4CH_3$$

$$CH_3O_4CH_3 \rightarrow \text{products}$$

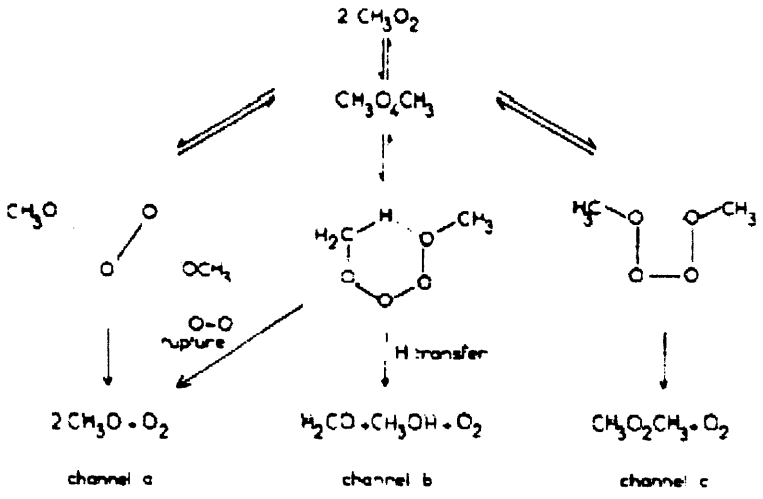

Figure 5.21 : Possible reaction pathways for the CH_3O_2 self-reaction. Reproduced from Lightfoot *et al.*[19] Note that the $CH_3O_4CH_3$ intermediate may not exist as a separate species to the individual structures shown in the figure.

The negative temperature dependence of the CH_3O_2 self-reaction has been attributed to increased vibrational stability of the tetroxide complex at low temperatures, making dissociation of the complex back to reactants less probable as the temperature is reduced. Support for such a mechanism has been provided by calculation of the CH_3O_2 self-reaction potential energy surface using *ab initio* methods.[46,47]

In contrast to the HO_2 self-reaction, previous studies of the CH_3O_2 self-reaction have generally revealed no dependence of $k_{5.3}$ on pressure.[8,11-14,16,19,21] The lack of pressure dependence of $k_{5.3}$ is thought to be due to the existence of a greater number of available vibrational modes in CH_3O_2 and $CH_3O_4CH_3$ than HO_2 and HO_4H, rendering collisional

stabilisation of the tetroxide intermediate less important in the case of the CH_3O_2 self-reaction.[13]

Jenkin and Cox,[21] however, reported a much weaker temperature dependence of $k_{5.3}$ at low pressure than at high pressure in an investigation of $k_{5.3}$ at total pressures of 10.8 and 760 Torr using molecular modulation spectrometry of $CH_3I/O_2/N_2$ mixtures. Such differences between Arrhenius parameters may have been due to a change in the branching ratio β with pressure, but no dependence of $k_{5.3}$ on pressure has been reported elsewhere, and Jenkin and Cox themselves observed $k_{5.3}$ to be independent of pressure between 10.8 and 760 Torr at 298 K. In addition, Jenkin and Cox observed significant absorptions over the entire experimental wavelength range of 210 to 320 nm due to production of transient species in the reaction mixture, indicating the presence of reactive species other than CH_3O_2. The transient species were thought to result from combination of radical species with iodine atoms, produced on photolysis of the CH_3I used as a source of methyl radicals, and may have influenced the observed kinetics to a greater extent at low pressure than at high.

This work reports an extremely weak, near zero, temperature dependence of $k_{5.3}$ after correction for enhancement in the observed rate of CH_3O_2 decay due to HO_2 radical production, with $-E/R = (8 \pm 140)$ K and $A = (4.14 \pm 2.21) \times 10^{-13}$ cm^3 s^{-1} determined using the chlorine system. Attempts were made in this work to determine β, but low steady state HO_2 concentrations at the temperatures employed in this study, coupled with low light intensities below approximately 220 nm due to absorptions by the laser optics in the path of the analysis beam, prevented accurate determination of HO_2 concentrations and hence of β. Current NASA recommendations[4] for the temperature dependence of β were therefore used in this work.

A comparison between investigations of the temperature dependence of $k_{5.3}$ is given in Figure 5.22, with the corresponding data displayed in Table 5.6. The present results are within the error limits of previous studies and current recommendations by NASA and Lightfoot *et al.*[19] This provides a sound basis for the study of the HO_2 + CH_3O_2 reaction described in Chapter 6.

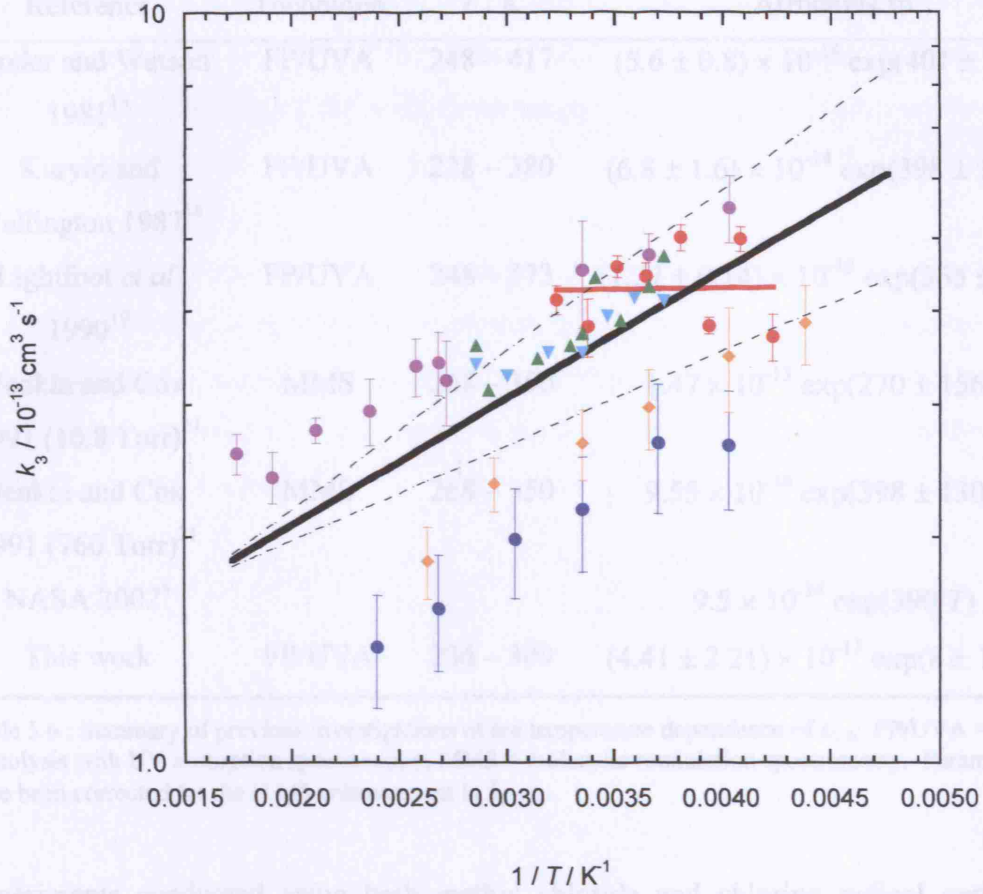

Figure 5.22 : Summary of previous investigations of the temperature dependence of $k_{5,3}$. Results shown are those of this work (red circles), Sander and Watson[13] (blue circles), Kurylo and Wallington[16] (orange diamonds), Jenkin and Cox[21] at 760 Torr (green triangles), Jenkin and Cox[21] at 10.8 Torr (light blue inverted triangles) and Lightfoot *et al.*[19] (purple circles). The fit to this work is given by the solid red line, and the NASA recommendation[4] by the solid black line. Upper and lower limits to the NASA recommendation are given by the broken black lines. All rate coefficients have been corrected for the $(1+\beta)$ enhancement. Errors for this work are 1σ and statistical only.

Reference	Technique	T / K	Arrhenius fit
Sander and Watson 1981[13]	FP/UVA	248 – 417	$(5.6 \pm 0.8) \times 10^{-14} \exp(401 \pm 74/T)$
Kurylo and Wallington 1987[16]	FP/UVA	228 – 380	$(6.8 \pm 1.6) \times 10^{-14} \exp(398 \pm 127/T)$
Lightfoot *et al.* 1990[19]	FP/UVA	248 – 573	$(1.27 \pm 0.14) \times 10^{-13} \exp(365 \pm 41/T)$
Jenkin and Cox 1991 (10.8 Torr)[21]	MMS	268 – 350	$1.47 \times 10^{-13} \exp(270 \pm 156/T)$
Jenkin and Cox 1991 (760 Torr)[21]	MMS	268 – 350	$9.55 \times 10^{-14} \exp(398 \pm 130/T)$
NASA 2002[4]			$9.5 \times 10^{-14} \exp(390/T)$
This work	FP/UVA	236 – 309	$(4.41 \pm 2.21) \times 10^{-13} \exp(8 \pm 140/T)$

Table 5.6 : Summary of previous investigations of the temperature dependence of $k_{5.3}$. FP/UVA = flash photolysis with UV absorption spectroscopy; MMS = molecular modulation spectrometry. Parameters have been corrected for the $(1+\beta)$ enhancement in $k_{5.3}$.

Experiments conducted using both methyl chloride and chlorine radical generation systems revealed $k_{5.3}$ to be independent of water vapour concentration, in contrast to the rate coefficient for the HO_2 self-reaction. As discussed in Chapter 4, enhancement of the rate coefficient for the HO_2 self-reaction in the presence of water vapour has been attributed to the formation a hydrogen bonded complex between HO_2 and H_2O. Since the CH_3O_2 radical has no significantly polar bonds, unlike the HO_2 radical, it lacks the capacity to form hydrogen bonds. CH_3O_2 therefore cannot combine with H_2O in an analogous manner to HO_2, and CH_3O_2 chemistry is consequently unaffected by the presence of water vapour.

5.8 Conclusions

The kinetics of the methylperoxy self-reaction have been investigated over a range of temperatures and initial conditions, using two different chemical systems to generate CH_3O_2 radicals.

Results obtained from the two chemical systems at ambient temperature are in good agreement with each other and with previous investigations. The use of methyl chloride

as a source of methylperoxy radicals did, however, indicate that the rate coefficient for reaction between Cl and CH_3Cl is relatively ill-defined in the literature, and that the kinetics and mechanism of the reaction between CH_3O_2 and $ClCH_2O_2$ require further experimental attention.

The temperature dependence of $k_{5.3}$ observed in this work is somewhat weaker than has been reported in previous work, but is consistent with proposed reaction mechanisms in the literature. No significant effects of water vapour on methylperoxy self-reaction kinetics were observed at 274 K and 296 K, in contrast to hydroperoxy self-reaction kinetics described in Chapter 4.

5.9 References

[1] R.P. Wayne, *Chemistry of Atmospheres*, Third edition, **2000**, Oxford University Press

[2] G. P. Brasseur, J. J. Orlando, G. S. Tyndall, *Atmospheric Chemistry and Global Climate Change*, **1999**, Oxford University Press

[3] P.D. Lightfoot, R.A. Cox, J.N. Crowley, M. Destriau, G.D. Hayman, M.E. Jenkin, G.K. Moortgat, F. Zabel, *Atmos. Environ.*, **1992**, 26A, 1805

[4] S. P. Sander, R. R. Friedl, D. M. Golden, M. J. Kurylo, R. E. Huie, V. L. Orkin, G. K. Moortgat, A. R. Ravishankara, C. E. Kolb, M. J. Molina, *Chemical Kinetics and Photochemical Data for Use in Atmospheric Studies*, **2002**, Evaluation Number 14, JPL Publication 02-25, Jet Propulsion Laboratory, Pasadena, CA., USA

[5] D.A. Parkes, *Int. J. Chem. Kinet.*, **1977**, 9, 451

[6] C.J. Hochanadel, J.A. Ghormley, J.W. Boyle, P.J. Ogren, *J. Phys. Chem.*, **1977**, 8, 1, 3

[7] C. Anastasi, I.W.M. Smith, D.A. Parkes, *J. Chem. Soc. Farad. Trans.*, **1978**, 74, 1, 1693

[8] C.S. Kan, R.D. McQuigg, M.R. Whitbeck, J.G. Calvert, *Int. J. Chem. Kinet.*, **1979**, 11, 921

[9] H. Adachi, N. Basco, D.G.L. James, *Int. J. Chem. Kinet.*, **1980**, 12, 949

[10] R. Cox and G.S. Tyndall, *J. Chem. Soc. Farad. Trans. II*, **1980**, 76, 153

[11] E. Sanhueza, R. Simonaitis, J. Heicklen, *Int. J. Chem. Kinet.*, **1979**, 11, 907

[12] S.P. Sander and R.T. Watson, *J. Phys. Chem.*, **1980**, 84, 1664

[13] S.P. Sander and R.T. Watson, *J. Phys. Chem.*, **1981**, 85, 2960

[14] K. McAdam, B. Veyret, R. Lesclaux, *Chem. Phys. Lett.*, **1987**, 133, 1, 39

[15] M.J. Kurylo, P. Dagaut, T.J. Wallington, D.M. Neuman, *Chem. Phys. Lett.*, **1987**, 139, 6, 513

[16] M.J. Kurylo and T.J. Wallington, *Chem. Phys. Lett.*, **1987**, 138, 6, 543

[17] M.E. Jenkin, R.A. Cox, G.D. Hayman, L.J. Whyte, *J. Chem. Soc. Farad. Trans. II*, **1988**, 84, 7, 913

[18] F.G. Simon and W. Schneider, G.K. Moortgat, *Int. J. Chem. Kinet.*, **1990**, 22, 791

[19] P.D. Lightfoot, R. Lesclaux, B. Veyret, *J. Phys. Chem.*, **1990**, 94, 700

[20] P.D. Lightfoot, P. Roussel, F. Caralp, R. Lesclaux, *J. Chem. Soc. Farad. Trans.*, **1991**, 87, 19, 3213

[21] M.E. Jenkin and R.A. Cox, *J. Phys. Chem.*, **1991**, 95, 3229

[22] E. Villenave and R. Lesclaux, *J. Phys. Chem.*, **1996**, 100, 14372

[23] P.D. Lightfoot and A.A. Jemi-Alade, *J. Photochem. Photobiol. A:Chem.*, **1991**, 59, 1-10

[24] C.S. Kan and J.G. Calvert, *Chem. Phys. Lett.*, **1979**, 63, 1, 111

[25] C.S. Kan, J.G. Calvert, J.H. Shaw, *J. Phys. Chem.*, **1980**, 84, 3411

[26] O. Horie, J.N. Crowley, G.K. Moortgat, *J. Phys. Chem.*, **1990**, 94, 8198

[27] H. Niki, P.D. Maker, C.M. Savage, L.P. Breitenbach, *J. Phys. Chem.*, **1981**, 85, 877

[28] G.S. Tyndall, T.J. Wallington, J.C. Ball, *J. Phys. Chem. A*, **1998**, 102, 2547

[29] J. Weaver, R. Shortridge, J. Meagher, J. Heicklen, *J. Photochem.*, **1975**, 4, 109

[30] K. Minschwaner, G.P. Anderson, L.A. Hall, K. Yoshino, *J. Geophys. Res.*, **1992**, 97, 10103

[31] P.B Roussel, P.D. Lightfoot, F. Caralp, V. Catoire, R. Lesclaux, W. Forst, *J. Chem. Soc. Farad. Trans.*, 87, **1991**, 2367

[32] P. Biggs, C.E. Canosa-Mas, C.J. Percival, D.E. Shallcross, R.P. Wayne, *Int. J. Chem. Kinet.*, **1999**, 31, 433

[33] IUPAC Subcommittee on Gas Data Evaluation – Data Sheet PCI11 http://www.iupac-kinetic.ch.cam.ac.uk

[34] R. Timonen, *Ann. Acad. Sci. Fenn. Ser. A2*, **1988**, 218, 5

[35] T.T. Song and T.M Su, *J. Phys. Chem.*, **1996**, 100, 13554

[36] W. Tsang and R.F. Hamilton, *J. Phys. Chem. Ref. Data*, **1986**, 15, 1087

[37] J. Espinosa-Garcia and J.C. Corchado, *J. Chem. Phys.*, **1996**, 105, 3517

[38] J. Heicklen, *Adv. Photochem.*, **1988**, 14, 177

[39] C.A. Cantrell, A. Zimmer, G.S.Tyndall, *Geophys. Res. Lett.*, **1997**, 24, 2195

[40] D. Maric, J.N. Crowley, J.P. Burrows, *J. Phys. Chem. A*, **1997**, 101, 2561

[41] V. Catoire, R. Lesclaux, P.D. Lightfoot, *J. Phys. Chem.*, **1994**, 98, 2889

[42] P. Beichart, L. Wingen, J. Lee, R. Vogt, M.J. Ezell, M. Ragains, R. Neavyn, B.J. Finlayson-Pitts, *J. Phys. Chem.*, **1995**, 99, 13156

[43] R. Manning and M.J. Kurylo, *J. Phys. Chem.*, **1977**, 81, 291

[44] T.J. Wallington, J.M. Andino, J.C. Ball, S.M. Japar, *J. Atmos. Chem.*, **1990**, 10, 301

[45] P. Ase, W. Bock, A. Snelson, *J. Phys. Chem.*, **1986**, 90, 2099

[46] G. Ghigo, A. Maranzana, G. Tonachini, *J. Chem. Phys.*, **2003**, 118, 10575

[47] L. Feria, C. Gonzalez, M. Castro, *Int. J. Quant. Chem.*, **2004**, 99, 605

Chapter 6

The Hydroperoxy-Methylperoxy Cross-Reaction

6.1 Introduction

The fate of peroxy radicals in the troposphere can have important consequences for atmospheric oxidation processes and pollution, as discussed in previous chapters. In the absence of nitrogen oxides, NO_x, the major fate for peroxy radicals, RO_2, in the troposphere is generally reaction with hydroperoxy radicals, HO_2:[1]

$$HO_2 + RO_2 \rightarrow ROOH + O_2 \qquad (6.1)$$

In the presence of nitrogen oxides the major fate for peroxy radicals is reaction with NO, resulting in production of NO_2, and ultimately regeneration of NO and production of ozone, O_3.

$$RO_2 + NO \rightarrow RO + NO_2 \qquad (6.2)$$

$$NO_2 + h\nu \rightarrow NO + O \qquad (6.3)$$

$$O_2 + O + M \rightarrow O_3 + M \qquad (6.4)$$

Production of large amounts of NO, NO_2 and O_3 can cause serious environmental problems, and, under certain meteorological conditions, can lead to formation of photochemical smog.[1,2]

The methylperoxy radical, CH_3O_2, is produced in the atmospheric oxidation of methane and other hydrocarbons. In the absence of NO, reaction with HO_2 provides the major loss pathway for CH_3O_2:

$$HO_2 + CH_3O_2 \rightarrow CH_3OOH + O_2 \qquad (6.5)$$

The methyl hydroperoxide product, CH_3OOH, experiences a similar fate to the hydrogen peroxide product of the HO_2 self-reaction, and is readily removed from the lower atmosphere during precipitation. Removal of CH_3OOH from the atmosphere

represents a loss process for HO_x, and hence a reduction in the oxidising capacity of the atmosphere. In some circumstances, however, CH_3OOH can become a source of CH_3O_2 by reaction with hydroxyl radicals, OH:

$$CH_3OOH + OH \rightarrow CH_3O_2 + H_2O \quad (6.6a)$$
$$\rightarrow CH_2OOH + H_2O \quad (6.6b)$$

and a source of CH_3O radicals by solar photolysis:

$$CH_3OOH + h\nu \rightarrow CH_3O + OH \quad (6.7)$$

Despite the possibility of CH_3OOH acting as a source for HO_x, atmospheric measurements of HO_2, CH_3O_2 and CH_3OOH have indicated not only that the HO_2-CH_3O_2 cross-reaction may be the single most important HO_x loss pathway in the upper troposphere, but also that its rate may be currently underpredicted in atmospheric models.[3,4]

6.2 Previous Work

Previous investigations of the kinetics of the hydroperoxy-methylperoxy cross-reaction have used both molecular modulation and flash photolysis techniques, revealing $k_{6.5}$ to display a negative temperature dependence between 248 and 573 K,[5] and to be independent of pressure in the range 10 to 760 Torr.[6] In contrast to the HO_2 self-reaction, but in keeping with the CH_3O_2 self-reaction, the rate coefficient for the HO_2-CH_3O_2 reaction has not been observed to be affected by the presence of water vapour at 298 K.[5,7] No investigation of any effects of methanol vapour on $k_{6.5}$ has been reported.

Cox and Tyndall were the first to investigate the kinetics of the HO_2-CH_3O_2 reaction, using molecular modulation spectrometry (MMS) of $Cl_2/H_2/CH_4/O_2/N_2$ mixtures between 274 and 338 K at 760 Torr.[8,9] Both HO_2 and CH_3O_2 were monitored at single wavelengths in the region 210 – 280 nm, and initial conditions were imposed such that both radicals were observed to decay at approximately the same rate, indicating that the decay of both radicals was dominated by the cross-reaction. A strong product

absorption was detected in the experimental wavelength range, and was attributed to the formation of CH_3OOH.

Observation of a negative temperature dependence for $k_{6.5}$ led Cox and Tyndall to propose of a mechanism analogous to that suggested for the HO_2 self-reaction,[10] involving formation of a CH_3O_4H intermediate:

$$HO_2 + CH_3O_2 (+M?) \leftrightarrow CH_3O_4H (+M?)$$
$$CH_3O_4H \rightarrow CH_3OOH + O_2$$

The requirement for the third body M in the reaction mechanism could not be determined by Cox and Tyndall since their investigation was conducted at a single pressure. Subsequent studies as a function of pressure have, however, revealed $k_{6.5}$ to be independent of pressure in the range 10 – 760 Torr.[5,6,7,11]

Investigation of the temperature dependence of $k_{6.5}$ has also been carried out by Dagaut *et al.*,[12] in the range 228 – 380 K at 760 Torr, and Lightfoot *et al.*,[5] in the range 248 – 573 K at 210 Torr and at 760 Torr, both using flash photolysis with UV absorption spectroscopy (FP/UVA) of $Cl_2/CH_3OH/CH_4/O_2/N_2$ mixtures. Lightfoot *et al.* and Dagaut *et al.* both report a negative temperature dependence for $k_{6.5}$, and are in good agreement with each other. There is poor agreement, however, between the results of Lightfoot *et al.* and Dagaut *et al.* and those of Cox and Tyndall.

Effects of water vapour on $k_{6.5}$ were investigated by Kurylo *et al.*[7] and Lightfoot *et al.*[5] at 298 K. No significant effects were observed, but no investigations have been conducted at sub-ambient temperatures, and possible effects of methanol vapour on $k_{6.5}$ have yet to be addressed.

Boyd *et al.*[13] investigated the kinetics of the HO_2-CH_3O_2 reaction using 248 nm laser flash photolysis of $H_2O_2/CH_4/O_2/N_2$ mixtures at 248 nm with UV absorption spectroscopy at 210 and 270 nm. Experiments were performed at 298 K and 760 Torr under pseudo-first order conditions, with HO_2 concentrations in excess of those of

CH_3O_2 by a factor of 4 to 10. Results were found to be in good agreement with previous studies.[5,6,8,9,11]

In an FTIR investigation of the CH_3O_2 self-reaction, Kan *et al.*[14] measured the rate of CH_3OOH production in the system and attributed this to the secondary reaction between HO_2 and CH_3O_2. Moortgat *et al.*[15] also attributed formation of CH_3OOH to the HO_2-CH_3O_2 reaction in an IR investigation of the photo-oxidation of CH_3CHO. Comparison of the rate of CH_3OOH production, measured by Kan *et al.* and Moortgat *et al.*, to measurement of HO_2 and CH_3O_2 decay rates in the direct study of the HO_2-CH_3O_2 reaction by Cox and Tyndall,[8,9] led McAdam *et al.*[11] and Moortgat *et al.*[15] to propose the possibility of an additional channel in the HO_2-CH_3O_2 reaction, resulting in HCHO production:

$$HO_2 + CH_3O_2 \rightarrow HCHO + H_2O + O_2 \qquad (6.5b)$$

The existence of additional reaction channels in the HO_2-CH_3O_2 reaction was also discussed by Jenkin *et al.*,[6] and IR experiments were performed to investigate the production of HDO in the reaction between HO_2 and CD_3O_2. Observation of HDO in the $Cl_2/CH_3OH/CD_4/O_2$ system could not be explained by reactions (6.9) to (6.14) alone, and it was therefore proposed that the branching ratio for channel (6.8b) may be as much as 0.4 at 298 K.

$$HO_2 + CD_3O_2 \rightarrow CD_3OOH + O_2 \qquad (6.8a)$$

$$\rightarrow DCDO + HDO + O_2 \qquad (6.8b)$$

$$Cl + CD_3OOH \rightarrow DCDO + DCl + OH \qquad (6.9)$$

$$OH + CD_4 \rightarrow CD_3 + HDO \qquad (6.10)$$

$$Cl + CD_4 \rightarrow CD_3 + DCl \qquad (6.11)$$

$$DCl\ (g) \rightarrow DCl\ (ads) \qquad (6.12)$$

$$DCl\ (ads) + H_2O\ (ads) \rightarrow HCl\ (ads) + HDO\ (ads) \qquad (6.13)$$

$$HDO\ (ads) \rightarrow HDO\ (g) \qquad (6.14)$$

Although not directly transferable to the reaction between HO_2 and CH_3O_2, evidence for HDO production in the HO_2-CD_3O_2 reaction by Jenkin *et al.* does provide some support for the potential existence of channel (6.5b) in the HO_2-CH_3O_2 cross-reaction.

More recent product studies of the reaction between HO_2 and CH_3O_2 using FTIR methods have not, however, revealed any evidence for HCHO production.[16,17] The channel producing CH_3OOH was found to account for 92 ± 8 % of the total reaction between HO_2 and CH_3O_2 at 295 K and 700 Torr,[16] and 92 ± 5 % between 15 and 700 Torr at 295 K.[17] However, a more recent investigation of the reaction products by Elrod *et al.*[18] at 100 Torr, using a turbulent flow technique with chemical ionisation mass spectrometry, indicates that a branching ratio of 0.11 for production of HCHO at 298 K, and 0.31 at 218 K. Thus far, theoretical investigations of the potential energy surface for interaction between HO_2 and CH_3O_2 have provided little evidence for production of HCHO.[19,20,21]

The aims of this work were to characterise the kinetics of the reaction between hydroperoxy and methylperoxy radicals under tropospheric conditions, and to investigate any possible effects of water and methanol vapours.

6.3 Radical Generation

Radicals were produced by laser flash photolysis, at 351 nm, of $Cl_2/CH_3OH/CH_4/O_2/N_2$ gas mixtures in the reaction sequence:

$Cl_2 + h\nu$	$\rightarrow$	2 Cl	($\lambda = 351$ nm)	(6.15)
$Cl + CH_3OH$	$\rightarrow$	$CH_2OH + HCl$		(6.16)
$CH_2OH + O_2$	$\rightarrow$	$HO_2 + HCHO$		(6.17)
$Cl + CH_4$	$\rightarrow$	$CH_3 + HCl$		(6.18)
$CH_3 + O_2 + M$	$\rightarrow$	$CH_3O_2 + M$		(6.19)

In order to design conditions to ensure rapid radical production with respect to decay, and to elucidate any effects of secondary chemistry on HO_2 and CH_3O_2, a model of the reaction system was constructed in FACSIMILE. The reactions included in the model are listed in Table 6.1.

Reaction label	Reaction	$k_{298\ K,\ 760\ Torr}$ / $cm^3\ s^{-1}$	Reference
a	$Cl + CH_4 \rightarrow CH_3 + HCl$	1×10^{-13}	22
b	$CH_3 + O_2 \rightarrow CH_3O_2$	1.15×10^{-12}	22
c	$Cl + CH_3OH \rightarrow CH_2OH + HCl$	5.5×10^{-11}	22
d	$CH_2OH + O_2 \rightarrow HO_2 + HCHO$	9.1×10^{-12}	22
e	$HO_2 + CH_3O_2 \rightarrow CH_3OOH + O_2$	5.2×10^{-12}	22
f	$HO_2 + HO_2 \rightarrow H_2O_2$	2.91×10^{-12}	22
g	$CH_3O_2 + CH_3O_2 \rightarrow CH_3OH + HCHO + O_2$	2.20×10^{-13}	22
h	$CH_3O_2 + CH_3O_2 \rightarrow 2\ CH_3O + O_2$	1.30×10^{-13}	22
i	$CH_3O_2 + CH_3O_2 \rightarrow PROD$	3.5×10^{-13}	22
j	$CH_3O + O_2 \rightarrow HO_2 + HCHO$	1.9×10^{-15}	22
k	$Cl_2 + CH_3 \rightarrow CH_3Cl + Cl$	2.14×10^{-12}	23
l	$Cl + Cl \rightarrow Cl_2$	5.5×10^{-33}	24
m	$Cl + O_2 \rightarrow ClOO$	2.7×10^{-33}	22
n	$Cl + CH_3O_2 \rightarrow PROD$	1.6×10^{-10}	22
o	$Cl + HCHO \rightarrow HCl + HCO$	7.3×10^{-11}	22
p	$Cl + HO_2 \rightarrow HCl + O_2$	3.2×10^{-11}	22
q	$Cl + HO_2 \rightarrow OH + ClO$	9.1×10^{-12}	22
r	$Cl + CH_3OOH \rightarrow PROD$	5.7×10^{-11}	22
s	$Cl + H_2O_2 \rightarrow HCl + HO_2$	4.1×10^{-13}	22
t	$CH_3 + CH_3O_2 \rightarrow 2\ CH_3O$	4×10^{-11}	25
u	$CH_3 + HCl \rightarrow CH_4 + Cl$	3×10^{-14}	26
v	$CH_3 + H_2O_2 \rightarrow CH_4 + HO_2$	5.5×10^{-14}	25
w	$CH_3 + CH_3O \rightarrow CH_3OCH_3$	2×10^{-11}	25
x	$CH_3 + CH_3O \rightarrow HCHO + CH_4$	4×10^{-11}	25
y	$CH_3 + HO_2 \rightarrow CH_4 + O_2$	6×10^{-12}	25
z	$CH_3 + HO_2 \rightarrow OH + CH_3O$	3×10^{-11}	25
a'	$CH_3O_2 + CH_3O \rightarrow PROD$	2.6×10^{-12}	25
b'	$HO_2 + HCHO \rightarrow ADDUCT$	5×10^{-14}	22

Table 6.1 : Reactions included in the sensitivity analysis for $k_{6.5}$. Where reactions are shown as having more than possible reaction channel, reactions g and h for example, the sensitivity analysis has been conducted on each individual channel separately, and then on the total rate coefficient for the reaction, with products not identified in the model. The model did not simultaneously include the total rate coefficient and each individual reaction channel, for example, the model either included reactions g and h, but not i, or i, but not g and h.

Initially, concentrations of precursor gases in the model were varied to minimise the flux of HO_2 and CH_3O_2 through their self-reactions and to maximise the reactive flux through their cross-reaction. Once the optimum conditions for investigation of the kinetics of the HO_2-CH_3O_2 cross-reaction had been established, a sensitivity analysis on each of the reactions included in the model, listed in Table 6.1, was conducted in order to determine possible effects of secondary chemistry on the expected observed decay of HO_2 and CH_3O_2 at 298 K. The method used to conduct the sensitivity analysis was as described in Chapter 4 for the HO_2 self-reaction. Each rate coefficient in the model was sequentially halved and doubled, and the output concentrations of HO_2 and CH_3O_2 from the model re-analysed in FACSIMILE to determine the apparent rate coefficient for the HO_2-CH_3O_2 cross-reaction. Results for the sensitivity analysis are shown in Figure 6.1. As can be seen, the major reactions affecting the returned value of $k_{6.5}$ are the cross-reaction itself, and the self-reactions of HO_2 and CH_3O_2. All other reactions in the model were seen to affect the returned value of $k_{6.5}$ by less than 5 %, under the experimental conditions designed.

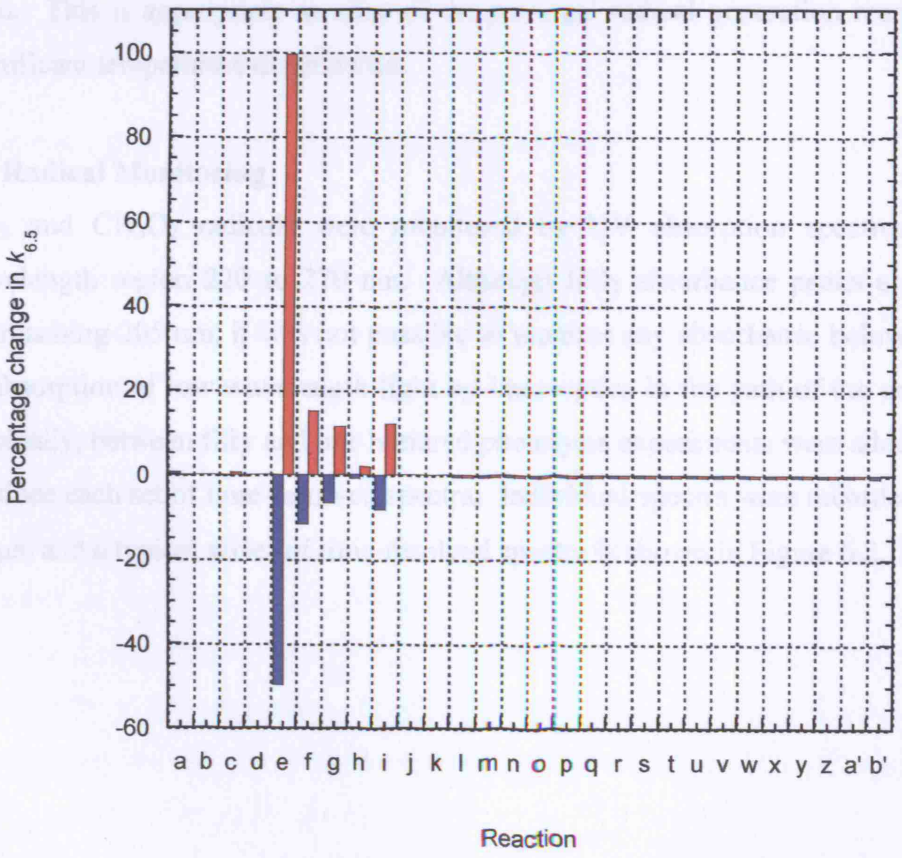

Figure 6.1 : Sensitivity analysis for $k_{6.5}$. Effect on $k_{6.5}$ of sequentially halving (blue) and doubling (red) each rate coefficient in the model for reactions as listed in Table 6.1.

Kinetics of the self-reactions of HO_2 and CH_3O_2 have been characterised directly in this work, and, as reported in Chapters 4 and 5, have errors well within the halving and doubling carried out in the sensitivity analysis. These reactions should therefore not significantly perturb the determination of the kinetics of the cross-reaction.

Although it was initially intended that experiments be conducted to give the maximum flux of HO_2 and CH_3O_2 through the cross-reaction, initial experiments performed under such conditions were found to give poor signal to noise ratios for HO_2, and it was necessary to adjust the initial concentrations of CH_3OH and CH_4 to improve the signal. Reagents and concentrations used were Cl_2 (5 % in N_2, BOC) $(2.51 - 4.48) \times 10^{16}$ cm^{-3}, CH_3OH (99.9 %, Riedel-de Haen) $(2.13 - 3.40) \times 10^{16}$ cm^{-3}, CH_4 (99.99 %, BOC) $(6.30 - 8.31) \times 10^{18}$ cm^{-3}, O_2 (99.99 %, BOC) $(1.26 - 2.28) \times 10^{18}$ cm^{-3} and N_2 (99.99 %, BOC) to balance. Under all circumstances, these conditions led to prompt radical formation with respect to decay. At temperatures other than 298 K, conditions were adapted to maintain number densities, but no significant changes to concentrations were used. This is appropriate as none of the principal radical generation reactions show a significant temperature dependence.

6.4 Radical Monitoring

HO_2 and CH_3O_2 radicals were monitored by UV absorption spectroscopy in the wavelength region 220 to 270 nm. Although HO_2 absorbance peaks at wavelengths approaching 205 nm, it was not possible to monitor any absorbance below 220 nm due to absorption of low wavelength light by laser optics in the path of the analysis beam. Typically, between fifty and one hundred photolysis experiments were added together to produce each set of time-resolved spectra. Individual spectra were recorded every 30 to 50 μs, and a typical series of time-resolved spectra is shown in Figure 6.2.

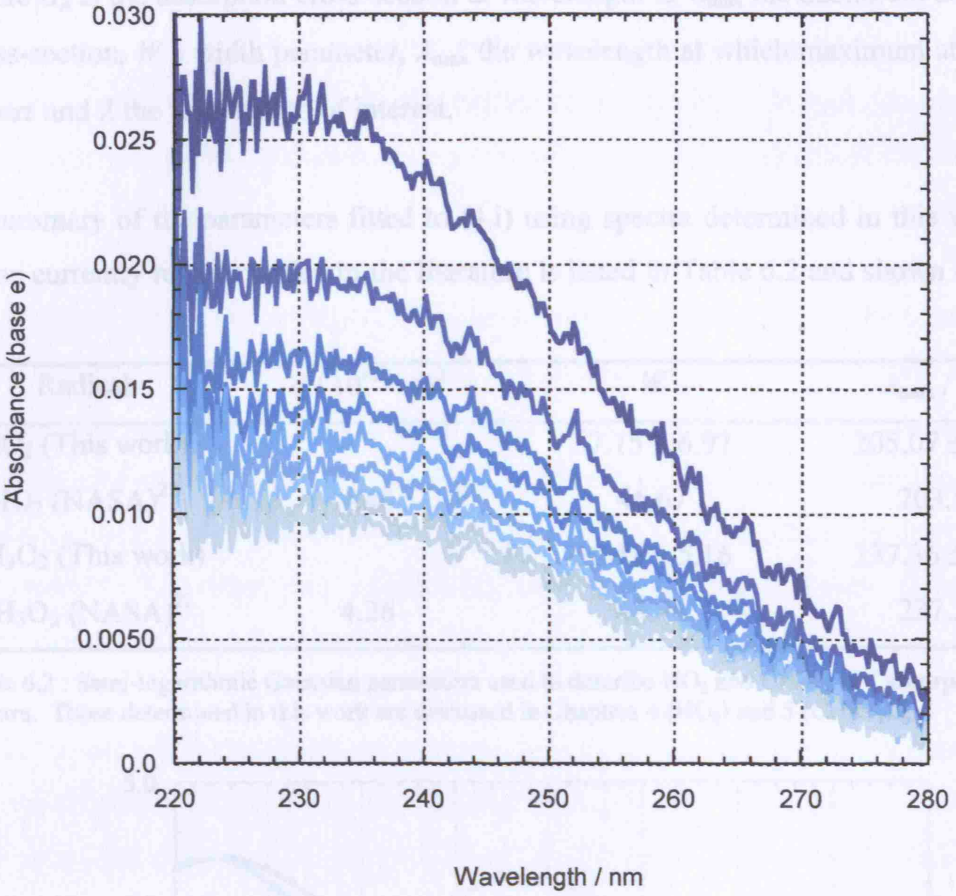

Figure 6.2 : Typical time-resolved absorbance spectra recorded at 2.5 ms intervals for the HO_2-CH_3O_2 cross-reaction.

Concentrations of HO_2 and CH_3O_2 were determined by fitting absorption cross-sections for the two species to the observed composite absorbance at each time point throughout the reaction. Cross-sections used for fitting were determined by normalisation of experimental absorption spectra, described by semi-logarithmic Gaussian functions to the maximum recommended absorption cross-sections,[22] as discussed in Chapters 4 and 5. The CH_3O_2 spectrum used was that determined using photolysis of $Cl_2/CH_4/O_2$ mixtures at 351 nm, section 5.4.2 (Chapter 5). Fitting two similar spectra to the observed absorbance is not trivial, but broadband monitoring of the absorbance, made possible by CCD detection, does offer advantages in this respect. Broadband spectroscopy enables the fitting procedure to take the shapes of the absorptions from the individual absorbers to be considered.

$$\sigma_\lambda = \sigma_{max} \exp\left\{-W\left[\ln\left(\frac{\lambda_{max}}{\lambda}\right)\right]^2\right\} \qquad (4.i)$$

where σ_λ is the absorption cross-section at wavelength λ, σ_{max} the maximum absorption cross-section, W a width parameter, λ_{max} the wavelength at which maximum absorption occurs and λ the wavelength of interest.

A summary of the parameters fitted to (4.i) using spectra determined in this work and those currently recommended in the literature is listed in Table 6.2 and shown in Figure 6.3.

Radical	σ / 10^{-18} cm^2	W	λ_{max} / nm
HO_2 (This work)		37.15 ± 6.97	205.07 ± 2.19
HO_2 (NASA)[22]	4.40	46.67	203.59
CH_3O_2 (This work)		50.41 ± 5.16	237.36 ± 0.99
CH_3O_2 (NASA)[22]	4.26	44.46	237.31

Table 6.2 : Semi-logarithmic Gaussian parameters used to describe HO_2 and CH_3O_2 UV absorption spectra. Those determined in this work are discussed in Chapters 4 (HO_2) and 5 (CH_3O_2).

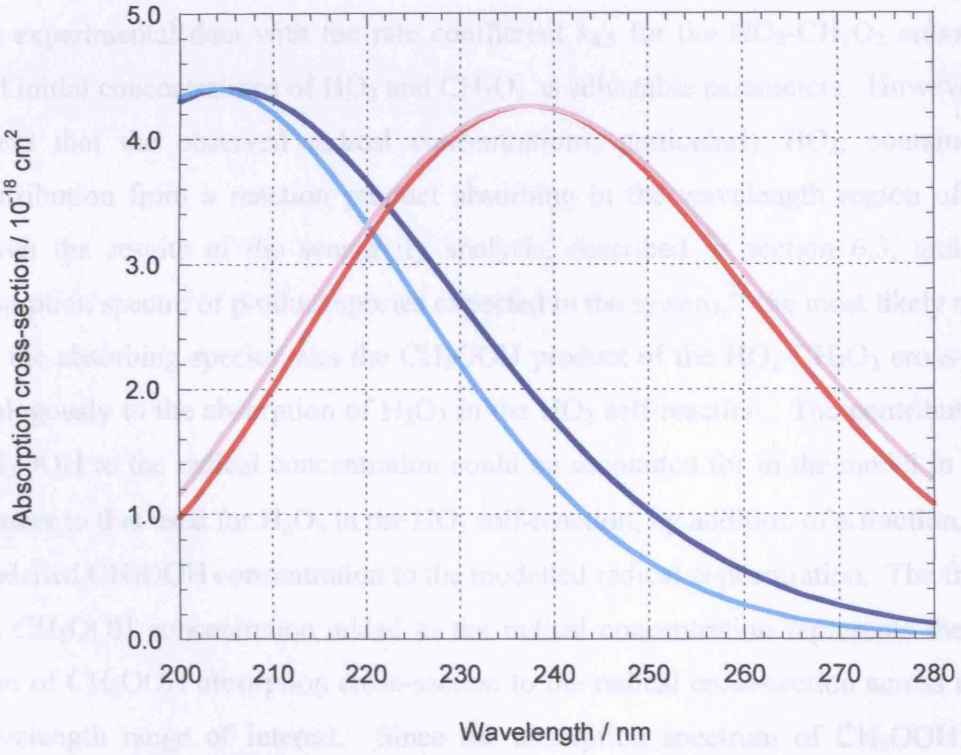

Figure 6.3 : HO_2 and CH_3O_2 UV absorption spectra. The dark blue line is the HO_2 spectrum determined in this work, normalised to the maximum absorption cross-section for the recommended HO_2 spectrum (light blue).[22] The red line shows the CH_3O_2 spectrum determined in this work using laser flash photolysis of $Cl_2/CH_4/O_2$ mixtures at 351 nm, normalised to the maximum absorption cross-section for the recommended CH_3O_2 spectrum (pink).[22]

6.5 Kinetic Analysis

Solutions to the differential equations describing the temporal behaviour of two cross-reacting species that are also both self-reacting are not trivial.[27] In such cases numerical integration is often used to simulate concentrations of species throughout the course of a reaction.

Kinetic parameters for the HO_2-CH_3O_2 cross-reaction were determined by fitting output from a model of the reaction system, constructed in the commercially available numerical integration package FACSIMILE, to the experimentally observed time-resolved concentrations of HO_2 and CH_3O_2. The model included the reactions listed in Table 6.1, with rate coefficients for the HO_2 and CH_3O_2 self-reactions as determined in this work. All other rate coefficients in the model were taken from current recommendations, and were as listed at 296 K in Table 6.1.

Initial experimental conditions were entered into the model, and the model used to fit to the experimental data with the rate coefficient $k_{6.5}$ for the HO_2-CH_3O_2 cross-reaction and initial concentrations of HO_2 and CH_3O_2 as adjustable parameters. However, it was found that the observed radical concentrations, particularly HO_2, contained some contribution from a reaction product absorbing in the wavelength region of interest. Given the results of the sensitivity analysis, described in section 6.3, and the UV absorption spectra of product species expected in the system,[22] the most likely candidate for the absorbing species was the CH_3OOH product of the HO_2-CH_3O_2 cross-reaction, analogously to the absorption of H_2O_2 in the HO_2 self-reaction. The contribution from CH_3OOH to the radical concentration could be accounted for in the model in a similar manner to that used for H_2O_2 in the HO_2 self-reaction, by addition of a fraction, γ, of the modelled CH_3OOH concentration to the modelled radical concentration. The fraction of the CH_3OOH concentration added to the radical concentration represents the average ratio of CH_3OOH absorption cross-section to the radical cross-section across the entire wavelength range of interest. Since the absorption spectrum of CH_3OOH is more similar to that of HO_2 than CH_3O_2, Figure 6.4, it was expected that the contribution from CH_3OOH would be manifested as HO_2 rather than CH_3O_2, as was indeed observed to be the case.

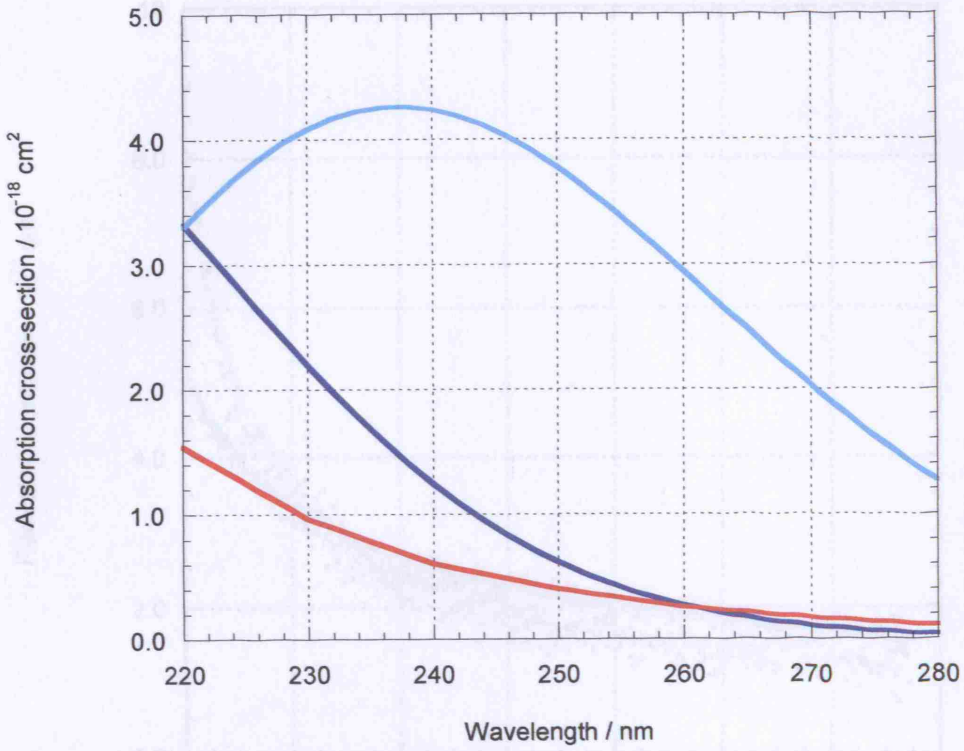

Figure 6.4 : Recommended[22] UV absorption spectra for HO_2 (dark blue), CH_3O_2 (light blue) and CH_3OOH (red). The CH_3OOH spectrum has been multiplied by a factor of ten to illustrate the similarities between the forms of HO_2 and CH_3OOH spectra.

The model was thus used to fit $k_{6.5}$, $[HO_2]_0$, $[CH_3O_2]_0$ and γ to the experimental data. A typical fit to the data is displayed in Figure 6.5.

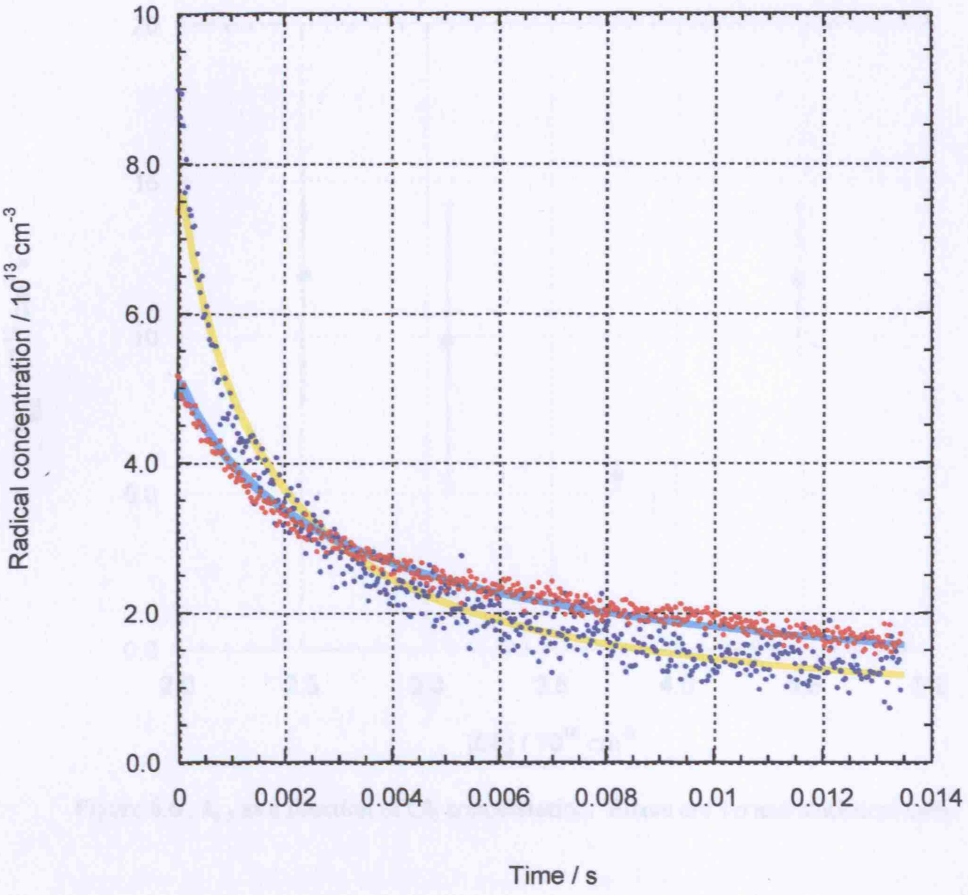

Figure 6.5 : Typical experimental time-resolved signals for HO_2 (blue) and CH_3O_2 (red) following photolysis. The fit to the data is given in yellow for HO_2, and light blue for CH_3O_2.

6.6 Results

At 296 K, $k_{6.5}$ was found to be $(6.94 \pm 2.35) \times 10^{-12}$ cm^3 s^{-1}, in reasonable agreement with the current NASA recommendation[22] of $\left(5.2^{+1.56}_{-1.20}\right)\times10^{-12}$ cm^3 s^{-1} at 298 K. Errors for this work are 1σ and statistical only. No significant dependence of $k_{6.5}$ on initial precursor concentrations was observed within the ranges $(2.51 - 4.48) \times 10^{16}$ cm^{-3} Cl_2, $(2.13 - 3.40) \times 10^{16}$ cm^{-3} CH_3OH, $(6.30 - 8.31) \times 10^{18}$ cm^{-3} CH_4, and $(1.26 - 2.28) \times 10^{18}$ cm^{-3} O_2, as shown in Figures 6.6 to 6.9. The factor γ was typically found to lie between 0.10 and 0.20, and was not observed to be dependent on experimental conditions. A full summary of results can be found in Appendix 6.

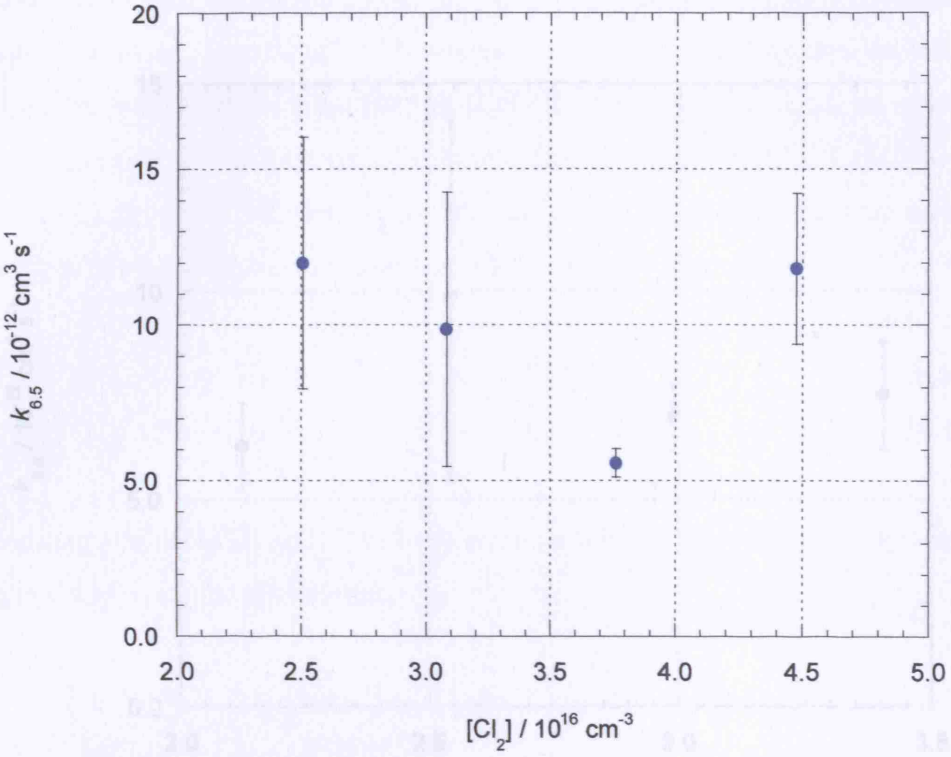

Figure 6.6 : $k_{6.5}$ as a function of Cl_2 concentration. Errors are 1σ and statistical only.

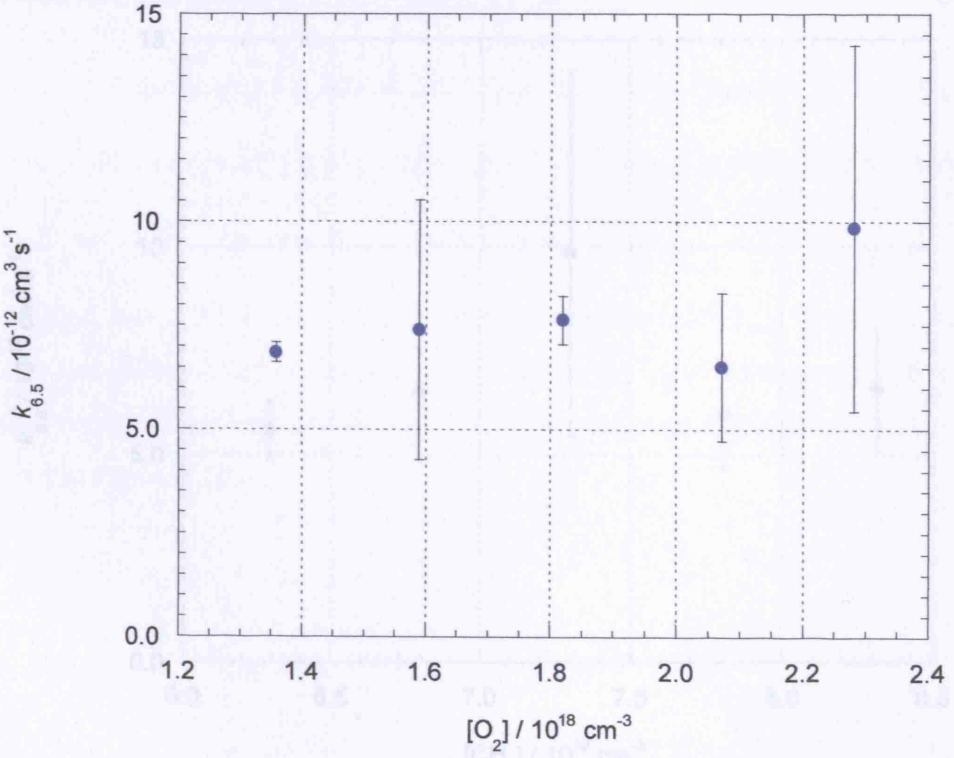

Figure 6.7 : $k_{6.5}$ as a function of O_2 concentration. Errors are 1σ and statistical only.

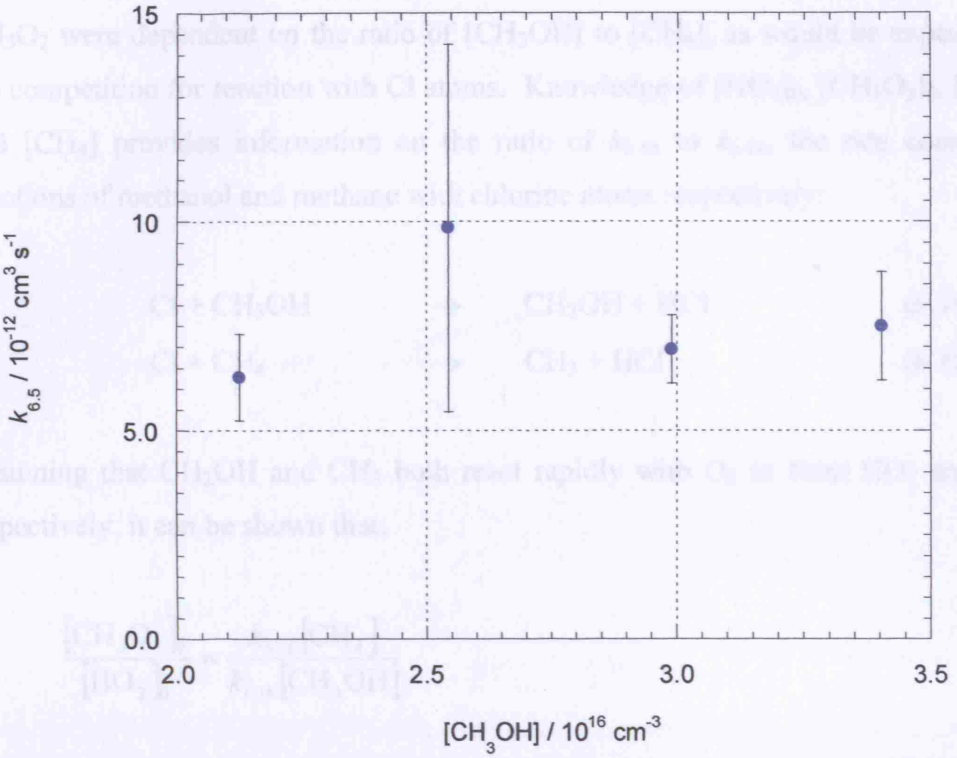

Figure 6.8 : $k_{6.5}$ as a function of CH_3OH concentration. Errors are 1σ and statistical only.

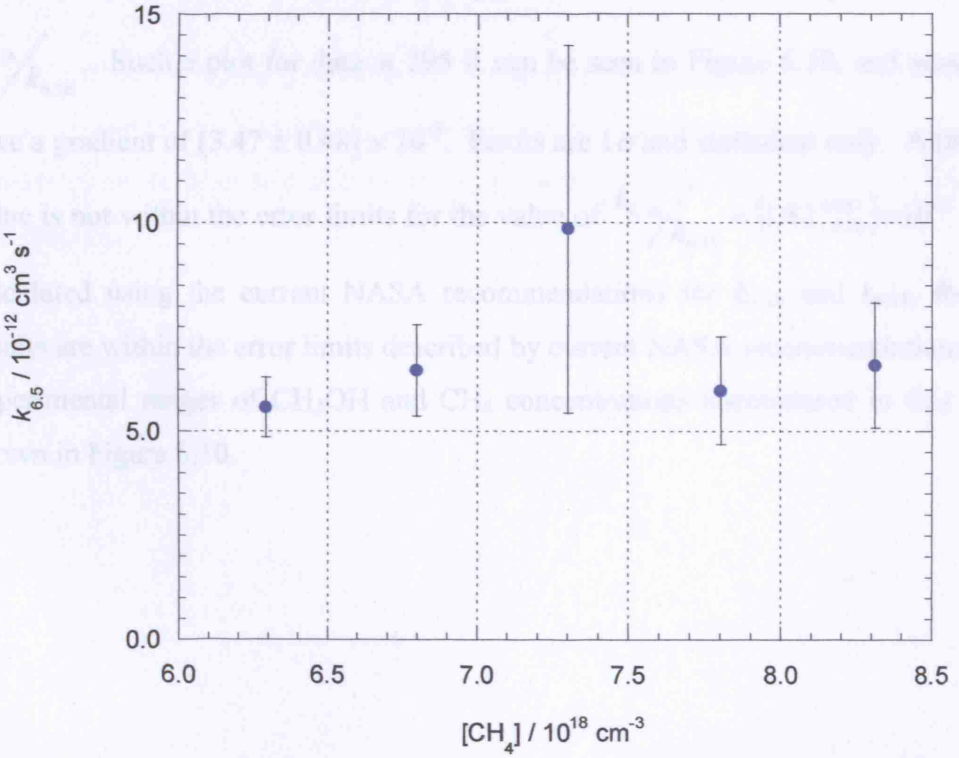

Figure 6.9 : $k_{6.5}$ as a function of CH_4 concentration. Errors are 1σ and statistical only.

Although $k_{6.5}$ was unaffected by the amount of methanol in the system, albeit over the limited range of concentrations investigated, the initial concentrations of HO_2 and CH_3O_2 were dependent on the ratio of $[CH_3OH]$ to $[CH_4]$, as would be expected from the competition for reaction with Cl atoms. Knowledge of $[HO_2]_0$, $[CH_3O_2]_0$, $[CH_3OH]$ and $[CH_4]$ provides information on the ratio of $k_{6.16}$ to $k_{6.18}$, the rate constants for reactions of methanol and methane with chlorine atoms respectively:

$$Cl + CH_3OH \rightarrow CH_2OH + HCl \qquad (6.16)$$

$$Cl + CH_4 \rightarrow CH_3 + HCl \qquad (6.18)$$

Assuming that CH_2OH and CH_3 both react rapidly with O_2 to form HO_2 and CH_3O_2 respectively, it can be shown that:

$$\frac{[CH_3O_2]_0}{[HO_2]_0} = \frac{k_{6.16}[CH_4]}{k_{6.18}[CH_3OH]}$$

Consequently, a plot of $[CH_3O_2]_0 / [HO_2]_0$ against $[CH_4] / [CH_3OH]$ has a gradient of $k_{6.16} / k_{6.18}$. Such a plot for data at 296 K can be seen in Figure 6.10, and was found to have a gradient of $(3.47 \pm 0.48) \times 10^{-3}$. Errors are 1σ and statistical only. Although this value is not within the error limits for the value of $k_{6.16} / k_{6.18} = \left(1.82^{+0.47}_{-0.38}\right) \times 10^{-3}$ at 298 K calculated using the current NASA recommendations for $k_{6.16}$ and $k_{6.18}$, the present results are within the error limits described by current NASA recommendations over the experimental ranges of CH_3OH and CH_4 concentrations encountered in this study, as shown in Figure 6.10.

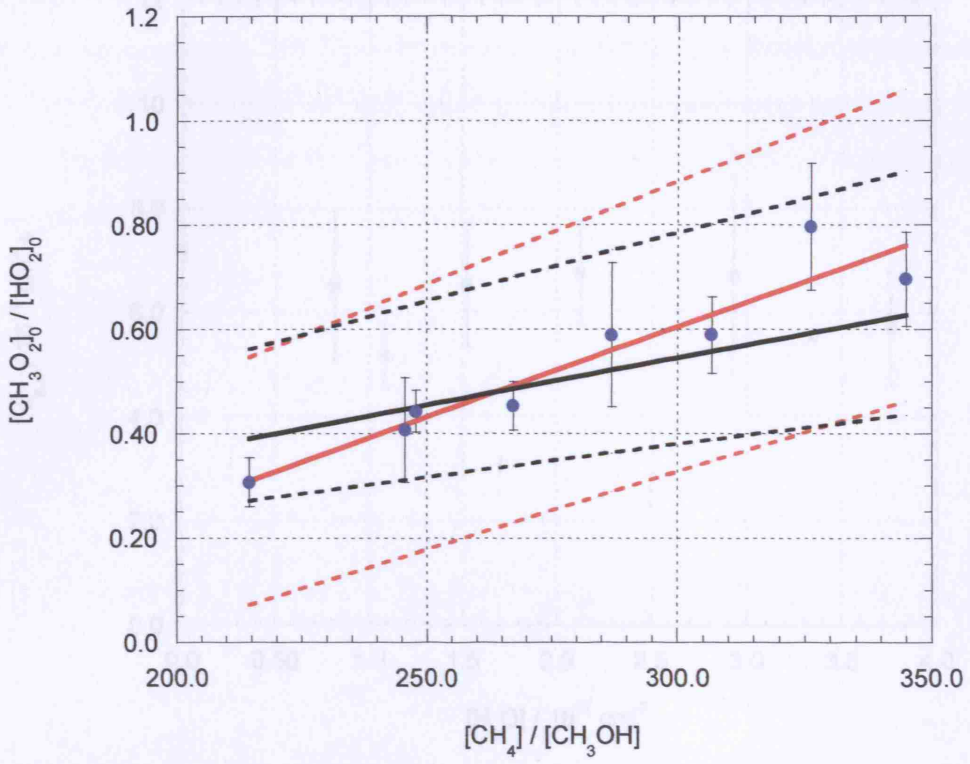

Figure 6.10 : Ratio of initial CH_3O_2 to HO_2 concentrations as a function of the ratio of CH_4 to CH_3OH. Results of this work are given by the blue points, with the fit to this data in red. The current NASA recommendation[22] is given by the black line. Upper and lower limits to this work and the NASA recommendation are given in the appropriately coloured broken lines. Errors are 1σ and statistical only.

Possible effects of water vapour on $k_{6.5}$ were investigated at both 296 K and 274 K. As shown in Figures 6.11 and 6.12, $k_{6.5}$ was not observed to be affected by the presence of water vapour at these two temperatures, in contrast to the rate coefficient for the HO_2 self-reaction.

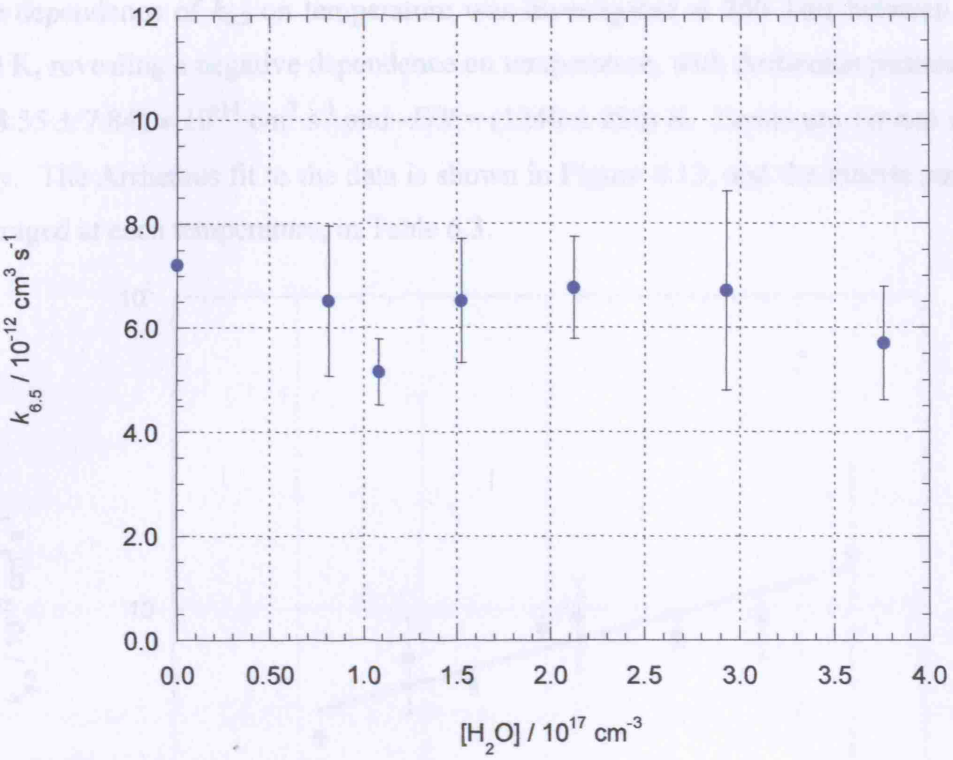

Figure 6.11 : $k_{6.5}$ as a function of H_2O concentration at 296 K. Errors are 1σ and statistical only.

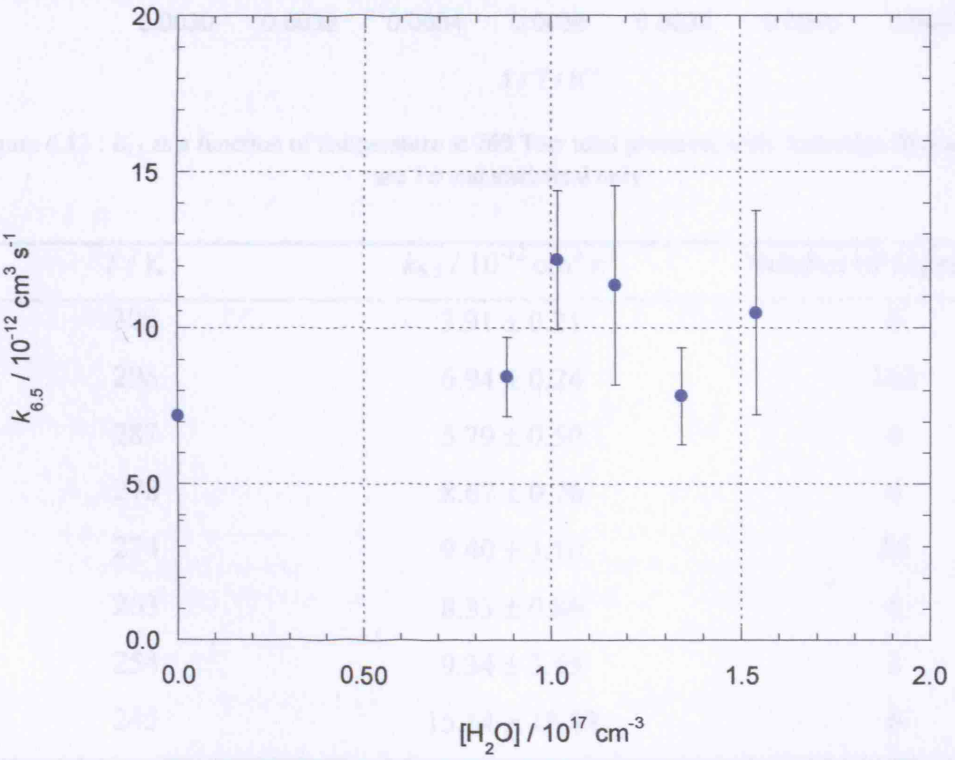

Figure 6.12 : $k_{6.5}$ as a function of H_2O concentration at 274 K. Errors are 1σ and statistical only.

The dependence of $k_{6.5}$ on temperature was investigated at 760 Torr between 245 and 309 K, revealing a negative dependence on temperature, with Arrhenius parameters of $A = (8.55 \pm 7.84) \times 10^{-14}$ cm^3 s^{-1} and $-E/R = (1240 \pm 250)$ K. Errors are 1σ and statistical only. The Arrhenius fit to the data is shown in Figure 6.13, and the kinetic parameters, averaged at each temperature, in Table 6.3.

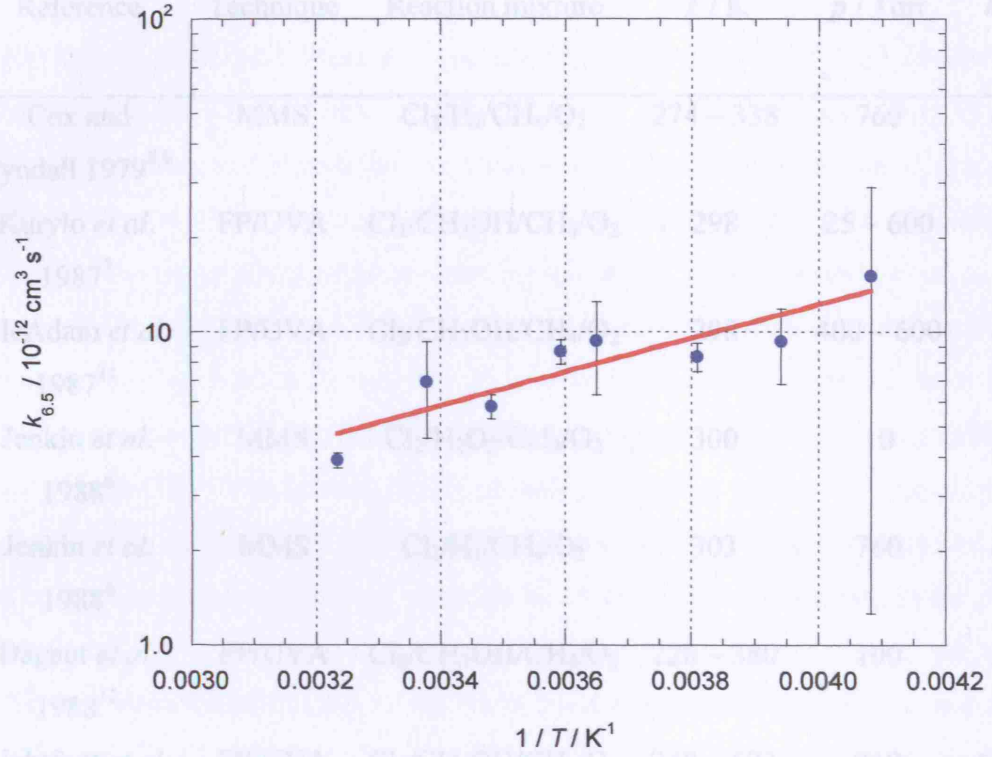

Figure 6.13 : $k_{6.5}$ as a function of temperature at 760 Torr total pressure, with Arrhenius fit (red). Errors are 1σ and statistical only.

T / K	$k_{6.5}$ / 10^{-12} cm^3 s^{-1}	Number of experiments
309	3.91 ± 0.21	6
296	6.94 ± 0.24	162
287	5.79 ± 0.50	6
278	8.67 ± 0.76	6
274	9.40 ± 3.10	26
263	8.33 ± 0.86	6
254	9.34 ± 2.55	2
245	15.14 ± 13.88	6

Table 6.3 : $k_{6.5}$ as a function of temperature at a pressure of 760 Torr.
Errors are are 1σ and statistical only.

6.7 Discussion

As shown in Table 6.4, values of $k_{6.5}$ at 296 K reported in this work are in excellent agreement with those of previous studies, with the exception of the results of Kurylo *et al.*[7] and Dagaut *et al.*[12]

Reference	Technique	Reaction mixture	T / K	p / Torr	$k_{6.5}$ / 10^{-12} cm^3 s^{-1}
Cox and Tyndall 1979[8,9]	MMS	$Cl_2/H_2/CH_4/O_2$	274 – 338	760	6.0 ± 0.9
Kurylo *et al.* 1987[7]	FP/UVA	$Cl_2/CH_3OH/CH_4/O_2$	298	25 – 600	2.9 ± 0.4
McAdam *et al.* 1987[11]	FP/UVA	$Cl_2/CH_3OH/CH_4/O_2$	298	400 – 600	6.4 ± 1.0
Jenkin *et al.* 1988[6]	MMS	$Cl_2/H_2O_2/CH_4/O_2$	300	10	5.4 ± 1.1
Jenkin *et al.* 1988[6]	MMS	$Cl_2/H_2/CH_4/O_2$	303	760	6.8 ± 0.9
Dagaut *et al.* 1988[12]	FP/UVA	$Cl_2/CH_3OH/CH_4/O_2$	228 – 380	100	2.9 ± 0.4
Lightfoot *et al.* 1990[5]	FP/UVA	$Cl_2/CH_3OH/CH_4/O_2$	248 – 573	210	5.43 ± 0.36
Lightfoot *et al.* 1990[5]	FP/UVA	$Cl_2/CH_3OH/CH_4/O_2$	248 – 573	760	6.2 ± 1.0
Boyd *et al.* 2003[13]	FP/UVA	$H_2O_2/CH_4/O_2$	298	760	5.13 ± 0.55
NASA 2002[22]			298	760	$5.2^{+1.56}_{-1.20}$
This work	FP/UVA	$Cl_2/CH_3OH/CH_4/O_2$	296	760	6.94 ± 2.35

Table 6.4 : Summary of previous investigations of $k_{6.5}$ at ambient temperature. MMS = molecular modulation spectrometry; FP = flash photolysis; UVA = ultraviolet absorption spectroscopy.

Slight differences between results reported in this work and those reported previously may be due to differences in the absorption cross-sections used for HO_2 and CH_3O_2 (all previous studies of HO_2 + CH_3O_2 reaction kinetics use UV absorption spectroscopy), or

differences in the rate coefficients for the HO_2 and CH_3O_2 self-reactions used in modelling of the cross-reaction. Such factors are not easily accounted for when re-analysing previous work considering reactions involving two distinct species, but it seems unlikely that differences in absorption cross-sections can explain the anomalous results of Kurylo *et al.*[7] and Dagaut *et al.*[12]

Both Kurylo *et al.* and Dagaut *et al.* used flash photolysis of $Cl_2/CH_3OH/CH_4/O_2$ mixtures coupled with UV absorption spectroscopy of CH_3O_2 radicals only to monitor the cross-reaction, and indeed the two studies were conducted by the same group at the National Bureau of Standards in Gathersburg, Maryland, with the work of Dagaut *et al.* extending the temperature range covered by the earlier work of Kurylo *et al.* at 298 K. However, the experiments of the Gathersburg group did not directly measure the initial concentrations of both HO_2 and CH_3O_2, and the initial concentrations were inferred from measurements of the fraction of Cl_2 photolysed, and initial concentrations of CH_3OH and CH_4. The fraction of Cl_2 photolysed under a given set of conditions was determined by measurement of the total absorbance in the absence of methanol, so that the only radical species produced was CH_3O_2. Subsequent experiments, in the presence of methanol, again measured the total absorbance of the reaction mixture, and used the previously determined fraction of Cl_2 photolysed to calculate the initial concentrations of HO_2 and CH_3O_2 from knowledge of $[CH_3OH]$ and $[CH_4]$, and of the rate coefficients for the reactions of CH_3OH and CH_4 with Cl atoms. This procedure relied on the invariance of the fraction of Cl_2 photolysed between experiments. It seems probable that the discrepancies between the Gathersburg group and other studies arise due to a systematic error in determination of the initial radical concentrations. Agreement between ($-E/R$) values of Dagaut *et al.* and Lightfoot *et al.*,[5] as listed in Table 6.5, also suggests that the discrepancies in the results of Kurylo *et al.* and Dagaut *et al.* are due to a systematic error.

Reference	Technique	T / K	Arrhenius fit
Cox and Tyndall[8,9]	MMS	274 – 338	$(7.7\ ^{+18.4}_{-5.4}) \times 10^{-14} \exp(1296 \pm 364/T)$
Dagaut *et al.*[12]	FP/UVA	228 – 380	$(3.0 \pm 1.2) \times 10^{-13} \exp(720 \pm 100/T)$
Lightfoot *et al.*[5]	FP/UVA	248 – 573	$(4.4 \pm 0.7) \times 10^{-13} \exp(780 \pm 55/T)$
NASA 2002[22]			$4.1 \times 10^{-13} \exp(750/T)$
This work	FP/UVA	245 – 309	$(8.55 \pm 7.84) \times 10^{-14} \exp(1240 \pm 250/T)$

Table 6.5 : Summary of Arrhenius parameters determined for $k_{6.5}$. MMS = molecular modulation spectrometry; FP = flash photolysis; UVA = ultraviolet absorption spectroscopy.

Measurements of $k_{6.5}$ made in this work between 245 and 309 K give Arrhenius parameters of $A = (8.55 \pm 7.84) \times 10^{-14}$ cm^3 s^{-1} and $-E/R = (1240 \pm 250)$ K. Errors are 1σ and statistical only. Results are in good agreement with previous work, as shown in Figures 6.14 and 6.15, and compare well to current recommendations[22] for $k_{6.5}$.

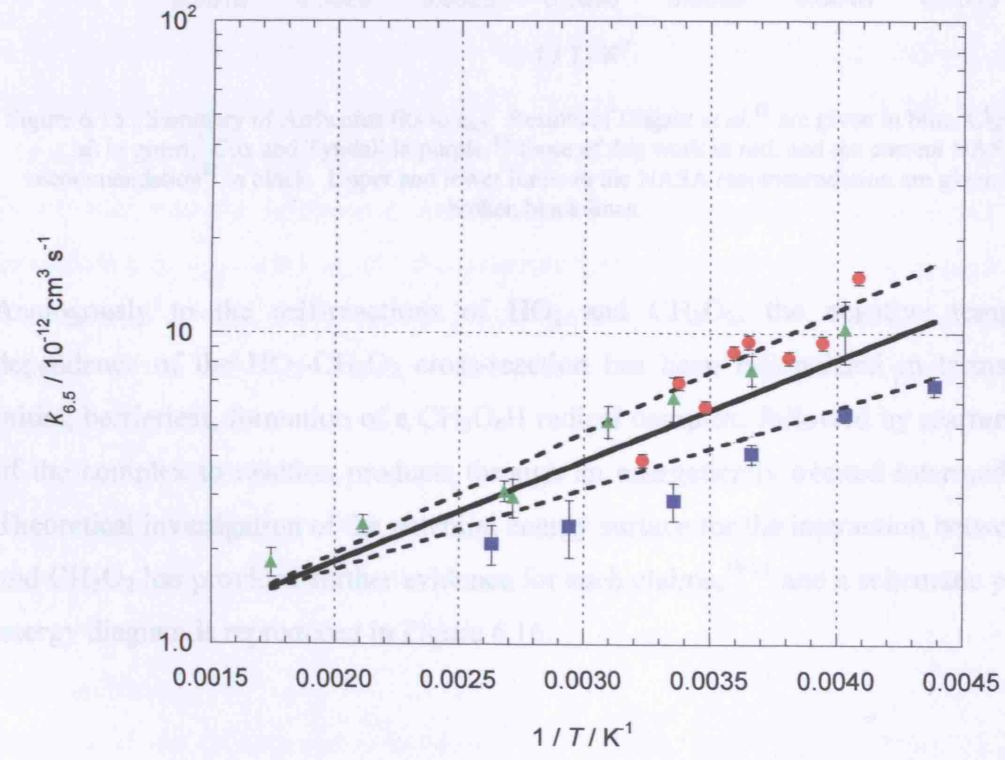

Figure 6.14 : Previous studies of $k_{6.5}$ as a function of temperature. Results of Dagaut *et al.*[12] are given in blue, with those of Lightfoot *et al.*[5] in green. Results for Cox and Tyndall[8,9] are not shown since no raw data were reported by these authors. Results of this work are shown in red, and the current NASA recommendation[22] above by the black line. Upper and lower limits to the NASA recommendation are given by the broken black lines. Errors for this work are 1σ and statistical only.

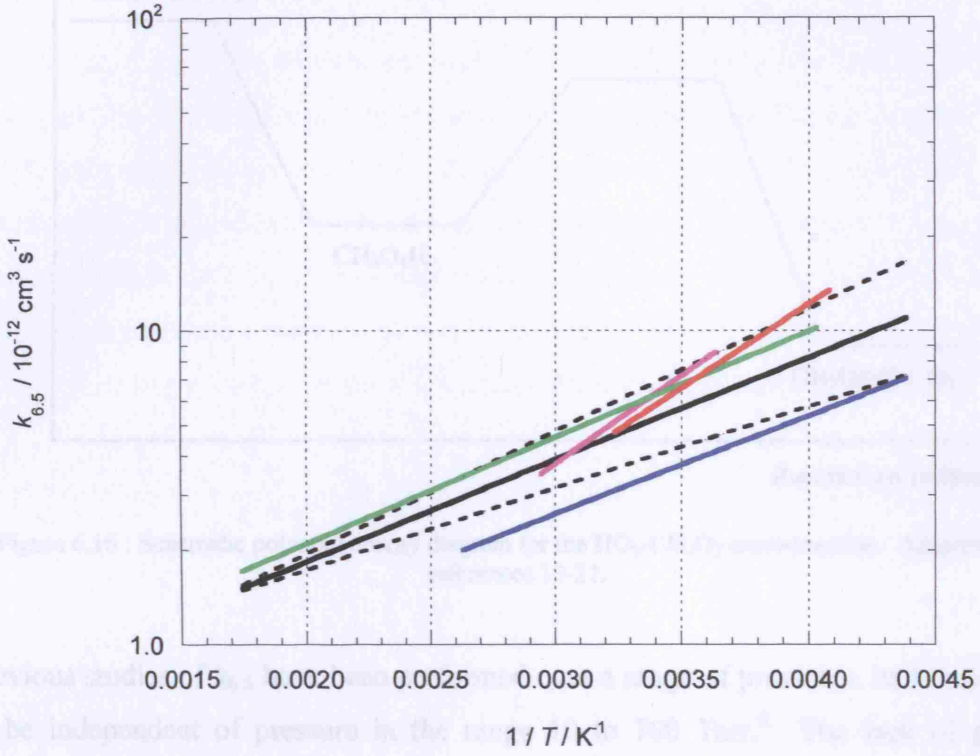

Figure 6.15 : Summary of Arrhenius fits to $k_{6.5}$. Results of Dagaut *et al.*[12] are given in blue, Lightfoot *et al.* in green,[5] Cox and Tyndall in purple,[8,9] those of this work in red, and the current NASA recommendation[22] in black. Upper and lower limits to the NASA recommendation are given by the broken black lines.

Analogously to the self-reactions of HO_2 and CH_3O_2, the negative temperature dependence of the HO_2-CH_3O_2 cross-reaction has been rationalised in terms of the initial, barrierless, formation of a CH_3O_4H radical complex, followed by rearrangement of the complex to reaction products through an energetically excited intermediate.[5,8,9] Theoretical investigation of the potential energy surface for the interaction between HO_2 and CH_3O_2 has provided further evidence for such claims,[19-21] and a schematic potential energy diagram is reproduced in Figure 6.16.

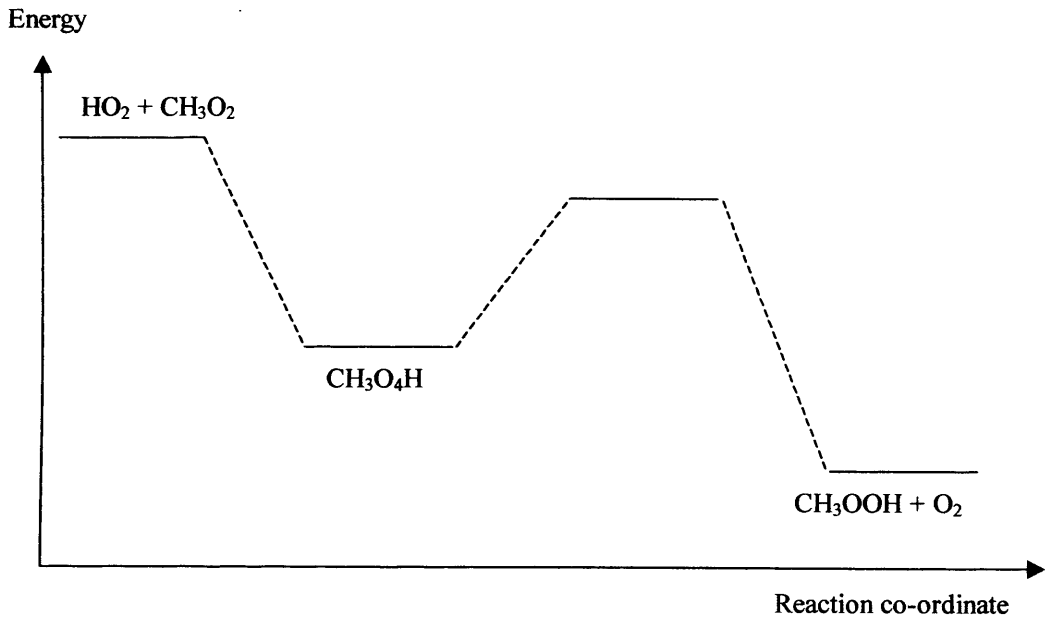

Figure 6.16 : Schematic potential energy diagram for the HO_2-CH_3O_2 cross-reaction. Adapted from references 19-21.

Previous studies of $k_{6.5}$ have been performed over a range of pressures, and indicate $k_{6.5}$ to be independent of pressure in the range 10 to 760 Torr.[6] The lack of pressure dependence suggests that the CH_3O_4H radical complex has sufficient degrees of vibrational freedom, compared to its HO_4H counterpart in the HO_2 self-reaction, to reduce the need for vibrational stabilisation by a third body. The apparent lack of dependence of $k_{6.5}$ on water and methanol vapours, as determined in this work and by Kurylo *et al.*[7] and Lightfoot *et al.*,[5] is also likely to be due to the increased vibrational stability of the CH_3O_4H complex compared to the HO_4H complex in the HO_2 self-reaction. The results of this investigation of $k_{6.5}$ therefore lend support to the theory that the effects of water and methanol on HO_2 self-reaction kinetics are due to vibrational stabilisation of the HO_4H complex, rather than a chaperone mechanism, as discussed in Chapter 4, and as discussed further in the concluding chapter.

6.8 Conclusions

Kinetics of the cross-reaction between HO_2 radicals and CH_3O_2 radicals have been investigated in this work at 760 Torr as a function of temperature, and of initial precursor gas concentrations between ranges that do not preclude rapid radical generation. An apparent negative activation energy for the reaction was observed, and Arrhenius parameters determined in this work are in good agreement with previous

studies. There is no evidence from this laboratory study to support the proposed underestimation of $k_{6.5}$ from model analysis of field data.[3,4]

The rate coefficient for reaction between HO_2 and CH_3O_2, $k_{6.5}$, was not observed to be dependent on the initial concentrations of precursor gases, including methanol, at 296 K. Results at 296 K compare well to those of previous studies. In addition, $k_{6.5}$ was not observed to be significantly affected by the presence of water vapour in the reaction system at 296 K or 274 K. Thus, whilst HO_2 is known to complex with water vapour at the temperatures and concentrations of water vapour adopted, this complex appears not to exert a strong influence on the kinetics of the HO_2-CH_3O_2 cross-reaction.

6.9 References

[1] R.P. Wayne, *Chemistry of Atmospheres*, Third edition, **2000**, Oxford University Press

[2] G. P. Brasseur, J. J. Orlando, G. S. Tyndall, *Atmospheric Chemistry and Global Climate Change*, **1999**, Oxford University Press

[3] F. Ravetta, D.J. Jacob, W.H. Brune, B.G. Heikes, B.E. Anderson, D.R. Blake, G.L. Gregory, G.W. Sasche, S.T. Sanholm, R.E. Shetter, H.B. Singh, R.W. Talbot, *J. Geophys. Res.*, **2001**, 106, 32709

[4] M.M. Frey, R.W. Stewart, J.R. McConnell, R.C. Bales, *J. Geophys. Res.*, **2005**, 110, 23301

[5] P.D. Lightfoot, R. Lesclaux, B. Veyret, *J. Phys. Chem.*, **1990**, 94, 708

[6] M.E. Jenkin, R.A. Cox, G.D. Hayman, L.J. Whyte, *J. Chem. Soc. Farad. Trans. II*, **1988**, 84, 7, 913

[7] M.J. Kurylo, P. Dagaut, T.J. Wallington, D.M. Neuman, *Chem. Phys. Lett.*, **1987**, 139, 6, 513

[8] R.A. Cox and G.S. Tyndall, *Chem. Phys. Lett.*, **1979**, 65, 357

[9] R. Cox and G.S. Tyndall, *J. Chem. Soc. Farad. Trans. II*, **1980**, 76, 153

[10] R. A. Cox and J. P. Burrows, *J. Phys. Chem.*, **1979**, 83, 2560

[11] K. McAdam, B. Veyret, R. Lesclaux, *Chem. Phys. Lett.*, **1987**, 133, 1, 39

[12] P. Dagaut, T.J. Wallington, M.J. Kurylo, *J. Phys. Chem.*, **1988**, 92, 3833

[13] A.A. Boyd, P.M. Flaud, N. Daugey, R. Lesclaux, *J. Phys. Chem. A*, **2003**, 107, 818

[14] C.S. Kan, J.G. Calvert, J.H. Shaw, *J. Phys. Chem.*, **1980**, 84, 3411

[15] G.K. Moortgat, R.A. Cox, G. Schuster, J.P.Burrows, G.S. Tyndall, *J. Chem. Soc. Farad. Trans. 2*, **1989**, 85, 809

[16] T.J. Wallington and S.M. Japar, *Chem. Phys. Lett.*, **1990**, 167, 513

[17] T.J. Wallington, *J. Chem. Soc. Farad. Trans.*, **1991**, 87, 2379

[18] M.J. Elrod, D.L. Ranschaert, N.J. Schneider, *Int. J. Chem. Kinet.*, **2001**, 33, 363

[19] H. Hou and B. Wang, *J. Phys. Chem. A*, **2005**, 109, 451

[20] X.M. Zhou, Z.Y. Zhou, Q.Y. Wu, A.F. Jalbout, N. Zhang, *Int. J. Quant. Chem.*, **2006**, 106, 514

[21] J.M. Anglada, S. Olivella, A. Sole, *J. Phys. Chem. A*, **2006**, 110, 6073

[22] S. P. Sander, R. R. Friedl, D. M. Golden, M. J. Kurylo, R. E. Huie, V. L. Orkin, G. K. Moortgat, A. R. Ravishankara, C. E. Kolb, M. J. Molina, *Chemical Kinetics and Photochemical Data for Use in Atmospheric Studies*, **2002**, Evaluation Number 14, JPL Publication 02-25, Jet Propulsion Laboratory, Pasadena, CA., USA

[23] R. Timonen, *Ann. Acad. Sci. Fenn. Ser. A2*, **1988**, 218, 5

[24] T.T. Song and T.M Su, *J. Phys. Chem.*, **1996**, 100, 13554

[25] W. Tsang and R.F. Hamilton, *J. Phys. Chem. Ref. Data*, **1986**, 15, 1087

[26] J. Espinosa-Garcia and J.C. Corchado, *J. Chem. Phys.*, **1996**, 105, 3517

[27] A.E. Croce, L.V. Mogni, C. Vicente Irrazabal, *Int. J. Chem. Kinet.*, **2003**, 35, 246

Chapter 7
Concluding Remarks

The results presented in this thesis represent extensive studies of the kinetics of the HO_2 and CH_3O_2 radical self-reactions, and of the cross-reaction between HO_2 and CH_3O_2 radicals. In particular, the investigation of HO_2 self-reaction kinetics reported in this work is the most extensive to date, and the rate coefficient for this reaction has been characterised in this work as a function of temperature, pressure and concentrations of water and methanol vapours in the reaction system. Results indicate that the rate of the HO_2 self-reaction in the atmosphere may be significantly greater than currently expected on the basis of previous studies, particularly at the low temperatures encountered in the tropical upper troposphere. Furthermore, the use of results reported in this work in atmospheric models has been shown to directly affect modelled H_2O_2 and to improve the agreement between modelled and observed concentrations of H_2O_2, the product of the HO_2 self-reaction.[1] Such results serve to highlight the need for direct kinetic measurements over relevant parameter space.

In addition, the discrepancies between this work and that of Christensen *et al.*[2,3] illustrate the need for repeated measurements of the same kinetic parameters in different laboratories, and particularly using complementary techniques. Indeed, the discrepancies indicate that investigation of the HO_2 self-reaction is still not complete, and that the effects of methanol – the most extensively used laboratory precursor to HO_2 – on HO_2 self-reaction kinetics are in need of further attention still.

Investigation of the CH_3O_2 self-reaction was conducted using two different chemical schemes for generation of the CH_3O_2 radical. The first of these employed laser flash photolysis of $CH_3Cl/CH_4/O_2$ mixtures at 193 nm, but this could only be used over a relatively narrow range of experimental conditions due to the occurrence of inevitable secondary chemistry attributed to the chlorinated peroxy radical $ClCH_2O_2$, formed from the parent molecule CH_3Cl. This study illustrated the need to design convenient radical source chemistry in flash photolysis studies, such that wherever possible radicals are produced cleanly and exclusively. The second method used for CH_3O_2 production, involving laser flash photolysis of $Cl_2/CH_4/O_2$ mixtures at 351 nm, was found to be far

more versatile than the first, and enabled investigation of CH_3O_2 self-reaction kinetics over a wider range of experimental conditions. In contrast to the HO_2 self-reaction, kinetics of the CH_3O_2 self-reaction were not observed to be affected by the presence of water vapour, even at reduced temperatures where radical complexation is generally stronger.

Kinetics of the cross-reaction between HO_2 and CH_3O_2 radicals, investigated over a range of tropospherically relevant conditions, were also characterised in this work. The results show excellent agreement with the majority of previous studies, and therefore do not support the proposal[4,5] that the HO_2-CH_3O_2 cross-reaction rate is underestimated in models. Furthermore, the kinetics of the HO_2-CH_3O_2 cross-reaction were observed to be unaffected by the presence of water vapour. As discussed in this work, the rate of reaction of HO_2 with itself is known to be enhanced in the presence of water vapour, and similar effects have been reported for the reaction of HO_2 with NO.[6,7] This is attributed to $HO_2.H_2O$ complexation, but it is not clear why certain reactions of HO_2 are affected by the presence of water vapour, while others are not.

Calculations have predicted that a significant fraction of HO_2 radicals in the troposphere exists in the complexed form $HO_2.H_2O$,[8,9] and the effects of H_2O on HO_2 chemistry are therefore potentially of extreme importance in the lower atmosphere. It is possible that the different effects of water on different reactions of HO_2 lie in the differences between vibrational stabilities of the reaction intermediates involved. It is proposed that the greater number of vibrational modes available in any HO_2 + CH_3O_2 reaction intermediate, compared to intermediates in the HO_2 + HO_2 and HO_2 + NO reactions, renders the HO_2 + CH_3O_2 intermediate less likely to be affected by the presence of additional vibrational modes afforded by complexation with water. This theory therefore supports the suggestion that the effects of water vapour on HO_2 self-reaction kinetics are due to the complexation, and the subsequent increase in stability due to the increased number of available vibrational modes, of the HO_4H reaction intermediate with water vapour.

Theoretical investigation of the potential energy surfaces for interaction between free HO_2 radicals and complexed $HO_2.H_2O$ species, and of the $HO_2.H_2O$ complex with other species such as CH_3O_2, would provide further insight into the mechanisms for the

effects of water on HO_2 chemistry. In addition, notwithstanding the experimental challenge, it would be interesting to conduct further experimental study HO_2 reaction kinetics with other tropospherically important species ($CH_3C(O)O_2$, O_3, BrO and IO, for example) to investigate the possibility of potential effects of water vapour on other reactions of HO_2, and indeed on the chemistry of the troposphere.

7.1 References

[1] J.R. Olson, J. Crawford, G. Chen, M. Pippin, AGU December 2005, Poster A43C-0072

[2] L.E. Christensen, M. Okumura, S. P. Sander, R. J. Salawitch, G. C. Toon, B. Sen, J. F. Blavier and K. W. Jucks, *Geophys. Res. Lett.*, **2002**, 29, 9

[3] L.E. Christensen, M. Okumura, J.C. Hansen, S.P. Sander, J.S. Francisco, *J. Phys. Chem. A*, **2006**, 110, 6948

[4] F. Ravetta, D.J. Jacob, W.H. Brune, B.G. Heikes, B.E. Anderson, D.R. Blake, G.L. Gregory, G.W. Sasche, S.T. Sanholm, R.E. Shetter, H.B. Singh, R.W. Talbot, *J. Geophys. Res.*, **2001**, 106, 32709

[5] M.M. Frey, R.W. Stewart, J.R. McConnell, R.C. Bales, *J. Geophys. Res.*, **2005**, 110, 23301

[6] C. C. Kircher and S. P. Sander, *J. Phys. Chem.*, **1984**, 88, 2082

[7] N.I. Butkovskaya, A. Kukui, N. Pouvesle, G. Le Bras, *J. Phys. Chem. A*, **2005**, 109, 6509

[8] S. Aloisio and J.S. Francisco, *J. Phys. Chem. A*, **1998**, 102, 1899

[9] K.S. Alongi, T.S. Dibble, G.C. Shields, K.N. Kirschner, *J. Phys. Chem. A*, **2006**, 110, 3686

Appendix 1
Calibration Procedures

A1.1 Gas Flow Rates

A1.1.1 Mass Flow Controllers

Mass flow controllers (MFCs) were calibrated by measuring the time taken for a set flow of gas to sweep out a known volume, determined by use of a modified burette. MFCs were connected to a burette *via* a tube fitted with a T-piece. Soapy water was injected into the flow of gas from the MFC *via* the T-piece, and the time taken for a meniscus to pass through a known volume in the burette was recorded. The procedure was repeated at different mass flow settings on each MFC, in random order, and, following corrections for standard conditions of temperature and pressure, calibration plots, such as that shown in Figure A1.1, were used to determine the actual flow of gas by linear regression.

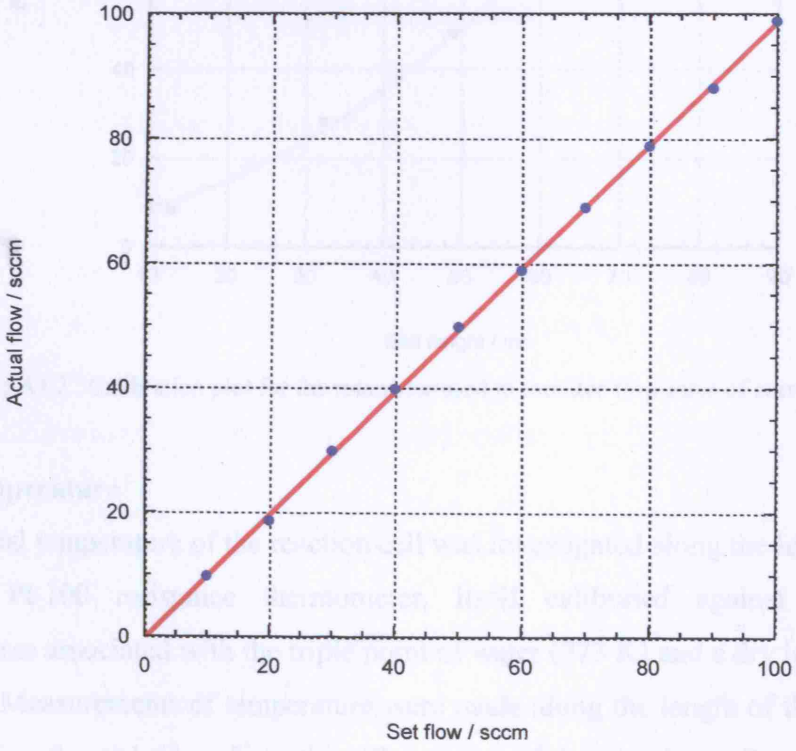

Figure A1.1 : Calibration plot for mass flow controllers.

A1.1.2 Rotameter

The rotameter, used to measure flows of corrosive gases such as Cl_2 (diluted in N_2), was calibrated by passing known flows of pure N_2, from a calibrated MFC, through the rotameter and noting the ball height. A calibration plot, such as that shown in Figure A1.2, was produced, and a polynomial equation least squares fitted to the data to allow determination of the actual flow rate of the gas from the ball height of the rotameter. The procedure was repeated at several flow rates in random order, and at several pressures.

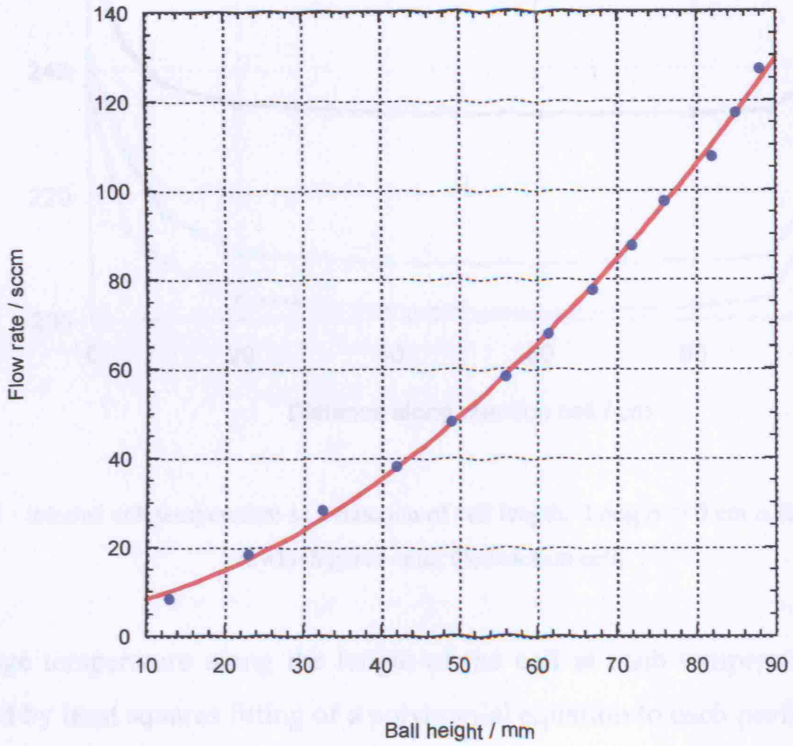

Figure A1.2 : Calibration plot for the rotameter used to monitor flow rates of corrosive gases.

A1.2 Temperature

The internal temperature of the reaction cell was investigated along the length of the cell using a Pt-100 resistance thermometer, itself calibrated against the literature temperatures associated with the triple point of water (273 K) and a dry ice/acetone bath (195 K). Measurements of temperature were made along the length of the reaction cell by removing the end piece from the effluent end of the reaction cell and inserting the thermometer into a typical experimental flow of 1000 sccm of N_2. The tip of the thermometer was prevented from making contact with the walls of the reaction cell by

use of a wire mesh. Measurements were made, in random order, at 10 cm intervals along the length of the cell. The procedure was repeated at a number of different temperature settings, and results are shown in Figure A1.3.

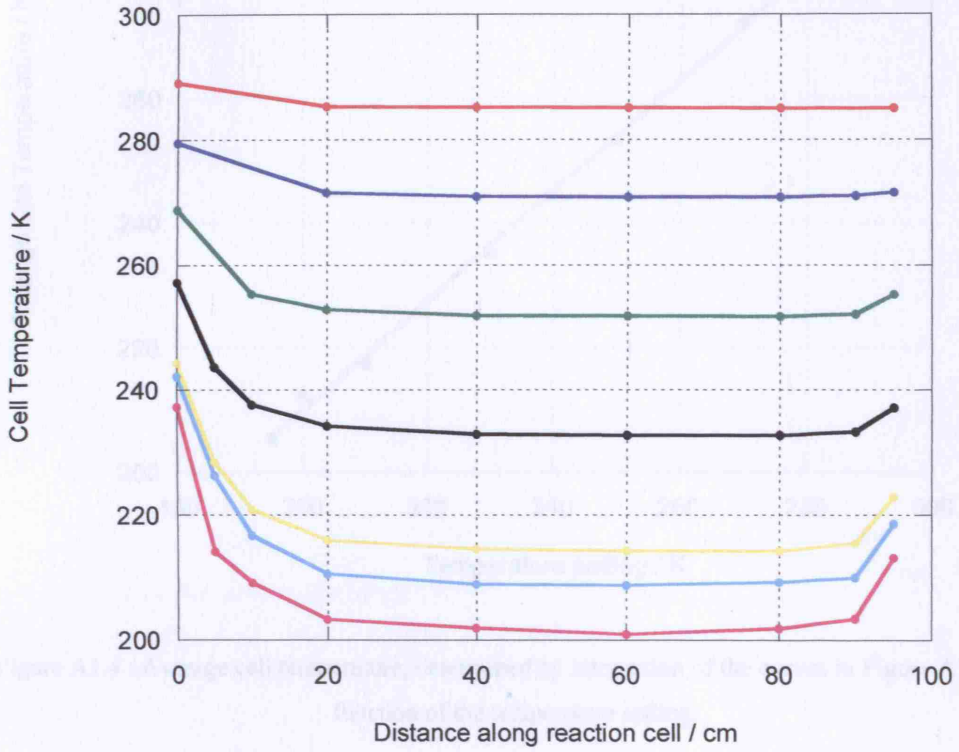

Figure A1.3 : Internal cell temperature as a function of cell length. Length = 0 cm is defined as the point at which gases enter the reaction cell.

The average temperature along the length of the cell at each temperature setting was determined by least squares fitting of a polynomial equation to each profile, followed by integration of the polynomial along the length of the cell. A plot of the average temperature in the cell against the temperature setting is given in Figure A1.4.

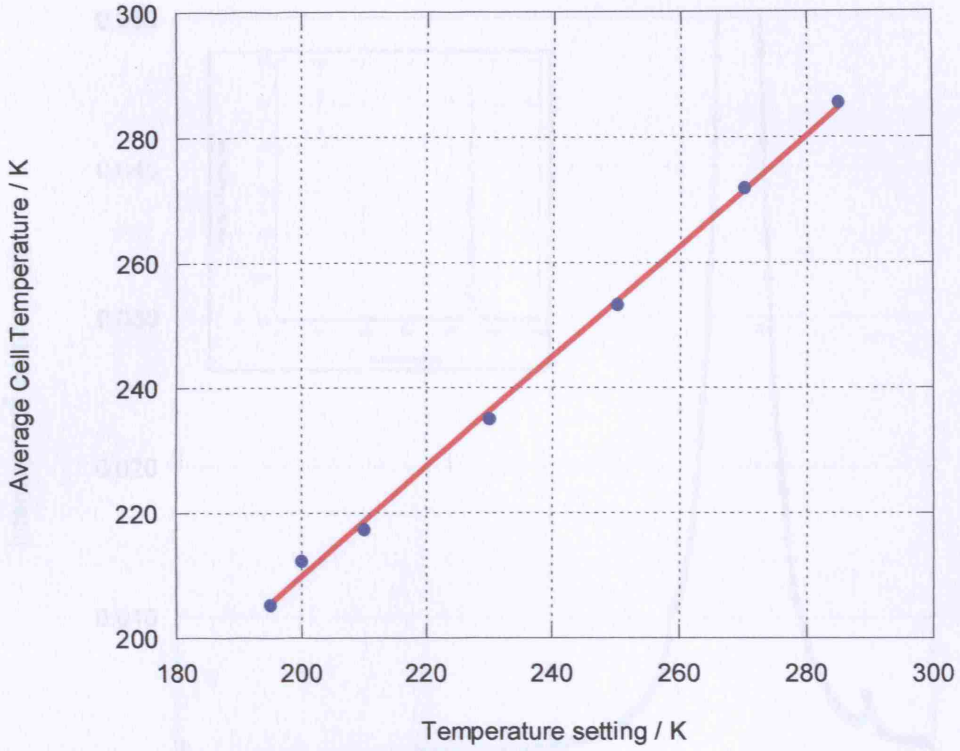

Figure A1.4 : Average cell temperature, determined by integration of the curves in Figure A1.3, as a function of the temperature setting.

A1.3 Wavelength

Wavelength calibration was conducted for each set of experiments. Calibration was achieved by recording the spectrum of a low pressure mercury pen-ray lamp (Oriel), under identical experimental conditions except for use of a narrow entrance slit width to the spectrograph. The Hg spectrum has well-defined sharp features, as shown in Figure A1.5.

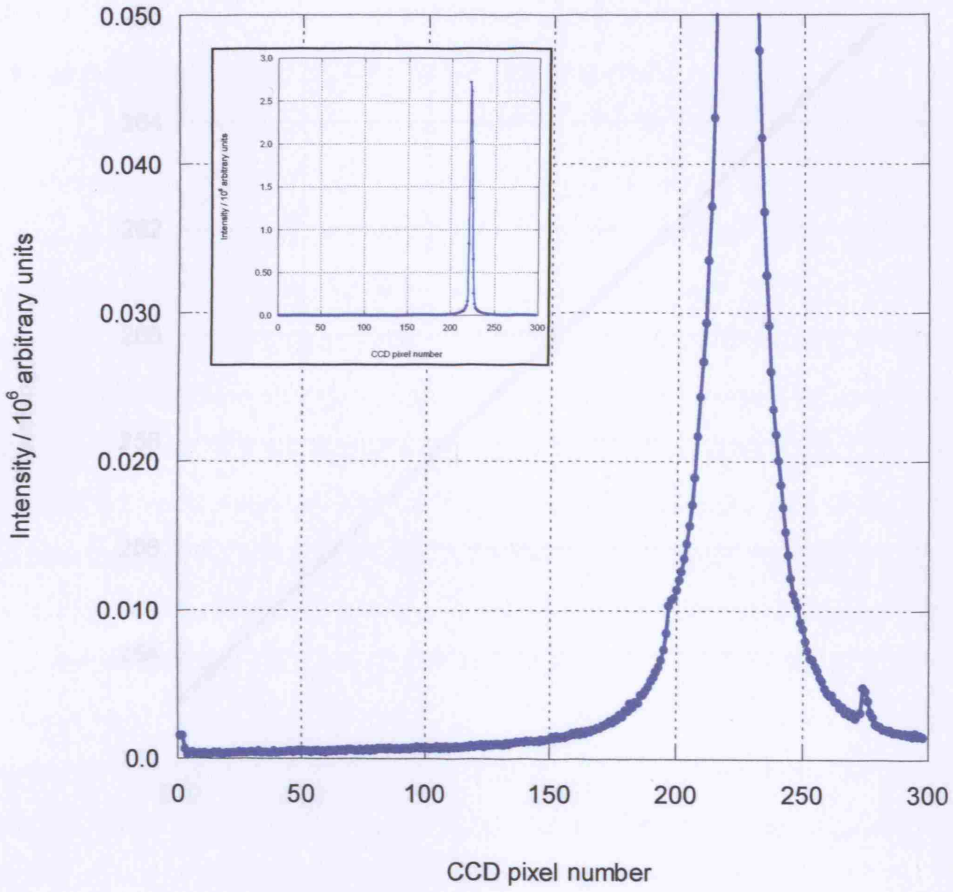

Figure A1.5 : Light intensity emitted by a low pressure Hg pen-ray lamp. Main figure shows a close-up of the recorded Hg spectrum, while the inset figure shows the full spectrum recorded.

By recording the CCD pixel number at which the well-defined Hg peaks were observed to occur it was possible to produce a calibration plot, such as that shown in Figure A1.6. The calibration plot could consequently be used to assign wavelength points to each pixel on the CCD using linear regression. In cases where only one Hg peak could be observed it was necessary to use the dispersion measured from other experiments with the same diffraction grating (0.226 nm per pixel for the 300 grooves per mm grating).

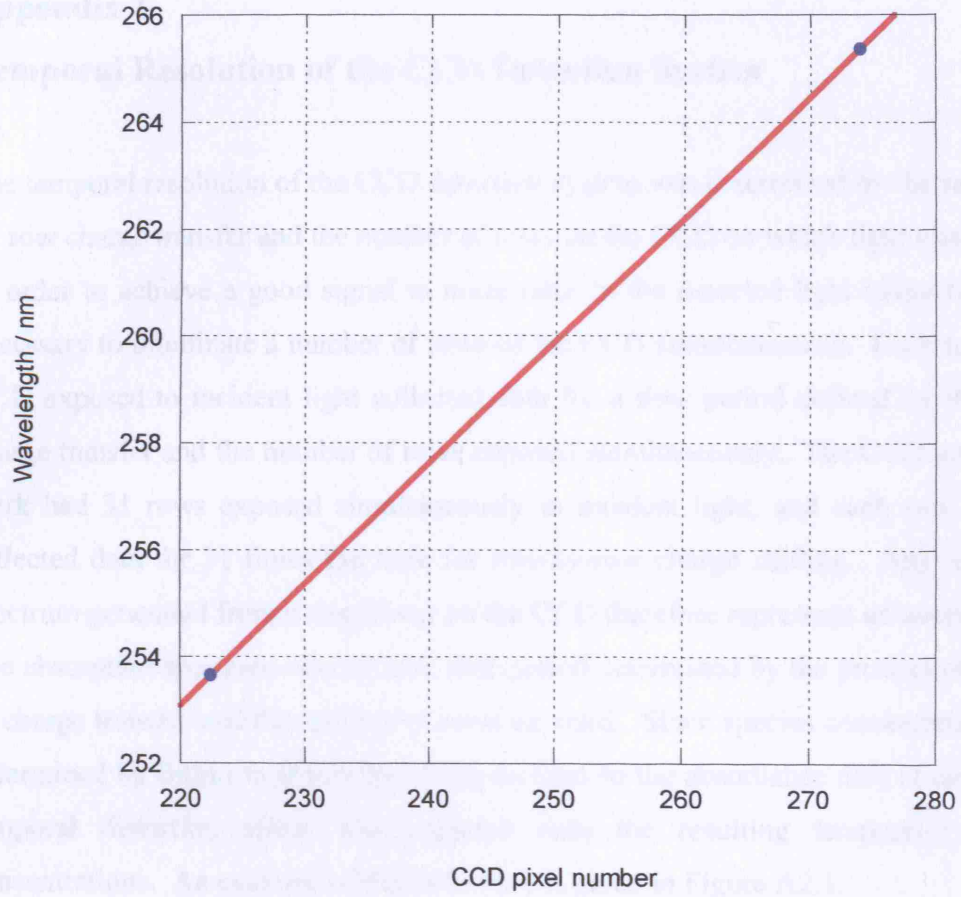

Figure A1.6 : Calibration plot for the wavelength axis of the CCD.

Appendix 2

Temporal Resolution of the CCD Detection System

The temporal resolution of the CCD detection system was determined by the rate of row by row charge transfer and the number of rows on the CCD on which light was incident. In order to achieve a good signal to noise ratio in the detected light intensities it was necessary to illuminate a number of rows of the CCD simultaneously. Each row on the CCD exposed to incident light collected data for a time period defined by the rate of charge transfer and the number of rows exposed simultaneously. The CCD used in this work had 31 rows exposed simultaneously to incident light, and each row therefore collected data for 31 times the time for row-by-row charge shifting. Any absorption spectrum generated from a single row on the CCD therefore represents an average of the true absorption spectrum over a finite time period determined by the product of the time of charge transfer and the number of rows exposed. Since species concentrations were determined by fitting to absorption cross-sections to the absorbance data at each row, a temporal distortion effect was imparted onto the resulting temporally resolved concentrations. An example of this distortion is given in Figure A2.1.

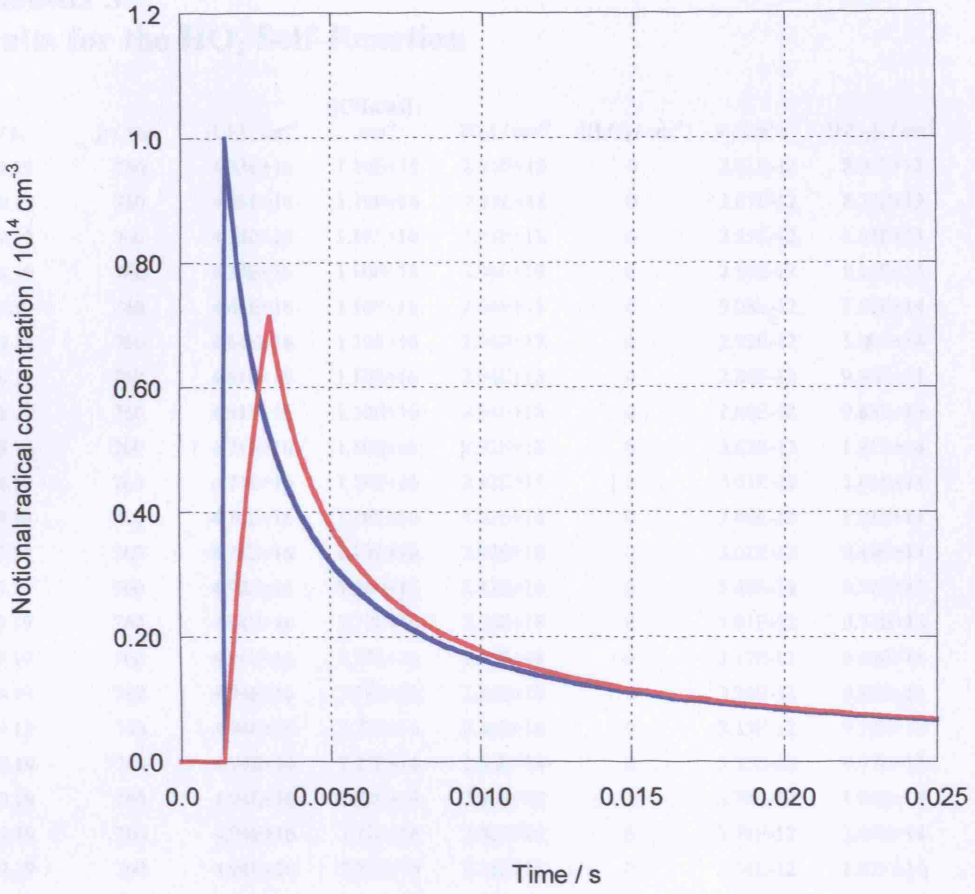

Figure A2.1 : Modelled effects of simultaneous illumination of 31 rows of the CCD. The undistorted time profile is shown in blue, with the temporally distorted profile shown in red.

Distortions in kinetic parameters inferred from the uncorrected temporally averaged concentration data were prevented by simulation of the distortion within the numerical model used to analyse a given data set. The true concentrations were simulated by classical or numerical integration techniques, and the temporal distortion imparted to the simulated data by application of an averaging function. The averaged simulation was subsequently least squares fitted to the experimental data to determine the desired kinetic parameters. Whilst the temporal distortion evidently degrades the time resolution of the apparatus it does so in a quantifiable fashion and therefore does not introduce any errors to the data.

Appendix 3
Results for the HO_2 Self-Reaction

T / K	p / Torr	$[Cl_2]$ / cm^{-3}	$[CH_3OH]$ / cm^{-3}	$[O_2]$ / cm^{-3}	$[H_2O]$ / cm^{-3}	k / $cm^3\ s^{-1}$	$[HO_2]_0$ / cm^{-3}	α
309.19	760	4.33E+16	1.10E+16	2.94E+18	0	2.61E-12	8.96E+13	0.0926
309.19	760	4.33E+16	1.10E+16	2.94E+18	0	2.67E-12	8.79E+13	0.1352
309.19	760	4.33E+16	1.10E+16	2.94E+18	0	2.55E-12	8.35E+13	0.0648
309.19	760	4.33E+16	1.10E+16	2.94E+18	0	2.55E-12	8.15E+13	0.0693
309.19	760	4.61E+16	1.10E+16	2.94E+18	0	3.08E-12	1.05E+14	0.1855
309.19	760	4.61E+16	1.10E+16	2.94E+18	0	2.93E-12	1.00E+14	0.1276
309.19	760	4.61E+16	1.10E+16	2.94E+18	0	2.84E-12	9.96E+13	0.1043
309.19	760	4.61E+16	1.10E+16	2.94E+18	0	2.80E-12	9.83E+13	0.1393
309.19	760	4.74E+16	1.10E+16	2.92E+18	0	3.62E-12	1.21E+14	0.1567
309.19	760	4.74E+16	1.10E+16	2.92E+18	0	3.01E-12	1.01E+14	0.1034
309.19	760	4.74E+16	1.10E+16	2.92E+18	0	3.40E-12	1.03E+14	0.1508
309.19	760	4.74E+16	1.10E+16	2.92E+18	0	3.02E-12	9.49E+13	0.1615
309.19	760	4.92E+16	3.36E+17	2.43E+18	0	5.48E-12	9.52E+13	0.0727
309.19	760	4.94E+16	7.77E+16	2.36E+18	0	3.01E-12	9.71E+13	0.0380
309.19	760	4.94E+16	7.77E+16	2.36E+18	0	3.17E-12	9.69E+13	0.0342
309.19	760	4.94E+16	7.77E+16	2.36E+18	0	3.24E-12	9.88E+13	0.0461
309.19	760	4.94E+16	7.77E+16	2.36E+18	0	3.25E-12	9.72E+13	0.0436
309.19	760	4.94E+16	7.77E+16	2.36E+18	0	3.33E-12	9.97E+13	0.0414
309.19	760	4.94E+16	7.77E+16	2.36E+18	0	3.78E-12	1.04E+14	0.0774
309.19	760	4.94E+16	7.77E+16	2.36E+18	0	3.74E-12	1.04E+14	0.0780
309.19	760	4.94E+16	7.77E+16	2.36E+18	0	3.56E-12	1.02E+14	0.0453
309.19	760	4.98E+16	1.62E+17	2.39E+18	0	3.94E-12	1.04E+14	0.0401
309.19	760	5.07E+16	3.36E+17	2.43E+18	0	5.24E-12	9.44E+13	0.0597
309.19	760	5.07E+16	3.36E+17	2.43E+18	0	5.21E-12	9.92E+13	0.0659
309.19	760	5.07E+16	3.36E+17	2.43E+18	0	5.87E-12	9.49E+13	0.0887
309.19	760	5.07E+16	3.36E+17	2.43E+18	0	5.66E-12	1.01E+14	0.0756
309.19	760	5.07E+16	3.36E+17	2.43E+18	0	5.26E-12	1.06E+14	0.0742
309.19	760	5.07E+16	3.36E+17	2.43E+18	0	5.10E-12	1.04E+14	0.0677
309.19	760	5.14E+16	1.62E+17	2.38E+18	0	4.08E-12	1.11E+14	0.0549
309.19	760	5.14E+16	1.62E+17	2.38E+18	0	4.38E-12	1.14E+14	0.0683
309.19	760	5.14E+16	1.62E+17	2.38E+18	0	4.21E-12	1.15E+14	0.0467
309.19	760	5.29E+16	1.62E+17	2.38E+18	0	3.96E-12	1.12E+14	0.0673
309.19	760	5.29E+16	1.62E+17	2.38E+18	0	3.73E-12	1.12E+14	0.0543
309.19	760	5.29E+16	1.62E+17	2.38E+18	0	3.96E-12	1.15E+14	0.0707
309.19	760	5.29E+16	1.62E+17	2.38E+18	0	3.75E-12	1.13E+14	0.0586
309.19	760	5.39E+16	3.35E+17	2.42E+18	0	4.97E-12	1.03E+14	0.0657
309.19	760	5.43E+16	4.15E+17	2.44E+18	0	5.19E-12	9.72E+13	0.0774
309.19	760	5.43E+16	4.15E+17	2.44E+18	0	5.57E-12	1.01E+14	0.0930
309.19	760	5.43E+16	4.15E+17	2.44E+18	0	5.43E-12	1.02E+14	0.0829
309.19	760	5.43E+16	4.15E+17	2.44E+18	0	5.79E-12	1.09E+14	0.0922
309.19	760	5.50E+16	2.47E+17	2.40E+18	0	5.18E-12	1.18E+14	0.0915
309.19	760	5.50E+16	2.47E+17	2.40E+18	0	4.69E-12	1.11E+14	0.0768
309.19	760	5.50E+16	2.47E+17	2.40E+18	0	4.22E-12	1.06E+14	0.0614
309.19	760	5.50E+16	2.47E+17	2.40E+18	0	4.33E-12	1.02E+14	0.0631
309.19	760	5.50E+16	2.47E+17	2.40E+18	0	4.68E-12	1.11E+14	0.0665
309.19	760	5.50E+16	2.47E+17	2.40E+18	0	4.22E-12	1.03E+14	0.0638

309.19	760	5.50E+16	2.47E+17	2.40E+18	0	4.36E-12	1.06E+14	0.0574
309.19	760	5.50E+16	2.47E+17	2.40E+18	0	4.02E-12	1.03E+14	0.0458
309.19	760	5.51E+16	1.11E+16	2.21E+18	0	3.19E-12	1.27E+14	0.1322
309.19	760	5.51E+16	1.11E+16	2.21E+18	0	3.19E-12	1.36E+14	0.0900
309.19	760	5.51E+16	1.11E+16	2.21E+18	0	2.92E-12	1.33E+14	0.1447
309.19	760	5.60E+16	4.14E+17	2.44E+18	0	6.18E-12	1.08E+14	0.1017
309.19	760	5.60E+16	4.14E+17	2.44E+18	0	5.75E-12	1.01E+14	0.0797
309.19	760	5.60E+16	4.14E+17	2.44E+18	0	5.52E-12	9.87E+13	0.0834
309.19	760	5.60E+16	4.14E+17	2.44E+18	0	6.06E-12	1.07E+14	0.0861
309.19	760	6.01E+16	1.11E+16	2.20E+18	0	3.08E-12	1.30E+14	0.0951
309.19	760	5.97E+16	1.13E+16	2.25E+18	1.20E+17	3.71E-12	1.20E+14	0.0603
309.19	760	5.97E+16	1.13E+16	2.25E+18	1.20E+17	3.41E-12	1.20E+14	0.0805
309.19	760	5.97E+16	1.13E+16	2.25E+18	1.20E+17	3.54E-12	1.23E+14	0.0656
309.19	760	5.97E+16	1.13E+16	2.25E+18	1.20E+17	3.93E-12	1.27E+14	0.1143
309.19	760	5.97E+16	1.13E+16	2.25E+18	1.20E+17	3.63E-12	1.24E+14	0.1532
309.19	760	5.97E+16	1.13E+16	2.25E+18	1.20E+17	3.78E-12	1.21E+14	0.1377
309.19	760	5.97E+16	1.13E+16	2.25E+18	1.20E+17	3.51E-12	1.21E+14	0.1135
309.19	760	5.97E+16	1.13E+16	2.25E+18	1.20E+17	3.55E-12	1.15E+14	0.1314
309.19	760	4.55E+16	1.12E+16	3.00E+18	1.56E+17	3.55E-12	1.03E+14	0.1285
309.19	760	4.55E+16	1.12E+16	3.00E+18	1.56E+17	3.67E-12	1.08E+14	0.1579
309.19	760	4.55E+16	1.12E+16	3.00E+18	1.56E+17	3.59E-12	1.05E+14	0.1303
309.19	760	4.55E+16	1.12E+16	3.00E+18	1.56E+17	3.69E-12	1.05E+14	0.1474
309.19	760	4.24E+16	1.13E+16	2.99E+18	1.56E+17	4.30E-12	7.51E+13	0.1747
309.19	760	4.24E+16	1.13E+16	2.99E+18	1.56E+17	3.44E-12	7.33E+13	0.1211
309.19	760	4.24E+16	1.13E+16	2.99E+18	1.56E+17	4.22E-12	8.10E+13	0.1416
309.19	760	4.24E+16	1.13E+16	2.99E+18	1.56E+17	4.40E-12	8.41E+13	0.1782
309.19	760	6.16E+16	1.13E+16	2.25E+18	1.59E+17	3.29E-12	1.25E+14	0.0416
309.19	760	6.16E+16	1.13E+16	2.25E+18	1.59E+17	3.46E-12	1.26E+14	0.0993
309.19	760	6.16E+16	1.13E+16	2.25E+18	1.59E+17	3.45E-12	6.96E+13	0.2007
309.19	760	6.16E+16	1.13E+16	2.25E+18	1.59E+17	3.45E-12	1.01E+14	0.1750
309.19	760	6.16E+16	1.13E+16	2.25E+18	1.59E+17	3.32E-12	1.21E+14	0.0257
309.19	760	5.99E+16	1.13E+16	2.26E+18	1.59E+17	3.26E-12	1.30E+14	0.0382
309.19	760	5.99E+16	1.13E+16	2.26E+18	1.59E+17	4.27E-12	6.82E+13	0.2996
309.19	760	6.46E+16	1.12E+16	2.23E+18	2.23E+17	3.99E-12	1.35E+14	0.1077
309.19	760	6.46E+16	1.12E+16	2.23E+18	2.23E+17	4.19E-12	1.36E+14	0.1325
309.19	760	6.11E+16	1.13E+16	2.23E+18	2.24E+17	3.64E-12	1.26E+14	0.1452
309.19	760	6.11E+16	1.13E+16	2.23E+18	2.24E+17	4.36E-12	1.27E+14	0.1286
309.19	760	6.11E+16	1.13E+16	2.23E+18	2.24E+17	4.08E-12	1.35E+14	0.1512
309.19	760	6.11E+16	1.13E+16	2.23E+18	2.24E+17	3.96E-12	1.29E+14	0.1208
309.19	760	6.11E+16	1.13E+16	2.23E+18	2.24E+17	4.16E-12	1.23E+14	0.0974
309.19	760	6.11E+16	1.13E+16	2.23E+18	2.24E+17	3.92E-12	1.21E+14	0.0679
309.19	760	4.69E+16	1.12E+16	2.98E+18	2.34E+17	3.85E-12	1.00E+14	0.0938
309.19	760	4.69E+16	1.12E+16	2.98E+18	2.34E+17	4.19E-12	1.00E+14	0.1626
309.19	760	4.69E+16	1.12E+16	2.98E+18	2.34E+17	3.99E-12	9.23E+13	0.1480
309.19	760	4.69E+16	1.12E+16	2.98E+18	2.34E+17	4.75E-12	1.22E+14	0.1893
309.19	760	6.44E+16	1.12E+16	2.22E+18	3.11E+17	4.48E-12	1.36E+14	0.1435
309.19	760	6.44E+16	1.12E+16	2.22E+18	3.11E+17	5.20E-12	1.32E+14	0.2000
309.19	760	6.44E+16	1.12E+16	2.22E+18	3.11E+17	5.19E-12	1.27E+14	0.1760
309.19	760	6.44E+16	1.12E+16	2.22E+18	3.11E+17	4.41E-12	1.23E+14	0.1584
309.19	760	5.75E+16	1.13E+16	2.23E+18	3.12E+17	3.95E-12	1.20E+14	0.0691
309.19	760	5.75E+16	1.13E+16	2.23E+18	3.12E+17	4.42E-12	1.21E+14	0.1548

309.19	760	5.75E+16	1.13E+16	2.23E+18	3.12E+17	3.75E-12	1.46E+14	0.1231
309.19	760	5.75E+16	1.13E+16	2.23E+18	3.12E+17	4.81E-12	1.47E+14	0.1478
309.19	760	6.23E+16	1.12E+16	2.21E+18	4.28E+17	3.75E-12	1.23E+14	0.0715
309.19	760	6.23E+16	1.12E+16	2.21E+18	4.28E+17	5.06E-12	1.27E+14	0.1775
309.19	760	6.23E+16	1.12E+16	2.21E+18	4.28E+17	4.12E-12	1.21E+14	0.0871
309.19	760	6.23E+16	1.12E+16	2.21E+18	4.28E+17	4.84E-12	1.23E+14	0.0691
309.19	760	6.23E+16	1.12E+16	2.21E+18	4.28E+17	4.38E-12	1.23E+14	0.0979
309.19	760	6.23E+16	1.12E+16	2.21E+18	4.28E+17	4.81E-12	1.24E+14	0.1429
309.19	760	5.89E+16	1.12E+16	2.22E+18	4.29E+17	4.03E-12	1.03E+14	0.1007
309.19	760	5.89E+16	1.12E+16	2.22E+18	4.29E+17	4.01E-12	1.24E+14	0.0791
309.19	760	6.20E+16	1.11E+16	2.20E+18	5.48E+17	4.91E-12	1.21E+14	0.0889
309.19	760	6.20E+16	1.11E+16	2.20E+18	5.48E+17	5.68E-12	1.29E+14	0.1827
309.19	760	6.20E+16	1.11E+16	2.20E+18	5.48E+17	5.52E-12	1.23E+14	0.1533
309.19	760	6.20E+16	1.11E+16	2.20E+18	5.48E+17	4.49E-12	1.20E+14	0.0799
309.19	760	6.20E+16	1.11E+16	2.20E+18	5.48E+17	5.69E-12	1.29E+14	0.1738
309.19	760	4.60E+16	1.10E+16	2.93E+18	5.71E+17	4.55E-12	8.96E+13	0.1497
309.19	760	4.60E+16	1.10E+16	2.93E+18	5.71E+17	4.98E-12	8.76E+13	0.2347
309.19	760	4.60E+16	1.10E+16	2.93E+18	5.71E+17	4.52E-12	7.89E+13	0.1127
309.19	760	4.60E+16	1.10E+16	2.93E+18	5.71E+17	4.92E-12	7.92E+13	0.1484
309.19	760	4.31E+16	1.11E+16	2.93E+18	5.72E+17	4.97E-12	8.43E+13	0.1732
309.19	760	4.31E+16	1.11E+16	2.93E+18	5.72E+17	4.92E-12	7.67E+13	0.1179
309.19	760	4.31E+16	1.11E+16	2.93E+18	5.72E+17	5.09E-12	7.79E+13	0.1412
309.19	760	4.31E+16	1.11E+16	2.93E+18	5.72E+17	4.48E-12	7.63E+13	0.1157
309.19	760	4.17E+16	1.11E+16	2.94E+18	5.73E+17	4.45E-12	7.40E+13	0.0809
309.19	760	4.17E+16	1.11E+16	2.94E+18	5.73E+17	4.80E-12	7.68E+13	0.0927
309.19	760	4.17E+16	1.11E+16	2.94E+18	5.73E+17	4.14E-12	7.37E+13	0.1032
309.19	760	4.17E+16	1.11E+16	2.94E+18	5.73E+17	4.80E-12	7.44E+13	0.1238
309.19	760	4.17E+16	1.11E+16	2.94E+18	5.73E+17	3.45E-12	6.99E+13	0.0363
309.19	760	4.17E+16	1.11E+16	2.94E+18	5.73E+17	3.75E-12	7.18E+13	0.0990
309.19	760	4.17E+16	1.11E+16	2.94E+18	5.73E+17	3.16E-12	6.80E+13	0.0684
309.19	760	4.17E+16	1.11E+16	2.94E+18	5.73E+17	3.56E-12	6.80E+13	0.0943
295.98	760	2.06E+16	1.40E+16	3.12E+18	0	2.78E-12	4.32E+13	0.0223
295.98	760	2.06E+16	1.40E+16	3.12E+18	0	2.76E-12	4.45E+13	0.0000
295.98	760	2.81E+16	4.43E+16	1.26E+19	0	3.63E-12	5.97E+13	0.0607
295.98	760	2.81E+16	4.43E+16	1.26E+19	0	3.19E-12	5.51E+13	0.0352
295.98	760	2.81E+16	4.43E+16	1.26E+19	0	3.14E-12	5.80E+13	0.0371
295.98	760	2.81E+16	4.43E+16	1.26E+19	0	3.75E-12	6.04E+13	0.0979
295.98	760	2.81E+16	4.43E+16	1.26E+19	0	3.67E-12	9.98E+13	0.0488
295.98	760	4.02E+16	1.38E+16	2.93E+18	0	3.03E-12	7.99E+13	0.0000
295.98	760	4.02E+16	1.38E+16	2.93E+18	0	2.72E-12	7.50E+13	0.0523
295.98	760	4.07E+16	1.38E+16	3.07E+18	0	3.14E-12	7.96E+13	0.0998
295.98	760	4.15E+16	1.38E+16	2.92E+18	0	3.48E-12	8.81E+13	0.3088
295.98	760	4.15E+16	1.38E+16	2.92E+18	0	2.93E-12	9.18E+13	0.2597
295.98	760	4.30E+16	3.71E+16	3.03E+18	0	3.51E-12	9.30E+13	0.0940
295.98	760	4.30E+16	3.71E+16	3.03E+18	0	3.65E-12	9.34E+13	0.1053
295.98	760	4.33E+16	2.95E+16	3.05E+18	0	3.20E-12	9.34E+13	0.0840
295.98	760	4.33E+16	2.95E+16	3.05E+18	0	3.45E-12	9.48E+13	0.0774
295.98	760	4.34E+16	1.38E+16	3.06E+18	0	2.94E-12	1.00E+14	0.1340
295.98	760	4.34E+16	1.38E+16	3.06E+18	0	2.67E-12	9.46E+13	0.1535
295.98	760	4.35E+16	1.38E+16	3.07E+18	0	3.28E-12	8.64E+13	0.0511
295.98	760	4.37E+16	1.38E+16	3.07E+18	0	3.44E-12	9.87E+13	0.1209

295.98	760	4.37E+16	1.38E+16	3.07E+18	0	3.24E-12	9.83E+13	0.0855
295.98	760	4.37E+16	1.38E+16	3.07E+18	0	3.05E-12	9.62E+13	0.1162
295.98	760	4.37E+16	1.38E+16	3.07E+18	0	2.91E-12	9.61E+13	0.0835
295.98	760	4.37E+16	1.38E+16	3.07E+18	0	3.20E-12	9.50E+13	0.0941
295.98	760	4.37E+16	1.38E+16	3.07E+18	0	3.27E-12	1.02E+14	0.1055
295.98	760	4.37E+16	2.18E+16	3.08E+18	0	3.40E-12	9.75E+13	0.1006
295.98	760	4.37E+16	2.18E+16	3.08E+18	0	3.24E-12	9.11E+13	0.0920
295.98	760	4.38E+16	1.38E+16	3.08E+18	0	2.35E-12	8.60E+13	0.0000
295.98	760	4.38E+16	1.38E+16	3.08E+18	0	3.22E-12	9.23E+13	0.0622
295.98	760	4.39E+16	1.38E+16	3.09E+18	0	3.01E-12	8.57E+13	0.0299
295.98	760	4.39E+16	1.38E+16	3.09E+18	0	3.13E-12	9.17E+13	0.0504
295.98	760	4.39E+16	1.38E+16	3.09E+18	0	2.60E-12	7.70E+13	0.1206
295.98	760	4.39E+16	1.38E+16	3.09E+18	0	2.56E-12	8.28E+13	0.0699
295.98	760	4.39E+16	1.38E+16	3.09E+18	0	3.46E-12	9.41E+13	0.0924
295.98	760	4.39E+16	1.38E+16	3.09E+18	0	3.27E-12	9.29E+13	0.0863
295.98	760	4.39E+16	1.38E+16	3.09E+18	0	3.10E-12	8.60E+13	0.0543
295.98	760	4.39E+16	1.38E+16	3.09E+18	0	3.05E-12	9.10E+13	0.0808
295.98	760	4.39E+16	1.38E+16	3.09E+18	0	2.93E-12	7.00E+13	0.0792
295.98	760	4.39E+16	1.38E+16	3.09E+18	0	2.93E-12	8.44E+13	0.0468
295.98	760	4.40E+16	5.84E+15	3.10E+18	0	3.12E-12	9.61E+13	0.1028
295.98	760	4.40E+16	5.84E+15	3.10E+18	0	3.00E-12	9.62E+13	0.1279
295.98	760	4.51E+16	1.38E+16	3.07E+18	0	3.15E-12	9.58E+13	0.1303
295.98	760	4.59E+16	1.38E+16	3.02E+18	0	2.86E-12	7.15E+13	0.0000
295.98	760	4.59E+16	1.38E+16	3.02E+18	0	2.92E-12	1.01E+14	0.0007
295.98	760	4.64E+16	1.37E+16	3.05E+18	0	3.13E-12	9.20E+13	0.0805
295.98	760	4.64E+16	1.37E+16	3.05E+18	0	3.35E-12	1.07E+14	0.0707
295.98	760	4.89E+16	1.37E+16	3.01E+18	0	3.46E-12	1.22E+14	0.1050
295.98	760	4.89E+16	1.37E+16	3.01E+18	0	3.14E-12	1.12E+14	0.0688
295.98	760	4.91E+16	1.36E+16	7.00E+17	0	3.33E-12	1.03E+14	0.1330
295.98	760	4.91E+16	1.36E+16	7.00E+17	0	3.52E-12	1.05E+14	0.2122
295.98	760	5.10E+16	1.71E+17	2.27E+18	0	5.31E-12	8.30E+13	0.1093
295.98	760	5.16E+16	8.11E+16	2.47E+18	0	3.84E-12	1.02E+14	0.0540
295.98	760	5.16E+16	8.11E+16	2.47E+18	0	3.36E-12	9.74E+13	0.0311
295.98	760	5.16E+16	8.11E+16	2.47E+18	0	4.00E-12	1.03E+14	0.0684
295.98	760	5.19E+16	3.79E+16	2.23E+18	0	3.74E-12	1.03E+14	0.1029
295.98	760	5.19E+16	3.79E+16	2.23E+18	0	3.72E-12	9.70E+13	0.1152
295.98	760	5.19E+16	3.79E+16	2.23E+18	0	3.54E-12	9.74E+13	0.0938
295.98	760	5.19E+16	3.79E+16	2.23E+18	0	3.91E-12	9.61E+13	0.0744
295.98	760	5.19E+16	3.79E+16	2.23E+18	0	3.67E-12	9.38E+13	0.0253
295.98	760	5.19E+16	3.79E+16	2.23E+18	0	3.82E-12	9.63E+13	0.0686
295.98	760	5.19E+16	3.79E+16	2.23E+18	0	3.58E-12	9.53E+13	0.0659
295.98	760	5.19E+16	3.79E+16	2.23E+18	0	3.86E-12	9.10E+13	0.0798
295.98	760	5.20E+16	1.62E+16	2.24E+18	0	4.08E-12	1.00E+14	0.2470
295.98	760	5.20E+16	1.62E+16	2.24E+18	0	4.29E-12	1.06E+14	0.2383
295.98	760	5.20E+16	1.62E+16	2.24E+18	0	3.95E-12	1.08E+14	0.2216
295.98	760	5.20E+16	1.62E+16	2.24E+18	0	4.07E-12	1.11E+14	0.2218
295.98	760	5.20E+16	1.62E+16	2.24E+18	0	3.33E-12	9.73E+13	0.0353
295.98	760	5.20E+16	1.62E+16	2.24E+18	0	3.91E-12	1.07E+14	0.1882
295.98	760	5.20E+16	1.62E+16	2.24E+18	0	3.39E-12	9.80E+13	0.0000
295.98	760	5.20E+16	1.62E+16	2.24E+18	0	3.38E-12	9.38E+13	0.0000
295.98	760	5.26E+16	1.71E+17	2.26E+18	0	5.34E-12	7.59E+13	0.0524

295.98	760	5.26E+16	1.71E+17	2.26E+18	0	5.09E-12	7.90E+13	0.0000
295.98	760	5.26E+16	1.71E+17	2.26E+18	0	5.56E-12	8.15E+13	0.1273
295.98	760	5.26E+16	1.71E+17	2.26E+18	0	4.99E-12	6.40E+13	0.0241
295.98	760	5.26E+16	1.71E+17	2.26E+18	0	5.15E-12	7.15E+13	0.2186
295.98	760	5.26E+16	1.71E+17	2.26E+18	0	5.57E-12	7.22E+13	0.1837
295.98	760	5.26E+16	1.71E+17	2.26E+18	0	5.50E-12	5.88E+13	0.5213
295.98	760	5.30E+16	2.62E+17	2.29E+18	0	6.19E-12	5.42E+13	0.3471
295.98	760	5.30E+16	2.62E+17	2.29E+18	0	7.48E-12	6.24E+13	0.3668
295.98	760	5.30E+16	2.62E+17	2.29E+18	0	7.53E-12	6.16E+13	0.3605
295.98	760	5.35E+16	1.48E+16	2.28E+18	0	3.15E-12	1.13E+14	0.0924
295.98	760	5.37E+16	8.19E+16	2.24E+18	0	5.22E-12	7.85E+13	0.4295
295.98	760	5.37E+16	8.19E+16	2.24E+18	0	5.15E-12	8.49E+13	0.2585
295.98	760	5.37E+16	8.19E+16	2.24E+18	0	6.40E-12	8.90E+13	0.1934
295.98	760	5.37E+16	8.19E+16	2.24E+18	0	4.57E-12	7.13E+13	0.1612
295.98	760	5.37E+16	8.19E+16	2.24E+18	0	5.75E-12	7.56E+13	0.1520
295.98	760	5.40E+16	4.39E+17	2.33E+18	0	8.56E-12	7.29E+13	0.1836
295.98	760	5.40E+16	4.39E+17	2.33E+18	0	8.88E-12	6.65E+13	0.1565
295.98	760	5.40E+16	4.39E+17	2.33E+18	0	7.21E-12	5.69E+13	0.0258
295.98	760	5.40E+16	4.39E+17	2.33E+18	0	9.34E-12	7.14E+13	0.0000
295.98	760	5.40E+16	4.39E+17	2.33E+18	0	6.48E-12	5.94E+13	0.0000
295.98	760	5.40E+16	4.39E+17	2.33E+18	0	6.57E-12	5.73E+13	0.0000
295.98	760	5.40E+16	4.39E+17	2.33E+18	0	7.05E-12	6.13E+13	0.1053
295.98	760	5.40E+16	4.39E+17	2.33E+18	0	6.56E-12	6.14E+13	0.1893
295.98	760	5.47E+16	2.62E+17	2.28E+18	0	6.72E-12	5.79E+13	0.3384
295.98	760	5.47E+16	2.62E+17	2.28E+18	0	7.51E-12	5.89E+13	0.4327
295.98	760	5.47E+16	2.62E+17	2.28E+18	0	6.12E-12	5.51E+13	0.3498
295.98	760	5.47E+16	2.62E+17	2.28E+18	0	7.96E-12	8.40E+13	0.1716
295.98	760	5.47E+16	2.62E+17	2.28E+18	0	8.26E-12	8.85E+13	0.2071
295.98	760	5.47E+16	2.62E+17	2.28E+18	0	9.05E-12	9.40E+13	0.2263
295.98	760	5.47E+16	2.62E+17	2.28E+18	0	8.03E-12	8.23E+13	0.2393
295.98	760	5.52E+16	3.54E+17	2.30E+18	0	7.45E-12	7.27E+13	0.0823
295.98	760	5.52E+16	3.54E+17	2.30E+18	0	7.48E-12	6.59E+13	0.0955
295.98	760	5.52E+16	3.54E+17	2.30E+18	0	8.51E-12	7.67E+13	0.1299
295.98	760	5.52E+16	3.54E+17	2.30E+18	0	8.35E-12	7.40E+13	0.1094
295.98	760	5.64E+16	2.61E+17	2.28E+18	0	7.68E-12	6.10E+13	0.4206
295.98	760	5.69E+16	1.48E+16	2.28E+18	0	3.10E-12	1.13E+14	0.0925
295.98	760	6.07E+16	1.58E+16	1.62E+18	0	3.23E-12	1.27E+14	0.0872
295.98	760	6.07E+16	1.58E+16	1.62E+18	0	3.07E-12	1.20E+14	0.0541
295.98	760	7.59E+16	3.95E+16	2.32E+18	0	4.03E-12	1.57E+14	0.0848
295.98	760	7.59E+16	3.95E+16	2.32E+18	0	3.97E-12	1.50E+14	0.0945
295.98	760	7.59E+16	3.95E+16	2.32E+18	0	3.93E-12	1.57E+14	0.0811
295.98	760	7.59E+16	3.95E+16	2.32E+18	0	3.87E-12	1.47E+14	0.0963
295.98	760	7.62E+16	8.21E+16	2.33E+18	0	4.24E-12	1.37E+14	0.0891
295.98	760	7.62E+16	8.21E+16	2.33E+18	0	4.04E-12	1.31E+14	0.0842
295.98	760	7.62E+16	8.21E+16	2.33E+18	0	4.86E-12	1.47E+14	0.0867
295.98	760	7.62E+16	8.21E+16	2.33E+18	0	3.76E-12	1.40E+14	0.0703
295.98	760	7.62E+16	8.21E+16	2.33E+18	0	4.36E-12	1.49E+14	0.0853
295.98	760	7.62E+16	8.21E+16	2.33E+18	0	3.63E-12	1.35E+14	0.0668
295.98	760	7.62E+16	8.21E+16	2.33E+18	0	3.92E-12	1.34E+14	0.0601
295.98	760	7.93E+16	1.25E+17	2.33E+18	0	4.96E-12	1.39E+14	0.0967
295.98	760	7.93E+16	1.25E+17	2.33E+18	0	4.92E-12	1.35E+14	0.1105

295.98	760	7.93E+16	1.25E+17	2.33E+18	0	5.50E-12	1.53E+14	0.0954
295.98	760	8.10E+16	1.34E+16	2.96E+18	0	3.10E-12	1.39E+14	0.1006
295.98	760	8.18E+16	8.17E+16	2.32E+18	0	4.34E-12	1.41E+14	0.0853
295.98	760	8.36E+16	1.24E+17	2.32E+18	0	5.57E-12	1.50E+14	0.0986
295.98	760	8.74E+16	2.31E+17	2.62E+18	0	6.24E-12	1.48E+14	0.1034
295.98	760	8.74E+16	2.31E+17	2.62E+18	0	6.49E-12	1.53E+14	0.1054
295.98	760	8.74E+16	2.31E+17	2.62E+18	0	6.29E-12	1.37E+14	0.1132
295.98	760	8.74E+16	2.31E+17	2.62E+18	0	6.26E-12	1.45E+14	0.1027
295.98	760	9.17E+16	1.86E+17	2.60E+18	0	5.88E-12	1.60E+14	0.1006
295.98	760	9.17E+16	1.86E+17	2.60E+18	0	5.70E-12	1.47E+14	0.1112
295.98	760	9.17E+16	1.86E+17	2.60E+18	0	5.43E-12	1.41E+14	0.1096
295.98	760	9.17E+16	1.86E+17	2.60E+18	0	5.62E-12	1.52E+14	0.1060
295.98	760	1.21E+17	7.97E+16	2.21E+18	0	4.63E-12	2.59E+14	0.1098
295.98	760	1.21E+17	7.97E+16	2.21E+18	0	4.68E-12	2.36E+14	0.1267
295.98	760	1.21E+17	7.97E+16	2.21E+18	0	4.72E-12	2.64E+14	0.1119
295.98	760	1.21E+17	7.97E+16	2.21E+18	0	4.52E-12	2.51E+14	0.1172
295.98	760	1.21E+17	7.97E+16	2.21E+18	0	4.16E-12	2.45E+14	0.1133
295.98	760	1.21E+17	7.97E+16	2.21E+18	0	4.51E-12	2.37E+14	0.1252
295.98	760	1.21E+17	7.97E+16	2.21E+18	0	4.33E-12	2.51E+14	0.1120
295.98	760	1.21E+17	7.97E+16	2.21E+18	0	4.58E-12	2.65E+14	0.1051
295.98	760	4.97E+16	1.39E+16	3.06E+18	2.39E+16	3.33E-12	1.00E+14	0.0575
295.98	760	4.97E+16	1.39E+16	3.06E+18	2.39E+16	3.39E-12	1.15E+14	0.0820
295.98	760	4.97E+16	1.39E+16	3.06E+18	2.39E+16	3.01E-12	9.78E+13	0.0742
295.98	760	4.97E+16	1.39E+16	3.06E+18	2.39E+16	3.48E-12	1.15E+14	0.0793
295.98	760	5.02E+16	1.41E+16	3.09E+18	5.57E+16	3.21E-12	1.09E+14	0.0528
295.98	760	5.02E+16	1.41E+16	3.09E+18	5.57E+16	3.26E-12	1.03E+14	0.0658
295.98	760	5.02E+16	1.41E+16	3.09E+18	5.57E+16	3.36E-12	1.15E+14	0.0759
295.98	760	5.02E+16	1.41E+16	3.09E+18	5.57E+16	3.43E-12	1.12E+14	0.0550
295.98	760	4.48E+16	1.41E+16	3.16E+18	1.32E+17	3.62E-12	5.02E+13	0.1280
295.98	760	4.48E+16	1.41E+16	3.16E+18	1.32E+17	3.78E-12	8.72E+13	0.0722
295.98	760	4.45E+16	1.40E+16	3.14E+18	2.00E+17	4.19E-12	7.01E+13	0.1047
295.98	760	4.45E+16	1.40E+16	3.14E+18	2.00E+17	3.99E-12	6.66E+13	0.0973
295.98	760	4.46E+16	1.40E+16	3.14E+18	2.45E+17	5.31E-12	8.69E+13	0.1095
295.98	760	4.46E+16	1.40E+16	3.14E+18	2.45E+17	4.87E-12	8.32E+13	0.1108
295.98	760	4.46E+16	1.40E+16	3.14E+18	2.45E+17	4.78E-12	8.45E+13	0.1001
295.98	760	4.46E+16	1.40E+16	3.14E+18	2.45E+17	4.54E-12	8.04E+13	0.0928
295.98	760	4.44E+16	1.40E+16	3.12E+18	2.99E+17	4.89E-12	7.48E+13	0.1206
295.98	760	4.44E+16	1.40E+16	3.12E+18	2.99E+17	4.98E-12	6.97E+13	0.1081
295.98	760	4.44E+16	1.39E+16	3.13E+18	3.86E+17	5.21E-12	8.07E+13	0.1014
295.98	760	4.44E+16	1.39E+16	3.13E+18	3.86E+17	5.63E-12	8.31E+13	0.1474
295.98	760	4.69E+16	1.39E+16	3.09E+18	4.11E+17	4.94E-12	7.32E+13	0.1167
295.98	760	4.39E+16	1.39E+16	3.09E+18	4.12E+17	4.06E-12	6.75E+13	0.0137
295.98	760	4.17E+16	1.39E+16	2.94E+18	4.97E+17	4.99E-12	6.57E+13	0.0821
295.98	760	4.17E+16	1.39E+16	2.94E+18	4.97E+17	5.06E-12	4.87E+13	0.0841
295.98	760	4.04E+16	1.39E+16	2.94E+18	4.97E+17	4.88E-12	6.64E+13	0.0609
295.98	760	4.04E+16	1.39E+16	2.94E+18	4.97E+17	5.39E-12	6.57E+13	0.1249
295.98	760	4.38E+16	1.38E+16	3.08E+18	5.62E+17	6.48E-12	8.01E+13	0.1321
295.98	760	4.38E+16	1.38E+16	3.08E+18	5.62E+17	5.23E-12	7.37E+13	0.0908
295.98	760	4.40E+16	1.38E+16	3.10E+18	5.97E+17	5.70E-12	7.40E+13	0.0879
295.98	760	4.40E+16	1.38E+16	3.10E+18	5.97E+17	5.93E-12	7.12E+13	0.1397
295.98	700	5.45E+16	1.25E+16	2.97E+18	0	3.78E-12	2.90E+13	0.0000

295.98	700	5.61E+16	1.24E+16	2.96E+18	0	3.42E-12	1.27E+14	0.1093
295.98	700	5.61E+16	1.24E+16	2.96E+18	0	3.69E-12	3.15E+13	0.0000
295.98	700	5.61E+16	1.24E+16	2.96E+18	0	4.17E-12	2.87E+13	0.0000
295.98	700	5.61E+16	1.24E+16	2.96E+18	0	3.12E-12	1.23E+14	0.0999
295.98	700	5.61E+16	1.24E+16	2.96E+18	0	3.20E-12	1.18E+14	0.1271
295.98	700	5.63E+16	1.24E+16	2.97E+18	0	3.05E-12	1.26E+14	0.1094
295.98	700	5.76E+16	1.24E+16	2.95E+18	0	2.88E-12	9.80E+13	0.0588
295.98	700	5.78E+16	1.24E+16	2.96E+18	0	3.23E-12	1.21E+14	0.0348
295.98	700	5.79E+16	1.24E+16	2.96E+18	0	2.94E-12	1.09E+14	0.0316
295.98	700	5.79E+16	1.24E+16	2.96E+18	0	2.90E-12	1.16E+14	0.0680
295.98	700	5.74E+16	1.27E+16	3.03E+18	1.20E+17	4.18E-12	1.12E+14	0.1225
295.98	700	5.73E+16	1.27E+16	3.03E+18	1.20E+17	3.99E-12	1.05E+14	0.1065
295.98	700	5.72E+16	1.27E+16	3.02E+18	1.20E+17	4.37E-12	1.15E+14	0.1452
295.98	700	5.72E+16	1.27E+16	3.02E+18	1.20E+17	4.01E-12	1.07E+14	0.1383
295.98	700	5.90E+16	1.26E+16	3.02E+18	1.58E+17	4.23E-12	1.10E+14	0.0873
295.98	700	5.88E+16	1.26E+16	3.01E+18	1.58E+17	4.12E-12	1.11E+14	0.0860
295.98	700	5.88E+16	1.26E+16	3.01E+18	1.58E+17	4.11E-12	1.10E+14	0.0816
295.98	700	5.88E+16	1.26E+16	3.01E+18	1.58E+17	4.10E-12	1.10E+14	0.0898
295.98	700	6.06E+16	1.26E+16	3.01E+18	2.22E+17	4.50E-12	1.16E+14	0.1426
295.98	700	6.06E+16	1.26E+16	3.01E+18	2.22E+17	3.82E-12	1.06E+14	0.0820
295.98	700	6.05E+16	1.26E+16	3.00E+18	2.22E+17	4.72E-12	1.21E+14	0.1663
295.98	700	6.04E+16	1.26E+16	2.99E+18	2.22E+17	4.27E-12	9.79E+13	0.0986
295.98	700	5.87E+16	1.26E+16	3.00E+18	3.10E+17	5.12E-12	1.16E+14	0.1067
295.98	700	5.86E+16	1.26E+16	3.00E+18	3.10E+17	4.62E-12	1.08E+14	0.0596
295.98	700	5.86E+16	1.26E+16	3.00E+18	3.10E+17	4.97E-12	1.16E+14	0.0992
295.98	700	5.85E+16	1.26E+16	2.99E+18	3.10E+17	4.42E-12	1.06E+14	0.0338
295.98	700	5.83E+16	1.25E+16	2.98E+18	4.26E+17	4.85E-12	9.67E+13	0.0674
295.98	700	5.82E+16	1.25E+16	2.98E+18	4.26E+17	5.02E-12	1.05E+14	0.0865
295.98	700	5.82E+16	1.25E+16	2.98E+18	4.26E+17	5.13E-12	9.83E+13	0.1208
295.98	700	5.82E+16	1.25E+16	2.98E+18	4.26E+17	5.53E-12	1.02E+14	0.1351
295.98	700	5.81E+16	1.24E+16	2.97E+18	5.46E+17	5.81E-12	1.03E+14	0.0965
295.98	700	5.81E+16	1.24E+16	2.97E+18	5.46E+17	5.60E-12	9.55E+13	0.0928
295.98	700	5.80E+16	1.24E+16	2.97E+18	5.46E+17	6.35E-12	1.02E+14	0.1282
295.98	700	5.79E+16	1.24E+16	2.96E+18	5.46E+17	5.67E-12	9.89E+13	0.1084
295.98	600	5.33E+16	1.46E+16	2.96E+18	0	2.54E-12	1.71E+13	0.1472
295.98	600	5.33E+16	1.46E+16	2.96E+18	0	2.71E-12	1.78E+13	0.0000
295.98	600	5.33E+16	1.46E+16	2.96E+18	0	4.54E-12	1.79E+13	0.3068
295.98	600	5.84E+16	1.45E+16	2.95E+18	0	3.27E-12	1.12E+14	0.1132
295.98	600	5.84E+16	1.45E+16	2.95E+18	0	3.25E-12	1.11E+14	0.0643
295.98	600	5.98E+16	1.45E+16	2.94E+18	0	3.68E-12	1.22E+14	0.1195
295.98	600	6.15E+16	1.45E+16	2.93E+18	0	2.68E-12	6.45E+13	0.0823
295.98	600	6.65E+16	1.44E+16	2.91E+18	0	3.39E-12	1.00E+14	0.1131
295.98	600	6.68E+16	1.44E+16	2.92E+18	0	3.15E-12	1.24E+14	0.0727
295.98	600	6.68E+16	1.44E+16	2.92E+18	0	3.11E-12	1.19E+14	0.0697
295.98	600	6.68E+16	1.44E+16	2.92E+18	0	2.76E-12	1.19E+14	0.0427
295.98	600	6.68E+16	1.61E+16	3.28E+18	1.11E+17	4.16E-12	1.08E+14	0.1011
295.98	600	6.68E+16	1.61E+16	3.28E+18	1.11E+17	3.52E-12	1.05E+14	0.0932
295.98	600	6.67E+16	1.61E+16	3.28E+18	1.11E+17	3.76E-12	1.09E+14	0.0944
295.98	600	6.67E+16	1.61E+16	3.28E+18	1.11E+17	3.71E-12	1.11E+14	0.1108
295.98	600	6.87E+16	1.61E+16	3.27E+18	1.47E+17	4.42E-12	9.95E+13	0.1786
295.98	600	6.86E+16	1.61E+16	3.27E+18	1.47E+17	4.04E-12	1.19E+14	0.0992

295.98	600	6.85E+16	1.61E+16	3.26E+18	1.47E+17	4.30E-12	1.19E+14	0.1078
295.98	600	6.65E+16	1.61E+16	3.26E+18	1.47E+17	4.77E-12	1.17E+14	0.0990
295.98	600	6.11E+16	1.62E+16	3.29E+18	2.09E+17	4.83E-12	1.18E+14	0.1318
295.98	600	6.10E+16	1.62E+16	3.28E+18	2.09E+17	4.70E-12	1.08E+14	0.1275
295.98	600	6.10E+16	1.62E+16	3.28E+18	2.09E+17	4.40E-12	1.12E+14	0.0892
295.98	600	6.09E+16	1.62E+16	3.27E+18	2.09E+17	4.63E-12	1.05E+14	0.1053
295.98	600	7.38E+16	1.59E+16	3.23E+18	2.86E+17	5.58E-12	1.09E+14	0.1236
295.98	600	7.38E+16	1.59E+16	3.23E+18	2.86E+17	5.10E-12	1.11E+14	0.1295
295.98	600	7.36E+16	1.59E+16	3.22E+18	2.86E+17	4.56E-12	1.06E+14	0.0984
295.98	600	7.36E+16	1.59E+16	3.22E+18	2.86E+17	5.08E-12	1.05E+14	0.1041
295.98	600	7.32E+16	1.58E+16	3.20E+18	3.94E+17	5.28E-12	1.11E+14	0.1259
295.98	600	7.32E+16	1.58E+16	3.20E+18	3.94E+17	5.55E-12	1.13E+14	0.1268
295.98	600	7.32E+16	1.58E+16	3.20E+18	3.94E+17	5.68E-12	1.11E+14	0.1085
295.98	600	7.32E+16	1.58E+16	3.20E+18	3.94E+17	5.25E-12	1.05E+14	0.1438
295.98	600	7.31E+16	1.57E+16	3.20E+18	5.05E+17	5.20E-12	1.02E+14	0.0932
295.98	600	7.31E+16	1.57E+16	3.20E+18	5.05E+17	5.50E-12	9.88E+13	0.1084
295.98	600	7.30E+16	1.57E+16	3.19E+18	5.05E+17	4.94E-12	9.54E+13	0.0772
295.98	600	7.30E+16	1.57E+16	3.19E+18	5.05E+17	5.06E-12	1.00E+14	0.1141
295.98	600	7.30E+16	1.57E+16	3.19E+18	5.05E+17	5.46E-12	1.01E+14	0.1107
295.98	600	7.28E+16	1.57E+16	3.19E+18	5.05E+17	4.96E-12	1.00E+14	0.0893
295.98	500	5.15E+16	1.83E+16	2.30E+18	0	3.47E-12	1.08E+14	0.0408
295.98	500	5.42E+16	1.82E+16	2.28E+18	0	2.99E-12	1.14E+14	0.0749
295.98	500	5.44E+16	1.82E+16	2.29E+18	0	3.00E-12	1.13E+14	0.0995
295.98	500	5.44E+16	1.82E+16	2.29E+18	0	3.31E-12	1.13E+14	0.1544
295.98	400	5.67E+16	2.31E+16	2.28E+18	0	3.57E-12	1.11E+14	0.0851
295.98	400	5.68E+16	2.31E+16	2.28E+18	0	3.64E-12	1.13E+14	0.0452
295.98	400	5.68E+16	2.31E+16	2.28E+18	0	4.14E-12	1.12E+14	0.0706
295.98	400	5.68E+16	2.31E+16	2.28E+18	0	3.71E-12	1.07E+14	0.0523
295.98	400	5.69E+16	2.31E+16	2.29E+18	0	3.37E-12	1.03E+14	0.1357
295.98	400	5.96E+16	2.29E+16	2.28E+18	0	3.03E-12	9.99E+13	0.0347
295.98	400	5.96E+16	2.29E+16	2.28E+18	0	2.89E-12	9.58E+13	0.0015
295.98	400	6.22E+16	2.28E+16	2.26E+18	0	3.43E-12	1.21E+14	0.1358
295.98	400	6.37E+16	2.28E+16	2.26E+18	0	2.85E-12	1.02E+14	0.0000
295.98	400	6.51E+16	2.27E+16	2.25E+18	0	2.85E-12	1.03E+14	0.0137
295.98	400	6.51E+16	2.27E+16	2.25E+18	0	3.06E-12	1.31E+14	0.0895
295.98	500	7.14E+16	1.71E+16	2.87E+18	0	4.57E-12	1.74E+13	0.2870
295.98	500	7.14E+16	1.71E+16	2.87E+18	0	4.24E-12	1.77E+13	0.1658
295.98	500	7.14E+16	1.71E+16	2.87E+18	0	4.31E-12	1.67E+13	0.1560
295.98	400	8.24E+16	2.10E+16	2.77E+18	0	2.78E-12	1.26E+14	0.1031
295.98	400	8.24E+16	2.10E+16	2.77E+18	0	2.87E-12	1.29E+14	0.1020
295.98	400	8.24E+16	2.10E+16	2.77E+18	0	2.55E-12	1.27E+14	0.0838
295.98	400	8.24E+16	2.10E+16	2.77E+18	0	2.84E-12	1.24E+14	0.0914
295.98	400	8.53E+16	2.08E+16	2.76E+18	0	2.64E-12	1.23E+14	0.0494
295.98	400	8.53E+16	2.08E+16	2.76E+18	0	2.74E-12	1.24E+14	0.0272
295.98	400	8.53E+16	2.08E+16	2.76E+18	0	2.95E-12	1.28E+14	0.0792
295.98	400	8.53E+16	2.08E+16	2.76E+18	0	3.11E-12	1.23E+14	0.1000
295.98	400	1.10E+17	1.99E+16	2.64E+18	0	2.44E-12	1.46E+14	0.1428
295.98	400	1.11E+17	1.99E+16	2.62E+18	0	2.69E-12	1.63E+14	0.1624
295.98	400	1.12E+17	1.99E+16	2.63E+18	0	3.23E-12	1.57E+14	0.0000
295.98	400	1.12E+17	1.99E+16	2.63E+18	0	2.40E-12	1.56E+14	0.1575
295.98	400	5.94E+16	2.40E+16	2.39E+18	8.60E+16	3.78E-12	9.50E+13	0.0239

295.98	400	5.93E+16	2.40E+16	2.38E+18	8.60E+16	3.69E-12	9.40E+13	0.0197
295.98	400	5.92E+16	2.40E+16	2.38E+18	8.60E+16	3.67E-12	9.05E+13	0.0398
295.98	400	5.92E+16	2.40E+16	2.38E+18	8.60E+16	3.76E-12	9.51E+13	0.0412
295.98	400	5.91E+16	2.40E+16	2.37E+18	8.60E+16	4.14E-12	9.55E+13	0.0615
295.98	400	5.91E+16	2.40E+16	2.37E+18	8.60E+16	3.70E-12	9.34E+13	0.0299
295.98	400	5.91E+16	2.40E+16	2.37E+18	8.60E+16	3.88E-12	9.25E+13	0.0445
295.98	400	1.08E+17	2.21E+16	2.93E+18	8.73E+16	2.45E-12	1.58E+14	0.3504
295.98	400	6.42E+16	2.53E+16	2.51E+18	1.01E+17	4.32E-12	1.06E+14	0.1529
295.98	400	6.42E+16	2.53E+16	2.51E+18	1.01E+17	4.09E-12	1.19E+14	0.0494
295.98	400	6.40E+16	2.54E+16	2.51E+18	1.01E+17	4.50E-12	9.44E+13	0.1709
295.98	400	6.27E+16	2.54E+16	2.52E+18	1.02E+17	3.99E-12	8.38E+13	0.0000
295.98	400	6.26E+16	2.54E+16	2.51E+18	1.02E+17	4.36E-12	8.68E+13	0.0932
295.98	400	5.69E+16	2.57E+16	2.54E+18	1.03E+17	4.23E-12	1.04E+14	0.1645
295.98	400	1.22E+17	2.15E+16	2.86E+18	1.13E+17	4.30E-12	1.60E+14	0.0000
295.98	400	1.21E+17	2.15E+16	2.85E+18	1.13E+17	3.85E-12	1.54E+14	0.0000
295.98	400	1.21E+17	2.15E+16	2.85E+18	1.13E+17	4.13E-12	1.74E+14	0.0000
295.98	400	1.21E+17	2.15E+16	2.84E+18	1.59E+17	3.69E-12	1.27E+14	0.0000
295.98	400	1.14E+17	2.17E+16	2.87E+18	1.61E+17	4.19E-12	1.38E+14	0.0000
295.98	400	5.95E+16	2.48E+16	2.45E+18	1.84E+17	4.00E-12	8.31E+13	0.0130
295.98	400	5.95E+16	2.48E+16	2.45E+18	1.84E+17	4.21E-12	9.30E+13	0.0145
295.98	400	5.95E+16	2.48E+16	2.45E+18	1.84E+17	4.50E-12	9.05E+13	0.0438
295.98	400	5.94E+16	2.48E+16	2.45E+18	1.84E+17	3.79E-12	8.27E+13	0.0095
295.98	400	5.82E+16	2.48E+16	2.46E+18	1.84E+17	4.06E-12	8.32E+13	0.0250
295.98	400	5.82E+16	2.48E+16	2.46E+18	1.84E+17	4.29E-12	9.01E+13	0.0355
295.98	400	5.82E+16	2.48E+16	2.46E+18	1.84E+17	3.86E-12	8.28E+13	0.0003
295.98	400	5.82E+16	2.48E+16	2.46E+18	1.84E+17	4.11E-12	8.57E+13	0.0000
295.98	400	1.03E+17	2.20E+16	2.91E+18	2.29E+17	4.24E-12	1.26E+14	0.0000
295.98	400	6.19E+16	2.51E+16	2.49E+18	2.65E+17	5.69E-12	9.91E+13	0.0740
295.98	400	6.19E+16	2.51E+16	2.49E+18	2.65E+17	5.83E-12	9.95E+13	0.0552
295.98	400	6.18E+16	2.51E+16	2.48E+18	2.65E+17	6.07E-12	9.59E+13	0.0470
295.98	400	6.18E+16	2.51E+16	2.48E+18	2.65E+17	7.25E-12	7.49E+13	0.2377
295.98	400	6.18E+16	2.51E+16	2.48E+18	2.65E+17	6.38E-12	1.10E+14	0.0854
295.98	400	6.17E+16	2.51E+16	2.48E+18	2.65E+17	6.13E-12	1.08E+14	0.0629
295.98	400	1.19E+17	2.12E+16	2.81E+18	3.06E+17	4.57E-12	1.35E+14	0.0143
295.98	400	1.19E+17	2.12E+16	2.81E+18	3.06E+17	3.67E-12	1.78E+14	0.4316
295.98	400	1.19E+17	2.12E+16	2.81E+18	3.06E+17	4.73E-12	1.46E+14	0.0202
295.98	400	1.02E+17	2.17E+16	2.88E+18	4.06E+17	4.73E-12	1.15E+14	0.0000
295.98	400	6.25E+16	2.47E+16	2.45E+18	4.68E+17	6.80E-12	9.39E+13	0.1725
295.98	400	6.23E+16	2.47E+16	2.44E+18	4.68E+17	5.59E-12	1.02E+14	0.0659
295.98	400	6.22E+16	2.47E+16	2.44E+18	4.68E+17	6.20E-12	1.01E+14	0.0608
295.98	400	5.98E+16	2.48E+16	2.47E+18	4.70E+17	6.73E-12	1.02E+14	0.2096
295.98	400	5.95E+16	2.48E+16	2.46E+18	4.70E+17	7.00E-12	6.74E+13	0.1697
295.98	400	5.94E+16	2.48E+16	2.45E+18	4.70E+17	6.39E-12	9.70E+13	0.0944
295.98	300	8.86E+16	2.71E+16	2.63E+18	0	2.84E-12	1.29E+14	0.1132
295.98	300	8.86E+16	2.71E+16	2.63E+18	0	2.77E-12	1.31E+14	0.0744
295.98	300	8.86E+16	2.71E+16	2.63E+18	0	2.63E-12	1.24E+14	0.0978
295.98	300	8.86E+16	2.71E+16	2.63E+18	0	2.57E-12	1.24E+14	0.0551
295.98	300	8.98E+16	2.70E+16	2.62E+18	0	2.59E-12	1.33E+14	0.0014
295.98	300	8.98E+16	2.70E+16	2.62E+18	0	2.79E-12	1.32E+14	0.0658
295.98	300	8.98E+16	2.70E+16	2.62E+18	0	2.80E-12	1.37E+14	0.0824
295.98	300	8.98E+16	2.70E+16	2.62E+18	0	2.58E-12	1.32E+14	0.0574

295.98	200	9.57E+16	3.91E+16	2.39E+18	0	2.66E-12	1.27E+14	0.1279
295.98	200	9.62E+16	3.90E+16	2.41E+18	0	2.65E-12	1.17E+14	0.0934
295.98	200	9.67E+16	3.90E+16	2.42E+18	0	2.80E-12	1.26E+14	0.0526
295.98	200	9.67E+16	3.90E+16	2.42E+18	0	2.93E-12	1.32E+14	0.0660
295.98	200	9.67E+16	3.90E+16	2.42E+18	0	2.91E-12	1.24E+14	0.0736
295.98	200	9.67E+16	3.90E+16	2.42E+18	0	2.73E-12	1.26E+14	0.0485
295.98	200	9.67E+16	3.90E+16	2.42E+18	0	2.81E-12	1.25E+14	0.0746
295.98	200	9.67E+16	3.90E+16	2.42E+18	0	2.85E-12	1.26E+14	0.0781
295.98	200	9.67E+16	3.90E+16	2.42E+18	0	2.95E-12	1.23E+14	0.1126
295.98	200	9.67E+16	3.90E+16	2.42E+18	0	2.68E-12	1.06E+14	0.0981
295.98	200	9.67E+16	3.90E+16	2.42E+18	0	2.55E-12	1.19E+14	0.0842
295.98	200	9.67E+16	3.90E+16	2.42E+18	0	2.72E-12	1.20E+14	0.1075
295.98	200	9.67E+16	3.90E+16	2.42E+18	0	2.47E-12	1.43E+14	0.0047
295.98	200	9.67E+16	3.90E+16	2.42E+18	0	2.54E-12	1.36E+14	0.0104
295.98	200	9.67E+16	3.90E+16	2.42E+18	0	3.08E-12	1.46E+14	0.0000
295.98	200	9.67E+16	3.90E+16	2.42E+18	0	2.88E-12	1.39E+14	0.0000
295.98	200	9.97E+16	4.05E+16	2.49E+18	3.95E+16	2.73E-12	9.51E+13	0.0429
295.98	200	9.97E+16	4.05E+16	2.49E+18	3.95E+16	2.67E-12	9.34E+13	0.0456
295.98	200	1.00E+17	4.04E+16	2.50E+18	5.26E+16	2.22E-12	1.64E+14	0.1758
295.98	200	1.00E+17	4.04E+16	2.50E+18	5.26E+16	2.24E-12	1.65E+14	0.1765
295.98	200	1.00E+17	4.04E+16	2.50E+18	5.26E+16	2.90E-12	1.63E+14	0.0000
295.98	200	9.97E+16	4.02E+16	2.49E+18	7.45E+16	3.06E-12	9.67E+13	0.0611
295.98	200	9.97E+16	4.02E+16	2.49E+18	7.45E+16	2.89E-12	9.37E+13	0.0528
295.98	200	9.91E+16	4.03E+16	2.48E+18	7.46E+16	3.00E-12	1.02E+14	0.0785
295.98	200	9.91E+16	4.03E+16	2.48E+18	7.46E+16	3.16E-12	9.89E+13	0.1080
295.98	200	9.92E+16	4.01E+16	2.48E+18	1.05E+17	3.10E-12	1.48E+14	0.0223
295.98	200	9.92E+16	4.01E+16	2.48E+18	1.05E+17	3.17E-12	1.49E+14	0.0075
295.98	200	9.92E+16	3.98E+16	2.48E+18	1.46E+17	2.40E-12	1.20E+14	0.2266
295.98	200	9.86E+16	3.96E+16	2.47E+18	1.90E+17	3.31E-12	1.47E+14	0.0388
295.98	200	9.86E+16	3.96E+16	2.47E+18	1.90E+17	3.17E-12	1.35E+14	0.0000
295.98	200	9.81E+16	3.96E+16	2.46E+18	1.90E+17	3.21E-12	1.43E+14	0.0558
295.98	200	9.81E+16	3.96E+16	2.46E+18	1.90E+17	2.93E-12	1.36E+14	0.0034
295.98	100	5.42E+16	8.81E+16	1.87E+18	0	3.07E-12	9.19E+13	0.0956
295.98	100	5.42E+16	8.81E+16	1.87E+18	0	2.98E-12	8.98E+13	0.1024
295.98	100	5.42E+16	8.81E+16	1.87E+18	0	2.82E-12	9.00E+13	0.1050
295.98	100	5.42E+16	8.81E+16	1.87E+18	0	2.94E-12	9.16E+13	0.0930
295.98	100	5.42E+16	8.81E+16	1.87E+18	0	2.46E-12	8.82E+13	0.0422
295.98	100	5.42E+16	8.81E+16	1.87E+18	0	2.78E-12	9.06E+13	0.0773
295.98	100	5.42E+16	8.81E+16	1.87E+18	0	3.09E-12	9.46E+13	0.0881
295.98	100	5.42E+16	8.81E+16	1.87E+18	0	2.73E-12	9.07E+13	0.0766
295.98	100	5.75E+16	9.35E+16	1.70E+18	8.13E+16	1.84E-12	6.37E+13	0.3171
295.98	100	5.54E+16	9.01E+16	1.62E+18	2.17E+17	2.52E-12	7.90E+13	0.3612
295.98	100	5.48E+16	9.03E+16	1.60E+18	2.17E+17	2.12E-12	6.58E+13	0.1068
295.98	100	5.25E+16	8.63E+16	1.49E+18	3.94E+17	2.92E-12	1.28E+14	0.2040
295.98	100	5.19E+16	8.64E+16	1.47E+18	3.94E+17	4.08E-12	1.11E+14	0.0000
287.18	760	4.00E+16	1.43E+16	3.02E+18	0	2.56E-12	4.22E+13	0.0015
287.18	760	4.00E+16	1.43E+16	3.02E+18	0	3.42E-12	7.69E+13	0.0584
287.18	760	4.04E+16	1.43E+16	3.17E+18	0	3.60E-12	7.30E+13	0.0879
287.18	760	4.05E+16	1.43E+16	3.17E+18	0	3.38E-12	8.02E+13	0.0355
287.18	760	4.34E+16	1.42E+16	3.16E+18	0	3.73E-12	8.96E+13	0.0948
287.18	760	4.34E+16	1.42E+16	3.16E+18	0	3.50E-12	8.73E+13	0.0796

287.18	760	4.34E+16	1.42E+16	3.17E+18	0	2.99E-12	7.21E+13	0.0288
287.18	760	4.34E+16	1.42E+16	3.17E+18	0	3.47E-12	8.40E+13	0.1271
287.18	760	4.34E+16	1.42E+16	3.17E+18	0	3.20E-12	8.62E+13	0.0442
287.18	760	4.48E+16	1.42E+16	3.16E+18	0	3.65E-12	8.73E+13	0.1020
287.18	760	4.49E+16	1.42E+16	3.16E+18	0	3.05E-12	6.83E+13	0.0296
287.18	760	4.49E+16	1.42E+16	3.16E+18	0	3.53E-12	9.26E+13	0.0879
287.18	760	4.49E+16	1.42E+16	3.16E+18	0	3.36E-12	9.25E+13	0.0815
287.18	760	4.49E+16	1.42E+16	3.16E+18	0	3.33E-12	8.83E+13	0.0532
287.18	760	4.49E+16	1.42E+16	3.16E+18	0	3.15E-12	8.20E+13	0.0522
287.18	760	4.49E+16	1.42E+16	3.16E+18	0	3.36E-12	8.73E+13	0.0508
287.18	760	4.64E+16	1.42E+16	3.16E+18	0	3.45E-12	9.17E+13	0.0644
287.18	760	4.66E+16	1.42E+16	3.17E+18	0	3.24E-12	7.96E+13	0.0093
287.18	760	4.72E+16	1.42E+16	3.00E+18	0	3.32E-12	9.39E+13	0.1199
287.18	760	4.79E+16	1.42E+16	3.15E+18	0	3.35E-12	9.20E+13	0.0901
287.18	760	4.79E+16	1.42E+16	3.15E+18	0	3.58E-12	9.81E+13	0.0734
287.18	760	4.81E+16	1.42E+16	3.16E+18	0	3.38E-12	8.30E+13	0.0000
287.18	760	4.81E+16	1.42E+16	3.16E+18	0	3.50E-12	9.95E+13	0.0705
287.18	760	4.81E+16	1.42E+16	3.16E+18	0	3.67E-12	1.08E+14	0.0875
287.18	760	4.87E+16	1.42E+16	3.00E+18	0	3.51E-12	9.96E+13	0.1222
287.18	760	4.94E+16	1.42E+16	3.14E+18	0	4.53E-12	8.41E+13	0.2413
287.18	760	4.97E+16	1.41E+16	3.16E+18	0	3.48E-12	8.95E+13	0.0296
287.18	760	4.97E+16	1.41E+16	3.16E+18	0	3.52E-12	1.01E+14	0.0901
287.18	760	4.97E+16	1.41E+16	3.16E+18	0	3.45E-12	7.00E+13	0.2408
287.18	760	5.04E+16	1.41E+16	3.10E+18	0	3.46E-12	1.08E+14	0.0717
287.18	760	5.04E+16	1.41E+16	3.10E+18	0	3.87E-12	1.04E+14	0.0989
287.18	760	5.04E+16	1.41E+16	3.10E+18	0	3.95E-12	1.09E+14	0.0938
287.18	760	5.10E+16	1.41E+16	3.14E+18	0	2.86E-12	4.46E+13	0.0937
287.18	760	5.20E+16	1.41E+16	3.10E+18	0	3.16E-12	8.20E+13	0.0570
287.18	760	5.21E+16	8.46E+16	2.32E+18	0	5.59E-12	7.76E+13	0.1619
287.18	760	5.21E+16	8.46E+16	2.32E+18	0	5.07E-12	6.74E+13	0.1721
287.18	760	5.21E+16	8.46E+16	2.32E+18	0	5.06E-12	8.41E+13	0.0815
287.18	760	5.37E+16	8.45E+16	2.31E+18	0	4.78E-12	7.87E+13	0.0793
287.18	760	5.37E+16	8.45E+16	2.31E+18	0	4.91E-12	7.96E+13	0.0787
287.18	760	5.37E+16	8.45E+16	2.31E+18	0	5.22E-12	8.20E+13	0.0973
287.18	760	5.37E+16	8.45E+16	2.31E+18	0	4.98E-12	8.17E+13	0.0807
287.18	760	5.37E+16	8.45E+16	2.31E+18	0	5.08E-12	8.01E+13	0.0958
287.18	760	5.42E+16	1.76E+17	2.33E+18	0	7.77E-12	8.99E+13	0.2079
287.18	760	5.42E+16	1.76E+17	2.33E+18	0	8.37E-12	8.65E+13	0.2388
287.18	760	5.42E+16	1.76E+17	2.33E+18	0	6.24E-12	7.64E+13	0.1594
287.18	760	5.42E+16	1.76E+17	2.33E+18	0	6.33E-12	7.40E+13	0.1808
287.18	760	5.42E+16	1.76E+17	2.33E+18	0	6.43E-12	7.17E+13	0.1094
287.18	760	5.42E+16	1.76E+17	2.33E+18	0	6.34E-12	7.11E+13	0.1288
287.18	760	5.42E+16	1.76E+17	2.33E+18	0	6.91E-12	7.25E+13	0.1699
287.18	760	5.42E+16	1.76E+17	2.33E+18	0	6.63E-12	6.70E+13	0.2071
287.18	760	5.47E+16	2.70E+17	2.36E+18	0	6.81E-12	5.88E+13	0.0962
287.18	760	5.47E+16	2.70E+17	2.36E+18	0	7.28E-12	5.35E+13	0.1378
287.18	760	5.47E+16	2.70E+17	2.36E+18	0	6.83E-12	6.21E+13	0.1048
287.18	760	5.47E+16	2.70E+17	2.36E+18	0	7.03E-12	6.26E+13	0.0769
287.18	760	5.47E+16	2.70E+17	2.36E+18	0	7.60E-12	5.39E+13	0.1656
287.18	760	5.47E+16	2.70E+17	2.36E+18	0	7.14E-12	6.09E+13	0.0792
287.18	760	5.47E+16	2.70E+17	2.36E+18	0	7.67E-12	6.72E+13	0.0851

287.18	760	5.47E+16	2.70E+17	2.36E+18	0	6.48E-12	5.73E+13	0.1610
287.18	760	5.47E+16	2.70E+17	2.36E+18	0	6.75E-12	6.55E+13	0.1755
287.18	760	5.47E+16	2.70E+17	2.36E+18	0	7.09E-12	5.07E+13	0.0670
287.18	760	5.47E+16	2.70E+17	2.36E+18	0	8.90E-12	6.49E+13	0.1103
287.18	760	5.52E+16	3.65E+17	2.38E+18	0	8.60E-12	6.87E+13	0.2301
287.18	760	5.52E+16	3.65E+17	2.38E+18	0	7.84E-12	7.50E+13	0.1747
287.18	760	5.52E+16	3.65E+17	2.38E+18	0	7.34E-12	7.37E+13	0.1747
287.18	760	5.52E+16	3.65E+17	2.38E+18	0	9.08E-12	5.78E+13	0.2249
287.18	760	5.52E+16	3.65E+17	2.38E+18	0	1.06E-11	6.23E+13	0.2757
287.18	760	5.52E+16	3.65E+17	2.38E+18	0	1.07E-11	6.92E+13	0.2404
287.18	760	5.52E+16	3.65E+17	2.38E+18	0	9.11E-12	6.00E+13	0.2505
287.18	760	5.52E+16	3.65E+17	2.38E+18	0	1.10E-11	6.68E+13	0.2712
287.18	760	5.56E+16	4.53E+17	2.40E+18	0	8.63E-12	5.21E+13	0.1387
287.18	760	5.56E+16	4.53E+17	2.40E+18	0	1.21E-11	6.42E+13	0.2390
287.18	760	5.56E+16	4.53E+17	2.40E+18	0	1.13E-11	6.94E+13	0.2364
287.18	760	5.56E+16	4.53E+17	2.40E+18	0	8.91E-12	5.31E+13	0.1835
287.18	760	5.56E+16	4.53E+17	2.40E+18	0	8.36E-12	5.18E+13	0.1853
287.18	760	5.56E+16	4.53E+17	2.40E+18	0	8.16E-12	4.35E+13	0.2070
287.18	760	5.56E+16	4.53E+17	2.40E+18	0	8.40E-12	3.76E+13	0.2378
287.18	760	5.56E+16	4.53E+17	2.40E+18	0	9.44E-12	5.39E+13	0.2005
287.18	760	5.59E+16	1.76E+17	2.33E+18	0	7.46E-12	8.56E+13	0.2494
287.18	760	5.59E+16	1.76E+17	2.33E+18	0	7.48E-12	8.32E+13	0.2480
287.18	760	5.59E+16	1.76E+17	2.33E+18	0	6.79E-12	8.13E+13	0.1785
287.18	760	5.59E+16	1.76E+17	2.33E+18	0	7.27E-12	7.36E+13	0.1745
287.18	760	5.69E+16	3.65E+17	2.37E+18	0	7.44E-12	4.88E+13	0.3172
287.18	760	5.86E+16	3.64E+17	2.37E+18	0	9.51E-12	6.10E+13	0.2729
287.18	760	5.86E+16	3.64E+17	2.37E+18	0	8.57E-12	6.67E+13	0.2117
287.18	760	5.86E+16	3.64E+17	2.37E+18	0	8.64E-12	5.79E+13	0.2529
287.18	760	5.04E+16	1.44E+16	3.21E+18	2.46E+16	3.76E-12	1.03E+14	0.1018
287.18	760	5.04E+16	1.44E+16	3.21E+18	2.46E+16	4.12E-12	9.97E+13	0.0516
287.18	760	5.04E+16	1.44E+16	3.21E+18	2.46E+16	3.57E-12	9.80E+13	0.0840
287.18	760	5.04E+16	1.44E+16	3.21E+18	2.46E+16	4.38E-12	1.03E+14	0.1059
287.18	760	5.15E+16	1.44E+16	3.17E+18	4.33E+16	4.06E-12	1.09E+14	0.0930
287.18	760	5.15E+16	1.44E+16	3.17E+18	4.33E+16	4.22E-12	1.12E+14	0.0937
287.18	760	5.10E+16	1.45E+16	3.25E+18	5.75E+16	4.26E-12	1.00E+14	0.0624
287.18	760	5.10E+16	1.45E+16	3.25E+18	5.75E+16	3.49E-12	8.83E+13	0.0514
287.18	760	5.10E+16	1.45E+16	3.25E+18	5.75E+16	4.32E-12	1.02E+14	0.1181
287.18	760	5.10E+16	1.45E+16	3.25E+18	5.75E+16	3.88E-12	9.20E+13	0.0200
287.18	760	5.24E+16	1.47E+16	3.22E+18	9.10E+16	4.74E-12	1.03E+14	0.1113
287.18	760	5.24E+16	1.47E+16	3.22E+18	9.10E+16	4.72E-12	1.04E+14	0.1043
287.18	760	4.58E+16	1.45E+16	3.23E+18	1.27E+17	4.75E-12	8.42E+13	0.0812
287.18	760	4.28E+16	1.45E+16	3.23E+18	1.27E+17	4.63E-12	7.78E+13	0.1036
287.18	760	4.73E+16	1.45E+16	3.22E+18	1.36E+17	5.55E-12	9.11E+13	0.1058
287.18	760	4.73E+16	1.45E+16	3.22E+18	1.36E+17	5.68E-12	9.19E+13	0.1322
287.18	760	4.60E+16	1.45E+16	3.24E+18	1.36E+17	4.76E-12	8.50E+13	0.0819
287.18	760	4.60E+16	1.45E+16	3.24E+18	1.36E+17	5.12E-12	8.43E+13	0.0862
287.18	760	5.32E+16	1.49E+16	3.28E+18	1.40E+17	4.89E-12	8.46E+13	0.1143
287.18	760	5.32E+16	1.49E+16	3.28E+18	1.40E+17	4.98E-12	9.46E+13	0.1114
287.18	760	4.57E+16	1.45E+16	3.22E+18	1.68E+17	4.45E-12	7.88E+13	0.0569
287.18	760	4.57E+16	1.45E+16	3.22E+18	1.68E+17	4.48E-12	8.03E+13	0.0573
287.18	760	4.44E+16	1.45E+16	3.24E+18	1.68E+17	5.52E-12	8.45E+13	0.0993

287.18	760	4.44E+16	1.45E+16	3.24E+18	1.68E+17	5.60E-12	8.57E+13	0.0904
287.18	760	4.90E+16	1.44E+16	3.22E+18	1.80E+17	6.04E-12	9.82E+13	0.1372
287.18	760	4.90E+16	1.44E+16	3.22E+18	1.80E+17	5.64E-12	9.21E+13	0.1507
287.18	760	4.27E+16	1.45E+16	3.23E+18	1.80E+17	5.84E-12	7.89E+13	0.1214
287.18	760	4.27E+16	1.45E+16	3.23E+18	1.80E+17	5.36E-12	7.71E+13	0.1081
287.18	760	5.41E+16	1.52E+16	3.33E+18	1.91E+17	5.73E-12	1.04E+14	0.1252
287.18	760	5.41E+16	1.52E+16	3.33E+18	1.91E+17	5.50E-12	9.66E+13	0.1327
287.18	760	4.56E+16	1.45E+16	3.21E+18	1.93E+17	5.28E-12	7.27E+13	0.1645
287.18	760	4.26E+16	1.45E+16	3.22E+18	1.93E+17	5.76E-12	7.23E+13	0.0982
287.18	760	4.74E+16	1.44E+16	3.22E+18	2.06E+17	5.40E-12	8.37E+13	0.0431
287.18	760	4.74E+16	1.44E+16	3.22E+18	2.06E+17	5.90E-12	9.03E+13	0.1104
287.18	760	4.42E+16	1.45E+16	3.22E+18	2.07E+17	4.79E-12	6.82E+13	0.0645
287.18	760	4.42E+16	1.45E+16	3.22E+18	2.07E+17	5.51E-12	6.89E+13	0.1124
287.18	760	4.87E+16	1.44E+16	3.20E+18	2.36E+17	6.19E-12	7.49E+13	0.1166
287.18	760	4.87E+16	1.44E+16	3.20E+18	2.36E+17	5.88E-12	6.98E+13	0.1184
287.18	760	4.56E+16	1.44E+16	3.21E+18	2.36E+17	6.39E-12	7.93E+13	0.1174
287.18	760	4.56E+16	1.44E+16	3.21E+18	2.36E+17	6.05E-12	7.40E+13	0.1180
287.18	760	5.50E+16	1.54E+16	3.38E+18	2.39E+17	5.85E-12	9.72E+13	0.1052
287.18	760	5.50E+16	1.54E+16	3.38E+18	2.39E+17	6.08E-12	9.26E+13	0.1501
287.18	760	4.56E+16	1.44E+16	3.21E+18	2.53E+17	5.48E-12	6.95E+13	0.0704
287.18	760	4.41E+16	1.44E+16	3.21E+18	2.53E+17	6.51E-12	7.82E+13	0.1498
287.18	760	4.86E+16	1.44E+16	3.20E+18	2.69E+17	6.04E-12	7.18E+13	0.1404
287.18	760	4.56E+16	1.44E+16	3.21E+18	2.70E+17	6.07E-12	7.43E+13	0.1137
287.18	760	4.56E+16	1.44E+16	3.21E+18	2.70E+17	5.32E-12	6.81E+13	0.0888
287.18	760	4.55E+16	1.44E+16	3.20E+18	2.70E+17	7.03E-12	8.04E+13	0.1647
287.18	760	4.40E+16	1.44E+16	3.21E+18	3.08E+17	6.20E-12	7.31E+13	0.0833
287.18	760	4.25E+16	1.44E+16	3.21E+18	3.09E+17	6.26E-12	6.32E+13	0.1213
287.18	760	4.05E+16	1.44E+16	3.06E+18	3.09E+17	5.14E-12	5.58E+13	0.0587
287.18	760	4.05E+16	1.44E+16	3.06E+18	3.09E+17	6.83E-12	7.42E+13	0.1451
278.38	760	4.37E+16	8.70E+16	2.65E+18	0	9.20E-12	7.79E+13	0.0823
278.38	760	4.37E+16	8.70E+16	2.65E+18	0	1.03E-11	8.39E+13	0.1027
278.38	760	4.65E+16	1.46E+16	3.27E+18	0	4.27E-12	8.30E+13	0.1077
278.38	760	4.65E+16	1.46E+16	3.27E+18	0	4.38E-12	8.33E+13	0.0898
278.38	760	4.67E+16	8.68E+16	2.64E+18	0	7.85E-12	7.03E+13	0.0912
278.38	760	4.76E+16	2.78E+17	2.69E+18	0	9.43E-12	4.76E+13	0.1298
278.38	760	4.76E+16	2.78E+17	2.69E+18	0	2.10E-11	6.53E+13	0.1632
278.38	760	4.76E+16	2.78E+17	2.69E+18	0	1.20E-11	5.13E+13	0.1689
278.38	760	4.76E+16	2.78E+17	2.69E+18	0	1.34E-11	5.71E+13	0.1408
278.38	760	4.76E+16	2.78E+17	2.69E+18	0	1.47E-11	5.34E+13	0.1536
278.38	760	4.76E+16	2.78E+17	2.69E+18	0	1.71E-11	7.34E+13	0.1024
278.38	760	4.80E+16	3.76E+17	2.72E+18	0	9.78E-12	3.78E+13	0.1420
278.38	760	4.80E+16	3.76E+17	2.72E+18	0	5.69E-12	3.41E+13	0.0114
278.38	760	4.80E+16	3.76E+17	2.72E+18	0	1.19E-11	4.05E+13	0.1554
278.38	760	4.80E+16	3.76E+17	2.72E+18	0	9.58E-12	3.63E+13	0.1471
278.38	760	4.80E+16	3.76E+17	2.72E+18	0	9.00E-12	4.00E+13	0.1684
278.38	760	4.80E+16	3.76E+17	2.72E+18	0	1.71E-11	5.42E+13	0.1858
278.38	760	4.80E+16	3.76E+17	2.72E+18	0	1.63E-11	5.26E+13	0.1587
278.38	760	4.80E+16	3.76E+17	2.72E+18	0	1.36E-11	4.53E+13	0.1734
278.38	760	4.83E+16	8.67E+16	2.64E+18	0	8.15E-12	7.41E+13	0.1121
278.38	760	4.83E+16	8.67E+16	2.64E+18	0	9.14E-12	7.92E+13	0.1036
278.38	760	4.83E+16	8.67E+16	2.64E+18	0	6.36E-12	6.96E+13	0.0743

278.38	760	4.83E+16	8.67E+16	2.64E+18	0	9.05E-12	7.56E+13	0.0998
278.38	760	4.83E+16	8.67E+16	2.64E+18	0	7.40E-12	8.08E+13	0.0909
278.38	760	4.96E+16	1.46E+16	3.26E+18	0	4.55E-12	9.75E+13	0.1165
278.38	760	4.96E+16	1.46E+16	3.26E+18	0	4.48E-12	9.48E+13	0.1255
278.38	760	5.36E+16	1.80E+17	2.65E+18	0	1.39E-11	7.25E+13	0.0967
278.38	760	5.36E+16	1.80E+17	2.65E+18	0	1.45E-11	7.52E+13	0.1263
278.38	760	5.36E+16	1.80E+17	2.65E+18	0	1.65E-11	8.17E+13	0.1389
278.38	760	5.36E+16	1.80E+17	2.65E+18	0	1.40E-11	7.35E+13	0.1410
278.38	760	5.36E+16	1.80E+17	2.65E+18	0	1.10E-11	6.95E+13	0.1443
278.38	760	5.36E+16	1.80E+17	2.65E+18	0	8.35E-12	5.86E+13	0.1387
278.38	760	5.36E+16	1.80E+17	2.65E+18	0	1.38E-11	7.19E+13	0.1257
278.38	760	5.36E+16	1.80E+17	2.65E+18	0	1.07E-11	6.29E+13	0.1170
278.38	760	5.46E+16	1.46E+16	3.25E+18	0	4.43E-12	1.04E+14	0.1017
278.38	760	5.46E+16	1.46E+16	3.25E+18	0	4.25E-12	9.60E+13	0.1065
278.38	760	5.46E+16	1.46E+16	3.25E+18	0	4.57E-12	1.08E+14	0.0952
278.38	760	5.46E+16	1.46E+16	3.25E+18	0	4.91E-12	1.11E+14	0.1069
278.38	760	5.46E+16	1.46E+16	3.25E+18	0	4.08E-12	1.02E+14	0.0845
278.38	760	5.46E+16	1.46E+16	3.25E+18	0	4.33E-12	1.07E+14	0.1014
278.38	760	5.51E+16	4.63E+17	2.72E+18	0	2.07E-11	6.32E+13	0.1474
278.38	760	5.51E+16	4.63E+17	2.72E+18	0	2.84E-11	7.36E+13	0.1701
278.38	760	5.51E+16	4.63E+17	2.72E+18	0	1.83E-11	5.36E+13	0.1764
278.38	760	5.51E+16	4.63E+17	2.72E+18	0	1.52E-11	5.00E+13	0.1707
278.38	760	5.51E+16	4.63E+17	2.72E+18	0	1.32E-11	4.72E+13	0.1806
278.38	760	5.51E+16	4.63E+17	2.72E+18	0	1.99E-11	6.33E+13	0.1626
278.38	760	5.51E+16	4.63E+17	2.72E+18	0	2.51E-11	6.79E+13	0.1715
278.38	760	5.51E+16	4.63E+17	2.72E+18	0	1.98E-11	5.58E+13	0.1781
278.38	760	5.20E+16	1.48E+16	3.31E+18	2.54E+16	4.93E-12	9.26E+13	0.0814
278.38	760	5.20E+16	1.48E+16	3.31E+18	2.54E+16	5.04E-12	9.82E+13	0.1008
278.38	760	4.72E+16	1.49E+16	3.32E+18	2.55E+16	4.83E-12	8.33E+13	0.0989
278.38	760	4.72E+16	1.49E+16	3.32E+18	2.55E+16	4.86E-12	8.18E+13	0.1042
278.38	760	5.25E+16	1.50E+16	3.34E+18	5.44E+16	5.42E-12	9.61E+13	0.1176
278.38	760	5.25E+16	1.50E+16	3.34E+18	5.44E+16	5.14E-12	8.69E+13	0.1088
278.38	760	4.93E+16	1.50E+16	3.35E+18	5.46E+16	5.41E-12	8.25E+13	0.1386
278.38	760	4.93E+16	1.50E+16	3.35E+18	5.46E+16	4.82E-12	6.41E+13	0.1643
278.38	760	5.83E+16	1.51E+16	3.37E+18	8.87E+16	5.43E-12	1.00E+14	0.1061
278.38	760	5.83E+16	1.51E+16	3.37E+18	8.87E+16	5.35E-12	9.50E+13	0.1181
278.38	760	5.15E+16	1.52E+16	3.39E+18	8.91E+16	6.49E-12	8.77E+13	0.1561
278.38	760	5.15E+16	1.52E+16	3.39E+18	8.91E+16	6.27E-12	8.96E+13	0.1191
278.38	760	5.37E+16	1.53E+16	3.41E+18	1.19E+17	6.35E-12	8.30E+13	0.1157
278.38	760	5.37E+16	1.53E+16	3.41E+18	1.19E+17	5.78E-12	6.57E+13	0.1273
278.38	760	5.20E+16	1.53E+16	3.42E+18	1.19E+17	6.53E-12	7.10E+13	0.1648
278.38	760	5.20E+16	1.53E+16	3.42E+18	1.19E+17	6.87E-12	9.47E+13	0.1353
278.38	760	5.20E+16	1.53E+16	3.42E+18	1.19E+17	6.43E-12	9.06E+13	0.1455
278.38	760	5.25E+16	1.55E+16	3.45E+18	1.50E+17	7.17E-12	9.02E+13	0.1453
278.38	760	5.25E+16	1.55E+16	3.45E+18	1.50E+17	6.91E-12	8.38E+13	0.1209
278.38	760	5.25E+16	1.55E+16	3.45E+18	1.50E+17	6.00E-12	7.76E+13	0.0879
278.38	760	5.25E+16	1.55E+16	3.45E+18	1.50E+17	6.84E-12	7.89E+13	0.1587
278.38	760	5.83E+16	1.56E+16	3.47E+18	1.81E+17	6.41E-12	9.48E+13	0.1192
278.38	760	5.83E+16	1.56E+16	3.47E+18	1.81E+17	6.50E-12	8.83E+13	0.1443
278.38	760	5.30E+16	1.56E+16	3.49E+18	1.82E+17	7.84E-12	9.28E+13	0.1249
278.38	760	5.30E+16	1.56E+16	3.49E+18	1.82E+17	8.09E-12	8.83E+13	0.1712

273.98	760	4.92E+16	1.25E+16	3.35E+18	0	4.97E-12	1.01E+14	0.1659
273.98	760	4.92E+16	1.25E+16	3.35E+18	0	4.94E-12	9.42E+13	0.2205
273.98	760	4.92E+16	1.25E+16	3.35E+18	0	5.28E-12	9.79E+13	0.2468
273.98	760	4.92E+16	1.25E+16	3.35E+18	0	5.08E-12	8.95E+13	0.1907
273.98	760	5.00E+16	1.49E+16	3.29E+18	0	4.88E-12	9.41E+13	0.1393
273.98	760	5.00E+16	1.49E+16	3.29E+18	0	4.71E-12	9.81E+13	0.1252
273.98	760	5.08E+16	1.24E+16	3.34E+18	0	3.91E-12	9.27E+13	0.1588
273.98	760	5.16E+16	1.48E+16	3.28E+18	0	4.22E-12	9.83E+13	0.1714
273.98	760	5.16E+16	1.48E+16	3.28E+18	0	4.98E-12	9.59E+13	0.1495
273.98	760	5.16E+16	1.48E+16	3.28E+18	0	5.02E-12	9.70E+13	0.1311
273.98	760	5.16E+16	1.48E+16	3.28E+18	0	4.38E-12	9.62E+13	0.1539
273.98	760	5.16E+16	1.48E+16	3.28E+18	0	4.53E-12	9.78E+13	0.1565
273.98	760	5.25E+16	1.24E+16	3.34E+18	0	4.65E-12	1.03E+14	0.1865
273.98	760	5.33E+16	1.48E+16	3.28E+18	0	4.40E-12	9.70E+13	0.1383
273.98	760	5.33E+16	1.48E+16	3.28E+18	0	4.83E-12	1.04E+14	0.1295
273.98	760	5.33E+16	1.48E+16	3.28E+18	0	4.42E-12	9.60E+13	0.1072
273.98	760	5.33E+16	1.48E+16	3.28E+18	0	4.40E-12	9.48E+13	0.1102
273.98	760	5.33E+16	1.48E+16	3.28E+18	0	4.66E-12	9.53E+13	0.1158
273.98	760	5.33E+16	1.48E+16	3.28E+18	0	5.00E-12	9.15E+13	0.1345
273.98	760	5.59E+16	1.24E+16	3.33E+18	0	4.82E-12	1.01E+14	0.1234
273.98	760	5.59E+16	1.24E+16	3.33E+18	0	4.17E-12	9.04E+13	0.1221
273.98	760	5.59E+16	1.24E+16	3.33E+18	0	4.70E-12	1.04E+14	0.1322
273.98	760	5.59E+16	1.24E+16	3.33E+18	0	4.74E-12	9.49E+13	0.1305
273.98	760	5.63E+16	8.85E+16	2.43E+18	0	7.05E-12	6.33E+13	0.2501
273.98	760	5.63E+16	8.85E+16	2.43E+18	0	7.05E-12	5.80E+13	0.2610
273.98	760	5.80E+16	8.84E+16	2.42E+18	0	7.23E-12	6.60E+13	0.3327
273.98	760	5.80E+16	8.84E+16	2.42E+18	0	8.71E-12	6.64E+13	0.2973
273.98	760	5.86E+16	1.85E+17	2.44E+18	0	8.43E-12	4.00E+13	0.4187
273.98	760	5.86E+16	1.85E+17	2.44E+18	0	9.18E-12	5.20E+13	0.2834
273.98	760	5.86E+16	1.85E+17	2.44E+18	0	9.51E-12	5.40E+13	0.3193
273.98	760	5.86E+16	1.85E+17	2.44E+18	0	7.96E-12	4.35E+13	0.2756
273.98	760	5.86E+16	1.85E+17	2.44E+18	0	9.19E-12	5.13E+13	0.3446
273.98	760	5.86E+16	1.85E+17	2.44E+18	0	8.19E-12	4.55E+13	0.2706
273.98	760	5.86E+16	1.85E+17	2.44E+18	0	8.40E-12	5.18E+13	0.2297
273.98	760	5.91E+16	2.83E+17	2.47E+18	0	8.52E-12	3.09E+13	0.3669
273.98	760	5.91E+16	2.83E+17	2.47E+18	0	1.02E-11	3.48E+13	0.3935
273.98	760	5.91E+16	2.83E+17	2.47E+18	0	8.37E-12	3.07E+13	0.3444
273.98	760	5.91E+16	2.83E+17	2.47E+18	0	9.87E-12	3.83E+13	0.3046
273.98	760	5.91E+16	2.83E+17	2.47E+18	0	8.06E-12	3.70E+13	0.2352
273.98	760	5.91E+16	2.83E+17	2.47E+18	0	8.11E-12	3.76E+13	0.2229
273.98	760	5.91E+16	2.83E+17	2.47E+18	0	9.70E-12	3.94E+13	0.3505
273.98	760	5.91E+16	2.83E+17	2.47E+18	0	9.75E-12	3.76E+13	0.2791
273.98	760	5.96E+16	3.83E+17	2.49E+18	0	8.59E-12	3.62E+13	0.4925
273.98	760	5.96E+16	3.83E+17	2.49E+18	0	1.22E-11	4.16E+13	0.4919
273.98	760	5.96E+16	3.83E+17	2.49E+18	0	1.23E-11	4.11E+13	0.4826
273.98	760	5.96E+16	3.83E+17	2.49E+18	0	1.79E-11	5.10E+13	0.5083
273.98	760	5.96E+16	3.83E+17	2.49E+18	0	1.22E-11	3.72E+13	0.3606
273.98	760	5.96E+16	3.83E+17	2.49E+18	0	9.38E-12	3.10E+13	0.3811
273.98	760	5.96E+16	3.83E+17	2.49E+18	0	1.13E-11	3.45E+13	0.3559
273.98	760	5.96E+16	3.83E+17	2.49E+18	0	1.30E-11	3.71E+13	0.3550
273.98	760	5.98E+16	8.83E+16	2.42E+18	0	8.73E-12	6.92E+13	0.3964

273.98	760	5.98E+16	8.83E+16	2.42E+18	0	8.53E-12	6.70E+13	0.2354
273.98	760	5.98E+16	8.83E+16	2.42E+18	0	7.55E-12	5.75E+13	0.2815
273.98	760	6.01E+16	4.74E+17	2.51E+18	0	1.38E-11	3.63E+13	0.5527
273.98	760	6.01E+16	4.74E+17	2.51E+18	0	1.52E-11	4.04E+13	0.5684
273.98	760	6.20E+16	4.73E+17	2.51E+18	0	1.47E-11	3.91E+13	0.5025
273.98	760	6.20E+16	4.73E+17	2.51E+18	0	1.59E-11	3.55E+13	0.4962
273.98	760	6.20E+16	4.73E+17	2.51E+18	0	1.13E-11	3.50E+13	0.4636
273.98	760	6.20E+16	4.73E+17	2.51E+18	0	1.68E-11	4.01E+13	0.4732
273.98	760	5.41E+16	1.50E+16	3.33E+18	2.58E+16	5.29E-12	9.13E+13	0.1193
273.98	760	5.67E+16	1.26E+16	3.38E+18	2.58E+16	5.89E-12	1.05E+14	0.1677
273.98	760	5.67E+16	1.26E+16	3.38E+18	2.58E+16	5.00E-12	9.82E+13	0.1674
273.98	760	5.25E+16	1.51E+16	3.34E+18	2.58E+16	5.26E-12	8.22E+13	0.1278
273.98	760	5.24E+16	1.51E+16	3.33E+18	2.58E+16	5.06E-12	1.01E+14	0.1395
273.98	760	5.24E+16	1.51E+16	3.33E+18	2.58E+16	5.07E-12	9.93E+13	0.1460
273.98	760	5.16E+16	1.26E+16	3.39E+18	2.59E+16	4.61E-12	8.20E+13	0.1511
273.98	760	5.16E+16	1.26E+16	3.39E+18	2.59E+16	4.47E-12	8.22E+13	0.1708
273.98	760	5.46E+16	1.52E+16	3.36E+18	5.52E+16	5.74E-12	9.53E+13	0.1324
273.98	760	5.46E+16	1.52E+16	3.36E+18	5.52E+16	5.21E-12	8.79E+13	0.1225
273.98	760	4.97E+16	1.52E+16	3.38E+18	5.54E+16	6.90E-12	6.94E+13	0.1759
273.98	760	4.97E+16	1.52E+16	3.38E+18	5.54E+16	7.44E-12	9.12E+13	0.1299
273.98	760	5.04E+16	1.28E+16	3.43E+18	5.56E+16	5.90E-12	7.62E+13	0.1721
273.98	760	5.04E+16	1.28E+16	3.43E+18	5.56E+16	5.57E-12	8.40E+13	0.1386
273.98	760	5.04E+16	1.28E+16	3.43E+18	5.56E+16	4.85E-12	7.46E+13	0.0975
273.98	760	5.04E+16	1.28E+16	3.43E+18	5.56E+16	5.04E-12	6.78E+13	0.1371
273.98	760	5.75E+16	1.28E+16	3.43E+18	7.02E+16	5.28E-12	8.30E+13	0.1872
273.98	760	5.75E+16	1.28E+16	3.43E+18	7.02E+16	5.79E-12	8.47E+13	0.1612
273.98	760	5.32E+16	1.53E+16	3.38E+18	7.03E+16	6.83E-12	9.94E+13	0.1852
273.98	760	5.32E+16	1.53E+16	3.38E+18	7.03E+16	6.20E-12	9.16E+13	0.2024
273.98	760	4.83E+16	1.53E+16	3.40E+18	7.05E+16	6.07E-12	8.44E+13	0.1081
273.98	760	4.83E+16	1.53E+16	3.40E+18	7.05E+16	6.12E-12	8.53E+13	0.1539
273.98	760	5.07E+16	1.28E+16	3.45E+18	7.06E+16	6.61E-12	8.09E+13	0.1811
273.98	760	5.07E+16	1.28E+16	3.45E+18	7.06E+16	6.33E-12	8.24E+13	0.1412
273.98	760	5.52E+16	1.54E+16	3.40E+18	9.03E+16	6.94E-12	9.79E+13	0.1433
273.98	760	5.52E+16	1.54E+16	3.40E+18	9.03E+16	5.90E-12	7.70E+13	0.1555
273.98	760	5.79E+16	1.29E+16	3.45E+18	9.04E+16	6.93E-12	9.08E+13	0.1758
273.98	760	5.79E+16	1.29E+16	3.45E+18	9.04E+16	5.96E-12	8.29E+13	0.1341
273.98	760	5.36E+16	1.54E+16	3.41E+18	9.05E+16	5.95E-12	8.22E+13	0.1288
273.98	760	5.36E+16	1.54E+16	3.41E+18	9.05E+16	5.86E-12	7.55E+13	0.1519
273.98	760	5.10E+16	1.29E+16	3.47E+18	9.09E+16	8.69E-12	8.37E+13	0.1948
273.98	760	5.10E+16	1.29E+16	3.47E+18	9.09E+16	7.99E-12	8.30E+13	0.1951
273.98	760	5.38E+16	1.55E+16	3.42E+18	1.06E+17	5.32E-12	7.86E+13	0.1546
273.98	760	5.38E+16	1.55E+16	3.42E+18	1.06E+17	5.64E-12	7.54E+13	0.1415
273.98	760	5.64E+16	1.29E+16	3.47E+18	1.06E+17	6.81E-12	9.41E+13	0.1373
273.98	760	5.64E+16	1.29E+16	3.47E+18	1.06E+17	6.27E-12	8.61E+13	0.1621
273.98	760	5.05E+16	1.55E+16	3.43E+18	1.06E+17	8.29E-12	9.11E+13	0.1427
273.98	760	5.05E+16	1.55E+16	3.43E+18	1.06E+17	6.41E-12	5.74E+13	0.1678
273.98	760	5.13E+16	1.30E+16	3.49E+18	1.06E+17	6.38E-12	7.76E+13	0.1344
273.98	760	5.13E+16	1.30E+16	3.49E+18	1.06E+17	7.63E-12	7.74E+13	0.2114
273.98	760	5.76E+16	1.55E+16	3.43E+18	1.26E+17	6.08E-12	8.03E+13	0.2051
273.98	760	5.76E+16	1.55E+16	3.43E+18	1.26E+17	6.80E-12	9.54E+13	0.1497
273.98	760	5.59E+16	1.55E+16	3.44E+18	1.26E+17	6.05E-12	7.31E+13	0.0815

273.98	760	5.59E+16	1.55E+16	3.44E+18	1.26E+17	6.69E-12	7.64E+13	0.1436
273.98	760	5.50E+16	1.30E+16	3.50E+18	1.27E+17	5.40E-12	7.15E+13	0.2176
273.98	760	5.50E+16	1.30E+16	3.50E+18	1.27E+17	5.76E-12	7.55E+13	0.2267
273.98	760	5.16E+16	1.31E+16	3.51E+18	1.27E+17	8.60E-12	9.49E+13	0.1446
273.98	760	5.16E+16	1.31E+16	3.51E+18	1.27E+17	7.97E-12	8.02E+13	0.2115
262.54	760	5.26E+16	1.30E+16	3.46E+18	0	7.04E-12	7.65E+13	0.1832
262.54	760	5.26E+16	1.30E+16	3.46E+18	0	7.26E-12	8.29E+13	0.1632
262.54	760	5.26E+16	1.30E+16	3.46E+18	0	7.44E-12	8.39E+13	0.1759
262.54	760	5.60E+16	1.30E+16	3.45E+18	0	6.71E-12	8.86E+13	0.1682
262.54	760	5.60E+16	1.30E+16	3.45E+18	0	5.48E-12	7.36E+13	0.1796
262.54	760	5.86E+16	1.93E+17	2.66E+18	0	2.60E-11	4.78E+13	0.1065
262.54	760	5.86E+16	1.93E+17	2.66E+18	0	2.57E-11	4.55E+13	0.0750
262.54	760	5.86E+16	1.93E+17	2.66E+18	0	2.87E-11	4.79E+13	0.1301
262.54	760	5.96E+16	1.29E+16	3.44E+18	0	6.04E-12	7.55E+13	0.0979
262.54	760	5.96E+16	1.29E+16	3.44E+18	0	7.78E-12	8.45E+13	0.1409
262.54	760	5.96E+16	1.29E+16	3.44E+18	0	6.05E-12	7.99E+13	0.0760
262.54	760	5.96E+16	1.29E+16	3.44E+18	0	6.00E-12	7.54E+13	0.1058
262.54	760	5.99E+16	9.22E+16	2.63E+18	0	1.68E-11	5.19E+13	0.1012
262.54	760	5.99E+16	9.22E+16	2.63E+18	0	1.75E-11	6.05E+13	0.0657
262.54	760	5.99E+16	9.22E+16	2.63E+18	0	1.77E-11	6.07E+13	0.0774
262.54	760	5.99E+16	9.22E+16	2.63E+18	0	1.86E-11	6.26E+13	0.1059
262.54	760	5.99E+16	9.22E+16	2.63E+18	0	1.87E-11	6.13E+13	0.1160
262.54	760	5.99E+16	9.22E+16	2.63E+18	0	1.94E-11	6.32E+13	0.1132
262.54	760	5.99E+16	9.22E+16	2.63E+18	0	1.83E-11	5.35E+13	0.1366
262.54	760	6.00E+16	9.14E+16	2.78E+18	0	1.29E-11	5.67E+13	0.1683
262.54	760	6.00E+16	9.14E+16	2.78E+18	0	1.27E-11	5.79E+13	0.1504
262.54	760	6.00E+16	9.14E+16	2.78E+18	0	1.48E-11	5.99E+13	0.1694
262.54	760	6.00E+16	9.14E+16	2.78E+18	0	1.19E-11	4.80E+13	0.1776
262.54	760	6.00E+16	9.14E+16	2.78E+18	0	1.37E-11	5.70E+13	0.2369
262.54	760	6.00E+16	9.14E+16	2.78E+18	0	1.16E-11	5.40E+13	0.2184
262.54	760	6.00E+16	9.14E+16	2.78E+18	0	1.11E-11	5.05E+13	0.2375
262.54	760	6.00E+16	9.14E+16	2.78E+18	0	1.43E-11	5.34E+13	0.2463
262.54	760	6.04E+16	1.93E+17	2.66E+18	0	2.87E-11	5.66E+13	0.0698
262.54	760	6.04E+16	1.93E+17	2.66E+18	0	3.08E-11	5.49E+13	0.1087
262.54	760	6.04E+16	1.93E+17	2.66E+18	0	3.08E-11	5.89E+13	0.0911
262.54	760	6.10E+16	2.95E+17	2.68E+18	0	2.50E-11	3.14E+13	0.1708
262.54	760	6.10E+16	2.95E+17	2.68E+18	0	4.46E-11	5.37E+13	0.1103
262.54	760	6.10E+16	2.95E+17	2.68E+18	0	3.93E-11	4.93E+13	0.1238
262.54	760	6.10E+16	2.95E+17	2.68E+18	0	3.28E-11	4.27E+13	0.0325
262.54	760	6.10E+16	2.95E+17	2.68E+18	0	3.76E-11	4.67E+13	0.1431
262.54	760	6.10E+16	2.95E+17	2.68E+18	0	3.87E-11	4.94E+13	0.1234
262.54	760	6.10E+16	2.95E+17	2.68E+18	0	3.63E-11	4.41E+13	0.1224
262.54	760	6.10E+16	2.95E+17	2.68E+18	0	3.80E-11	4.96E+13	0.1294
262.54	760	6.15E+16	3.99E+17	2.70E+18	0	4.70E-11	4.95E+13	0.0294
262.54	760	6.15E+16	3.99E+17	2.70E+18	0	4.17E-11	4.14E+13	0.0000
262.54	760	6.15E+16	3.99E+17	2.70E+18	0	3.74E-11	2.45E+13	0.1369
262.54	760	6.15E+16	3.99E+17	2.70E+18	0	3.96E-11	4.20E+13	0.0471
262.54	760	6.15E+16	3.99E+17	2.70E+18	0	4.15E-11	5.00E+13	0.0870
262.54	760	6.16E+16	3.95E+17	2.86E+18	0	3.22E-11	4.63E+13	0.1259
262.54	760	6.16E+16	3.95E+17	2.86E+18	0	2.85E-11	4.05E+13	0.1825
262.54	760	6.16E+16	3.95E+17	2.86E+18	0	2.96E-11	4.28E+13	0.1179

262.54	760	6.16E+16	3.95E+17	2.86E+18	0	3.13E-11	4.10E+13	0.2246
262.54	760	6.23E+16	1.91E+17	2.80E+18	0	2.80E-11	5.82E+13	0.2178
262.54	760	6.23E+16	1.91E+17	2.80E+18	0	2.51E-11	5.60E+13	0.2247
262.54	760	6.23E+16	1.91E+17	2.80E+18	0	1.88E-11	4.05E+13	0.2991
262.54	760	6.23E+16	1.91E+17	2.80E+18	0	3.26E-11	6.78E+13	0.2014
262.54	760	6.23E+16	1.91E+17	2.80E+18	0	2.13E-11	5.14E+13	0.2218
262.54	760	6.23E+16	1.91E+17	2.80E+18	0	2.94E-11	5.75E+13	0.2323
262.54	760	6.23E+16	1.91E+17	2.80E+18	0	2.22E-11	4.79E+13	0.2592
262.54	760	6.23E+16	1.91E+17	2.80E+18	0	2.11E-11	4.77E+13	0.2571
262.54	760	6.29E+16	2.92E+17	2.83E+18	0	3.63E-11	4.82E+13	0.2325
262.54	760	6.29E+16	2.92E+17	2.83E+18	0	2.93E-11	4.13E+13	0.2933
262.54	760	6.29E+16	2.92E+17	2.83E+18	0	2.74E-11	4.27E+13	0.2713
262.54	760	6.29E+16	2.92E+17	2.83E+18	0	1.71E-11	3.47E+13	0.2538
262.54	760	6.29E+16	2.92E+17	2.83E+18	0	1.99E-11	3.59E+13	0.2136
262.54	760	6.29E+16	2.92E+17	2.83E+18	0	3.81E-11	5.30E+13	0.1900
262.54	760	6.29E+16	2.92E+17	2.83E+18	0	1.88E-11	2.94E+13	0.3175
262.54	760	6.34E+16	3.98E+17	2.70E+18	0	4.52E-11	4.76E+13	0.0434
262.54	760	6.34E+16	3.98E+17	2.70E+18	0	3.81E-11	4.57E+13	0.0537
262.54	760	6.35E+16	3.95E+17	2.85E+18	0	2.09E-11	2.85E+13	0.1219
262.54	760	6.35E+16	3.95E+17	2.85E+18	0	2.01E-11	2.81E+13	0.1364
262.54	760	6.35E+16	3.95E+17	2.85E+18	0	2.66E-11	3.28E+13	0.1945
262.54	760	6.35E+16	3.95E+17	2.85E+18	0	2.78E-11	3.94E+13	0.1534
262.54	760	6.52E+16	1.31E+16	2.61E+18	0	9.16E-12	9.86E+13	0.1741
262.54	760	6.75E+16	1.31E+16	2.62E+18	0	8.78E-12	9.17E+13	0.0929
262.54	760	6.75E+16	1.31E+16	2.62E+18	0	8.25E-12	9.72E+13	0.0919
262.54	760	6.75E+16	1.31E+16	2.62E+18	0	7.98E-12	9.49E+13	0.0993
262.54	760	6.75E+16	1.31E+16	2.62E+18	0	8.01E-12	9.87E+13	0.0803
262.54	760	6.91E+16	1.31E+16	2.60E+18	0	8.96E-12	1.01E+14	0.1656
262.54	760	7.11E+16	1.31E+16	2.60E+18	0	1.13E-11	1.14E+14	0.1663
262.54	760	7.11E+16	1.31E+16	2.60E+18	0	1.03E-11	1.08E+14	0.2186
262.54	760	5.29E+16	1.31E+16	3.48E+18	1.73E+15	7.34E-12	8.44E+13	0.1163
262.54	760	5.29E+16	1.31E+16	3.48E+18	1.73E+15	6.99E-12	8.18E+13	0.1377
262.54	760	5.29E+16	1.31E+16	3.48E+18	1.73E+15	8.39E-12	8.50E+13	0.1613
262.54	760	5.29E+16	1.31E+16	3.48E+18	1.73E+15	6.82E-12	8.17E+13	0.1410
262.54	760	4.96E+16	1.31E+16	3.50E+18	6.77E+15	7.54E-12	8.01E+13	0.1802
262.54	760	4.96E+16	1.31E+16	3.50E+18	6.77E+15	8.68E-12	8.51E+13	0.1787
262.54	760	4.96E+16	1.31E+16	3.50E+18	6.77E+15	6.62E-12	7.25E+13	0.1539
262.54	760	4.96E+16	1.31E+16	3.50E+18	6.77E+15	6.69E-12	7.58E+13	0.1349
262.54	760	7.79E+16	1.31E+16	2.61E+18	6.86E+15	1.02E-11	1.08E+14	0.1334
262.54	760	7.79E+16	1.31E+16	2.61E+18	6.86E+15	7.91E-12	9.37E+13	0.0519
262.54	760	7.79E+16	1.31E+16	2.61E+18	6.86E+15	8.28E-12	9.66E+13	0.0118
262.54	760	7.79E+16	1.31E+16	2.61E+18	6.86E+15	8.73E-12	1.08E+14	0.0000
262.54	760	7.79E+16	1.31E+16	2.61E+18	6.86E+15	8.12E-12	1.12E+14	0.0762
262.54	760	7.79E+16	1.31E+16	2.61E+18	6.86E+15	9.92E-12	1.23E+14	0.1497
262.54	760	7.00E+16	1.32E+16	2.64E+18	7.36E+15	9.00E-12	1.06E+14	0.1045
262.54	760	7.00E+16	1.32E+16	2.64E+18	7.36E+15	7.99E-12	1.04E+14	0.0627
262.54	760	7.00E+16	1.32E+16	2.64E+18	7.36E+15	8.66E-12	1.04E+14	0.1047
262.54	760	7.00E+16	1.32E+16	2.64E+18	7.36E+15	7.85E-12	9.91E+13	0.0872
262.54	760	6.81E+16	1.32E+16	2.64E+18	7.37E+15	8.23E-12	1.02E+14	0.0836
262.54	760	6.81E+16	1.32E+16	2.64E+18	7.37E+15	7.76E-12	1.00E+14	0.0926
262.54	760	6.81E+16	1.32E+16	2.64E+18	7.37E+15	8.13E-12	1.00E+14	0.0646

262.54	760	6.81E+16	1.32E+16	2.64E+18	7.37E+15	8.18E-12	1.02E+14	0.0889
262.54	760	5.31E+16	1.31E+16	3.49E+18	1.18E+16	7.27E-12	7.76E+13	0.1956
262.54	760	5.31E+16	1.31E+16	3.49E+18	1.18E+16	7.13E-12	7.66E+13	0.1987
262.54	760	5.31E+16	1.31E+16	3.49E+18	1.18E+16	8.04E-12	7.70E+13	0.2045
262.54	760	5.31E+16	1.31E+16	3.49E+18	1.18E+16	8.32E-12	8.03E+13	0.2071
262.54	760	5.49E+16	1.31E+16	3.49E+18	1.68E+16	7.21E-12	7.70E+13	0.1816
262.54	760	5.49E+16	1.31E+16	3.49E+18	1.68E+16	8.69E-12	8.60E+13	0.1892
262.54	760	5.49E+16	1.31E+16	3.49E+18	1.68E+16	5.98E-12	7.24E+13	0.1690
262.54	760	4.98E+16	1.32E+16	3.51E+18	1.69E+16	7.15E-12	7.85E+13	0.1760
262.54	760	7.40E+16	1.32E+16	2.62E+18	1.72E+16	8.35E-12	1.20E+14	0.1985
262.54	760	7.40E+16	1.32E+16	2.62E+18	1.72E+16	9.40E-12	1.20E+14	0.1745
262.54	760	7.40E+16	1.32E+16	2.62E+18	1.72E+16	9.66E-12	1.18E+14	0.1391
262.54	760	7.40E+16	1.32E+16	2.62E+18	1.72E+16	1.12E-11	1.20E+14	0.1268
262.54	760	7.40E+16	1.32E+16	2.62E+18	1.72E+16	1.03E-11	1.16E+14	0.1690
262.54	760	7.40E+16	1.32E+16	2.62E+18	1.72E+16	9.60E-12	1.18E+14	0.1187
262.54	760	7.03E+16	1.32E+16	2.65E+18	1.84E+16	8.56E-12	1.06E+14	0.1090
262.54	760	7.03E+16	1.32E+16	2.65E+18	1.84E+16	9.21E-12	1.06E+14	0.0985
262.54	760	6.83E+16	1.33E+16	2.65E+18	1.84E+16	8.78E-12	9.86E+13	0.0983
262.54	760	6.83E+16	1.33E+16	2.65E+18	1.84E+16	9.33E-12	1.01E+14	0.1034
262.54	760	6.83E+16	1.33E+16	2.65E+18	1.84E+16	9.68E-12	9.91E+13	0.1477
262.54	760	6.83E+16	1.33E+16	2.65E+18	1.84E+16	9.67E-12	9.84E+13	0.1461
262.54	760	5.16E+16	1.34E+16	2.68E+18	1.86E+16	8.77E-12	8.88E+13	0.1244
262.54	760	5.16E+16	1.34E+16	2.68E+18	1.86E+16	9.06E-12	8.91E+13	0.1363
262.54	760	5.33E+16	1.32E+16	3.50E+18	2.19E+16	7.30E-12	7.75E+13	0.1769
262.54	760	5.33E+16	1.32E+16	3.50E+18	2.19E+16	7.64E-12	6.77E+13	0.2143
262.54	760	5.33E+16	1.32E+16	3.50E+18	2.19E+16	7.46E-12	7.50E+13	0.1853
262.54	760	5.33E+16	1.32E+16	3.50E+18	2.19E+16	8.68E-12	7.57E+13	0.2358
262.54	760	5.16E+16	1.32E+16	3.51E+18	2.20E+16	7.17E-12	6.78E+13	0.1968
262.54	760	5.16E+16	1.32E+16	3.51E+18	2.20E+16	8.19E-12	7.81E+13	0.1829
262.54	760	5.16E+16	1.32E+16	3.51E+18	2.20E+16	7.85E-12	7.70E+13	0.1911
262.54	760	5.16E+16	1.32E+16	3.51E+18	2.20E+16	8.30E-12	7.61E+13	0.2061
262.54	760	5.16E+16	1.32E+16	3.51E+18	2.71E+16	5.37E-12	6.09E+13	0.1094
262.54	760	5.16E+16	1.32E+16	3.51E+18	2.71E+16	7.80E-12	6.98E+13	0.2049
262.54	760	5.16E+16	1.32E+16	3.51E+18	2.71E+16	8.38E-12	7.13E+13	0.2029
262.54	760	5.16E+16	1.32E+16	3.51E+18	2.71E+16	6.44E-12	6.50E+13	0.2092
262.54	760	7.42E+16	1.32E+16	2.63E+18	2.75E+16	1.04E-11	1.22E+14	0.2164
262.54	760	7.42E+16	1.32E+16	2.63E+18	2.75E+16	1.10E-11	1.26E+14	0.1683
262.54	760	7.42E+16	1.32E+16	2.63E+18	2.75E+16	1.10E-11	1.23E+14	0.1661
262.54	760	7.42E+16	1.32E+16	2.63E+18	2.75E+16	1.06E-11	1.21E+14	0.1835
262.54	760	7.42E+16	1.32E+16	2.63E+18	2.75E+16	1.27E-11	1.31E+14	0.1765
262.54	760	7.42E+16	1.32E+16	2.63E+18	2.75E+16	1.09E-11	1.21E+14	0.1416
262.54	760	6.85E+16	1.33E+16	2.66E+18	2.95E+16	9.11E-12	1.01E+14	0.1312
262.54	760	6.85E+16	1.33E+16	2.66E+18	2.95E+16	9.91E-12	9.75E+13	0.1241
262.54	760	6.66E+16	1.34E+16	2.66E+18	3.82E+16	1.06E-11	1.03E+14	0.2323
262.54	760	6.66E+16	1.34E+16	2.66E+18	3.82E+16	1.03E-11	9.58E+13	0.0829
262.54	760	6.66E+16	1.34E+16	2.66E+18	3.82E+16	1.30E-11	4.74E+13	0.3768
262.54	760	6.66E+16	1.34E+16	2.66E+18	3.82E+16	1.05E-11	5.18E+13	0.3665
262.54	760	6.66E+16	1.34E+16	2.66E+18	3.82E+16	8.74E-12	7.16E+13	0.1263
262.54	760	6.66E+16	1.34E+16	2.66E+18	3.82E+16	9.43E-12	1.01E+14	0.1895
262.54	760	7.89E+16	1.33E+16	2.64E+18	4.83E+16	9.13E-12	1.06E+14	0.2343
262.54	760	7.89E+16	1.33E+16	2.64E+18	4.83E+16	9.03E-12	1.05E+14	0.1645

253.74	760	5.07E+16	1.35E+16	3.57E+18	0	9.78E-12	7.08E+13	0.2443
253.74	760	5.07E+16	1.35E+16	3.57E+18	0	6.28E-12	5.78E+13	0.2062
253.74	760	5.07E+16	1.35E+16	3.57E+18	0	1.02E-11	7.21E+13	0.2588
253.74	760	5.07E+16	1.35E+16	3.57E+18	0	1.18E-11	7.69E+13	0.2175
253.74	760	5.77E+16	1.34E+16	3.55E+18	0	8.84E-12	7.81E+13	0.2793
253.74	760	5.77E+16	1.34E+16	3.55E+18	0	1.06E-11	9.03E+13	0.2876
253.74	760	5.77E+16	1.34E+16	3.55E+18	0	7.92E-12	7.01E+13	0.2695
253.74	760	5.77E+16	1.34E+16	3.55E+18	0	7.62E-12	6.77E+13	0.2018
253.74	760	6.14E+16	1.34E+16	3.54E+18	0	8.11E-12	7.64E+13	0.1853
253.74	760	6.14E+16	1.34E+16	3.54E+18	0	7.84E-12	7.20E+13	0.2138
253.74	760	6.14E+16	1.34E+16	3.54E+18	0	7.14E-12	6.41E+13	0.1995
253.74	760	6.14E+16	1.34E+16	3.54E+18	0	7.43E-12	6.86E+13	0.2082
253.74	760	6.37E+16	1.36E+16	2.71E+18	0	1.23E-11	8.75E+13	0.1915
253.74	760	6.37E+16	1.36E+16	2.71E+18	0	1.46E-11	8.78E+13	0.2410
253.74	760	6.37E+16	1.36E+16	2.71E+18	0	1.09E-11	8.36E+13	0.1778
253.74	760	6.39E+16	4.41E+16	2.72E+18	0	1.58E-11	6.49E+13	0.1040
253.74	760	6.39E+16	4.41E+16	2.72E+18	0	1.54E-11	6.01E+13	0.0900
253.74	760	6.39E+16	4.41E+16	2.72E+18	0	1.82E-11	6.21E+13	0.1506
253.74	760	6.39E+16	4.41E+16	2.72E+18	0	1.69E-11	6.15E+13	0.1368
253.74	760	6.57E+16	1.36E+16	2.71E+18	0	1.00E-11	9.07E+13	0.0962
253.74	760	6.57E+16	1.36E+16	2.71E+18	0	9.98E-12	9.41E+13	0.0840
253.74	760	6.57E+16	1.36E+16	2.71E+18	0	1.04E-11	9.62E+13	0.0915
253.74	760	6.57E+16	1.36E+16	2.71E+18	0	9.91E-12	8.69E+13	0.0642
253.74	760	6.76E+16	1.36E+16	2.70E+18	0	1.27E-11	8.13E+13	0.1800
253.74	760	6.76E+16	1.36E+16	2.70E+18	0	1.62E-11	9.21E+13	0.3226
253.74	760	6.79E+16	4.40E+16	2.72E+18	0	1.57E-11	6.16E+13	0.1391
253.74	760	6.79E+16	4.40E+16	2.72E+18	0	1.77E-11	6.37E+13	0.1871
253.74	760	6.82E+16	9.50E+16	2.73E+18	0	2.23E-11	4.38E+13	0.1217
253.74	760	6.82E+16	9.50E+16	2.73E+18	0	2.34E-11	4.14E+13	0.2044
253.74	760	6.82E+16	9.50E+16	2.73E+18	0	2.14E-11	4.45E+13	0.1685
253.74	760	6.85E+16	1.46E+17	2.74E+18	0	3.24E-11	4.30E+13	0.2131
253.74	760	6.85E+16	1.46E+17	2.74E+18	0	2.71E-11	4.03E+13	0.1728
253.74	760	6.85E+16	1.46E+17	2.74E+18	0	2.80E-11	3.90E+13	0.1532
253.74	760	6.85E+16	1.46E+17	2.74E+18	0	3.40E-11	4.50E+13	0.1547
253.74	760	6.85E+16	1.46E+17	2.74E+18	0	3.32E-11	4.51E+13	0.1186
253.74	760	6.85E+16	1.46E+17	2.74E+18	0	3.54E-11	4.57E+13	0.1464
253.74	760	6.85E+16	1.46E+17	2.74E+18	0	3.79E-11	4.81E+13	0.1556
253.74	760	6.96E+16	1.36E+16	2.70E+18	0	1.06E-11	9.57E+13	0.1207
253.74	760	6.96E+16	1.36E+16	2.70E+18	0	1.29E-11	9.99E+13	0.1565
253.74	760	7.16E+16	1.35E+16	2.70E+18	0	3.47E-12	1.35E+14	0.0517
253.74	760	7.16E+16	1.35E+16	2.70E+18	0	3.32E-12	1.29E+14	0.0584
253.74	760	7.16E+16	1.35E+16	2.70E+18	0	3.12E-12	1.25E+14	0.0407
253.74	760	7.16E+16	1.35E+16	2.70E+18	0	3.48E-12	1.25E+14	0.0535
253.74	760	7.16E+16	1.35E+16	2.70E+18	0	3.61E-12	1.28E+14	0.0641
253.74	760	7.16E+16	1.35E+16	2.70E+18	0	3.56E-12	1.26E+14	0.0607
253.74	760	7.16E+16	1.35E+16	2.70E+18	0	3.24E-12	1.21E+14	0.0361
253.74	760	7.16E+16	1.35E+16	2.70E+18	0	1.22E-11	9.30E+13	0.1253
253.74	760	7.16E+16	1.35E+16	2.70E+18	0	1.13E-11	8.64E+13	0.0963
253.74	760	7.17E+16	6.88E+16	2.70E+18	0	2.08E-11	4.85E+13	0.1689
253.74	760	7.17E+16	6.88E+16	2.70E+18	0	2.13E-11	4.77E+13	0.1297
253.74	760	7.17E+16	6.88E+16	2.70E+18	0	1.98E-11	4.57E+13	0.0975

253.74	760	7.17E+16	6.88E+16	2.70E+18	0	2.22E-11	5.15E+13	0.1425
253.74	760	7.17E+16	6.88E+16	2.70E+18	0	2.42E-11	5.15E+13	0.1847
253.74	760	7.17E+16	6.88E+16	2.70E+18	0	2.24E-11	5.16E+13	0.1289
253.74	760	7.17E+16	6.88E+16	2.70E+18	0	2.19E-11	5.06E+13	0.1891
253.74	760	7.19E+16	4.38E+16	2.71E+18	0	1.82E-11	6.92E+13	0.1800
253.74	760	7.19E+16	4.38E+16	2.71E+18	0	1.55E-11	6.53E+13	0.1484
253.74	760	7.20E+16	1.20E+17	2.71E+18	0	2.06E-11	3.85E+13	0.1652
253.74	760	7.20E+16	1.20E+17	2.71E+18	0	2.54E-11	3.81E+13	0.1424
253.74	760	7.20E+16	1.20E+17	2.71E+18	0	2.58E-11	3.83E+13	0.1786
253.74	760	7.20E+16	1.20E+17	2.71E+18	0	2.22E-11	4.00E+13	0.1529
253.74	760	7.20E+16	1.20E+17	2.71E+18	0	2.71E-11	4.14E+13	0.1455
253.74	760	7.20E+16	1.20E+17	2.71E+18	0	2.65E-11	3.91E+13	0.1114
253.74	760	7.20E+16	1.20E+17	2.71E+18	0	2.59E-11	3.98E+13	0.1347
253.74	760	7.20E+16	1.20E+17	2.71E+18	0	2.91E-11	4.35E+13	0.1214
253.74	760	7.35E+16	1.35E+16	2.69E+18	0	1.26E-11	9.23E+13	0.1744
253.74	760	7.35E+16	1.35E+16	2.69E+18	0	1.09E-11	8.98E+13	0.2061
253.74	760	7.35E+16	1.35E+16	2.69E+18	0	1.60E-11	1.08E+14	0.2603
253.74	760	7.35E+16	1.35E+16	2.69E+18	0	1.18E-11	9.77E+13	0.1877
253.74	760	7.37E+16	1.35E+16	2.69E+18	0	1.09E-11	9.41E+13	0.0953
253.74	760	7.37E+16	1.35E+16	2.69E+18	0	1.18E-11	8.74E+13	0.1105
253.74	760	7.43E+16	9.45E+16	2.72E+18	0	1.88E-11	4.33E+13	0.1738
253.74	760	7.43E+16	9.45E+16	2.72E+18	0	1.83E-11	4.29E+13	0.1458
253.74	760	7.43E+16	9.45E+16	2.72E+18	0	1.96E-11	4.45E+13	0.1892
253.74	760	7.57E+16	1.35E+16	2.69E+18	0	1.19E-11	1.09E+14	0.2242
253.74	760	7.57E+16	1.35E+16	2.69E+18	0	1.19E-11	1.11E+14	0.2387
253.74	760	7.57E+16	1.35E+16	2.69E+18	0	1.19E-11	1.14E+14	0.2312
253.74	760	7.57E+16	1.35E+16	2.69E+18	0	1.07E-11	1.05E+14	0.2016
253.74	760	7.57E+16	1.35E+16	2.69E+18	0	1.06E-11	1.07E+14	0.2049
253.74	760	7.57E+16	1.35E+16	2.69E+18	0	1.02E-11	9.45E+13	0.1915
253.74	760	7.57E+16	1.35E+16	2.69E+18	0	1.10E-11	9.14E+13	0.2014
253.74	760	7.57E+16	1.35E+16	2.69E+18	0	1.08E-11	1.04E+14	0.1622
253.74	760	7.57E+16	1.35E+16	2.69E+18	0	1.10E-11	1.05E+14	0.1593
253.74	760	7.57E+16	1.35E+16	2.69E+18	0	1.13E-11	1.09E+14	0.1784
253.74	760	8.58E+16	1.31E+16	3.49E+18	0	2.05E-12	1.03E+14	0.0367
253.74	760	8.58E+16	1.31E+16	3.49E+18	0	2.95E-12	1.05E+14	0.0610
253.74	760	8.58E+16	1.31E+16	3.49E+18	0	2.79E-12	1.12E+14	0.0000
253.74	760	8.58E+16	1.31E+16	3.49E+18	0	3.06E-12	9.41E+13	0.0000
253.74	760	8.58E+16	1.31E+16	3.49E+18	0	3.41E-12	1.06E+14	0.0000
253.74	760	8.58E+16	1.31E+16	3.49E+18	0	4.47E-12	1.28E+14	0.0611
253.74	760	8.58E+16	1.31E+16	3.49E+18	0	2.25E-12	8.87E+13	0.1315
253.74	760	9.02E+16	1.31E+16	3.48E+18	0	2.25E-12	1.05E+14	0.0486
253.74	760	5.46E+16	1.35E+16	3.59E+18	4.62E+14	9.09E-12	7.35E+13	0.1577
253.74	760	5.46E+16	1.35E+16	3.59E+18	4.62E+14	8.49E-12	6.80E+13	0.2049
253.74	760	5.46E+16	1.35E+16	3.59E+18	4.62E+14	1.10E-11	7.93E+13	0.2027
253.74	760	5.46E+16	1.35E+16	3.59E+18	4.62E+14	9.91E-12	8.08E+13	0.1953
253.74	760	6.81E+16	1.37E+16	2.72E+18	1.67E+15	1.20E-11	9.38E+13	0.0870
253.74	760	6.81E+16	1.37E+16	2.72E+18	1.67E+15	1.40E-11	8.60E+13	0.1300
253.74	760	6.81E+16	1.37E+16	2.72E+18	1.67E+15	1.24E-11	9.02E+13	0.1100
253.74	760	6.81E+16	1.37E+16	2.72E+18	1.67E+15	1.24E-11	9.35E+13	0.1201
253.74	760	6.81E+16	1.37E+16	2.72E+18	1.67E+15	1.25E-11	9.42E+13	0.1513
253.74	760	6.81E+16	1.37E+16	2.72E+18	1.67E+15	1.23E-11	9.23E+13	0.1463

253.74	760	6.41E+16	1.37E+16	2.73E+18	1.67E+15	1.25E-11	8.66E+13	0.1522
253.74	760	6.41E+16	1.37E+16	2.73E+18	1.67E+15	1.22E-11	8.69E+13	0.1078
253.74	760	5.29E+16	1.36E+16	3.60E+18	1.80E+15	9.61E-12	6.95E+13	0.2045
253.74	760	5.29E+16	1.36E+16	3.60E+18	1.80E+15	1.05E-11	6.97E+13	0.1815
253.74	760	5.29E+16	1.36E+16	3.60E+18	1.80E+15	9.10E-12	6.80E+13	0.2104
253.74	760	5.29E+16	1.36E+16	3.60E+18	1.80E+15	1.09E-11	7.29E+13	0.2364
253.74	760	7.62E+16	1.36E+16	2.70E+18	1.82E+15	1.06E-11	9.41E+13	0.3165
253.74	760	7.62E+16	1.36E+16	2.70E+18	1.82E+15	1.01E-11	9.27E+13	0.2573
253.74	760	7.62E+16	1.36E+16	2.70E+18	1.82E+15	1.01E-11	8.67E+13	0.2093
253.74	760	6.81E+16	1.37E+16	2.72E+18	1.84E+15	1.13E-11	7.48E+13	0.4102
253.74	760	6.81E+16	1.37E+16	2.72E+18	1.84E+15	1.21E-11	6.83E+13	0.4211
253.74	760	6.81E+16	1.37E+16	2.72E+18	1.84E+15	1.01E-11	7.59E+13	0.2319
253.74	760	6.81E+16	1.37E+16	2.72E+18	1.84E+15	1.08E-11	8.46E+13	0.2017
253.74	760	6.81E+16	1.37E+16	2.72E+18	1.84E+15	1.21E-11	5.97E+13	0.4076
253.74	760	5.65E+16	1.36E+16	3.60E+18	3.14E+15	1.01E-11	7.29E+13	0.3028
253.74	760	5.65E+16	1.36E+16	3.60E+18	3.14E+15	6.12E-12	5.29E+13	0.1991
253.74	760	5.65E+16	1.36E+16	3.60E+18	3.14E+15	1.03E-11	7.09E+13	0.2437
253.74	760	5.65E+16	1.36E+16	3.60E+18	3.14E+15	1.60E-11	8.85E+13	0.2033
253.74	760	7.23E+16	1.37E+16	2.72E+18	6.49E+15	1.29E-11	9.65E+13	0.1301
253.74	760	7.23E+16	1.37E+16	2.72E+18	6.49E+15	1.24E-11	9.24E+13	0.1418
253.74	760	7.23E+16	1.37E+16	2.72E+18	6.49E+15	1.24E-11	8.80E+13	0.1327
253.74	760	7.23E+16	1.37E+16	2.72E+18	6.49E+15	1.30E-11	9.61E+13	0.1572
253.74	760	7.23E+16	1.37E+16	2.72E+18	6.49E+15	1.14E-11	8.35E+13	0.1356
253.74	760	7.23E+16	1.37E+16	2.72E+18	6.49E+15	1.14E-11	8.40E+13	0.1239
253.74	760	7.23E+16	1.37E+16	2.72E+18	6.49E+15	1.18E-11	9.39E+13	0.1471
253.74	760	7.23E+16	1.37E+16	2.72E+18	6.49E+15	1.16E-11	8.41E+13	0.1164
253.74	760	6.42E+16	1.37E+16	2.74E+18	7.19E+15	1.71E-11	5.11E+13	0.2837
253.74	760	6.42E+16	1.37E+16	2.74E+18	7.19E+15	1.14E-11	7.96E+13	0.1859
253.74	760	6.42E+16	1.37E+16	2.74E+18	7.19E+15	1.33E-11	7.12E+13	0.2680
253.74	760	6.42E+16	1.37E+16	2.74E+18	7.19E+15	1.08E-11	7.80E+13	0.0816
253.74	760	7.03E+16	1.37E+16	2.73E+18	1.14E+16	1.27E-11	9.02E+13	0.1454
253.74	760	7.03E+16	1.37E+16	2.73E+18	1.14E+16	1.21E-11	8.56E+13	0.1428
253.74	760	7.03E+16	1.37E+16	2.73E+18	1.14E+16	1.30E-11	8.65E+13	0.1255
253.74	760	7.03E+16	1.37E+16	2.73E+18	1.17E+16	1.37E-11	8.98E+13	0.1792
253.74	760	7.03E+16	1.37E+16	2.73E+18	1.17E+16	1.16E-11	8.07E+13	0.1458
253.74	760	7.03E+16	1.37E+16	2.73E+18	1.17E+16	1.19E-11	7.98E+13	0.1578
253.74	760	7.03E+16	1.37E+16	2.73E+18	1.17E+16	1.21E-11	8.04E+13	0.1315
253.74	760	7.03E+16	1.37E+16	2.73E+18	1.17E+16	1.23E-11	7.52E+13	0.1570
253.74	760	6.43E+16	1.38E+16	2.74E+18	1.25E+16	1.74E-11	1.05E+14	0.2584
253.74	760	6.43E+16	1.38E+16	2.74E+18	1.25E+16	1.48E-11	9.28E+13	0.1988
253.74	760	6.43E+16	1.38E+16	2.74E+18	1.25E+16	1.70E-11	9.47E+13	0.2577
253.74	760	6.43E+16	1.38E+16	2.74E+18	1.25E+16	1.58E-11	8.93E+13	0.2075
253.74	760	6.43E+16	1.38E+16	2.74E+18	1.25E+16	1.43E-11	8.14E+13	0.3063
244.94	760	8.89E+16	1.36E+16	3.61E+18	0	3.31E-12	8.06E+13	0.2694
244.94	760	8.89E+16	1.36E+16	3.61E+18	0	2.62E-12	7.17E+13	0.0725
244.94	760	8.89E+16	1.36E+16	3.61E+18	0	3.76E-12	8.04E+13	0.0478
244.94	760	8.89E+16	1.36E+16	3.61E+18	0	5.27E-12	9.74E+13	0.0000
244.94	760	8.89E+16	1.36E+16	3.61E+18	0	4.01E-12	8.27E+13	0.0789
244.94	760	8.89E+16	1.36E+16	3.61E+18	0	3.52E-12	7.95E+13	0.1662
244.94	760	8.89E+16	1.36E+16	3.61E+18	0	2.76E-12	6.70E+13	0.0476
244.94	760	8.89E+16	1.36E+16	3.61E+18	0	3.66E-12	6.98E+13	0.0830

244.94	760	8.89E+16	1.36E+16	3.61E+18	0	4.81E-12	8.39E+13	0.0000
244.94	760	8.89E+16	1.36E+16	3.61E+18	0	3.15E-12	6.24E+13	0.0810
244.94	760	6.94E+16	1.41E+16	2.77E+18	0	1.49E-11	7.07E+13	0.1562
244.94	760	6.94E+16	1.41E+16	2.77E+18	0	1.62E-11	6.95E+13	0.1797
244.94	760	6.94E+16	1.41E+16	2.77E+18	0	1.38E-11	3.67E+13	0.2271
244.94	760	6.94E+16	1.41E+16	2.77E+18	0	1.54E-11	6.69E+13	0.1566
244.94	760	6.73E+16	1.41E+16	2.78E+18	0	1.63E-11	7.29E+13	0.1478
244.94	760	6.73E+16	1.41E+16	2.78E+18	0	1.34E-11	6.41E+13	0.0888
244.94	760	6.73E+16	1.41E+16	2.78E+18	0	1.45E-11	6.24E+13	0.1081
244.94	760	6.73E+16	1.41E+16	2.78E+18	0	1.42E-11	6.20E+13	0.1075
244.94	760	6.56E+16	5.62E+16	2.79E+18	0	2.11E-11	3.58E+13	0.2069
244.94	760	6.56E+16	5.62E+16	2.79E+18	0	1.84E-11	2.93E+13	0.1540
244.94	760	6.56E+16	5.62E+16	2.79E+18	0	1.53E-11	2.74E+13	0.1213
244.94	760	6.56E+16	5.62E+16	2.79E+18	0	1.78E-11	3.00E+13	0.1348
244.94	760	6.56E+16	5.62E+16	2.79E+18	0	1.69E-11	2.78E+13	0.1100
244.94	760	6.56E+16	5.62E+16	2.79E+18	0	1.36E-11	2.53E+13	0.0470
244.94	760	6.56E+16	5.62E+16	2.79E+18	0	1.96E-11	3.05E+13	0.1818
244.94	760	6.56E+16	5.62E+16	2.79E+18	0	1.53E-11	2.42E+13	0.0083
244.94	760	6.56E+16	5.62E+16	2.79E+18	0	1.79E-11	2.90E+13	0.1886
244.94	760	6.56E+16	5.62E+16	2.79E+18	0	1.79E-11	2.81E+13	0.1273
244.94	760	6.56E+16	5.62E+16	2.79E+18	0	2.32E-11	2.90E+13	0.1095
244.94	760	6.56E+16	5.62E+16	2.79E+18	0	1.66E-11	2.67E+13	0.0242
244.94	760	6.55E+16	3.51E+16	2.79E+18	0	2.29E-11	3.74E+13	0.2618
244.94	760	6.55E+16	3.51E+16	2.79E+18	0	2.47E-11	3.82E+13	0.2835
244.94	760	6.55E+16	3.51E+16	2.79E+18	0	2.43E-11	5.16E+13	0.1619
244.94	760	6.55E+16	3.51E+16	2.79E+18	0	2.28E-11	4.56E+13	0.1945
244.94	760	6.55E+16	3.51E+16	2.79E+18	0	1.82E-11	2.98E+13	0.1434
244.94	760	6.55E+16	3.51E+16	2.79E+18	0	2.46E-11	3.91E+13	0.1969
244.94	760	6.55E+16	3.51E+16	2.79E+18	0	2.14E-11	4.44E+13	0.1509
244.94	760	6.55E+16	3.51E+16	2.79E+18	0	2.56E-11	4.33E+13	0.1886
244.94	760	6.55E+16	3.51E+16	2.79E+18	0	1.76E-11	3.36E+13	0.1847
244.94	760	6.55E+16	3.51E+16	2.79E+18	0	2.03E-11	4.16E+13	0.1988
244.94	760	6.55E+16	3.51E+16	2.79E+18	0	1.98E-11	3.83E+13	0.1800
244.94	760	6.55E+16	3.51E+16	2.79E+18	0	1.87E-11	3.93E+13	0.2292
244.94	760	6.53E+16	1.41E+16	2.78E+18	0	1.99E-11	5.76E+13	0.1826
244.94	760	6.53E+16	1.41E+16	2.78E+18	0	1.75E-11	5.84E+13	0.1425
244.94	760	6.53E+16	1.41E+16	2.78E+18	0	1.71E-11	6.38E+13	0.1511
244.94	760	6.28E+16	7.77E+16	2.71E+18	0	5.39E-12	2.14E+13	0.5660
244.94	760	6.28E+16	7.77E+16	2.71E+18	0	7.80E-12	2.51E+13	0.7460
244.94	760	6.28E+16	7.77E+16	2.71E+18	0	7.07E-12	2.44E+13	0.4826
244.94	760	6.28E+16	7.77E+16	2.71E+18	0	8.70E-12	1.99E+13	0.6218
244.94	760	6.27E+16	5.64E+16	2.70E+18	0	3.30E-12	2.45E+13	0.0000
244.94	760	6.27E+16	5.64E+16	2.70E+18	0	3.49E-12	2.64E+13	0.4470
244.94	760	6.27E+16	5.64E+16	2.70E+18	0	4.23E-12	2.62E+13	0.5615
244.94	760	6.27E+16	5.64E+16	2.70E+18	0	4.37E-12	2.65E+13	0.5402
244.94	760	6.27E+16	5.64E+16	2.70E+18	0	7.70E-12	2.45E+13	0.4468
244.94	760	6.27E+16	5.64E+16	2.70E+18	0	6.19E-12	2.11E+13	0.0986
244.94	760	6.27E+16	5.64E+16	2.70E+18	0	2.52E-12	2.34E+13	0.4495
244.94	760	6.27E+16	5.64E+16	2.70E+18	0	3.13E-12	2.26E+13	0.6039
244.94	760	6.27E+16	1.10E+16	2.70E+18	0	5.23E-12	5.23E+13	0.5359
244.94	760	6.27E+16	1.10E+16	2.70E+18	0	5.59E-12	4.56E+13	0.3831

244.94	760	6.27E+16	1.10E+16	2.70E+18	0	5.45E-12	4.29E+13	0.0772
244.94	760	6.27E+16	1.10E+16	2.70E+18	0	4.96E-12	4.20E+13	0.0733
244.94	760	6.27E+16	1.10E+16	2.70E+18	0	4.38E-12	3.65E+13	0.2438
244.94	760	6.27E+16	1.10E+16	2.70E+18	0	6.84E-12	4.91E+13	0.5185
244.94	760	6.27E+16	1.10E+16	2.70E+18	0	5.57E-12	4.62E+13	0.5658
244.94	760	6.26E+16	3.53E+16	2.70E+18	0	7.68E-12	3.03E+13	0.5109
244.94	760	6.26E+16	3.53E+16	2.70E+18	0	8.30E-12	3.04E+13	0.5829
244.94	760	6.26E+16	3.53E+16	2.70E+18	0	4.10E-12	2.57E+13	0.3529
244.94	760	6.26E+16	3.53E+16	2.70E+18	0	4.21E-12	2.61E+13	0.2564
244.94	760	6.26E+16	3.53E+16	2.70E+18	0	4.24E-12	2.54E+13	0.2873
244.94	760	6.26E+16	3.53E+16	2.70E+18	0	5.02E-12	2.60E+13	0.3429
244.94	760	6.26E+16	3.53E+16	2.70E+18	0	5.75E-12	2.70E+13	0.5685
244.94	760	6.14E+16	3.46E+16	2.64E+18	0	6.44E-12	3.14E+13	0.5854
244.94	760	6.09E+16	7.78E+16	2.71E+18	0	9.26E-12	2.24E+13	0.3130
244.94	760	5.90E+16	7.79E+16	2.71E+18	0	5.69E-12	1.97E+13	0.0096
244.94	760	5.90E+16	7.79E+16	2.71E+18	0	1.28E-11	2.59E+13	0.7009
244.94	760	5.90E+16	7.79E+16	2.71E+18	0	1.58E-11	3.01E+13	0.6227
244.94	760	5.89E+16	1.11E+16	2.71E+18	0	4.79E-12	4.24E+13	0.2520
244.94	760	5.43E+16	1.39E+16	3.70E+18	0	1.00E-11	4.95E+13	0.2072
244.94	760	5.43E+16	1.39E+16	3.70E+18	0	9.24E-12	4.78E+13	0.2327
244.94	760	5.43E+16	1.39E+16	3.70E+18	0	1.78E-11	7.13E+13	0.2204
244.94	760	5.43E+16	1.39E+16	3.70E+18	0	1.16E-11	5.54E+13	0.2819
244.94	760	5.43E+16	1.39E+16	3.70E+18	0	1.33E-11	6.04E+13	0.3056
244.94	760	5.43E+16	1.39E+16	3.70E+18	0	9.02E-12	5.00E+13	0.2998
244.94	760	5.43E+16	1.39E+16	3.70E+18	0	1.33E-11	5.93E+13	0.2952
236.14	760	5.63E+16	1.45E+16	3.83E+18	0	1.87E-11	4.50E+13	0.4537
236.14	760	5.63E+16	1.45E+16	3.83E+18	0	1.66E-11	4.17E+13	0.5176
236.14	760	5.63E+16	1.45E+16	3.83E+18	0	2.08E-11	5.64E+13	0.4164
236.14	760	5.63E+16	1.45E+16	3.83E+18	0	2.88E-11	6.75E+13	0.3303
236.14	760	5.63E+16	1.45E+16	3.83E+18	0	1.15E-11	3.58E+13	0.3718
236.14	760	5.63E+16	1.45E+16	3.83E+18	0	1.64E-11	4.01E+13	0.4063
236.14	760	5.63E+16	1.45E+16	3.83E+18	0	5.24E-12	3.00E+13	0.4148
236.14	760	5.63E+16	1.45E+16	3.83E+18	0	1.54E-11	3.56E+13	0.5796

Appendix 4

Derivation of Equation Describing HO_2 Decay to Equilibrium

$HO_2 + CH_3OH \rightarrow HO_2.CH_3OH \qquad k_f$

$HO_2.CH_3OH \rightarrow HO_2 + CH_3OH \qquad k_r$

At equilibrium $\frac{-d[HO_2]}{dt} = k_f[HO_2][CH_3OH] - k_r[HO_2.CH_3OH] = 0$ (i)

Let

$x = [HO_2]_t - [HO_2]_e$ (ii)

Thus

$[HO_2.CH_3OH]_t = [HO_2.CH_3OH]_e - x$ (iii)

$\frac{-dx}{dt} = \frac{-d[HO_2]}{dt}$ (iv)

Substituting (i), (ii) and (iii) into (iv) gives:

$$\begin{aligned}\frac{-dx}{dt} &= k_f([HO_2]_e + x)[CH_3OH] - k_r([HO_2.CH_3OH]_e - x) \\ &= k_f[HO_2]_e[CH_3OH] + k_f x[CH_3OH] - k_r[HO_2.CH_3OH]_e + k_r x \\ &= k_f x[CH_3OH] + k_r x + k_f[HO_2]_e[CH_3OH] - k_r[HO_2.CH_3OH]_e \\ &= k_f x[CH_3OH] + k_r x\end{aligned} \quad \text{(v)}$$

Since $k_f[HO_2]_e[CH_3OH] - k_r[HO_2.CH_3OH]_e = 0$ at equilibrium.

Therefore $\frac{-dx}{dt} = (k_f[CH_3OH] + k_r)x$, and integration between limits of $t = 0$ and $t = t$ gives:

$$x_t = x_0 \exp(-\{k_f[CH_3OH] + k_r\}t) \qquad \text{(vi)}$$

Therefore

$$[HO_2]_t - [HO_2]_e = ([HO_2]_0 - [HO_2]_e)\exp(-\{k_f[CH_3OH] + k_r\}t) \qquad \text{(vii)}$$

$$[HO_2]_t - [HO_2]_e = ([HO_2]_0 - [HO_2]_e)\exp(-\{k_f[CH_3OH] + k_r\}t) \qquad \text{(viii)}$$

$K_c = \frac{k_f}{k_r}$, hence substituting $k_r = \frac{k_f}{K_c} = k_f K_c^{-1}$ into (viii) gives:

$$[HO_2]_t = [HO_2]_e + ([HO_2]_0 - [HO_2]_e)\exp(-\{k_f[CH_3OH] + k_f K_c^{-1}\}t) \qquad \text{(ix)}$$

$$[HO_2]_t = [HO_2]_e + ([HO_2]_0 - [HO_2]_e)\exp(-k_f t\{[CH_3OH] + K_c^{-1}\}) \qquad \text{(x)}$$

If $[HO_2]_0 - [HO_2]_e = [HO_2.CH_3OH]_e$ then,

$$K_c = \frac{[HO_2.CH_3OH]_e}{[HO_2]_e[CH_3OH]} = \frac{[HO_2]_0 - [HO_2]_e}{[HO_2]_e.[CH_3OH]} \qquad \text{(xi)}$$

Therefore $[HO_2]_0 - [HO_2]_e = K_c[HO_2]_e[CH_3OH]$ (xii)

and it can be shown that

$$\begin{aligned}[HO_2]_0 &= [HO_2]_e + K_c[HO_2]_e[CH_3OH] \\ &= [HO_2]_e(1 + K_c[CH_3OH])\end{aligned} \qquad \text{(xiii)}$$

Rearranging gives $[HO_2]_e = \frac{[HO_2]_0}{1 + K_c[CH_3OH]}$ (xiv)

Substituting (xii) and (xiv) into (vii) gives

$$[HO_2]_t = \frac{[HO_2]_0}{1 + K_c[CH_3OH]} + K_c[HO_2]_e[CH_3OH]\exp\left(-k_f t\left\{[CH_3OH] + K_c^{-1}\right\}\right)$$

$$= \frac{[HO_2]_0}{1 + K_c[CH_3OH]} + \frac{K_c[HO_2]_0[CH_3OH]}{1 + K_c[CH_3OH]}\exp\left(-k_f t\left\{[CH_3OH] + K_c^{-1}\right\}\right)$$

(xv)

Dividing by K_c gives

$$[HO_2]_t = \frac{[HO_2]_0 K_c^{-1}}{K_c^{-1} + [CH_3OH]} + \frac{[HO_2]_0[CH_3OH]}{K_c^{-1} + [CH_3OH]}\exp\left(-k_f t\left\{[CH_3OH] + K_c^{-1}\right\}\right)$$

$$= \frac{[HO_2]_0 K_c^{-1} + [HO_2]_0[CH_3OH]\exp\left(-k_f t\left\{[CH_3OH] + K_c^{-1}\right\}\right)}{K_c^{-1} + [CH_3OH]}$$

$$= \frac{[HO_2]_0}{K_c^{-1} + [CH_3OH]}\left\{K_c^{-1} + [CH_3OH]\exp\left(-k_f t\left\{[CH_3OH] + K_c^{-1}\right\}\right)\right\}$$

(xvi)

Appendix 5
Results for the CH_3O_2 Self-Reaction

A5.1 Methyl Chloride System

T / K	p / Torr	$[CH_3Cl]$ / cm^{-3}	$[CH_4]$ / cm^{-3}	$[O_2]$ / cm^{-3}	$[H_2O]$ / cm^{-3}	k_{obs} / cm^3 s^{-1}	$[CH_3O_2]_0$ / cm^{-3}
295.98	760	2.36E+16	7.23E+18	2.26E+18	0	3.32E-13	6.23E+13
295.98	760	2.36E+16	7.23E+18	2.26E+18	0	2.82E-13	6.27E+13
295.98	760	2.36E+16	7.23E+18	2.26E+18	0	3.29E-13	6.02E+13
295.98	760	2.36E+16	7.23E+18	2.26E+18	0	3.47E-13	6.04E+13
295.98	760	3.91E+16	2.29E+18	2.25E+18	0	5.04E-13	7.23E+13
295.98	760	3.91E+16	2.29E+18	2.25E+18	0	5.44E-13	7.12E+13
295.98	760	3.92E+16	3.53E+18	2.25E+18	0	4.51E-13	7.25E+13
295.98	760	3.92E+16	3.53E+18	2.25E+18	0	4.29E-13	7.14E+13
295.98	760	3.93E+16	7.21E+18	1.12E+18	0	3.79E-13	6.00E+13
295.98	760	3.93E+16	7.21E+18	1.12E+18	0	3.70E-13	5.90E+13
295.98	760	3.93E+16	7.22E+18	1.35E+18	0	4.04E-13	5.56E+13
295.98	760	3.93E+16	7.22E+18	1.35E+18	0	3.82E-13	5.79E+13
295.98	760	3.93E+16	4.76E+18	2.26E+18	0	3.55E-13	9.16E+13
295.98	760	3.93E+16	4.76E+18	2.26E+18	0	4.08E-13	8.90E+13
295.98	760	3.93E+16	7.23E+18	1.58E+18	0	3.56E-13	6.27E+13
295.98	760	3.93E+16	7.23E+18	1.58E+18	0	3.67E-13	6.39E+13
295.98	760	3.94E+16	7.24E+18	1.81E+18	0	3.64E-13	6.04E+13
295.98	760	3.94E+16	7.24E+18	1.81E+18	0	3.75E-13	5.91E+13
295.98	760	3.94E+16	6.01E+18	2.26E+18	0	4.29E-13	9.62E+13
295.98	760	3.94E+16	6.01E+18	2.26E+18	0	3.86E-13	8.31E+13
295.98	760	3.94E+16	6.01E+18	2.26E+18	0	3.88E-13	8.40E+13
295.98	760	3.94E+16	7.25E+18	2.04E+18	0	3.70E-13	6.27E+13
295.98	760	3.94E+16	7.25E+18	2.04E+18	0	3.71E-13	6.08E+13
295.98	760	3.95E+16	7.26E+18	2.27E+18	0	4.20E-13	6.02E+13
295.98	760	3.95E+16	7.26E+18	2.27E+18	0	3.93E-13	6.02E+13
295.98	760	3.95E+16	7.26E+18	2.27E+18	0	3.70E-13	6.21E+13
295.98	760	3.95E+16	7.26E+18	2.27E+18	0	3.90E-13	6.26E+13
295.98	760	3.95E+16	7.26E+18	2.27E+18	0	3.54E-13	6.16E+13
295.98	760	3.95E+16	7.26E+18	2.27E+18	0	3.68E-13	6.13E+13
295.98	760	3.95E+16	7.26E+18	2.27E+18	0	3.25E-13	1.02E+14
295.98	760	3.95E+16	7.26E+18	2.27E+18	0	3.57E-13	9.17E+13
295.98	760	3.95E+16	7.26E+18	2.27E+18	0	3.72E-13	9.10E+13
295.98	760	3.95E+16	7.26E+18	2.27E+18	0	3.61E-13	9.20E+13
295.98	760	3.95E+16	7.26E+18	2.27E+18	0	3.72E-13	9.70E+13
295.98	760	3.95E+16	7.26E+18	2.27E+18	0	3.65E-13	9.33E+13
295.98	760	3.95E+16	7.26E+18	2.27E+18	0	3.67E-13	9.32E+13
295.98	760	3.95E+16	7.26E+18	2.27E+18	0	3.84E-13	9.05E+13
295.98	760	3.95E+16	7.26E+18	2.27E+18	0	2.98E-13	9.34E+13
295.98	760	3.95E+16	7.26E+18	2.27E+18	0	3.27E-13	9.31E+13
295.98	760	3.95E+16	7.26E+18	2.27E+18	0	3.37E-13	9.99E+13
295.98	760	3.95E+16	7.26E+18	2.27E+18	0	3.16E-13	9.96E+13
295.98	760	3.96E+16	8.52E+18	2.27E+18	0	3.17E-13	1.03E+14
295.98	760	3.96E+16	8.52E+18	2.27E+18	0	3.10E-13	1.07E+14
295.98	760	3.96E+16	8.52E+18	2.27E+18	0	3.26E-13	9.93E+13

295.98	760	3.96E+16	8.52E+18	2.27E+18	0	3.19E-13	1.01E+14
295.98	760	3.97E+16	9.78E+18	2.28E+18	0	3.17E-13	1.03E+14
295.98	760	3.97E+16	9.78E+18	2.28E+18	0	3.03E-13	9.80E+13
295.98	760	3.97E+16	9.78E+18	2.28E+18	0	3.01E-13	9.63E+13
295.98	760	3.97E+16	9.78E+18	2.28E+18	0	3.16E-13	1.03E+14
295.98	760	3.98E+16	1.10E+19	2.28E+18	0	3.07E-13	1.14E+14
295.98	760	3.98E+16	1.10E+19	2.28E+18	0	3.12E-13	1.18E+14
295.98	760	3.98E+16	1.10E+19	2.28E+18	0	3.01E-13	1.20E+14
295.98	760	3.98E+16	1.10E+19	2.28E+18	0	3.01E-13	1.20E+14
295.98	760	8.92E+16	7.27E+18	2.27E+18	0	4.03E-13	9.59E+13
295.98	760	8.92E+16	7.27E+18	2.27E+18	0	4.15E-13	9.53E+13
295.98	760	8.92E+16	7.27E+18	2.27E+18	0	4.21E-13	9.31E+13
295.98	760	8.92E+16	7.27E+18	2.27E+18	0	4.23E-13	9.46E+13
295.98	760	1.62E+17	7.20E+18	2.25E+18	0	4.90E-13	1.10E+14
295.98	760	1.62E+17	7.20E+18	2.25E+18	0	4.62E-13	1.08E+14
295.98	760	1.62E+17	7.20E+18	2.25E+18	0	4.80E-13	1.10E+14
295.98	760	1.62E+17	7.20E+18	2.25E+18	0	4.67E-13	1.08E+14
295.98	760	2.54E+17	7.07E+18	2.21E+18	0	4.97E-13	1.14E+14
295.98	760	2.54E+17	7.07E+18	2.21E+18	0	4.98E-13	1.13E+14
295.98	760	2.54E+17	7.07E+18	2.21E+18	0	4.97E-13	1.14E+14
295.98	760	2.54E+17	7.07E+18	2.21E+18	0	4.76E-13	1.12E+14
295.98	760	3.63E+17	6.88E+18	2.15E+18	0	6.12E-13	1.07E+14
295.98	760	3.63E+17	6.88E+18	2.15E+18	0	6.09E-13	1.05E+14
295.98	760	3.63E+17	6.88E+18	2.15E+18	0	7.34E-13	1.07E+14
295.98	760	3.63E+17	6.88E+18	2.15E+18	0	7.05E-13	1.06E+14
295.98	760	4.19E+16	7.71E+18	2.41E+18	8.46E+16	3.27E-13	9.60E+13
295.98	760	4.19E+16	7.71E+18	2.41E+18	8.46E+16	3.28E-13	9.23E+13
295.98	760	4.19E+16	7.71E+18	2.41E+18	8.46E+16	3.44E-13	9.23E+13
295.98	760	4.19E+16	7.71E+18	2.41E+18	8.46E+16	3.55E-13	9.09E+13
295.98	760	4.19E+16	7.70E+18	2.41E+18	1.12E+17	3.77E-13	9.77E+13
295.98	760	4.19E+16	7.70E+18	2.41E+18	1.12E+17	3.41E-13	1.00E+14
295.98	760	4.19E+16	7.70E+18	2.41E+18	1.12E+17	3.45E-13	9.93E+13
295.98	760	4.19E+16	7.70E+18	2.41E+18	1.12E+17	3.55E-13	9.68E+13
295.98	760	4.18E+16	7.69E+18	2.40E+18	1.58E+17	3.39E-13	1.02E+14
295.98	760	4.18E+16	7.69E+18	2.40E+18	1.58E+17	3.53E-13	1.04E+14
295.98	760	4.18E+16	7.69E+18	2.40E+18	1.58E+17	3.44E-13	1.03E+14
295.98	760	4.18E+16	7.69E+18	2.40E+18	1.58E+17	3.53E-13	1.03E+14
295.98	760	4.17E+16	7.67E+18	2.40E+18	2.20E+17	3.82E-13	9.57E+13
295.98	760	4.17E+16	7.67E+18	2.40E+18	2.20E+17	3.78E-13	9.57E+13
295.98	760	4.17E+16	7.67E+18	2.40E+18	2.20E+17	3.70E-13	1.02E+14
295.98	760	4.17E+16	7.67E+18	2.40E+18	2.20E+17	3.81E-13	9.26E+13
295.98	760	4.16E+16	7.64E+18	2.39E+18	3.03E+17	3.33E-13	9.45E+13
295.98	760	4.16E+16	7.64E+18	2.39E+18	3.03E+17	3.29E-13	9.51E+13
295.98	760	4.16E+16	7.64E+18	2.39E+18	3.03E+17	3.43E-13	9.67E+13
295.98	760	4.16E+16	7.64E+18	2.39E+18	3.03E+17	3.74E-13	9.61E+13
295.98	760	4.14E+16	7.62E+18	2.38E+18	3.89E+17	4.01E-13	9.88E+13
295.98	760	4.14E+16	7.62E+18	2.38E+18	3.89E+17	3.75E-13	1.01E+14
295.98	760	4.14E+16	7.62E+18	2.38E+18	3.89E+17	3.63E-13	1.00E+14
295.98	760	4.14E+16	7.62E+18	2.38E+18	3.89E+17	3.48E-13	9.66E+13

A5.2 Chlorine System

T / K	p / Torr	$[Cl_2]$ / cm^{-3}	$[CH_4]$ / cm^{-3}	$[O_2]$ / cm^{-3}	$[H_2O]$ / cm^{-3}	k_{obs} / cm^3 s^{-1}	$[CH_3O_2]_0$ / cm^{-3}
309.19	760	1.89E+16	6.95E+18	2.17E+18	0	5.47E-13	1.10E+14
309.19	760	1.89E+16	6.95E+18	2.17E+18	0	5.57E-13	1.08E+14
309.19	760	1.89E+16	6.95E+18	2.17E+18	0	5.68E-13	9.91E+13
309.19	760	1.89E+16	6.95E+18	2.17E+18	0	5.59E-13	1.03E+14
309.19	760	1.89E+16	6.95E+18	2.17E+18	0	5.92E-13	1.03E+14
309.19	760	1.89E+16	6.95E+18	2.17E+18	0	6.03E-13	1.04E+14
309.19	760	1.89E+16	6.95E+18	2.17E+18	0	5.97E-13	1.01E+14
309.19	760	1.89E+16	6.95E+18	2.17E+18	0	6.17E-13	1.05E+14
295.98	760	4.46E+16	7.27E+18	2.27E+18	0	4.96E-13	1.32E+14
295.98	760	4.46E+16	7.27E+18	2.27E+18	0	5.00E-13	1.39E+14
295.98	760	4.46E+16	7.27E+18	2.27E+18	0	5.11E-13	1.31E+14
295.98	760	4.46E+16	7.27E+18	2.27E+18	0	5.34E-13	1.27E+14
295.98	760	3.07E+16	7.27E+18	2.27E+18	0	4.55E-13	1.77E+14
295.98	760	3.07E+16	7.27E+18	2.27E+18	0	4.57E-13	1.78E+14
295.98	760	3.07E+16	7.27E+18	2.27E+18	0	4.66E-13	1.74E+14
295.98	760	3.07E+16	7.27E+18	2.27E+18	0	4.48E-13	1.73E+14
295.98	760	2.47E+16	7.23E+18	2.26E+18	0	4.82E-13	1.54E+14
295.98	760	2.47E+16	7.23E+18	2.26E+18	0	4.67E-13	1.58E+14
295.98	760	2.47E+16	7.23E+18	2.26E+18	0	4.79E-13	1.60E+14
295.98	760	2.47E+16	7.23E+18	2.26E+18	0	4.80E-13	1.58E+14
295.98	760	1.98E+16	8.52E+18	2.27E+18	0	5.59E-13	9.12E+13
295.98	760	1.98E+16	8.52E+18	2.27E+18	0	5.71E-13	9.15E+13
295.98	760	1.98E+16	8.52E+18	2.27E+18	0	5.46E-13	8.90E+13
295.98	760	1.98E+16	8.52E+18	2.27E+18	0	5.57E-13	8.99E+13
295.98	760	1.97E+16	7.26E+18	2.27E+18	0	5.80E-13	7.17E+13
295.98	760	1.97E+16	7.26E+18	2.27E+18	0	5.79E-13	7.03E+13
295.98	760	1.97E+16	7.26E+18	2.27E+18	0	6.07E-13	6.78E+13
295.98	760	1.97E+16	7.26E+18	2.27E+18	0	5.97E-13	6.68E+13
295.98	760	1.97E+16	7.25E+18	2.04E+18	0	5.16E-13	1.20E+14
295.98	760	1.97E+16	7.25E+18	2.04E+18	0	5.09E-13	1.21E+14
295.98	760	1.97E+16	7.25E+18	2.04E+18	0	5.30E-13	1.14E+14
295.98	760	1.97E+16	7.25E+18	2.04E+18	0	5.10E-13	1.15E+14
295.98	760	1.97E+16	6.01E+18	2.26E+18	0	5.61E-13	8.80E+13
295.98	760	1.97E+16	6.01E+18	2.26E+18	0	5.75E-13	9.44E+13
295.98	760	1.97E+16	6.01E+18	2.26E+18	0	5.55E-13	9.73E+13
295.98	760	1.97E+16	6.01E+18	2.26E+18	0	5.67E-13	9.97E+13
295.98	760	1.97E+16	7.24E+18	1.81E+18	0	4.79E-13	1.10E+14
295.98	760	1.97E+16	7.24E+18	1.81E+18	0	4.95E-13	1.10E+14
295.98	760	1.97E+16	7.24E+18	1.81E+18	0	4.97E-13	1.08E+14
295.98	760	1.97E+16	7.24E+18	1.81E+18	0	5.10E-13	1.10E+14
295.98	760	1.97E+16	7.23E+18	1.58E+18	0	4.99E-13	1.20E+14
295.98	760	1.97E+16	7.23E+18	1.58E+18	0	4.98E-13	1.17E+14
295.98	760	1.97E+16	7.23E+18	1.58E+18	0	4.87E-13	1.24E+14
295.98	760	1.97E+16	7.23E+18	1.58E+18	0	4.89E-13	1.27E+14
295.98	760	1.97E+16	4.76E+18	2.26E+18	0	5.78E-13	8.90E+13
295.98	760	1.97E+16	4.76E+18	2.26E+18	0	5.82E-13	9.25E+13
295.98	760	1.97E+16	4.76E+18	2.26E+18	0	5.69E-13	8.68E+13
295.98	760	1.97E+16	4.76E+18	2.26E+18	0	5.83E-13	8.65E+13

295.98	760	1.96E+16	7.22E+18	1.35E+18	0	4.87E-13	1.24E+14
295.98	760	1.96E+16	7.22E+18	1.35E+18	0	4.94E-13	1.23E+14
295.98	760	1.96E+16	7.22E+18	1.35E+18	0	4.99E-13	1.23E+14
295.98	760	1.96E+16	7.22E+18	1.35E+18	0	5.07E-13	1.13E+14
295.98	760	1.96E+16	7.21E+18	1.12E+18	0	4.92E-13	1.15E+14
295.98	760	1.96E+16	7.21E+18	1.12E+18	0	4.81E-13	1.17E+14
295.98	760	1.96E+16	7.21E+18	1.12E+18	0	4.83E-13	1.25E+14
295.98	760	1.96E+16	7.21E+18	1.12E+18	0	4.92E-13	1.22E+14
295.98	760	1.96E+16	3.53E+18	2.25E+18	0	5.66E-13	9.69E+13
295.98	760	1.96E+16	3.53E+18	2.25E+18	0	5.85E-13	8.83E+13
295.98	760	1.96E+16	3.53E+18	2.25E+18	0	5.74E-13	9.51E+13
295.98	760	1.96E+16	3.53E+18	2.25E+18	0	5.72E-13	8.75E+13
295.98	760	1.53E+16	7.21E+18	2.25E+18	0	5.35E-13	1.03E+14
295.98	760	1.53E+16	7.21E+18	2.25E+18	0	5.08E-13	9.94E+13
295.98	760	1.53E+16	7.21E+18	2.25E+18	0	5.31E-13	1.04E+14
295.98	760	1.53E+16	7.21E+18	2.25E+18	0	5.19E-13	1.05E+14
295.98	760	1.18E+16	7.23E+18	2.26E+18	0	5.25E-13	8.12E+13
295.98	760	1.18E+16	7.23E+18	2.26E+18	0	5.23E-13	7.70E+13
295.98	760	1.18E+16	7.23E+18	2.26E+18	0	5.06E-13	7.33E+13
295.98	760	1.18E+16	7.23E+18	2.26E+18	0	5.29E-13	7.12E+13
295.98	760	9.02E+15	7.25E+18	2.26E+18	0	4.23E-13	5.30E+13
295.98	760	9.02E+15	7.25E+18	2.26E+18	0	4.66E-13	5.12E+13
295.98	760	9.02E+15	7.25E+18	2.26E+18	0	4.80E-13	5.51E+13
295.98	760	9.02E+15	7.25E+18	2.26E+18	0	4.97E-13	5.53E+13
295.98	760	2.10E+16	7.71E+18	2.41E+18	8.46E+16	6.01E-13	1.05E+14
295.98	760	2.10E+16	7.71E+18	2.41E+18	8.46E+16	5.86E-13	1.05E+14
295.98	760	2.10E+16	7.71E+18	2.41E+18	8.46E+16	5.80E-13	1.07E+14
295.98	760	2.10E+16	7.71E+18	2.41E+18	8.46E+16	5.82E-13	1.08E+14
295.98	760	2.09E+16	7.70E+18	2.41E+18	1.12E+17	4.67E-13	1.03E+14
295.98	760	2.09E+16	7.70E+18	2.41E+18	1.12E+17	4.81E-13	1.02E+14
295.98	760	2.09E+16	7.70E+18	2.41E+18	1.12E+17	4.99E-13	9.91E+13
295.98	760	2.09E+16	7.70E+18	2.41E+18	1.12E+17	4.70E-13	1.03E+14
295.98	760	2.09E+16	7.69E+18	2.40E+18	1.58E+17	5.66E-13	1.16E+14
295.98	760	2.09E+16	7.69E+18	2.40E+18	1.58E+17	5.71E-13	1.17E+14
295.98	760	2.09E+16	7.69E+18	2.40E+18	1.58E+17	5.70E-13	1.18E+14
295.98	760	2.09E+16	7.69E+18	2.40E+18	1.58E+17	5.63E-13	1.18E+14
295.98	760	2.09E+16	7.67E+18	2.40E+18	2.20E+17	5.13E-13	1.04E+14
295.98	760	2.09E+16	7.67E+18	2.40E+18	2.20E+17	5.03E-13	1.03E+14
295.98	760	2.09E+16	7.67E+18	2.40E+18	2.20E+17	5.33E-13	1.03E+14
295.98	760	2.09E+16	7.67E+18	2.40E+18	2.20E+17	5.39E-13	1.08E+14
295.98	760	2.08E+16	7.64E+18	2.39E+18	3.03E+17	5.41E-13	1.10E+14
295.98	760	2.08E+16	7.64E+18	2.39E+18	3.03E+17	5.31E-13	1.06E+14
295.98	760	2.08E+16	7.64E+18	2.39E+18	3.03E+17	5.19E-13	1.06E+14
295.98	760	2.08E+16	7.64E+18	2.39E+18	3.03E+17	5.26E-13	1.07E+14
295.98	760	2.07E+16	7.62E+18	2.38E+18	3.89E+17	3.75E-13	9.27E+13
295.98	760	2.07E+16	7.62E+18	2.38E+18	3.89E+17	4.09E-13	9.12E+13
295.98	760	2.07E+16	7.62E+18	2.38E+18	3.89E+17	4.81E-13	9.22E+13
295.98	760	2.07E+16	7.62E+18	2.38E+18	3.89E+17	4.88E-13	9.29E+13
273.98	760	2.13E+16	7.84E+18	2.45E+18	0	5.55E-13	1.05E+14
273.98	760	2.13E+16	7.84E+18	2.45E+18	0	5.69E-13	1.11E+14
273.98	760	2.13E+16	7.84E+18	2.45E+18	0	5.58E-13	1.18E+14

273.98	760	2.13E+16	7.84E+18	2.45E+18	0	5.47E-13	1.18E+14
284.54	760	2.05E+16	7.55E+18	2.36E+18	0	6.00E-13	1.14E+14
284.54	760	2.05E+16	7.55E+18	2.36E+18	0	6.06E-13	1.14E+14
284.54	760	2.05E+16	7.55E+18	2.36E+18	0	6.29E-13	1.17E+14
284.54	760	2.05E+16	7.55E+18	2.36E+18	0	6.44E-13	1.18E+14
284.54	760	2.05E+16	7.55E+18	2.36E+18	0	5.82E-13	1.19E+14
284.54	760	2.05E+16	7.55E+18	2.36E+18	0	5.95E-13	1.20E+14
284.54	760	2.05E+16	7.55E+18	2.36E+18	0	5.99E-13	1.17E+14
284.54	760	2.05E+16	7.55E+18	2.36E+18	0	6.18E-13	1.19E+14
273.98	760	2.14E+16	7.88E+18	2.46E+18	4.14E+16	5.81E-13	1.15E+14
273.98	760	2.14E+16	7.88E+18	2.46E+18	4.14E+16	5.79E-13	1.15E+14
273.98	760	2.14E+16	7.88E+18	2.46E+18	4.14E+16	6.06E-13	1.13E+14
273.98	760	2.14E+16	7.88E+18	2.46E+18	4.14E+16	6.21E-13	1.12E+14
273.98	760	2.15E+16	7.92E+18	2.47E+18	6.10E+16	6.07E-13	1.11E+14
273.98	760	2.15E+16	7.92E+18	2.47E+18	6.10E+16	6.09E-13	1.17E+14
273.98	760	2.15E+16	7.92E+18	2.47E+18	6.10E+16	5.84E-13	1.27E+14
273.98	760	2.15E+16	7.92E+18	2.47E+18	6.10E+16	6.08E-13	1.17E+14
273.98	760	2.17E+16	7.97E+18	2.49E+18	8.08E+16	5.87E-13	1.07E+14
273.98	760	2.17E+16	7.97E+18	2.49E+18	8.08E+16	5.70E-13	1.18E+14
273.98	760	2.17E+16	7.97E+18	2.49E+18	8.08E+16	5.79E-13	1.26E+14
273.98	760	2.17E+16	7.97E+18	2.49E+18	8.08E+16	5.74E-13	1.24E+14
273.98	760	2.18E+16	8.01E+18	2.50E+18	1.01E+17	5.64E-13	1.13E+14
273.98	760	2.18E+16	8.01E+18	2.50E+18	1.01E+17	5.71E-13	1.13E+14
273.98	760	2.18E+16	8.01E+18	2.50E+18	1.01E+17	5.41E-13	1.13E+14
273.98	760	2.18E+16	8.01E+18	2.50E+18	1.01E+17	5.44E-13	1.12E+14
273.98	760	2.19E+16	8.06E+18	2.52E+18	1.21E+17	5.38E-13	1.03E+14
273.98	760	2.19E+16	8.06E+18	2.52E+18	1.21E+17	5.42E-13	9.78E+13
273.98	760	2.19E+16	8.06E+18	2.52E+18	1.21E+17	5.56E-13	1.03E+14
273.98	760	2.19E+16	8.06E+18	2.52E+18	1.21E+17	5.53E-13	1.01E+14
273.98	760	2.20E+16	8.10E+18	2.53E+18	1.42E+17	5.96E-13	1.12E+14
273.98	760	2.20E+16	8.10E+18	2.53E+18	1.42E+17	6.13E-13	1.13E+14
273.98	760	2.20E+16	8.10E+18	2.53E+18	1.42E+17	5.86E-13	1.14E+14
273.98	760	2.20E+16	8.10E+18	2.53E+18	1.42E+17	5.99E-13	1.14E+14
262.54	760	2.23E+16	8.18E+18	2.56E+18	0	5.68E-13	1.22E+14
262.54	760	2.23E+16	8.18E+18	2.56E+18	0	6.35E-13	1.17E+14
262.54	760	2.23E+16	8.18E+18	2.56E+18	0	6.28E-13	1.15E+14
262.54	760	2.23E+16	8.18E+18	2.56E+18	0	6.29E-13	1.11E+14
262.54	760	2.23E+16	8.18E+18	2.56E+18	0	6.47E-13	1.14E+14
262.54	760	2.23E+16	8.18E+18	2.56E+18	0	6.36E-13	1.10E+14
262.54	760	2.23E+16	8.18E+18	2.56E+18	0	6.60E-13	1.13E+14
262.54	760	2.23E+16	8.18E+18	2.56E+18	0	6.43E-13	1.07E+14
262.54	760	2.23E+16	8.18E+18	2.56E+18	0	6.32E-13	1.10E+14
253.74	760	2.30E+16	8.47E+18	2.65E+18	0	4.56E-13	9.63E+13
253.74	760	2.30E+16	8.47E+18	2.65E+18	0	4.67E-13	9.90E+13
253.74	760	2.30E+16	8.47E+18	2.65E+18	0	4.85E-13	1.04E+14
253.74	760	2.30E+16	8.47E+18	2.65E+18	0	4.75E-13	9.22E+13
244.94	760	2.39E+16	8.77E+18	2.74E+18	0	6.17E-13	1.26E+14
244.94	760	2.39E+16	8.77E+18	2.74E+18	0	6.00E-13	1.33E+14
244.94	760	2.39E+16	8.77E+18	2.74E+18	0	5.86E-13	1.36E+14
244.94	760	2.39E+16	8.77E+18	2.74E+18	0	5.81E-13	1.36E+14
244.94	760	2.39E+16	8.77E+18	2.74E+18	0	5.70E-13	1.24E+14

244.94	760	2.39E+16	8.77E+18	2.74E+18	0	6.16E-13	1.24E+14
244.94	760	2.39E+16	8.77E+18	2.74E+18	0	6.34E-13	1.22E+14
236.14	760	2.48E+16	9.10E+18	2.84E+18	0	4.74E-13	8.21E+13
236.14	760	2.48E+16	9.10E+18	2.84E+18	0	4.45E-13	9.78E+13
236.14	760	2.48E+16	9.10E+18	2.84E+18	0	4.18E-13	9.59E+13
236.14	760	2.48E+16	9.10E+18	2.84E+18	0	4.01E-13	9.21E+13

Appendix 6
Results for the HO_2-CH_3O_2 Cross-Reaction

T / K	p / Torr	$[Cl_2]$ / cm^{-3}	$[CH_4]$ / cm^{-3}	$[CH_3OH]$ / cm^{-3}	$[O_2]$ / cm^{-3}	$[H_2O]$ / cm^{-3}	k / cm^3 s^{-1}	$[HO_2]_0$ / cm^{-3}	$[RO_2]_0$ / cm^{-3}	γ
309.19	760	2.95E+16	6.99E+18	2.44E+16	2.18E+18	0	3.78E-12	9.71E+13	6.33E+13	0.0273
309.19	760	2.95E+16	6.99E+18	2.44E+16	2.18E+18	0	3.82E-12	1.07E+14	6.54E+13	0.1319
309.19	760	2.95E+16	6.99E+18	2.44E+16	2.18E+18	0	4.01E-12	9.95E+13	6.54E+13	0.1206
309.19	760	2.95E+16	6.99E+18	2.44E+16	2.18E+18	0	4.29E-12	1.00E+14	6.86E+13	0.0748
309.19	760	2.95E+16	6.99E+18	2.44E+16	2.18E+18	0	3.72E-12	1.05E+14	6.12E+13	0.1426
309.19	760	2.95E+16	6.99E+18	2.44E+16	2.18E+18	0	3.82E-12	1.04E+14	6.11E+13	0.2241
295.98	760	4.48E+16	7.30E+18	2.54E+16	2.28E+18	0	1.49E-11	1.97E+14	1.64E+14	0.3893
295.98	760	4.48E+16	7.30E+18	2.54E+16	2.28E+18	0	1.17E-11	2.06E+14	9.66E+13	0.1758
295.98	760	4.48E+16	7.30E+18	2.54E+16	2.28E+18	0	9.03E-12	1.76E+14	8.89E+13	0.1348
295.98	760	4.48E+16	7.30E+18	2.54E+16	2.28E+18	0	1.16E-11	1.90E+14	9.38E+13	0.1798
295.98	760	3.76E+16	7.34E+18	2.56E+16	2.29E+18	0	5.58E-12	1.15E+14	6.22E+13	0.1435
295.98	760	3.76E+16	7.34E+18	2.56E+16	2.29E+18	0	5.87E-12	1.01E+14	6.38E+13	0.1629
295.98	760	3.76E+16	7.34E+18	2.56E+16	2.29E+18	0	5.91E-12	1.15E+14	6.76E+13	0.1079
295.98	760	3.76E+16	7.34E+18	2.56E+16	2.29E+18	0	4.93E-12	1.22E+14	6.24E+13	0.1531
295.98	760	3.14E+16	7.45E+18	2.60E+16	2.09E+18	0	5.85E-12	9.23E+13	5.13E+13	0.0000
295.98	760	3.14E+16	7.45E+18	2.60E+16	2.09E+18	0	4.49E-12	9.52E+13	4.61E+13	0.1333
295.98	760	3.14E+16	7.45E+18	2.60E+16	2.09E+18	0	5.87E-12	1.03E+14	5.49E+13	0.0299
295.98	760	3.14E+16	7.45E+18	2.60E+16	2.09E+18	0	5.94E-12	1.10E+14	5.59E+13	0.0110
295.98	760	3.14E+16	7.45E+18	2.60E+16	2.09E+18	0	5.24E-12	1.00E+14	5.17E+13	0.2906
295.98	760	3.14E+16	7.45E+18	2.60E+16	2.09E+18	0	6.00E-12	1.02E+14	5.20E+13	0.3054
295.98	760	3.14E+16	7.45E+18	2.60E+16	2.09E+18	0	6.77E-12	8.95E+13	4.93E+13	0.3526
295.98	760	3.14E+16	7.45E+18	2.60E+16	2.09E+18	0	7.25E-12	8.10E+13	5.06E+13	0.2255
295.98	760	3.13E+16	7.40E+18	2.15E+16	2.08E+18	0	7.16E-12	8.04E+13	6.16E+13	0.1364
295.98	760	3.13E+16	7.40E+18	2.15E+16	2.08E+18	0	5.06E-12	8.65E+13	5.40E+13	0.1507
295.98	760	3.13E+16	7.40E+18	2.15E+16	2.08E+18	0	4.93E-12	8.58E+13	5.33E+13	0.0000
295.98	760	3.13E+16	7.40E+18	2.15E+16	2.08E+18	0	5.95E-12	9.12E+13	5.67E+13	0.0000
295.98	760	3.13E+16	7.40E+18	2.15E+16	2.08E+18	0	4.63E-12	7.05E+13	4.91E+13	0.1501
295.98	760	3.13E+16	7.40E+18	2.15E+16	2.08E+18	0	4.98E-12	8.70E+13	4.86E+13	0.1784
295.98	760	3.13E+16	7.40E+18	2.15E+16	2.08E+18	0	6.73E-12	7.68E+13	5.57E+13	0.2604
295.98	760	3.13E+16	7.40E+18	2.15E+16	2.08E+18	0	8.27E-12	6.96E+13	6.18E+13	0.1485
295.98	760	3.11E+16	7.37E+18	2.57E+16	2.07E+18	0	1.24E-11	8.24E+13	7.11E+13	0.0000
295.98	760	3.11E+16	7.37E+18	2.57E+16	2.07E+18	0	5.42E-12	7.58E+13	4.78E+13	0.0265
295.98	760	3.11E+16	7.37E+18	2.57E+16	2.07E+18	0	6.35E-12	8.22E+13	5.38E+13	0.0000
295.98	760	3.11E+16	7.37E+18	2.57E+16	2.07E+18	0	7.99E-12	7.02E+13	9.77E+13	0.0000
295.98	760	3.10E+16	7.35E+18	2.99E+16	2.29E+18	0	5.88E-12	9.07E+13	3.79E+13	0.3055
295.98	760	3.10E+16	7.35E+18	2.99E+16	2.29E+18	0	7.80E-12	8.01E+13	5.01E+13	0.0691
295.98	760	3.10E+16	7.35E+18	2.99E+16	2.29E+18	0	7.57E-12	8.83E+13	4.18E+13	0.3326
295.98	760	3.10E+16	7.35E+18	2.99E+16	2.29E+18	0	6.14E-12	1.07E+14	3.67E+13	0.3100
295.98	760	3.10E+16	7.35E+18	2.99E+16	2.29E+18	0	7.70E-12	1.38E+14	5.11E+13	0.0000
295.98	760	3.10E+16	7.35E+18	2.99E+16	2.29E+18	0	6.35E-12	1.53E+14	5.05E+13	0.0720
295.98	760	3.10E+16	7.35E+18	2.99E+16	2.29E+18	0	6.43E-12	1.26E+14	4.54E+13	0.1168
295.98	760	3.10E+16	7.35E+18	2.99E+16	2.29E+18	0	7.68E-12	1.49E+14	5.09E+13	0.1221
295.98	760	3.10E+16	7.34E+18	2.13E+16	2.29E+18	0	5.97E-12	8.40E+13	6.13E+13	0.0000
295.98	760	3.10E+16	7.34E+18	2.13E+16	2.29E+18	0	6.21E-12	7.26E+13	6.26E+13	0.0042
295.98	760	3.10E+16	7.34E+18	2.13E+16	2.29E+18	0	6.30E-12	8.36E+13	6.23E+13	0.0621
295.98	760	3.10E+16	7.34E+18	2.13E+16	2.29E+18	0	5.22E-12	7.91E+13	5.57E+13	0.0836

295.98	760	3.10E+16	7.34E+18	2.13E+16	2.29E+18	0	5.86E-12	7.75E+13	5.15E+13	0.0000
295.98	760	3.10E+16	7.34E+18	2.13E+16	2.29E+18	0	8.09E-12	9.41E+13	6.22E+13	0.0000
295.98	760	3.10E+16	7.34E+18	2.13E+16	2.29E+18	0	5.15E-12	8.14E+13	4.80E+13	0.0000
295.98	760	3.10E+16	7.34E+18	2.13E+16	2.29E+18	0	7.50E-12	8.02E+13	5.51E+13	0.0000
295.98	760	3.09E+16	8.31E+18	2.55E+16	2.29E+18	0	9.61E-12	7.54E+13	7.85E+13	0.0000
295.98	760	3.09E+16	8.31E+18	2.55E+16	2.29E+18	0	5.23E-12	7.49E+13	5.73E+13	0.1032
295.98	760	3.09E+16	8.31E+18	2.55E+16	2.29E+18	0	7.34E-12	7.37E+13	6.36E+13	0.0403
295.98	760	3.09E+16	8.31E+18	2.55E+16	2.29E+18	0	6.86E-12	7.54E+13	6.32E+13	0.0765
295.98	760	3.09E+16	8.31E+18	2.55E+16	2.29E+18	0	5.26E-12	7.27E+13	5.48E+13	0.0000
295.98	760	3.09E+16	8.31E+18	2.55E+16	2.29E+18	0	7.16E-12	7.95E+13	6.23E+13	0.0000
295.98	760	3.09E+16	8.31E+18	2.55E+16	2.29E+18	0	5.77E-12	7.86E+13	5.33E+13	0.0330
295.98	760	3.09E+16	8.31E+18	2.55E+16	2.29E+18	0	5.41E-12	7.55E+13	4.90E+13	0.1044
295.98	760	3.09E+16	7.31E+18	3.40E+16	2.28E+18	0	8.41E-12	1.22E+14	3.77E+13	0.2109
295.98	760	3.09E+16	7.31E+18	3.40E+16	2.28E+18	0	8.23E-12	1.23E+14	3.90E+13	0.2969
295.98	760	3.09E+16	7.31E+18	3.40E+16	2.28E+18	0	8.54E-12	1.14E+14	3.98E+13	0.1987
295.98	760	3.09E+16	7.31E+18	3.40E+16	2.28E+18	0	7.81E-12	1.25E+14	3.61E+13	0.3987
295.98	760	3.09E+16	7.31E+18	3.40E+16	2.28E+18	0	8.53E-12	1.02E+14	3.70E+13	0.0944
295.98	760	3.09E+16	7.31E+18	3.40E+16	2.28E+18	0	5.37E-12	1.12E+14	2.37E+13	0.4183
295.98	760	3.09E+16	7.31E+18	3.40E+16	2.28E+18	0	7.53E-12	1.05E+14	3.47E+13	0.1230
295.98	760	3.09E+16	7.31E+18	3.40E+16	2.28E+18	0	5.61E-12	9.38E+13	2.71E+13	0.3037
295.98	760	3.09E+16	7.81E+18	2.55E+16	2.28E+18	0	5.92E-12	7.79E+13	5.34E+13	0.0681
295.98	760	3.09E+16	7.81E+18	2.55E+16	2.28E+18	0	4.67E-12	1.01E+14	5.59E+13	0.0235
295.98	760	3.09E+16	7.81E+18	2.55E+16	2.28E+18	0	4.49E-12	9.08E+13	4.94E+13	0.1130
295.98	760	3.09E+16	7.81E+18	2.55E+16	2.28E+18	0	4.81E-12	1.01E+14	4.93E+13	0.0231
295.98	760	3.09E+16	7.81E+18	2.55E+16	2.28E+18	0	7.03E-12	7.71E+13	5.17E+13	0.2535
295.98	760	3.09E+16	7.81E+18	2.55E+16	2.28E+18	0	7.70E-12	7.90E+13	5.21E+13	0.1192
295.98	760	3.09E+16	7.81E+18	2.55E+16	2.28E+18	0	5.71E-12	8.40E+13	4.50E+13	0.0251
295.98	760	3.09E+16	7.81E+18	2.55E+16	2.28E+18	0	7.47E-12	8.75E+13	4.98E+13	0.0960
295.98	760	3.08E+16	7.30E+18	2.54E+16	2.28E+18	0	1.35E-11	1.03E+14	7.49E+13	0.2361
295.98	760	3.08E+16	7.30E+18	2.54E+16	2.28E+18	0	1.32E-11	1.08E+14	7.12E+13	0.2269
295.98	760	3.08E+16	7.30E+18	2.54E+16	2.28E+18	0	1.47E-11	1.43E+14	7.60E+13	0.2211
295.98	760	3.08E+16	7.30E+18	2.54E+16	2.28E+18	0	4.12E-12	7.87E+13	4.48E+13	0.0791
295.98	760	3.08E+16	7.30E+18	2.54E+16	2.28E+18	0	1.40E-11	1.12E+14	7.66E+13	0.1381
295.98	760	3.08E+16	7.30E+18	2.54E+16	2.28E+18	0	1.46E-11	1.36E+14	7.82E+13	0.1989
295.98	760	3.08E+16	7.30E+18	2.54E+16	2.28E+18	0	3.17E-12	9.30E+13	4.40E+13	0.0000
295.98	760	3.08E+16	7.30E+18	2.54E+16	2.28E+18	0	1.08E-11	1.40E+14	7.24E+13	0.1339
295.98	760	3.08E+16	7.30E+18	2.54E+16	2.28E+18	0	7.66E-12	8.61E+13	5.39E+13	0.1523
295.98	760	3.08E+16	7.30E+18	2.54E+16	2.28E+18	0	1.17E-11	1.20E+14	6.48E+13	0.2071
295.98	760	3.08E+16	7.30E+18	2.54E+16	2.28E+18	0	5.41E-12	9.07E+13	4.47E+13	0.0784
295.98	760	3.08E+16	7.30E+18	2.54E+16	2.28E+18	0	5.40E-12	8.93E+13	4.86E+13	0.1339
295.98	760	3.08E+16	6.80E+18	2.54E+16	2.28E+18	0	5.90E-12	8.95E+13	3.68E+13	0.0240
295.98	760	3.08E+16	6.80E+18	2.54E+16	2.28E+18	0	8.47E-12	8.64E+13	4.70E+13	0.0525
295.98	760	3.08E+16	6.80E+18	2.54E+16	2.28E+18	0	7.09E-12	7.63E+13	3.65E+13	0.0484
295.98	760	3.08E+16	6.80E+18	2.54E+16	2.28E+18	0	7.25E-12	8.27E+13	3.96E+13	0.0405
295.98	760	3.08E+16	6.80E+18	2.54E+16	2.28E+18	0	6.54E-12	8.50E+13	3.87E+13	0.1517
295.98	760	3.08E+16	6.80E+18	2.54E+16	2.28E+18	0	5.72E-12	8.47E+13	3.41E+13	0.2513
295.98	760	3.08E+16	6.80E+18	2.54E+16	2.28E+18	0	5.50E-12	8.36E+13	3.55E+13	0.2618
295.98	760	3.08E+16	6.80E+18	2.54E+16	2.28E+18	0	5.21E-12	8.10E+13	3.48E+13	0.3034
295.98	760	3.08E+16	7.29E+18	2.54E+16	2.05E+18	0	5.80E-12	1.14E+14	5.04E+13	0.2544
295.98	760	3.08E+16	7.29E+18	2.54E+16	2.05E+18	0	6.46E-12	1.17E+14	5.15E+13	0.1694
295.98	760	3.08E+16	7.29E+18	2.54E+16	2.05E+18	0	5.47E-12	1.05E+14	4.72E+13	0.1648

295.98	760	3.08E+16	7.29E+18	2.54E+16	2.05E+18	0	6.82E-12	1.14E+14	5.12E+13	0.0599
295.98	760	3.08E+16	6.30E+18	2.54E+16	2.28E+18	0	5.34E-12	8.35E+13	3.87E+13	0.2020
295.98	760	3.08E+16	6.30E+18	2.54E+16	2.28E+18	0	6.70E-12	9.57E+13	4.24E+13	0.2790
295.98	760	3.08E+16	6.30E+18	2.54E+16	2.28E+18	0	5.10E-12	8.46E+13	3.73E+13	0.1803
295.98	760	3.08E+16	6.30E+18	2.54E+16	2.28E+18	0	6.66E-12	7.50E+13	3.93E+13	0.1691
295.98	760	3.08E+16	6.30E+18	2.54E+16	2.28E+18	0	5.55E-12	8.35E+13	3.81E+13	0.1703
295.98	760	3.08E+16	6.30E+18	2.54E+16	2.28E+18	0	5.13E-12	8.69E+13	3.58E+13	0.1447
295.98	760	3.08E+16	6.30E+18	2.54E+16	2.28E+18	0	4.78E-12	8.22E+13	3.24E+13	0.1206
295.98	760	3.08E+16	6.30E+18	2.54E+16	2.28E+18	0	5.35E-12	7.95E+13	3.27E+13	0.1184
295.98	760	3.07E+16	7.28E+18	2.54E+16	1.82E+18	0	7.33E-12	1.33E+14	5.86E+13	0.1925
295.98	760	3.07E+16	7.28E+18	2.54E+16	1.82E+18	0	8.40E-12	1.23E+14	6.14E+13	0.1963
295.98	760	3.07E+16	7.28E+18	2.54E+16	1.82E+18	0	7.74E-12	1.33E+14	6.24E+13	0.1761
295.98	760	3.07E+16	7.28E+18	2.54E+16	1.82E+18	0	7.08E-12	1.35E+14	5.93E+13	0.1301
295.98	760	3.07E+16	7.27E+18	2.53E+16	1.59E+18	0	6.05E-12	1.17E+14	5.50E+13	0.1228
295.98	760	3.07E+16	7.27E+18	2.53E+16	1.59E+18	0	7.33E-12	1.27E+14	6.09E+13	0.1186
295.98	760	3.07E+16	7.27E+18	2.53E+16	1.59E+18	0	4.48E-12	1.06E+14	4.17E+13	0.0000
295.98	760	3.07E+16	7.27E+18	2.53E+16	1.59E+18	0	1.18E-11	1.15E+14	6.14E+13	0.0850
295.98	760	3.07E+16	7.27E+18	2.53E+16	1.36E+18	0	7.07E-12	1.05E+14	5.53E+13	0.3744
295.98	760	3.07E+16	7.27E+18	2.53E+16	1.36E+18	0	6.94E-12	1.08E+14	5.35E+13	0.2916
295.98	760	3.07E+16	7.27E+18	2.53E+16	1.36E+18	0	6.92E-12	1.01E+14	5.23E+13	0.2352
295.98	760	3.07E+16	7.27E+18	2.53E+16	1.36E+18	0	6.51E-12	9.94E+13	5.19E+13	0.4844
295.98	760	2.51E+16	7.34E+18	2.56E+16	2.29E+18	0	1.20E-11	1.34E+14	6.02E+13	0.1481
295.98	760	2.51E+16	7.34E+18	2.56E+16	2.29E+18	0	6.27E-12	9.77E+13	5.12E+13	0.1168
295.98	760	2.51E+16	7.34E+18	2.56E+16	2.29E+18	0	1.49E-11	1.24E+14	6.57E+13	0.1748
295.98	760	2.51E+16	7.34E+18	2.56E+16	2.29E+18	0	1.48E-11	1.20E+14	5.95E+13	0.1418
295.98	760	3.13E+16	7.40E+18	2.58E+16	2.31E+18	8.17E+16	9.15E-12	5.54E+13	4.98E+13	0.0000
295.98	760	3.13E+16	7.40E+18	2.58E+16	2.31E+18	8.17E+16	6.13E-12	4.98E+13	3.96E+13	0.0541
295.98	760	3.13E+16	7.40E+18	2.58E+16	2.31E+18	8.17E+16	4.90E-12	5.55E+13	3.63E+13	0.0000
295.98	760	3.13E+16	7.40E+18	2.58E+16	2.31E+18	8.17E+16	6.81E-12	5.68E+13	4.10E+13	0.1228
295.98	760	3.13E+16	7.40E+18	2.58E+16	2.31E+18	8.17E+16	5.88E-12	6.79E+13	3.78E+13	0.0563
295.98	760	3.13E+16	7.40E+18	2.58E+16	2.31E+18	8.17E+16	6.13E-12	6.71E+13	3.85E+13	0.0000
295.98	760	3.13E+16	7.40E+18	2.58E+16	2.31E+18	8.17E+16	8.04E-12	6.67E+13	4.63E+13	0.0000
295.98	760	3.13E+16	7.40E+18	2.58E+16	2.31E+18	8.17E+16	5.13E-12	6.69E+13	3.68E+13	0.1245
295.98	760	3.12E+16	7.39E+18	2.58E+16	2.31E+18	1.08E+17	5.52E-12	8.44E+13	4.81E+13	0.1702
295.98	760	3.12E+16	7.39E+18	2.58E+16	2.31E+18	1.08E+17	4.88E-12	8.68E+13	4.62E+13	0.0645
295.98	760	3.12E+16	7.39E+18	2.58E+16	2.31E+18	1.08E+17	5.20E-12	8.37E+13	4.58E+13	0.0441
295.98	760	3.12E+16	7.39E+18	2.58E+16	2.31E+18	1.08E+17	6.02E-12	9.11E+13	4.90E+13	0.0000
295.98	760	3.12E+16	7.39E+18	2.58E+16	2.31E+18	1.08E+17	4.27E-12	9.69E+13	4.46E+13	0.0829
295.98	760	3.12E+16	7.39E+18	2.58E+16	2.31E+18	1.08E+17	4.68E-12	8.35E+13	4.64E+13	0.2111
295.98	760	3.12E+16	7.39E+18	2.58E+16	2.31E+18	1.08E+17	5.93E-12	8.21E+13	4.99E+13	0.1033
295.98	760	3.12E+16	7.39E+18	2.58E+16	2.31E+18	1.08E+17	4.72E-12	9.44E+13	4.70E+13	0.0000
295.98	760	3.12E+16	7.38E+18	2.57E+16	2.31E+18	1.53E+17	8.14E-12	6.31E+13	4.88E+13	0.0000
295.98	760	3.12E+16	7.38E+18	2.57E+16	2.31E+18	1.53E+17	6.66E-12	6.81E+13	4.45E+13	0.0000
295.98	760	3.12E+16	7.38E+18	2.57E+16	2.31E+18	1.53E+17	6.99E-12	6.43E+13	4.46E+13	0.0000
295.98	760	3.12E+16	7.38E+18	2.57E+16	2.31E+18	1.53E+17	4.49E-12	6.33E+13	3.54E+13	0.0416
295.98	760	3.12E+16	7.38E+18	2.57E+16	2.31E+18	1.53E+17	6.17E-12	6.58E+13	4.23E+13	0.0000
295.98	760	3.12E+16	7.38E+18	2.57E+16	2.31E+18	1.53E+17	6.69E-12	5.95E+13	4.27E+13	0.0000
295.98	760	3.11E+16	7.36E+18	2.57E+16	2.30E+18	2.13E+17	7.80E-12	6.20E+13	4.31E+13	0.0000
295.98	760	3.11E+16	7.36E+18	2.57E+16	2.30E+18	2.13E+17	4.75E-12	6.83E+13	3.69E+13	0.0000
295.98	760	3.11E+16	7.36E+18	2.57E+16	2.30E+18	2.13E+17	6.43E-12	5.80E+13	4.19E+13	0.0000
295.98	760	3.11E+16	7.36E+18	2.57E+16	2.30E+18	2.13E+17	7.70E-12	6.06E+13	4.86E+13	0.0000

295.98	760	3.11E+16	7.36E+18	2.57E+16	2.30E+18	2.13E+17	6.50E-12	6.99E+13	4.46E+13	0.0000
295.98	760	3.11E+16	7.36E+18	2.57E+16	2.30E+18	2.13E+17	7.33E-12	5.96E+13	4.61E+13	0.0000
295.98	760	3.11E+16	7.36E+18	2.57E+16	2.30E+18	2.13E+17	6.57E-12	5.72E+13	4.50E+13	0.0000
295.98	760	3.11E+16	7.36E+18	2.57E+16	2.30E+18	2.13E+17	7.09E-12	6.10E+13	4.72E+13	0.0000
295.98	760	3.10E+16	7.34E+18	2.56E+16	2.29E+18	2.93E+17	5.40E-12	8.38E+13	4.77E+13	0.2136
295.98	760	3.10E+16	7.34E+18	2.56E+16	2.29E+18	2.93E+17	6.10E-12	8.91E+13	5.08E+13	0.0493
295.98	760	3.10E+16	7.34E+18	2.56E+16	2.29E+18	2.93E+17	4.60E-12	8.95E+13	4.33E+13	0.0935
295.98	760	3.10E+16	7.34E+18	2.56E+16	2.29E+18	2.93E+17	5.17E-12	9.36E+13	4.55E+13	0.1658
295.98	760	3.10E+16	7.34E+18	2.56E+16	2.29E+18	2.93E+17	7.18E-12	8.13E+13	5.60E+13	0.0000
295.98	760	3.10E+16	7.34E+18	2.56E+16	2.29E+18	2.93E+17	8.02E-12	7.57E+13	5.96E+13	0.0829
295.98	760	3.10E+16	7.34E+18	2.56E+16	2.29E+18	2.93E+17	6.66E-12	8.02E+13	5.17E+13	0.0746
295.98	760	3.10E+16	7.34E+18	2.56E+16	2.29E+18	2.93E+17	1.05E-11	1.04E+14	8.19E+13	0.4131
295.98	760	3.09E+16	7.32E+18	2.55E+16	2.29E+18	3.76E+17	7.06E-12	7.53E+13	4.51E+13	0.0000
295.98	760	3.09E+16	7.32E+18	2.55E+16	2.29E+18	3.76E+17	5.80E-12	7.32E+13	4.10E+13	0.0497
295.98	760	3.09E+16	7.32E+18	2.55E+16	2.29E+18	3.76E+17	7.33E-12	9.52E+13	5.16E+13	0.0000
295.98	760	3.09E+16	7.32E+18	2.55E+16	2.29E+18	3.76E+17	4.96E-12	9.78E+13	4.64E+13	0.0814
295.98	760	3.09E+16	7.32E+18	2.55E+16	2.29E+18	3.76E+17	4.20E-12	1.05E+14	4.07E+13	0.3793
295.98	760	3.09E+16	7.32E+18	2.55E+16	2.29E+18	3.76E+17	4.74E-12	8.78E+13	4.43E+13	0.1591
295.98	760	3.09E+16	7.32E+18	2.55E+16	2.29E+18	3.76E+17	5.96E-12	8.35E+13	5.02E+13	0.1968
295.98	760	3.09E+16	7.32E+18	2.55E+16	2.29E+18	3.76E+17	5.59E-12	8.40E+13	4.76E+13	0.0756
287.18	760	3.18E+16	7.53E+18	2.62E+16	2.35E+18	0	5.22E-12	1.04E+14	4.73E+13	0.0000
287.18	760	3.18E+16	7.53E+18	2.62E+16	2.35E+18	0	5.49E-12	1.05E+14	4.67E+13	0.1903
287.18	760	3.18E+16	7.53E+18	2.62E+16	2.35E+18	0	5.62E-12	1.08E+14	5.13E+13	0.1028
287.18	760	3.18E+16	7.53E+18	2.62E+16	2.35E+18	0	6.43E-12	1.07E+14	5.00E+13	0.1575
287.18	760	3.18E+16	7.53E+18	2.62E+16	2.35E+18	0	6.40E-12	1.08E+14	5.06E+13	0.0892
287.18	760	3.18E+16	7.53E+18	2.62E+16	2.35E+18	0	5.61E-12	1.11E+14	4.38E+13	0.1674
278.38	760	3.28E+16	7.76E+18	2.70E+16	2.43E+18	0	8.38E-12	1.33E+14	4.17E+13	0.3143
278.38	760	3.28E+16	7.76E+18	2.70E+16	2.43E+18	0	9.40E-12	1.22E+14	4.66E+13	0.2743
278.38	760	3.28E+16	7.76E+18	2.70E+16	2.43E+18	0	9.41E-12	1.24E+14	4.69E+13	0.1930
278.38	760	3.28E+16	7.76E+18	2.70E+16	2.43E+18	0	7.47E-12	1.08E+14	3.61E+13	0.1830
278.38	760	3.28E+16	7.76E+18	2.70E+16	2.43E+18	0	9.07E-12	1.20E+14	4.48E+13	0.1525
278.38	760	3.28E+16	7.76E+18	2.70E+16	2.43E+18	0	8.29E-12	1.20E+14	4.04E+13	0.2349
273.98	760	3.40E+16	8.05E+18	2.80E+16	1.98E+18	0	7.62E-12	4.87E+13	2.19E+13	0.0000
273.98	760	3.40E+16	8.05E+18	2.80E+16	1.98E+18	0	6.92E-12	5.22E+13	1.82E+13	0.1112
273.98	760	3.40E+16	8.05E+18	2.80E+16	1.98E+18	0	3.63E-12	4.35E+13	2.01E+13	0.0000
273.98	760	3.40E+16	8.05E+18	2.80E+16	1.98E+18	0	4.19E-12	4.79E+13	1.46E+13	0.6658
273.98	760	3.40E+16	8.05E+18	2.80E+16	1.98E+18	0	1.31E-11	5.17E+13	1.58E+13	0.5580
273.98	760	3.40E+16	8.05E+18	2.80E+16	1.98E+18	0	7.73E-12	4.04E+13	1.47E+13	1.5891
273.98	760	3.38E+16	8.00E+18	2.79E+16	2.50E+18	8.83E+16	7.51E-12	3.91E+13	1.77E+13	0.1799
273.98	760	3.38E+16	8.00E+18	2.79E+16	2.50E+18	8.83E+16	7.24E-12	4.21E+13	2.38E+13	0.3533
273.98	760	3.38E+16	8.00E+18	2.79E+16	2.50E+18	8.83E+16	9.11E-12	4.95E+13	3.17E+13	0.0000
273.98	760	3.38E+16	8.00E+18	2.79E+16	2.50E+18	8.83E+16	9.88E-12	4.66E+13	3.09E+13	0.1393
273.98	760	3.37E+16	7.99E+18	2.78E+16	2.50E+18	1.02E+17	1.29E-11	5.22E+13	3.46E+13	0.0292
273.98	760	3.37E+16	7.99E+18	2.78E+16	2.50E+18	1.02E+17	1.22E-11	5.07E+13	2.91E+13	0.0123
273.98	760	3.37E+16	7.99E+18	2.78E+16	2.50E+18	1.02E+17	9.19E-12	4.12E+13	2.61E+13	0.0856
273.98	760	3.37E+16	7.99E+18	2.78E+16	2.50E+18	1.02E+17	1.45E-11	4.27E+13	3.11E+13	0.1263
273.98	760	3.37E+16	7.99E+18	2.78E+16	2.50E+18	1.17E+17	1.57E-11	4.87E+13	2.85E+13	0.3449
273.98	760	3.37E+16	7.99E+18	2.78E+16	2.50E+18	1.17E+17	1.17E-11	5.00E+13	3.01E+13	0.2016
273.98	760	3.37E+16	7.99E+18	2.78E+16	2.50E+18	1.17E+17	8.67E-12	4.56E+13	2.64E+13	0.1390
273.98	760	3.37E+16	7.99E+18	2.78E+16	2.50E+18	1.17E+17	9.38E-12	4.40E+13	2.68E+13	0.0579
273.98	760	3.37E+16	7.98E+18	2.78E+16	2.49E+18	1.34E+17	7.44E-12	3.96E+13	2.11E+13	0.0000

273.98	760	3.37E+16	7.98E+18	2.78E+16	2.49E+18	1.34E+17	7.11E-12	4.07E+13	2.20E+13	0.0000
273.98	760	3.37E+16	7.98E+18	2.78E+16	2.49E+18	1.34E+17	6.63E-12	4.12E+13	2.06E+13	0.0000
273.98	760	3.37E+16	7.98E+18	2.78E+16	2.49E+18	1.34E+17	1.01E-11	4.05E+13	2.41E+13	0.0000
273.98	760	3.37E+16	7.98E+18	2.78E+16	2.49E+18	1.54E+17	1.46E-11	4.57E+13	2.92E+13	0.1200
273.98	760	3.37E+16	7.98E+18	2.78E+16	2.49E+18	1.54E+17	1.12E-11	3.95E+13	2.54E+13	0.1785
273.98	760	3.37E+16	7.98E+18	2.78E+16	2.49E+18	1.54E+17	6.79E-12	4.18E+13	2.48E+13	0.3020
273.98	760	3.37E+16	7.98E+18	2.78E+16	2.49E+18	1.54E+17	9.38E-12	4.42E+13	2.85E+13	0.1781
253.74	760	3.67E+16	8.69E+18	3.03E+16	2.13E+18	0	1.11E-11	4.63E+13	2.09E+13	0.2717
253.74	760	3.67E+16	8.69E+18	3.03E+16	2.13E+18	0	7.54E-12	4.85E+13	1.86E+13	0.2611
262.54	760	3.48E+16	8.23E+18	2.87E+16	2.57E+18	0	7.73E-12	1.33E+14	2.90E+13	0.5967
262.54	760	3.48E+16	8.23E+18	2.87E+16	2.57E+18	0	8.65E-12	1.24E+14	3.06E+13	0.3223
262.54	760	3.48E+16	8.23E+18	2.87E+16	2.57E+18	0	7.67E-12	1.24E+14	3.00E+13	0.1256
262.54	760	3.48E+16	8.23E+18	2.87E+16	2.57E+18	0	8.65E-12	1.35E+14	2.65E+13	0.4005
262.54	760	3.48E+16	8.23E+18	2.87E+16	2.57E+18	0	7.52E-12	1.52E+14	3.04E+13	0.4079
262.54	760	3.48E+16	8.23E+18	2.87E+16	2.57E+18	0	9.76E-12	1.55E+14	3.51E+13	0.3373
244.94	760	3.73E+16	8.82E+18	3.07E+16	2.76E+18	0	1.16E-11	5.54E+13	2.72E+13	0.0000
244.94	760	3.73E+16	8.82E+18	3.07E+16	2.76E+18	0	1.38E-11	5.81E+13	3.01E+13	0.0000
244.94	760	3.73E+16	8.82E+18	3.07E+16	2.76E+18	0	3.57E-12	6.37E+13	1.76E+13	0.3967
244.94	760	3.73E+16	8.82E+18	3.07E+16	2.76E+18	0	1.04E-11	5.59E+13	2.18E+13	0.0000
244.94	760	3.73E+16	8.82E+18	3.07E+16	2.76E+18	0	8.92E-12	5.36E+13	2.20E+13	0.0000
244.94	760	3.73E+16	8.82E+18	3.07E+16	2.76E+18	0	4.26E-11	7.01E+13	3.54E+13	0.2559